Università degli Studi di Ferrara

DOCTORAL COURSE IN
PHYSICS

CYCLE XXXVII

COORDINATOR Prof. Paolo Lenisa

Cosmological cross-correlations as a probe of new physics

Scientific/Disciplinary (SDS) FIS/02

Candidate
Stefano Arcari

Supervisor
Dr. Alessandro Gruppuso

Co-advisor
Dr. Massimiliano Lattanzi

Years 2021-2024

DOCTORAL COURSE IN
PHYSICS

CYCLE XXXVII

COORDINATOR Prof. Paolo Lenisa

Cosmological cross-correlations as a probe of new physics

Scientific/Disciplinary (SDS) FIS/02

Candidate
Stefano Arcari

Supervisor
Dr. Alessandro Gruppuso

Co-advisor
Dr. Massimiliano Lattanzi

Years 2021-2024

The dark side of the force is a pathway to many abilities some consider to be unnatural.
— Chancellor Palpatine

Non c'è sconfitta nel cuore di chi se ne sbatte il c∗∗∗o.
— Dott. xxx

Abstract

In an era of precision cosmology, cross-correlations between cosmological observables offer a powerful approach to testing new physics beyond the standard model and deepening our understanding of the universe. This thesis explores the potential of these techniques to probe fundamental phenomena, exploiting them as tools to reveal subtle signals that might otherwise remain hidden. Our work begins by developing a novel framework that leverages cosmic voids as unique environments for investigating particle dark matter. By cross-correlating unresolved gamma-ray background radiation with gravitational tracers like cosmic shear and galaxy number counts, we uncover that cosmic voids offer a particularly promising "background-free" region for detecting signals from dark matter decay. While current instruments such as the *Fermi*-LAT telescope are not yet sensitive enough, we demonstrate that future detectors with improved angular resolution and exposure could significantly constrain the properties of dark matter, particularly its decay lifetime, across a wide range of masses. We then shift our focus to parity violating physics, presenting the first-ever cross-correlation between anisotropic cosmic birefringence and the spatial distribution of galaxys as a probe of axion physics. By exploring ultralight axion models, our analysis constrains the axion-photon coupling with an unprecedented level of precision, showing how the combination of cosmic birefringence and galaxy surveys can provide a powerful probe of parity-violating physics in the dark sector. Lastly, we turn to the upcoming *Euclid* mission, whose data will revolutionize our understanding of the large-scale structure of the universe. We establish a robust framework for cross-correlating *Euclid*'s galaxy clustering data with the late integrated Sachs-Wolfe effect, showing how this synergy will refine constraints on cosmological parameters and offer deeper insights into the effects of dark energy on cosmic evolution. This thesis demonstrates how cross-correlations between cosmological probes can unlock new avenues for exploring the fundamental laws of nature, providing a versatile and promising method to test the most pressing questions about the universe's composition and its ongoing expansion.

The important thing is not to stop questioning. Curiosity has its own reason for existence. One cannot help but be in awe when he contemplates the mysteries of eternity, of life, of the marvelous structure of reality. It is enough if one tries merely to comprehend a little of this mystery each day.
— Albert Einstein

Acknowledgments

Nulla malesuada porttitor diam. Donec felis erat, congue non, volutpat at, tincidunt tristique, libero. Vivamus viverra fermentum felis. Donec nonummy pellentesque ante. Phasellus adipiscing semper elit. Proin fermentum massa ac quam. Sed diam turpis, molestie vitae, placerat a, molestie nec, leo. Maecenas lacinia. Nam ipsum ligula, eleifend at, accumsan nec, suscipit a, ipsum. Morbi blandit ligula feugiat magna. Nunc eleifend consequat lorem. Sed lacinia nulla vitae enim. Pellentesque tincidunt purus vel magna. Integer non enim. Praesent euismod nunc eu purus. Donec bibendum quam in tellus. Nullam cursus pulvinar lectus. Donec et mi. Nam vulputate metus eu enim. Vestibulum pellentesque felis eu massa.

Quisque ullamcorper placerat ipsum. Cras nibh. Morbi vel justo vitae lacus tincidunt ultrices. Lorem ipsum dolor sit amet, consectetuer adipiscing elit. In hac habitasse platea dictumst. Integer tempus convallis augue. Etiam facilisis. Nunc elementum fermentum wisi. Aenean placerat. Ut imperdiet, enim sed gravida sollicitudin, felis odio placerat quam, ac pulvinar elit purus eget enim. Nunc vitae tortor. Proin tempus nibh sit amet nisl. Vivamus quis tortor vitae risus porta vehicula.

Fusce mauris. Vestibulum luctus nibh at lectus. Sed bibendum, nulla a faucibus semper, leo velit ultricies tellus, ac venenatis arcu wisi vel nisl. Vestibulum diam. Aliquam pellentesque, augue quis sagittis posuere, turpis lacus congue quam, in hendrerit risus eros eget felis. Maecenas eget erat in sapien mattis porttitor. Vestibulum porttitor. Nulla facilisi. Sed a turpis eu lacus commodo facilisis. Morbi fringilla, wisi in dignissim interdum, justo lectus sagittis dui, et vehicula libero dui cursus dui. Mauris tempor ligula sed lacus. Duis cursus enim ut augue. Cras ac magna. Cras nulla. Nulla egestas. Curabitur a leo. Quisque egestas wisi eget nunc. Nam feugiat lacus vel est. Curabitur consectetuer.

Publications

This thesis is based on the results of the following papers:

- **Got plenty of nothing: cosmic voids as a probe of particle dark matter** [1]
  S. Arcari, E. Pinetti and N. Fornengo,
  Journal of Cosmology and Astroparticle Physics (JCAP) 11 (2022) 011

- *Euclid. I. Overview of the Euclid mission* [2]
  Euclid collaboration,
  Submitted to Astronomy & Astrophysics (A&A)

- **Conversations in the dark: cross-correlating birefringence and LSS to constrain axions** [3]
  S. Arcari, N. Bartolo, A. Greco, A. Gruppuso, M. Lattanzi and P. Natoli,
  Journal of Cosmology and Astroparticle Physics (JCAP) 10 (2024) 101

- **Stairway to Axions: the cross-correlation of birefringence and galaxies from NPIPE and Quaia** [4]
  S. Arcari, N. Bartolo, G. Fabbian, A. Greco, A. Gruppuso, M. Lattanzi, P. Natoli, L. Pagano and G. Zagatti,
  To be submitted to JCAP

- **Euclid Preparation: Estimators of the ISW-GC cross-correlation** [5]
  Euclid collaboration (S. Arcari among corresponding authors),
  To be submitted to A&A

- **Euclid Preparation: Cosmology Likelihood for Observables in Euclid (CLOE): Code implementation** [6]
  Euclid collaboration (S. Arcari among corresponding authors),
  To be submitted to A&A

A special mention goes to the unseen "Force" that shapes the cosmos, which inspired me through my cosmological journey:

- **Echoes from a long time ago: Chewbacca inflation** [7]
  D. Sidious, S. Arcari et al.
  Annals of Improbable Research 04 (2024) 01

Contents

Chapter 1

Introduction

"Silence... Emptiness... Blackness... Zilcho... Zero-zippo... Diddy-squat...
A long time ago in a galaxy far, far way... "

"Wait, what is a galaxy?"

"Alright, alright peanut. Let's start over.
A long time ago in a hell far, far away... "

"Are we sure it was far?"

"Oh dear, you are starting to piss me off. Poetic license, okay?"

"Calm down mate, just sayin'... "

"A long time ago in a hell far, far away there was... well, nothing. Not even the kind of nothing you find in the back of your fridge when you need a snack—just absolute, cosmic-level nothingness!"

"Interesting, I always have snacks in the fridge, though."

"... You're hopeless. Even in a universe of nothing, you're still thinking about snacks! The story will be long, so just shut up already."

"... "

"... Where were we?... Oh, right. Silence... Finally."

At some point, time decided to throw a party, and with a colossal "bang" (not the kind that comes from a birthday cake), the universe was born! Strangely, no one really knows why or how this cosmic confetti explosion happened—perhaps the universe was just bored and wanted to spice things up. In the chaotic aftermath, the universe expanded faster than a kid's imagination, giving birth to atoms, stars, and galaxies like a cosmic chef whipping up a bizarre stew. Over billions of years, these ingredients simmered down, creating planets and the delightful mess we call life. Yet, even with all our telescopes and theories, we're left scratching our heads over mysteries like dark matter, dark energy, and why we can never find the socks that disappear in the dryer. Each of these questions keeps scientists up at night, proving that the universe is not just complex—it's also a hilarious puzzle waiting to be solved!

Welcome to the universe's grand mystery tour, where the questions just keep piling up like socks in a dryer! In the last twenty years, cosmologists have gathered a staggering amount of data that has helped us stitch together a clearer picture of the cosmos, encapsulated in the concordance model known as ΛCDM [8–12]. It's like a universal blueprint, but even with this impressive model in hand, we still find ourselves scratching our heads over the ultimate puzzle: the nature of dark matter and dark energy.

Imagine the universe as a cosmic smoothie: all the ingredients are there—stars, galaxies, and the mysterious dark components—but we still can't quite figure out how to blend them into a coherent recipe. Upcoming galaxy surveys, like the ambitious *Euclid* [2, 13, 14] project, promise to map the distribution of matter across the extragalactic sky, using everything from galaxy clusters to the subtle art of weak gravitational lensing [15–17]. These surveys will allow us to test gravity on grand scales and better understand the perplexing phenomenon of the universe's accelerated expansion.

The Cosmic Microwave Background (CMB) [8, 9, 11], a faint afterglow from the universe's infancy, is our cosmic selfie from when the universe was just a teenager—hot, dense, and full of potential. While we've extracted a treasure trove of information from the CMB temperature anisotropies thanks to satellites like *Planck* [18–21], there's still plenty hidden in the polarization data, which holds clues to primordial gravitational waves. Detecting these B-modes of polarization is akin to finding the secret sauce for understanding inflation, and upcoming experiments like LiteBIRD (LB) [22], the Simons Observatory (SO) [23] and CMB Stage-4 (CMB-S4) [24] aim to bring this elusive ingredient to light.

As we dig deeper, the large-scale structure (LSS) [10, 12] of the universe reveals even more about its complex nature. Baryon Acoustic Oscillations (BAO) act as a cosmic ruler, helping us refine our measurements of the universe's expansion and the distribution of matter. BAO data are extracted from galaxy surveys such as BOSS DR12 [25], 6dFGS [26] and SDSS-MGS [27]. This interplay between CMB and LSS data will yield a wealth of information, but understanding how to extract that information effectively remains a formidable challenge—akin to trying to solve a Rubik's cube blindfolded!

Despite the successes of the ΛCDM model, fundamental questions linger [8–12]. What exactly is dark matter? Is it Weakly Interactive Massive Particles (WIMPs), axions, or perhaps something entirely different, like the elusive Macroscopic Dark Matter? And dark energy—why does it seem to be accelerating the universe's expansion? These questions have become even more pressing as our observational capabilities have advanced, allowing cosmology to become a powerful probe for testing fundamental physics scenarios that extend beyond the standard models of cosmology and particle physics.

As we embark on this journey through the cosmos, it's clear that we are living in a golden age of cosmology, where observational data is abundant and the mysteries are profound. Each new piece of information brings us closer to unraveling the universe's secrets, while also reminding us that in the grand scheme of things, we're just tiny specks trying to comprehend a vast and whimsical cosmos!

Outline of the thesis. In Chapter 1, we explore the pressing questions in cosmology and examine potential theories and observational approaches to address them. We delve into the Cosmic Microwave Background (CMB) as the earliest probe of the Universe's infancy, highlighting its polarization features. Next, we identify candidates for dark matter, focusing on WIMPs and axions. We also provide a brief overview of the formation of the Universe's large-scale structure—the cosmic web—and emphasize its significance in constraining new physics. Finally, we discuss the role of cross-correlations in cosmology, which will serve as the narrative thread throughout this thesis.

Chapter 2 proposes the Halo-Void Model (HVM) [28] as an innovative framework for in-

vestigating particle dark matter. In this approach, we cross-correlate unresolved sky radiation with gravitational tracers located in the Universe's most desolate areas—cosmic voids. By taking advantage of the diminished astrophysical background in these regions, we aim to isolate a dark matter signal resulting from decaying WIMPs within the mass range of 10 GeV to 1 TeV. Through this novel methodology, we present competitive constraints on the lifetime of decaying dark matter and explore the potential sensitivity to lower-energy candidates, such as axions.

Chapter 3 delves into parity-violating physics with a focus on the rotation of linearly polarized waves, namely cosmic birefringence (CB), which may be induced by axion-like particles (ALPs). After examining the diverse phenomenology responsible for this effect, we propose a theoretical framework to analyze the cross-correlation between CB and galaxy number counts. We investigate a broad range of axion parameters and calculate the signal-to-noise ratio derived from upcoming surveys. Utilizing birefringence data and galaxy maps from *Planck* PR4 [29] and Quaia [30], we present the first-ever measurement of the underlying cross-correlation. Finally, employing a Gaussian likelihood analysis, we derive an unprecedented upper limit on the axion-photon coupling for ultralight candidates.

In Chapter 4, we examine the efforts of the *Euclid* CMB Cross-Correlation Science Working Group (CMBX-SWG) to prepare for a cosmological analysis of the late integrated Sachs-Wolfe (iSW) effect of the CMB via cross-correlation with the galaxy clustering data from *Euclid* [17]. After outlining the anticipated survey capabilities, we demonstrate how variations in analysis settings influence the ability to constrain various cosmological parameters.

Finally, Chapter 5 summarizes my work throughout these exciting years of my PhD, drawing conclusions and highlighting the innovative aspects of my projects.

1.1 The cosmic microwave background

The Cosmic Microwave Background (CMB) is the remnant radiation from the early Universe, specifically originating from the epoch of recombination, which occurred around $z_{\rm rec} \approx 1100$ or approximately 380,000 years after the Big Bang [8, 9, 11]. During this pivotal period, the Universe was primarily composed of ionized hydrogen, free electrons, and photons. As the Universe expanded and cooled, the temperature dropped below roughly 3000 K, allowing electrons to combine with protons and form neutral hydrogen atoms. This significant event drastically reduced the number of free electrons, leading to a decline in Thomson scattering and enabling photons to travel freely. The equivalence of the interaction rate of photons Γ_γ and the expansion rate of the Universe H marks this important moment in cosmic history, as it signifies the transition from an opaque to a transparent Universe, where $\Gamma_\gamma(z_{\rm rec}) \sim H(z_{\rm rec})$. Consequently, this transition allows the CMB to escape from the dense plasma, providing a snapshot of the Universe at this crucial stage and revealing vital information about its initial conditions.

The CMB exhibits a nearly perfect black body spectrum, characterized by a specific temperature and distribution of photon energies. The spectral energy density of a black body is described by Planck's law [31],

$$I(\nu, T_0) = 4\pi\nu^3 \frac{1}{e^{\frac{2\pi\nu}{T_0}} - 1}\,, \tag{1.1}$$

where $I(\nu, T_0)$ is the intensity of radiation at frequency ν, in natural units, and T_0 is the temperature of the black body. In the early 1990s, the FIRAS instrument aboard the COBE satellite [32] conducted the first measurements of the CMB temperature T. Their findings confirmed that the CMB spectrum conforms to the form described in eq. (1.1), yielding a temperature of $T_0 = 2.72548 \pm 0.00057$ K [33].

The CMB is remarkably isotropic, with a mean temperature T_0 given by [11]

$$T_0 = \frac{1}{4\pi} \int \mathrm{d}\Omega \, T(\hat{\mathbf{n}}) \,, \tag{1.2}$$

where $T(\hat{\mathbf{n}})$ is the CMB temperature measured in the direction of the unit vector $\hat{\mathbf{n}}$. Despite its isotropy, tiny fluctuations in temperature exist [8, 9, 11], denoted as $\delta T(\hat{\mathbf{n}}) \equiv T(\hat{\mathbf{n}}) - T_0$. Some of these fluctuations, known as primary anisotropies, originate from cosmological perturbations generated during inflation and are imprinted in the photon-baryon plasma. In addition, other inhomogeneities in the average temperature field arise from interactions between photons and matter following decoupling or, e.g., dark energy effects, referred to as secondary anisotropies. Fig. 1.1 displays the latest map of temperature fluctuations in the CMB, as captured by the Planck satellite [20].

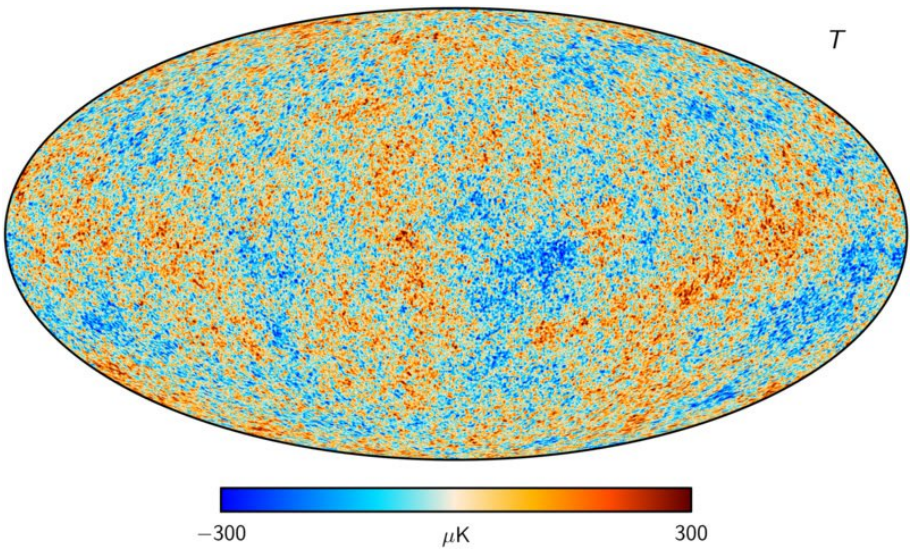

Figure 1.1: CMB temperature map from *Planck* 2018 data release [20].

The temperature fluctuations in the CMB can be analyzed through their expansion in spherical harmonics $Y_{\ell m}$. The fluctuation field $\delta T(\hat{\mathbf{n}})$ can be expressed as

$$\delta T(\hat{\mathbf{n}}) = \sum_{\ell=1}^{\infty} \sum_{m=-l}^{l} a^T_{\ell m} Y_{\ell m}(\hat{\mathbf{n}}) \,, \tag{1.3}$$

where $a^T_{\ell m}$ are the expansion coefficients satisfying the relation

$$a^{*T}_{\ell m} = (-1)^m a^T_{\ell,-m} \,, \tag{1.4}$$

since $\delta T(\hat{\mathbf{n}})$ is a real function. These coefficients can be computed using the orthogonality of spherical harmonics:

$$a^T_{\ell m} = \int \mathrm{d}\Omega \, T(\hat{\mathbf{n}}) Y^*_{\ell m}(\hat{\mathbf{n}}) \,. \tag{1.5}$$

The fluctuation coefficients $a^T_{\ell m}$ are stochastic variables related to the initial conditions of the Universe and can be characterized by n-point correlation functions [11]. Assuming a Gaussian distribution and isotropy, they can be fully described by the two-point correlation function or equivalently by its harmonic counterpart, the power spectrum [8, 9, 11]

$$C^{TT}_\ell \equiv \langle a^T_{\ell m} a^{*T}_{\ell' m'} \rangle \delta_{\ell\ell'} \delta_{mm'} \,. \tag{1.6}$$

In the ideal case of full-sky observations, we can construct an unbiased estimator for the angular power spectrum C^{TT}_ℓ [11]:

$$\hat{C}^{TT}_\ell = \frac{1}{2\ell+1} \sum_{m=-\ell}^{\ell} |a^T_{\ell m}|^2 \,. \tag{1.7}$$

The angular power spectrum is typically expressed in terms of

$$D^{TT}_\ell \equiv \frac{\ell(\ell+1)}{2\pi} C^{TT}_\ell \,. \tag{1.8}$$

Assuming ergodicity, this can be rewritten as an average over the $2\ell+1$ values of m for a given multipole ℓ. At low multipoles, the limited number of m values leads to larger uncertainty in the average, resulting in what is known as cosmic variance, an "error" that predominantly affects small multipoles [11, 20] (see fig. 1.2).

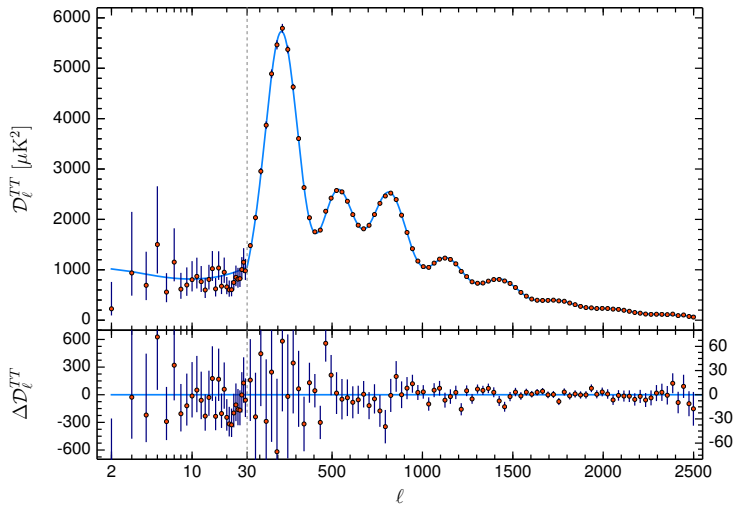

Figure 1.2: Angular power spectrum of CMB temperature anisotropies from *Planck* 2018 data release [20]. The cyan curve represents the black body radiation of eq. (1.1), and the *bottom* panel displays discrepancies of the data points from it. **CREDIT: *Planck* collaboration**.

The fluctuations observed in the CMB temperature spectrum can be categorized into three main regimes, each reflecting distinct physical processes (refer to [34] for a more detailed discussion):

1. **Large angular scales (low multipoles)**: the spectrum shows a flat plateau due to the Sachs-Wolfe effect [35]. Here, fluctuations with wavelengths larger than the sound horizon at recombination are frozen in their initial configuration, providing direct information about

primordial perturbations from inflation. The temperature anisotropies observed today relate to fluctuations in the gravitational potential Φ on the last scattering surface

$$\frac{\Delta T}{T} = \frac{\Phi}{3}\,. \tag{1.9}$$

2. **Intermediate scales**: this region exhibits an oscillatory behavior corresponding to perturbations that entered the horizon or were already sub-horizon before recombination. The competition between gravity and radiation pressure generates acoustic oscillations in the pre-recombination plasma, resulting in a series of peaks. The first peak at $l \sim 200$ is particularly significant, as it reflects the angular scale under which we observe the sound horizon at recombination. This peak's position constrains the curvature of the Universe, consistent with observations of a spatially flat Universe [21].

3. **Small angular scales (high multipoles)**: The amplitude of temperature fluctuations is damped due to the random walk of CMB photons between collisions with free electrons during recombination. Photons with wavelengths shorter than the photon mean free path mix between hot and cold regions, smoothing temperature fluctuations and resulting in an exponential damping of the acoustic peaks [36].

Cosmological Implications

The features observed in the CMB spectrum are strongly dependent on cosmological parameters, enabling their use as a powerful probe to test the standard ΛCDM model and potential extensions (refer to [8, 9, 11] for a more thorough discussion of the following). The six key parameters of the ΛCDM model are[1]:

- the baryon density $\Omega_b h^2$,
- the cold dark matter density $\Omega_c h^2$,
- the amplitude of primordial curvature perturbations A_s,
- the scalar spectral index n_s,
- the optical depth τ,
- the angular size of the sound horizon $\theta_* = r_s(z_{\rm rec})/d_A(z_{\rm rec})$, where $r_s(z_{\rm rec})$ and $d_A(z_{\rm rec})$ are respectively the comoving sound horizon and the comoving angular diameter distance at decoupling.

Each parameter influences the CMB spectrum in distinct ways. For instance, varying A_s results in an overall vertical shift of the spectrum, while changes to n_s tilt the CMB spectrum, increasing power at small scales for $n_s > 1$ and decreasing it for $n_s < 1$.

Modifying the baryon density affects the speed of acoustic waves, altering the comoving sound horizon at decoupling and shifting the CMB spectrum. Increasing baryon density enhances the inertia of the baryon-photon fluid, amplifying compression peaks and reducing rarefaction peaks. This also decreases the mean free path of photons, shifting the Silk damping scale to larger multipoles.

In contrast, varying the cold dark matter abundance changes the total matter density Ω_m, affecting the epoch of matter-radiation equality. A lower matter density shifts this equality

[1] $h = H_0/(100\ \mathrm{km\,s^{-1}Mpc^{-1}})$ is the reduced Hubble constant.

closer to recombination, altering the oscillations in the baryon-photon fluid and increasing power around the scales of the first peak. Additionally, potential wells are deepened, resulting in more distant peaks.

The optical depth τ, related to the reionization of the Universe at redshift $z \sim 7$, can partially damp CMB anisotropies due to scattering by free electrons after reionization. This effect suppresses the CMB spectrum at scales within the horizon at the reionization epoch ($\ell \lesssim 10$).

Finally, variations in θ_* affect the comoving sound horizon at decoupling, resulting in an overall shift of the CMB spectrum. Scenarios that extend the ΛCDM model by adding new parameters can also be constrained using CMB observations. For instance, introducing new light particle species increases the radiation energy density, enhancing the early expansion rate of the Universe. This change affects the Hubble rate H, which influences both the damping scale k_d and the position of the first peak in the power spectrum. To eliminate the dependence on d_A, which itself is a function of the Hubble rate, it is useful to consider the ratio of the angular scales of the damping length and the sound horizon: $\theta_d = 1/(k_d d_A)$ and $\theta_* = r_s/d_A$. The ratio between these two scales is [37]

$$\frac{\theta_d}{\theta_*} \propto H_{\rm rec}^{1/2}\,, \tag{1.10}$$

Increasing the energy density of light relics (and hence H) leads to a larger θ_d if θ_* is kept constant, resulting in a shift of the damping scale to larger angular scales (smaller multipoles) and reducing power at small scales. Therefore, observations of the CMB temperature power spectrum are instrumental in constraining the energy of additional light relics.

In summary, the CMB serves as a vital tool for understanding the early Universe, providing insights into its composition, dynamics, and evolution. By analyzing the temperature fluctuations and power spectrum of the CMB, cosmologists can extract valuable information about the underlying physics governing the cosmos.

1.1.1 CMB polarization

CMB radiation is characterized not only by temperature anisotropies but also by its polarization, which provides critical insights into cosmology [8, 9, 11, 20]. CMB polarization arises primarily from Thomson scattering between photons and free electrons during recombination and reionization. This polarization serves as a complementary probe to temperature anisotropies, encoding additional information about the early Universe and cosmological parameters.

CMB polarization is typically described using the Stokes parameters I, Q, U, and V [38, 39]. Here, I represents the total intensity of the radiation, while Q and U describe the linear polarization, and V characterizes the circular polarization (which is not expected to be generated during recombination but could arise from later interactions [40–52]). The linear polarization fields, Q and U, depend on the coordinate system, transforming under rotations in the plane transverse to the direction of photon propagation. For a rotation by an angle ψ, Q and U transform as:

$$\begin{aligned} Q &\to Q\cos(2\psi) - U\sin(2\psi)\,, \\ U &\to Q\sin(2\psi) + U\cos(2\psi)\,. \end{aligned} \tag{1.11}$$

To simplify this analysis, it is convenient to combine Q and U into the complex quantities $Q \pm iU$,

which transform as spin-2 fields [11, 38]

$$\begin{aligned}(Q+iU) &\to e^{2i\psi}(Q+iU)\,,\\ (Q-iU) &\to e^{-2i\psi}(Q-iU)\,.\end{aligned} \tag{1.12}$$

These spin-2 fields can be expanded in terms of spin-weighted spherical harmonics ${}_{\pm2}Y_{\ell m}$, yielding the following expansions:

$$\begin{aligned}(Q+iU)(\hat{\mathbf{n}}) &= \sum_{\ell m} a_{2,\ell m}\,{}_2Y_{\ell m}(\hat{\mathbf{n}})\,,\\ (Q-iU)(\hat{\mathbf{n}}) &= \sum_{\ell m} a_{-2,\ell m}\,{}_{-2}Y_{\ell m}(\hat{\mathbf{n}})\,.\end{aligned} \tag{1.13}$$

However, it is often more convenient to work with quantities that behave as scalars under rotations [11]. By applying the spin-raising and spin-lowering operators to $Q \pm iU$, we can construct the E-mode and B-mode polarization fields, which are scalar quantities:

$$\begin{aligned}E(\hat{\mathbf{n}}) &= \sum_{\ell m} a^E_{\ell m} Y_{\ell m}(\hat{\mathbf{n}})\,,\\ B(\hat{\mathbf{n}}) &= \sum_{\ell m} a^B_{\ell m} Y_{\ell m}(\hat{\mathbf{n}})\,,\end{aligned} \tag{1.14}$$

where the expansion coefficients $a^E_{\ell m}$ and $a^B_{\ell m}$ are related to $a_{2,\ell m}$ and $a_{-2,\ell m}$ by [38]

$$\begin{aligned}a^E_{\ell m} &= -\frac{1}{2}(a_{2,\ell m} + a_{-2,\ell m})\,,\\ a^B_{\ell m} &= \frac{i}{2}(a_{2,\ell m} - a_{-2,\ell m})\,.\end{aligned} \tag{1.15}$$

E-modes represent the curl-free component of the polarization, while B-modes correspond to the divergence-free, curl-like component [8, 9, 11]. E-modes are sourced by scalar perturbations, such as those from acoustic oscillations in the photon-baryon plasma, and exhibit acoustic peaks similar to the temperature anisotropy spectrum [20] (see fig. 1.3). The B-modes, on the other hand, cannot arise, at linear level, from scalar modes but may emerge from tensor perturbations such as primordial gravitational waves or from gravitational lensing of E-modes by large-scale structure [53, 54].

One of the most important aspects of the E and B decomposition is their behavior under parity transformations. Under a parity transformation, which flips spatial coordinates as $\mathbf{x} \to -\mathbf{x}$, the E-mode polarization remains invariant, while the B-mode polarization changes sign [34, 53],

$$\begin{aligned}E(\hat{\mathbf{n}}) &\to E(-\hat{\mathbf{n}})\,,\\ B(\hat{\mathbf{n}}) &\to -B(-\hat{\mathbf{n}})\,.\end{aligned} \tag{1.16}$$

This property allows us to use B-modes as a probe for parity-violating physics. In the standard cosmological model, certain correlations, namely $\langle EB\rangle$ and $\langle TB\rangle$, are expected to vanish due

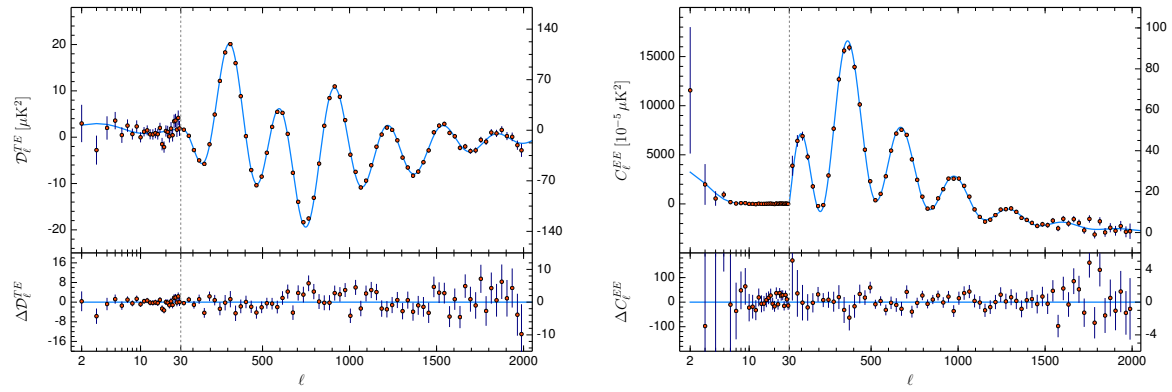

Figure 1.3: Angular power spectrum of CMB polarization from *Planck* 2018 data release [20]. **CREDIT: *Planck* collaboration**.

to parity conservation [11, 20, 34, 53]. However, if these correlations were observed to be non-zero, they would provide clear evidence for new physics involving parity violation [55–57], such as interactions with axion-like particles, dark matter models, or other beyond-Standard-Model (BSM) scenarios (see chapter 3 for more details).

The B-modes, in particular, hold the promise of detecting primordial gravitational waves generated during inflation [7, 53, 54, 58, 59]. Such a detection would provide a direct measurement of the energy scale of inflation and offer insight into the physics of the very early Universe. Furthermore, circular polarization, though expected to be absent at the time of last scattering, could be generated as CMB photons propagate across the Universe. While known physical processes produce only small amounts of circular polarization[40–47], certain BSM scenarios predict a significant degree of circular polarization [48–52], making it another possible signature of new physics.

Future experiments, such as LiteBIRD [22], the Simons Observatory [23], and CMB-S4 [24], are designed to improve the precision of CMB polarization measurements. These experiments will focus on both E- and B-mode polarization to refine constraints on cosmological parameters, search for primordial gravitational waves, and test for possible new physics. In particular, the detection of non-zero $\langle EB \rangle$ or $\langle TB \rangle$ correlations would open new avenues for exploring parity-violating phenomena and BSM interactions.

In summary, CMB polarization is a powerful tool for cosmology, offering insights into the physics of the early Universe, inflationary gravitational waves, and potential new physics beyond the Standard Model. The ongoing and upcoming experiments will help push the boundaries of our understanding of the cosmos, utilizing the full potential of E- and B-mode polarization data.

1.2 The large scale structure of the universe

The large-scale structure (LSS) of the Universe refers to the intricate and interconnected distribution of galaxies, galaxy clusters, filaments, and vast cosmic voids [9, 10, 12, 60]. This so-called cosmic web is the product of billions of years of gravitational collapse, acting on the tiny density fluctuations present in the early universe. These initial fluctuations are observed in the cosmic microwave background, but while the CMB reveals the universe's early conditions, the LSS probes the late-time dynamics, where gravitational interactions have grown significantly more complex [10–12].

One of the key differences between the CMB and the LSS is their respective levels of non-

linearity. The CMB's fluctuations are mostly in the linear regime, allowing for straightforward theoretical modeling. In contrast, the LSS evolves into a highly non-linear regime, particularly at smaller scales where galaxies cluster and interact [60, 61]. This makes studying the LSS far more challenging than analyzing the relatively well-behaved CMB data. Non-linear gravitational collapse leads to dense structures such as galaxy clusters and the empty voids between them, making it difficult to model the LSS with simple linear perturbation theory.

Despite these challenges, the LSS is an essential cosmological probe. By studying the spatial distribution of galaxies, we can trace the three-dimensional distribution of matter in the Universe. Observations of galaxy clustering enable direct measurements of the cosmic expansion history and provide insights into the growth of cosmic structures. This is done by measuring the angular positions of galaxies in the sky and analyzing their redshifts. The latter reveals the galaxies' distances from us, allowing for a 3D mapping of the cosmos. Galaxy clustering is quantified by the two-point correlation function $\xi(\mathbf{r})$, which measures the excess probability of finding a galaxy at a distance r from another galaxy at position $\mathbf{r_1}$, compared to a random distribution [60]

$$\xi(\mathbf{r}) = \frac{\langle n(\mathbf{r}_1) n(\mathbf{r}_1 + \mathbf{r}) \rangle}{\bar{n}^2} - 1 \,, \tag{1.17}$$

where $n(\mathbf{r})$ is the galaxy number density at position $\mathbf{r}$ and $\bar{n}$ is the average number density of galaxies. This function encodes how galaxies cluster on different scales, allowing us to probe the distribution of matter in the universe.

A particularly powerful tool in LSS studies is the observation of baryon acoustic oscillations [60, 62], a feature in the matter power spectrum that originates from sound waves in the early photon-baryon plasma. These oscillations imprint a characteristic scale r_s, the sound horizon at the time of recombination, in the distribution of galaxies. The BAO scale serves as a "standard ruler" for measuring distances in the universe, helping to constrain the expansion rate.

The galaxy distribution, however, does not perfectly trace the underlying matter distribution. Instead, it is biased by a factor b, which depends on the galaxy sample and redshift [60, 63]. This relationship is typically assumed to be linear on large scales,

$$\delta_g(\mathbf{x}) = b\, \delta_m(\mathbf{x}) \,, \tag{1.18}$$

where $\delta_g(\mathbf{x})$ is the galaxy density perturbation and $\delta_m(\mathbf{x})$ is the underlying matter density perturbation. Here, $\mathbf{x} = (z, \theta, \phi)$ represents the three-dimensional position of the galaxy, with z being the redshift and (θ, ϕ) the angular coordinates.

Further complicating the study of LSS are the so-called redshift-space distortions (RSD) [10, 60, 64]. The redshifts of galaxies are affected not only by the Hubble flow but also by their peculiar velocities due to local gravitational interactions. These peculiar motions distort the apparent clustering pattern of galaxies in redshift space. On large scales, galaxies are seen to move towards overdense regions, which squashes the density field along the line of sight, making the galaxy clustering appear stronger. On smaller scales, the random motions within galaxy clusters lead to the opposite effect, reducing the clustering amplitude, an effect known as the "fingers of God."

The redshift-space density perturbation is modeled as [60]

$$\delta_{g,\,\mathrm{RSD}}(\mathbf{x}) = b\, \delta_m(\mathbf{x}) - \frac{\partial}{\partial \mathbf{x}} \left(\frac{u_m(\mathbf{x}) \cdot \hat{\mathbf{z}}}{aH} \right) \,, \tag{1.19}$$

where $u_m(x)$ is the peculiar velocity field, a is the scale factor, and H is the Hubble parameter. Since the time evolution of large-scale perturbations δ_m is captured by the growth factor D_+, in Fourier space, the peculiar velocity can be related to the matter perturbations through the Euler equation [10, 60]

$$u_m(\mathbf{k},\eta) = \frac{i\mathbf{k}}{k^2}\frac{\dot{D}_+}{D_+}\delta_m(\mathbf{k},\eta) = aHf\frac{i\mathbf{k}}{k^2}\delta_m(\mathbf{k},\eta)\,. \tag{1.20}$$

Here, $f = \mathrm{d}\ln D_+/\mathrm{d}\ln a$ is the linear growth rate, which quantifies the growth of cosmic structures over time. For a ΛCDM cosmology, $f \simeq [\Omega_m(z)]^{0.55}$, where $\Omega_m(z)$ is the matter density parameter.

In Fourier space, the galaxy perturbations in redshift space are given by

$$\delta_{g,\,\mathrm{RSD}}(\mathbf{k}) = \left(b + f\mu_k^2\right)\delta_m(\mathbf{k})\,, \tag{1.21}$$

where μ_k is the cosine of the angle between the wavevector $\mathbf{k}$ and the line of sight. This shows that the observed power spectrum in redshift space is enhanced in the direction along the line of sight.

The galaxy power spectrum, including the effects of redshift-space distortions, becomes

$$P_{g,\,\mathrm{RSD}}(k,\mu_k,z) = P_L(k,z)\left(b + f\mu_k^2\right)^2\,, \tag{1.22}$$

where $P_L(k,z)$ is the linear matter power spectrum. The combination of BAO and RSD measurements provides valuable information about the growth of structure and the expansion history of the Universe [10, 12, 60].

Despite the significant progress made in our understanding of galaxy clustering, baryon acoustic oscillations, and redshift-space distortions through current observations—such as those from the Sloan Digital Sky Survey (SDSS) [65, 66], the Dark Energy Survey (DES) [67], the Baryon Oscillation Spectroscopic Survey (BOSS) [25], and the extended BOSS (eBOSS) [68]—our knowledge of large-scale structure remains incomplete. These surveys have provided critical insights, allowing for refined measurements of the matter power spectrum, clustering statistics, and the imprint of BAO as a standard ruler for cosmological distances. Furthermore, RSD analysis from these observations has helped probe the growth of cosmic structures by revealing how peculiar velocities of galaxies induce anisotropies in their spatial distribution. Nevertheless, the large-scale structure of the Universe is highly non-linear, and understanding its evolution—particularly on smaller, non-linear scales—poses significant challenges that current observations can only partially address. Even though these surveys have considerably improved the precision of cosmological parameters, much of the late-time universe remains unexplored.

Looking ahead, future large-scale surveys, such as *Euclid* [2, 13, 14], the Dark Energy Spectroscopic Instrument (DESI) [67, 69], and the Vera C. Rubin Observatory's Legacy Survey of Space and Time (LSST) [70], will be crucial for advancing this field. These surveys are designed to map the distribution of galaxies over much larger volumes and to greater depths, spanning from the local universe to distant epochs. For instance, Euclid will provide an unprecedented 3D map of galaxies by combining wide-field imaging with deep spectroscopy, enabling precise measurements of both BAO and RSD on a larger scale and across a broader redshift range.

The DESI survey, with its focus on obtaining millions of galaxy spectra, will complement Euclid by providing highly accurate redshifts and detailed information about galaxy clustering.

The combination of BAO and RSD data from DESI will not only constrain the nature of dark energy but also test modifications to general relativity by examining how structures grow over time. This will be critical for distinguishing between different models of gravity and for exploring the possibility of new physics.

Moreover, LSST will provide the deepest and most extensive photometric survey of the sky, vastly expanding our view of the cosmic web. By observing billions of galaxies and their distribution over time, LSST will further our understanding of how galaxies form, cluster, and evolve within the cosmic web's network of filaments, halos, and voids. It will also improve our understanding of dark matter and its role in shaping large-scale structure.

Together, these upcoming surveys will offer tighter constraints on cosmological parameters than ever before, including those related to dark energy and the growth rate of cosmic structures. By probing the distribution of galaxies and the matter field with increased precision, they will help address some of the most pressing questions in cosmology—particularly those that cannot be fully answered by observations of the cosmic microwave background alone. In contrast to the CMB, which primarily probes the early universe, these future galaxy surveys will shed light on the more recent stages of cosmic evolution, providing insights into the formation of large-scale structure over cosmic time.

1.3 Dark matter

One of the most remarkable findings in modern cosmology is that ordinary matter, which makes up stars, planets, and everything we observe directly, constitutes only a small fraction of the total matter content of the universe. The dominant form of matter is an unknown substance called dark matter (DM), which interacts only weakly, if at all, with ordinary matter and radiation, except through gravity. Dark Matter plays a critical role in the formation and evolution of cosmic structures, yet its nature remains one of the biggest unsolved mysteries in both cosmology and particle physics [71].

The need for dark matter arises from several key observations. Studies of the LSS of the universe indicate that DM must be non-relativistic (cold) by the time structures such as galaxies form, giving rise to the cold dark matter (CDM) model [72–74]. CDM is essential for explaining how tiny fluctuations in the CMB grew over time to form galaxies, clusters, and the large-scale structures we observe today.

The evidence for dark matter comes from a wide range of astrophysical and cosmological observations [75, 76]:

- **Galactic scales**: the most compelling evidence comes from the rotation curves of spiral galaxies [77, 78]. The observed circular velocity of stars, $v_c(r)$, at different distances from the galactic center deviates from the expected Keplerian decline, $v_c(r) \propto 1/\sqrt{r}$, at large radii. This suggests the presence of an unseen mass component surrounding galaxies, forming what is known as a dark matter halo.

- **Galaxy clusters scales**: on larger scales, two critical pieces of evidence come from observations of the Coma Cluster [78] and the Bullet Cluster [79–81]. In the Coma Cluster, the observed velocity dispersion of galaxies exceeds the prediction from visible matter, implying a dark matter component. The Bullet Cluster provides further evidence, where gravitational lensing maps show a mass distribution that does not align with the hot gas distribution observed via X-ray emissions. This suggests the existence of matter that interacts only gravitationally, but not electromagnetically.

- **Cosmological scales**: measurements of the CMB anisotropies provide strong evidence for dark matter [21, 82]. The relative abundances of total matter, $\Omega_m h^2$, and baryonic matter,

$\Omega_b h^2$, show that the baryon density is insufficient to account for the total matter content, confirming the presence of a non-baryonic dark matter component. The latest Planck results yield a CDM abundance of $\Omega_c h^2 = 0.1200 \pm 0.0012$ [21]. This result is consistent with big bang nucleosynthesis (BBN), which constrains the baryon density to values smaller than the total matter density, reinforcing the need for a dark matter component.

Despite the overwhelming evidence for the existence of dark matter, its fundamental nature remains elusive. The most widely studied models for dark matter propose new particles beyond the Standard Model of particle physics. Some of the leading candidates include (refer to [75, 76, 83] for a more detailed discussion):

- **Weakly interacting massive particles (WIMPs)**: perhaps the most studied DM candidates, WIMPs are particles that were in thermal equilibrium with the early universe. As the universe expanded and cooled, WIMPs "froze out," leaving behind a relic density that matches the observed Dark Matter abundance. The required interaction cross-section for WIMPs is around the weak scale, a coincidence known as the "WIMP miracle." A classic WIMP candidate is the neutralino, which arises in supersymmetric models.

- **Axions**: axions are light, weakly interacting bosons that were originally introduced to solve the strong CP problem in quantum chromodynamics (QCD) [84, 85]. They are also viable dark matter candidates. Axions are thought to form a Bose-Einstein condensate and behave like cold dark matter, making them attractive candidates for solving both particle physics and cosmological puzzles. Further extensions of the Standard Model may lead to weakly interacting particles with axion-like properties and an expanded viable parameter space. These axion-like particles (ALPs) could act as both dark matter and dark energy.

- **Sterile neutrinos**: these neutrinos do not interact through the standard weak force[2], only through gravity, making them a good candidate for warm dark matter (WDM). Sterile neutrinos could explain the small masses of active neutrinos via the seesaw mechanism and provide a solution to the observed neutrino oscillations [86, 87].

- **Macro dark matter (MDM)**: a more unconventional candidate, MDM refers to large macroscopic objects that could make up dark matter. These objects, if massive enough, would have a low number density but could still account for the observed gravitational effects of dark matter [88]. The interaction cross-section of such objects would be small because of their low number density, rather than their intrinsic weak interactions.

- **Primordial black holes (PBHs)**: these are black holes that could have formed in the early universe due to the collapse of high-density regions [89, 90]. PBHs could account for dark matter if they were formed in sufficient numbers with appropriate mass distributions. Recent interest in PBHs has been renewed due to their potential link with gravitational wave detections and their role in explaining the observed dark matter density. However, significant challenges arise from observational constraints that suggest PBHs alone cannot account for the totality of dark matter in the universe [91, 92].

- **Other exotic candidates**: other possibilities include self-interacting dark matter [93, 94], where dark matter particles have non-negligible interactions with themselves but not

[2]Sterile neutrinos are hypothesized to interact weakly with other particles, but their interactions are heavily suppressed because they only interact through mixing with active neutrinos (the standard types of neutrinos that participate in weak interactions). This mixing is characterized by a small "mixing angle," which determines the probability of a sterile neutrino oscillating into an active neutrino. Since the mixing angle is very small, the likelihood of these oscillations occurring is correspondingly low, meaning that any weak interactions of sterile neutrinos—mediated only through their conversion into active neutrinos—are highly infrequent. Consequently, their interaction rate is suppressed, making sterile neutrinos very challenging to detect.

with baryons. Additionally, certain modifications to gravity (such as MOND, modified Newtonian dynamics [95, 96]) have been proposed, although they are generally less favored due to their inability to explain all observations, especially at cosmological scales.

While these candidates are well-motivated theoretically, direct experimental evidence for dark matter has yet to be found. Direct detection experiments search for interactions between dark matter and detectors, but no confirmed signals have been observed. Indirect detection methods, such as looking for high-energy neutrinos from dark matter annihilations or effects on cosmological expansion, have similarly provided constraints without conclusive results.

Cosmological probes, including CMB and LSS observations, offer another route to constraining dark matter properties, though these constraints are model-dependent. As the quest to unveil the true nature of dark matter continues, it remains one of the most pressing and intriguing problems in both cosmology and particle physics.

In the next sections, I review in more detail two compelling candidates of particle DM (WIMPs and axions) which will be key to both chapter 2 and 3.

1.3.1 WIMPs

Weakly interacting massive particles have long been considered one of the most compelling candidates for dark matter due to their theoretical foundations, compatibility with cosmological observations, and the naturalness of their predicted properties. Originating from extensions of the Standard Model of particle physics, WIMPs typically arise in supersymmetric theories [97–104] and other BSM frameworks (see, e.g, [105–107]). Their interaction strength is expected to be weak, leading to a characteristic mass range that aligns well with astrophysical observations of dark matter.

One attractive feature of WIMPs is their ability to provide a viable mechanism for the observed dark matter density in the universe. The so-called "WIMP miracle" refers to the relationship between the mass of WIMPs and their interaction cross-section, which allows for a thermal relic density consistent with the cosmological measurements. Specifically, in the early universe, WIMPs are assumed to be in thermal equilibrium with the plasma of particles. As the universe expands and cools, WIMPs eventually "freeze out" when their interaction rate falls below the expansion rate, leading to a stable relic density. The resulting density of WIMPs today can be expressed as [75, 76]

$$\Omega_c h^2 \approx \frac{1.07 \times 10^9\,\mathrm{GeV}^{-1}}{g_*^{1/2}\langle\sigma v\rangle}\,, \tag{1.23}$$

where Ω_c is the dark matter density parameter, g_* is the effective number of degrees of freedom at freeze-out, and $\langle\sigma v\rangle$ is the thermally averaged cross-section for WIMP annihilation. For WIMPs to account for the observed dark matter density, a typical annihilation cross-section on the order of $\langle\sigma v\rangle \sim 3 \times 10^{-26}\,\mathrm{cm}^3/\mathrm{s}$ is needed, which conveniently coincides with electroweak-scale interactions [76, 97].

WIMPs are typically predicted to have masses in the range of a few GeV to several TeV. This mass range is particularly compelling because it overlaps with the energy scales accessible at particle colliders like the Large Hadron Collider (LHC) and can also be probed by direct detection experiments. Theoretical models such as the minimal supersymmetric Standard Model (MSSM) [108] and other extensions often yield WIMP candidates like the neutralino, which is the lightest supersymmetric particle. The MSSM predicts a variety of interaction channels for WIMPs, such as elastic scattering with nucleons and annihilation into standard model particles.

Despite the strong theoretical motivation for WIMPs, significant challenges remain. Notably, no direct detection of WIMPs has been confirmed in experiments like LUX-ZEPLIN [109, 110],

XENON1T [111], or at collider experiments like the LHC. This absence of detection has led to an increasing search for alternative dark matter candidates or modifications to existing WIMP models. One of the critical drawbacks of the WIMP paradigm is the tension between the predicted interaction rates and the results from direct detection experiments. The sensitivity of these experiments continues to improve, but the failure to observe WIMPs has raised questions about their properties and mass.

Detection techniques for WIMPs primarily fall into two categories: direct detection [112] and indirect detection [113]. In direct detection, experiments aim to measure the recoil of nuclei caused by WIMP-nucleus interactions. Common methods use cryogenic detectors, liquid noble gases, or semiconductor detectors to look for tiny energy deposits corresponding to WIMP interactions. Current experiments are designed to be sensitive to the expected signals, although background noise from cosmic rays and radioactive decay presents a considerable challenge. Indirect detection focuses on identifying the products of WIMP annihilations or decays in regions of high dark matter density, such as the center of the Milky Way or in nearby dwarf galaxies. This can include the detection of high-energy photons (gamma-rays), neutrinos, or cosmic rays produced from WIMP annihilation/decay events. Instruments like the Fermi Gamma-ray Space Telescope [114, 115] and IceCube Neutrino Observatory [116, 117] have searched for such signals, but definitive evidence remains elusive.

In summary, WIMPs stand as a compelling dark matter candidate due to their theoretical underpinnings, predicted mass range, and natural fit within the framework of particle physics. Despite ongoing efforts, the lack of experimental evidence poses significant challenges. The landscape of dark matter research continues to evolve, and the search for WIMPs remains a crucial focus in understanding the fundamental nature of the universe.

1.3.2 Axions and axion-like particles

The strong CP problem of quantum chromodynamics [84, 85] arises from the observed smallness of the neutron electric dipole moment (nEDM) and the absence of CP violation in strong interactions. The QCD Lagrangian, given the symmetry of the theory, allows for the so called θ-term, which can lead to significant CP violation.[3] However, experimental limits on the nEDM [119] suggest that θ must be exceedingly small, typically $|\theta| \lesssim 10^{-10}$. This puzzling situation indicates a fine-tuning problem within the framework of the Standard Model, as no natural explanation for such small values exists.

A compelling solution to the strong CP problem is provided by the introduction of the QCD axion, a hypothetical pseudoscalar particle first proposed by Peccei and Quinn in 1977 [84, 85, 118]. This particle arises from the spontaneous breaking of the Peccei-Quinn (PQ) symmetry, which introduces an additional global $U(1)$ symmetry into the theory, spontaneously breaking at an energy scale f_a. This symmetry breaking gives rise to a new degree of freedom, a Nambu-Goldstone boson called the axion [120, 121]. The axion field dynamically replaces the CP-violating θ-term in QCD, driving it to a CP-conserving phase, ensuring the conservation of CP symmetry in the QCD sector. The QCD axion is a hypothetical pseudoscalar particle whose properties, such as its mass and coupling to other particles, are determined by the decay constant f_a. In the original PQWW (Weinberg-Wilczek) model [120, 121], an extra Higgs doublet is introduced to enforce the $U(1)_{\mathrm{PQ}}$ symmetry, with the SM quarks charged under this symmetry, generating an anomaly in the PQ current. However, this model leads to an axion decay constant of order of the electroweak scale, $f_a \sim v_{EW} \sim 246$ GeV, making the axion too heavy and too strongly coupled to be viable, resulting in its disfavor by experimental searches [122–125].

To address these issues, so-called "invisible" axion models were proposed, wherein $f_a \gg v_{EW}$, leading to a much lighter and weakly coupled axion. The two primary prototypes of

[3] Ref. [118] shows how this term arises naturally by studying the QCD vacuum structure.

these models are the Kim-Shifman-Vainshtein-Zakharov (KSVZ) model [126, 127] and the Dine-Fischler-Srednicki-Zhitnitsky (DFSZ) model [128, 129]. Both models maintain the theoretical motivation of resolving the strong CP problem while providing axions that can also serve as candidates for dark matter.

Beyond QCD axions, various extensions of the SM predict the existence of axion-like particles that share similar properties, arising from spontaneous breaking of additional global symmetries [130–133], Goldstone modes from string theory compactification [134–142], or accidental symmetries [143, 144]. These axion-like particles can contribute to the present DM budget [145, 146] and potentially play significant roles in cosmological scenarios such as inflation [147], baryogenesis [148], and dark energy (see also [138, 140]). Unlike QCD axions, ALPs do not necessarily adhere to the relationships among their mass m_a, couplings g_a, and decay constants f_a. Thus, the parameter space for ALPs is broader than that of QCD axions.

The effective Lagrangian for axion-like particles below the energy scale f_a can be expressed as [140]

$$\mathcal{L} \supset \frac{1}{2}(\partial^\mu a)(\partial_\mu a) - \frac{1}{2}m_0^2 a^2 + \frac{\alpha_s}{8\pi f_a} C_g a G^i_{\mu\nu}\tilde{G}^{\mu\nu,\,i} + \frac{1}{4} g^0_{a\gamma} a F_{\mu\nu}\tilde{F}^{\mu\nu}\,, \tag{1.24}$$

where $g_{a\gamma}$ is the axion-photon coupling, and C_g is the coupling of the axion to gluons. Notably, the inclusion of an explicit mass term m_0 in the Lagrangian signifies a soft breaking of the shift symmetry, distinguishing the axion-like particle model from the strict QCD axion scenario.[4] The Lagrangian in eq. (1.24) can be transformed into a chiral axion Lagrangian through a rotation of the quark fields, which eliminates the axion-gluon interaction term [149]. After incorporating the effects of explicit mass breaking, the resulting axion mass, m_a, and axion-photon coupling, $g_{a\gamma}$, are given by [149, 150]:

$$\begin{aligned} m_a^2 &\simeq m_0^2 + \left[5.7\left(\frac{10^{12}\,\mathrm{GeV}}{f_a/C_g}\right)\mu\mathrm{eV}\right]^2\,, \\ g_{a\gamma} &\simeq g^0_{a\gamma} - 2.3\times 10^{-15}\left(\frac{10^{12}\,\mathrm{GeV}}{f_a/C_g}\right)\,\mathrm{GeV}^{-1}\,. \end{aligned} \tag{1.25}$$

The production mechanisms for axions and ALPs can broadly be categorized into non-thermal and thermal processes. Non-thermally produced axions primarily emerge through the vacuum realignment (VR) mechanism [135–137], closely linked to the evolution of the PQ symmetry. This process leads to a population of cold axions that represent viable candidates for cold dark matter [151–153].

In the context of the QCD axion, the emergence of axions as physical degrees of freedom occurs following the spontaneous symmetry breaking of the PQ symmetry. Initially, there exists no potential for the axion, allowing the field misalignment $\theta = a/f_a$ to take any value between $-\pi$ and π [140]. At the QCD scale, instanton effects activate a potential for the axion. When this potential becomes relevant, the axion field does not necessarily reside at the minimum of the potential, which is characterized by an initial misalignment angle $\theta_i \equiv a_i/f_a$ [140]. If there is a non-zero initial misalignment, the axion field oscillates around the minimum of this potential. During these oscillations, the axions behave as a non-relativistic component, and the energy stored in these oscillations contributes to the overall density of cold dark matter.

To evaluate the relic abundance of cold axions produced via the VR mechanism, we must consider two distinct scenarios:

1. In the pre-inflation scenario, the PQ symmetry is broken during inflation and remains

[4] The QCD axion is recovered by setting $m_0 = 0$ and $C_g = 1$.

unbroken thereafter. Inflation results in a selection of a single patch of the Universe with a specific value of θ_i, which is subsequently expanded to a size greater than the observable Universe. This leads to a homogeneous value for the initial misalignment angle θ_i, which serves as a free and unpredictable parameter of the model. In this case, the relic abundance of axions produced via the VR mechanism is given by [140, 144, 154]

$$\Omega_a h^2 \simeq 0.12 \left(\frac{f_a}{9 \times 10^{11}\,\mathrm{GeV}} \right)^{7/6} \theta_i^2 F(\theta_i)\,, \tag{1.26}$$

where $F(\theta_i)$ accounts for anharmonicities in the axion potential. For a typical value of $F(\theta_i) \sim 1$, the PQ scale must be $f_a \lesssim 10^{12}$ GeV (or equivalently $m_a \gtrsim 6\mu$eV) to avoid exceeding the observed cold dark matter density, $\Omega_c h^2 \sim 0.12$. Larger values of the PQ scale and smaller axion masses may be permissible with fine-tuning of θ_i to very small values. The former case is often referred to as the "natural" axion scenario, while the latter is known as the "anthropic" window. Importantly, topological defects generated during the spontaneous symmetry breaking of the PQ symmetry are inflated away, rendering axion production from their decay negligible.

2. In the post-inflation scenario, the PQ transition occurs after inflation, or the PQ symmetry is restored post-inflation. The Universe remains divided into various patches, each randomly sampling values of θ_i with equal probability. The relic density of cold axions in this case can be computed by averaging the misalignment angle, yielding an average $\langle \theta_i^2 \rangle^{1/2} = \pi/\sqrt{3} \sim 1.81$. The resulting axion relic abundance is then given by [140, 144, 154]

$$\Omega_a h^2 \simeq 0.12 \left(\frac{f_a}{1.9 \times 10^{11}\,\mathrm{GeV}} \right)^{7/6} . \tag{1.27}$$

The correct cold dark matter density is achieved for $f_a \sim 2 \times 10^{11}$ GeV, or $m_a \sim 30\mu$eV. Additionally, in this scenario, the decay of topological defects formed during the PQ phase transition via the Kibble mechanism [155] contributes significantly to axion production. This contribution, particularly from the decay of cosmic axion strings, can numerically be one to two orders of magnitude greater than that from the VR mechanism [151–153, 156–159]. Consequently, this increases the lower limit on the axion mass to $m_a \sim$ meV.

Analogously to the QCD axion, axion-like particles can also be produced via the vacuum realignment mechanism, contributing to the abundance of cold dark matter [140, 145, 160]. For axion decay constants $f_a \leq 10^{16}$ GeV, axions can account for the entirety of the cold dark matter abundance for axion masses around $m_a \approx 10^{-19}$ eV [140]. These very light axions, commonly referred to as ultralight axions (ULAs), arise from scenarios such as string theory compactifications. ULAs exhibit an associated de Broglie wavelength $\lambda_{\mathrm{dB}} \sim$ kpc, categorizing them as fuzzy dark matter. This property results in the suppression of structure formation at small scales, offering a potential solution to the so-called “CDM small-scale crisis" [161, 162]. For ULAs to contribute meaningfully to the dark matter energy density, oscillations of the axion field must commence prior to matter-radiation equality, leading to a lower limit on the mass of ULAs as dark matter candidates given by $m_a \gtrsim 10^{-27}$ eV. CMB observations provide constraints of $m_a > 10^{-24}$ eV for ULAs to account for all dark matter [139]. This constraint is derived from a combination of *Planck* temperature data, WMAP large-scale polarization data [163, 164], and small-scale data from the Atacama Cosmology Telescope (ACT) [82] and the South Pole Telescope (SPT) [165]. When *Planck* data is combined with results from the DES year 1 [166],

this bound improves to $m_a > 10^{-23}$ eV. Furthermore, stronger constraints are obtained by examining the small-scale matter power spectrum, with Lyman-α forest data yielding a bound of $m_a \gtrsim 10^{-21}$ eV [167]. Nonetheless, even lighter candidates might still be contributing to dark energy (refer to chapter 3 for a thorough discussion about the behavior of ULAs).

On the contrary, thermal production of axions occurs from scatterings involving particles in the early cosmological plasma, allowing for a potential contribution to hot, warm, or cold dark matter depending on the axion mass [168–172].

The search for axions and axion-like particles involves various detection techniques [140, 154, 173–175]. Haloscopes are designed to detect axions through their conversion into photons in strong magnetic fields (see, e.g., [176, 177]), while helioscopes aim to observe solar axions produced by nuclear reactions in the Sun [178–180]. Furthermore, astrophysical observations [181–187] and cosmological data [188–194] play crucial roles in constraining axion parameters. For instance, constraints from CMB observations and large-scale structure data provide valuable insights into the mass and coupling of axions and ALPs. A comprehensive collection of currents bounds with graphical representation can be found in ref. [175] and will be discussed in chapter 3.

The theoretical richness of axions and axion-like particles positions them as compelling candidates for addressing fundamental questions in particle physics and cosmology. Their potential role in the dark sector as both dark matter and dark energy candidates highlights their significance in the broader understanding of the universe. The ongoing experimental searches and theoretical developments promise to shed light on these elusive particles, potentially transforming our comprehension of the cosmos.

1.4 Cross-correlations in cosmology

Cross-correlations in cosmology refer to the statistical measure of how two different observables relate to each other across the sky or in redshift space. Mathematically, the cross-correlation F^{XY} between two fields, say X and Y, can be expressed as the expectation value of their product over the sky:

$$F^{XY}(\hat{\mathbf{n}}, \hat{\mathbf{n}}') = \langle X(\hat{\mathbf{n}}) Y(\hat{\mathbf{n}}') \rangle \,, \tag{1.28}$$

with $\hat{\mathbf{n}}$ and $\hat{\mathbf{n}}'$ being directions on the sky. When applied to the spherical harmonic decomposition of these fields, in the assumption of isotropy, the cross-correlation appears as a cross-angular power spectrum C_ℓ^{XY}, which quantifies how the two fields correlate as a function of the angular scale ℓ,

$$C_\ell^{XY} = \langle a_{\ell m}^X a_{\ell m}^{Y*} \rangle \,, \tag{1.29}$$

where $a_{\ell m}^X$ and $a_{\ell m}^Y$ are the spherical harmonic coefficients of fields X and Y, respectively. This angular power spectrum encapsulates how much two observables are correlated at different multipoles ℓ, where smaller ℓ corresponds to larger angular scales. Cross-correlation power spectra have proven to be a highly effective method for reducing noise and systematics in cosmological analyses, while extracting valuable information that might be inaccessible via auto-correlations alone.

Cross-correlations have been instrumental in a wide range of cosmological studies, providing additional constraints and improving the accuracy of parameter estimation. For example, the *Planck* collaboration exploited the temperature-polarization (TE) cross-correlation to achieve tighter constraints on cosmological parameters [21], with respect to those achievable only from temperature (TT) and polarization (EE) power spectra, alongside CMB lensing and baryon acoustic oscillations. The use of cross-correlation in this context was crucial for breaking de-

generacies in parameter space and mitigating the impact of noise and systematic uncertainties, resulting in the most precise measurements of cosmological parameters. Also, cross-correlating E- and B-modes offers as a powerful probe of parity-violating extensions of standard electromagnetism [57, 195–200].

Additionally, cross-correlation between gravitational tracers and other cosmological probes has significantly advanced our understanding of the Universe. For instance, the spatial distribution of galaxies from large-scale structure surveys has been cross-correlated with the CMB temperature anisotropies, leading to the detection of the integrated Sachs-Wolfe (iSW) effect, which provides independent evidence for the existence of dark energy and the late-time acceleration of the Universe [201]. This effect arises from the time evolution of gravitational potentials in the presence of dark energy, which leads to subtle shifts in the energy of CMB photons as they traverse large-scale structure. Cross-correlating galaxies with CMB data enhanced the signal, providing critical support for dark energy models.

Another example involves cross-correlating the Lyman-α forest with galaxy clustering to refine measurements of the matter power spectrum. The Lyman-α forest traces neutral hydrogen in the intergalactic medium and allows cosmologists to probe smaller scales and higher redshifts than galaxy surveys alone can access. By combining Lyman-α data with galaxy surveys, cosmologists have obtained tighter constraints on the amplitude of primordial fluctuations, the matter density Ω_m, and the sum of neutrino masses (see, e.g., [202]). This cross-correlation has expanded our ability to study the Universe at both large and small scales, improving models of cosmic inflation and dark matter.

Cross-correlation techniques are not only limited to cosmology but are also widely used in astrophysics and other scientific fields. For instance, in exoplanet studies, cross-correlating radial velocity measurements with transit data allows for precise determinations of planetary masses and radii, revealing the planet's composition and structure (see, e.g., [203, 204]). In gravitational wave astronomy, cross-correlating signals from multiple detectors reduces noise and improves the precision of source localization [205, 206].

In this thesis, cross-correlation analyses will be employed to investigate three distinct phenomena:

1. **Particle dark matter**: in chapter 2 we will use cross-correlations between the unresolved radiation background and large-scale structure, focusing on cosmic voids. Cosmic voids are underdense regions that are highly sensitive to dark matter annihilation or decay signals, and cross-correlating them with the unresolved radiation background could provide new insights into the nature of particle dark matter.

2. **Axions and cosmic birefringence**: in chapter 3 we will cross-correlate galaxy number counts with the birefringence signal induced by axion-like particles. ALPs, if present, could induce a rotation of the plane of polarization of CMB photons, leading to a cosmic birefringence effect. By cross-correlating this birefringence with galaxy number counts, we aim to place constraints on the ALP mass and couplings.

3. **Late integrated Sachs-Wolfe effect**: in chapter 4 we will study the late-ISW effect by cross-correlating the temperature anisotropies of the CMB with galaxies from the *Euclid* mission. This cross-correlation will help to further constrain dark energy models and provide a deeper understanding of the late-time evolution of the Universe's gravitational potentials.

In conclusion, cross-correlations are a powerful and versatile tool in cosmology, allowing us to extract the maximum amount of information from available data, reduce systematics, and gain a clearer picture of the Universe. As future observational missions come online, the ability to combine and cross-correlate diverse data sets will become even more critical in advancing our understanding of the fundamental properties of the cosmos.

Chapter 2

Cosmic voids as a probe of the dark sector of the universe

The evidence for the presence of dark matter in the Universe, while being overwhelming, still lacks of an understanding of the nature of what we call dark matter. A natural explanation relies on the existence of one (or more) new type(s) of elementary particle(s), which would form the dark matter, as outlined in section 1.3. A test of the particle physics interpretation of dark matter in terms of a new elementary particle is expected to produce a variety of signals which are possible due to its particle physics nature. One of the most investigated channels involves the production of cosmic radiation, spanning from radio waves to gamma-rays (depending on the particle's mass, which determines the maximal energy of the emitted signal), or the generation of neutrinos.

Dark matter particles could decay or annihilate into various channels, producing secondary particles such as photons or neutrinos [207–210]. Because these interactions could happen throughout the universe, across large scales, they would contribute to the overall cosmic radiation in a diffuse and unresolved manner. This unresolved radiation would be blended into the background and added to the emissions from unresolved astrophysical sources such as faint galaxies, star-forming regions, or active galactic nuclei (AGN) [211, 212]. As a result, distinguishing the dark matter signal from other cosmic sources of radiation becomes a complex challenge. The key lies in accurately modeling both the expected dark matter distribution and the astrophysical backgrounds, to isolate any potential excesses in the observed radiation that could point to dark matter interactions.

Despite the potential for dark matter signals to emerge from any cosmic structure—whether in galaxies, galaxy clusters, or the filamentary networks connecting them—most particle physics models predict that such signals are extremely faint. As a result, the dark matter signal is often masked by dominant astrophysical backgrounds, making its detection difficult even in regions rich in dark matter. In order to attempt to extract the dark matter signal from the backgrounds, in refs. [213, 214] it was proposed to look for the cross-correlation between a gravitational tracer of dark matter (like the cosmic shear[5] or the galaxy distribution) and cosmic radiation fields (like gamma-rays, for heavy dark matter like WIMPs - see also [208]). The correlated information between where dark matter is and the ensuing fluctuations induced on the radiation fields could give a handle to separate the two signals, since spatial fluctuations in the radiation field due to astrophysical sources (which are essentially pointlike) and dark matter emissions (more diffuse) have different features.

This has been further elaborated and explored on data for the cross-correlation between dark matter gamma-ray emission with galaxies [215–223], clusters [224–227], CMB lensing [228, 229]

[5]Cosmic shear denotes tiny shape distortions of distant galaxy images that arise from weak gravitational lensing of light by the LSS of the Universe.

and cosmic shear [230–234], discussed in different energy bands like X-rays [235, 236] and the NIRB [237–239] or extended to different gravitational tracers like the HI intensity mapping [240].

In the previous literature, the cross-correlation technique has been proposed and adopted for dark matter studies by looking at dark matter halos (overdensities). In the following analysis we investigate the possibility to extend the cross-correlation technique by using the information on dark matter distribution offered by cosmic voids, for which catalogs start to become available [241–243]. While the signal originating in cosmic voids is expected to be weaker than that produced in dark matter halos—owing to the lower density of voids and the consequently smaller electromagnetic emission from dark matter annihilation or decay—we will demonstrate that the relative strength of the dark matter signal compared to the cross-correlation signal from astrophysical sources, such as active galactic nuclei or star-forming galaxies (SFG), is actually more favorable in voids than in halos. Therefore, selecting cosmic voids as large-scale structure tracers can potentially offer a cleaner signal compared to overdense regions, where the signal may be stronger but is accompanied by more substantial background noise. This makes the cross-correlation signal in voids an intriguing counterpart to that in halos, balancing a weaker but clearer signal against a stronger one with higher levels of contamination. The results of this analysis have been published in [1].

Throughout the analysis we assume a flat ΛCDM cosmology with cosmological parameters as derived by the *Planck* satellite in 2018 [21] + BAO: $H_0 = 67.66$ km s^{-1} Mpc^{-1}, $\Omega_m = 0.3111$, $\Omega_\Lambda = 0.6889$.

2.1 A cross-correlation analysis of the unresolved sky

The dark matter signal we consider is the statistical cross-correlation between the unresolved gamma-ray emission from particle dark matter annihilation or decay and the distribution of mass in the universe. This mass distribution can be traced either through cosmic shear or the distribution of galaxies. The unresolved radiation in the sky is a mix of emission from astrophysical sources, such as active galactic nuclei and star-forming galaxies (SFG), as well as potential signals from dark matter decays or annihilations. To disentangle these components, an effective approach is to cross-correlate this unresolved radiation with gravitational tracers of large-scale structure, like galaxies or cosmic shear, which reflect the overall distribution of mass in the universe. Cross-correlation techniques capitalize on the expectation that dark matter annihilation or decay will follow the large-scale distribution of matter. By comparing the spatial distribution of unresolved gamma-ray emissions with gravitational tracers, we can enhance the dark matter signal and distinguish it from the astrophysical background. This method is particularly useful in helping identify whether the unresolved gamma-ray background is linked to dark matter or to conventional astrophysical sources.

In this section, we briefly review the basic elements of the formalism used to cross-correlate two density fields via the angular power spectrum, a tool that measures statistical correlations between different spatial distributions. In subsequent sections, we will specify in detail the ingredients determining the angular power spectrum (APS) for the relevant density fields. Our approach follows the formalism introduced in previous works, such as refs. [208, 213], but extends it to include cosmic voids as additional tracers of large-scale structure.

Cosmic voids, being low-density regions, provide a unique setting for cross-correlation studies. Although voids contain fewer astrophysical sources, they may still harbor dark matter, offering a cleaner environment to isolate the dark matter signal. Including voids as tracers, alongside overdense regions like galaxy clusters, enhances our ability to detect the dark matter contribution to the unresolved radiation sky. This approach presents a valuable counterpart to traditional methods, providing a balanced perspective between weaker but cleaner signals in voids and stronger signals with more background noise in dense regions.

The source intensity of an observable i, taken along a given direction $\vec{n}$, can be written as:

$$I_i(\vec{n}) = \int \mathrm{d}\chi \; g_i(\chi,\; \vec{n})\tilde{W}(\chi) \; , \tag{2.1}$$

where χ is the comoving radial distance, $g_i(\chi,\; \vec{n})$ represents the density field of the source i and $\tilde{W}(\chi)$ is a window function characterizing the average intensity field as a function of distance (or equivalently of redshift). It is convenient to define a normalized window function $W(\chi) = \langle g_i(\chi,\; \vec{n})\rangle\tilde{W}(\chi)$ such that $\langle I_i\rangle = \int \mathrm{d}\chi \; W(\chi)$. By expanding the intensity fluctuations of two given fields i and j in spherical harmonics, we can compute the cross-correlation angular power spectrum (CAPS):

$$C_\ell^{ij} = \int \frac{\mathrm{d}\chi}{\chi^2} \; W_i(\chi)W_j(\chi)P_{ij}\left(k = \frac{\ell}{\chi},\; \chi\right) \; , \tag{2.2}$$

where the window function $W_i(\chi)$ describes how the observable i is distributed in redshift and its shape strongly depends on the physics behind the chosen signal. The 3D power spectrum is defined through $\langle f_i(\chi,\; \boldsymbol{k})f_j(\chi,\; \boldsymbol{k})\rangle = (2\pi)^3\delta_D(\boldsymbol{k} - \boldsymbol{k'})P_{ij}(k,\; \chi)$ where $f_i = g_i - \langle g_i\rangle$ is the fluctuation of the density field. In eq. (2.2) we adopt the Limber approximation [244–247], which is typically valid for the relevant scales explored in cross-correlation studies involving gamma rays [208, 214, 240].

In the halo model [248], the 3D power spectrum can be split into two terms, taking into account the correlations between source fields either from the same halo (1Halo) or from two different halos (2Halo). In this work we extend the CAPS formalism in a Halo-Void Model of LSS [28], allowing matter to lie within halos and voids. The model can be further extended to include a dust component [28], but we leave this further level of complexity to future works. Introducing more structures in the model leads to new correlation terms, therefore the power spectrum will be decomposed not only into 1Halo (1H) and 2Halo (2H) terms, but it will also include 1Void (1V) and 2Void (2V) components as well as the Halo-Void (HV) mixed term. A detailed derivation of the relevant terms will be given in the next sections.

Under the hypothesis of gaussianity, the variance of the predicted CAPS is (see e.g. [240]):

$$(\Delta C_\ell^{ij})^2 = \frac{1}{(2\ell+1)f_{\rm sky}}\left[(C_\ell^{ij})^2 + \left(C_\ell^{ii} + \frac{N^i}{(B_\ell^i)^2}\right)\left(C_\ell^{jj} + \frac{N^j}{(B_\ell^j)^2}\right)\right] \; , \tag{2.3}$$

where $f_{\rm sky}$ is the observed fraction of the sky, C_ℓ^{ii} and C_ℓ^{jj} represent the auto-correlation angular power spectra associated to the observable i and j, respectively, whereas N^i and N^j are their corresponding noises. Their beam functions B_ℓ^i and B_ℓ^j in harmonic space refer to the angular resolution of the chosen detector. Eq. (2.3) represents the uncertainty on the predicted CAPS, and will be used to determine whether the signal is detectable.

All quantities in eqs. (2.2) and (2.3) will be explicitly specified below. In the following, i labels the gamma-ray intensity, either from astrophysical sources or annihilating/decaying particle dark matter, while j represents the gravitational tracer under consideration in our analysis, that is cosmic shear and galaxy distribution.

2.2 The halo-void model

An overwhelming amount of theoretical and observational evidences favors the idea that structure in the Universe has risen out of a nearly homogeneous primordial cosmos through gravitational instability. The process of structure formation is hierarchical (larger clustering are formed through the continuous merging of smaller structures), as backed by most existing theories, and therefore strongly depends on initial conditions, whose knowledge is one of the primary questions in cosmology.

Tracing back the evolution of structures retains the potential to broaden our understanding on the primordial Universe and much effort has been put into developing both analytical and numerical schemes to explain such phenomena. On one hand, linear and higher order perturbation theory descriptions of gravitational clustering [61, 249–251] from Gaussian initial conditions explain the evolution and mildly non-linear clustering of dark matter, but break in highly non-linear regimes [252] (i.e. at scales smaller than few megaparsecs) and do not provide a rigorous framework to describe the clustering of galaxies. Also, very large scales are troublesome to work with, from the observational side, because of the small amount of data available. On the other hand, smaller non-linear scales can only be described by numerical dark matter simulations of the LSS clustering [253, 254]. The latter show that an initially smooth matter distribution evolves into a complex web of knots, sheets and filaments. These numerical simulations provide detailed information on the distribution of mass within these structures [255, 256] when performed at high resolution but relatively small volume, but they are also useful to constrain the abundance and spatial distribution of structures in the Universe when performed at lower resolution with large volume [257, 258]. The drawback is that simulations are usually computationally expensive and unable to provide an analytical description of the initial conditions, on which they are highly dependent.

Data from forthcoming large-area imaging and redshift surveys of galaxies [70] and weak lensing [14, 67] will provide constraints on the dark matter distribution on large scales as well as on the galaxy formation history. At the same time, the Sunyaev–Zel'dovich effect [259] probes the distribution of the pressure on large scales, and can be observed through wide-field surveys [82]. Moreover, dark and/or baryonic matter leave their imprints on CMB in the form of secondary temperature fluctuations on small scales [35, 44, 259].

The halo model (HM) [248] has been, up to today, the uttermost successful analytical description of non-linear scales and provides a self-consistent explanation of the observations discussed above. This model relies on the central assumption that all matter in the Universe lies within dark matter halos and offers a simple framework to explain the transition between non-linear and linear scales, which are dominated by the 1Halo and 2Halo terms, respectively. However, the predicted power spectrum is in accordance with N-body simulations only within 20% around the transition and, at the same time, it either requires a normalization of the 2Halo term or for the halo abundance to be integrated down to very low and untested masses ($M \ll 10^4\ h^{-1}\ M_\odot$), in order to account for all matter in the Universe. As discussed in [28], there have been several attempts to modify the HM [260–263]. These alternative models typically either introduce new free parameters that cannot be fitted using only halo properties, or do not significantly improve the HM predictions.

Recently, a successful self-consistent modification of the HM has been proposed by ref. [28], namely the halo-void model (HVM). This model is based on relaxing the central assumption of the HM and allowing matter to lie not only within halos but also within cosmic voids.

Including voids as building blocks of the Universe leads to new terms in the prediction of the cross-correlation signal: the 1Void, 2Void, and Halo-Void terms, in addition to the 1Halo and 2Halo contributions (already present in the HM). In the past decades, the scientific community has mostly focused on modeling the dark matter halos, while cosmic voids have been largely

unappreciated. Nevertheless, voids constitute the dominant volume fraction of the Universe and can be used as powerful, independent probes for our theories of structure formation. Underdense regions are indeed ideal environments to constrain dark energy [264–267] and modified gravity [268–271]. In addition, thanks to their extreme sensitivity to background cosmological changes, voids are more closely related to initial conditions [272–274] and can be valuable in order to constrain cosmology [275–281]. Also, they are the perfect case-study for the excursion set theory[6] [282] given their rather spherical symmetry[7] and the existence of a refined repertory of fitting prescriptions for their density profile, mass function and linear bias.

The HVM requires the following ingredients: the halo and void density profile, the halo and void mass function and the halo and void linear bias. The model computes the halo and void statistics through the excursion set formalism [282] with two barriers [271, 283–285]. This approach guarantees a fully self-consistent model that takes into account the void-in-cloud, void-in-void and cloud-in-void effects, in addition to the cloud-in-cloud effect that appears in the HM. Moreover, there is no need for a normalization on large scales or for the abundances to be integrated down to very low halo masses, as the matter within smaller halos is taken into account in larger voids. Ref. [28] also show how considering both halos and voids improves the transition between the 2Halo and the 1Halo term.

Following the prescriptions of the HVM, the total matter density field is given by the sum of the halo and void contributions:

$$\rho(\mathbf{x}) = \sum_{i}^{\text{halos}} \rho_h(\mathbf{x} - \mathbf{x}_i \,|\, M_i) + \sum_{j}^{\text{voids}} \rho_v(\mathbf{x} - \mathbf{x}_j \,|\, M_j) \,, \tag{2.4}$$

where $\rho_h(\mathbf{x}-\mathbf{x}_i \,|\, M_i)$ is the density profile of a halo with mass M_i centered at x_i and $\rho_v(\mathbf{x}-\mathbf{x}_j \,|\, M_j)$ is the density profile of a void with mass M_j centered at x_j. Note how the HM is recovered when the last term in eq. (2.4) is neglected, i.e. if we set the matter density in voids to zero across the whole Universe. We can rewrite eq. (2.4) as:

$$\begin{aligned}\rho(\mathbf{x}) = \int \mathrm{d}M \int \mathrm{d}^3x' \Bigg[&\sum_{i}^{\text{halos}} \delta_D(M - M_i)\delta_D(\mathbf{x}' - \mathbf{x}_i)\rho_h(\mathbf{x} - \mathbf{x}' \,|\, M) \\ &+ \sum_{j}^{\text{voids}} \delta_D(M - M_j)\delta_D(\mathbf{x}' - \mathbf{x}_j)\rho_v(\mathbf{x} - \mathbf{x}' \,|\, M) \Bigg] \,.\end{aligned} \tag{2.5}$$

The 2-point correlation function reads

$$\xi(\mathbf{r}) = \frac{1}{\overline{\rho}_m^2} \langle \rho(\mathbf{x})\rho(\mathbf{x}+\mathbf{r}) \rangle - 1 \,, \tag{2.6}$$

where $\overline{\rho}_m$ is the average matter density in the Universe. Plugging eq. (2.5) into eq. (2.6), we get that eq. (2.6) can be written as the sum of three terms: a pure halo term (containing the correlation between particles within one or two halos), a pure void term (containing the correlation between particles within one or two voids) and a mixed term (containing the correlation between

[6] The excursion set approach provides a useful framework to describe the formation histories of gravitationally bound structures such as virialized halos or cosmic voids.

[7] Unlike the evolution of density peaks, primordial asphericity of negative density perturbations is quickly lost as they expand [283].

two particles within a halo and a void, respectively). In particular, the pure halo correlation reads:

$$\xi_h(\mathbf{r}) = \frac{1}{\overline{\rho}_m^2}\int \mathrm{d}M_1\mathrm{d}M_2\mathrm{d}^3x_1\mathrm{d}^3x_2\ \rho_h(\mathbf{x}-\mathbf{x}_1\,|\,M_1)\rho_h(\mathbf{x}-\mathbf{x}_2+\mathbf{r}\,|\,M_2) \\ \times\left\langle\sum_{i,\,j}\delta_D(M_1-M_i)\delta_D(M_2-M_j)\delta_D(\mathbf{x}_1-\mathbf{x}_i)\delta_D(\mathbf{x}_2-\mathbf{x}_j)\right\rangle\ , \tag{2.7}$$

where we can distinguish two terms: the 1Halo term for particles residing within the same halo and the 2Halo term for particles residing in different halos:

$$I^{1H} = \delta_D(M_1-M_2)\delta_D(\mathbf{x}_1-\mathbf{x}_2)\frac{\mathrm{d}n_h}{\mathrm{d}M_1} \tag{2.8}$$

$$I^{2H} = \frac{\mathrm{d}n_h}{\mathrm{d}M_1}\frac{\mathrm{d}n_h}{\mathrm{d}M_2}[1+\xi_{hh}(\mathbf{x}_1-\mathbf{x}_2\,|\,M_1,\,M_2)]\ , \tag{2.9}$$

where $\mathrm{d}n_h/\mathrm{d}M$ denotes the halo mass function, which measures the differential number density of halos in the mass range $[M,\ M+\mathrm{d}M]$:

$$\frac{\mathrm{d}n_h}{\mathrm{d}M_1} = \left\langle\sum_i\delta_D(M_1-M_i)\delta_D(\mathbf{x}_1-\mathbf{x}_i)\right\rangle \tag{2.10}$$

and $\xi_{hh}(\mathbf{x}_1-\mathbf{x}_2\,|\,M_1,\,M_2)$ is the halo-halo 2-point correlation function of halos with mass M_1 and M_2. A similar discussion applies to the other terms of the 2-point correlation function. However, for the cross-correlation the only non vanishing term is naturally the one with particles residing in two distinct structures. The terms appearing in eq. (2.6) can be summarized as:

$$\xi^{1H}(\mathbf{r}) = \frac{1}{\overline{\rho}_m^2}\int \mathrm{d}M\,\frac{\mathrm{d}n_h}{\mathrm{d}M}\int \mathrm{d}^3y\,\rho_h(\mathbf{y}|M)\rho_h(\mathbf{y}+\mathbf{r}|M) \tag{2.11}$$

$$\xi^{2H}(\mathbf{r}) = \frac{1}{\overline{\rho}_m^2}\int \mathrm{d}M_1\,\frac{\mathrm{d}n_h}{\mathrm{d}M_1}b_h(M_1)\int \mathrm{d}M_2\,\frac{\mathrm{d}n_h}{\mathrm{d}M_2}b_h(M_2) \\ \times\int \mathrm{d}^3y_1\,\rho_h(\mathbf{y}_1|M_1)\int \mathrm{d}^3y_2\,\rho_h(\mathbf{y}_2|M_2)\xi^L(\mathbf{y}_1-\mathbf{y}_2) \tag{2.12}$$

$$\xi^{1V}(\mathbf{r}) = \frac{1}{\overline{\rho}_m^2}\int \mathrm{d}M\,\frac{\mathrm{d}n_v}{\mathrm{d}M}\int \mathrm{d}^3y\,\rho_v(\mathbf{y}|M)\rho_v(\mathbf{y}+\mathbf{r}|M) \tag{2.13}$$

$$\xi^{2V}(\mathbf{r}) = \frac{1}{\overline{\rho}_m^2}\int \mathrm{d}M_1\,\frac{\mathrm{d}n_v}{\mathrm{d}M_1}b_v(M_1)\int \mathrm{d}M_2\,\frac{\mathrm{d}n_v}{\mathrm{d}M_2}b_v(M_2) \\ \times\int \mathrm{d}^3y_1\,\rho_v(\mathbf{y}_1|M_1)\int \mathrm{d}^3y_2\,\rho_v(\mathbf{y}_2|M_2)\xi^L(\mathbf{y}_1-\mathbf{y}_2) \tag{2.14}$$

$$\xi^{HV}(\mathbf{r}) = \frac{1}{\overline{\rho}_m^2}\int \mathrm{d}M_1\,\frac{\mathrm{d}n_h}{\mathrm{d}M_1}b_h(M_1)\int \mathrm{d}M_2\,\frac{\mathrm{d}n_v}{\mathrm{d}M_2}b_v(M_2) \\ \times\int \mathrm{d}^3y_1\,\rho_h(\mathbf{y}_1|M_1)\int \mathrm{d}^3y_2\,\rho_v(\mathbf{y}_2|M_2)\xi^L(\mathbf{y}_1-\mathbf{y}_2)\ , \tag{2.15}$$

where we have used the linear approximation (tree-level) for the structure-structure 2-point correlation (ξ_{xy} for $x, y = h,\, v$). The density contrast $\delta_x(\mathbf{x}\,|\,M)$ is then obtained from the linear matter density contrast $\delta_m^L(\mathbf{x})$ as (see e.g. [28, 248]):

$$\delta_x(\mathbf{x}\,|\,M) = b_x^L(M)\delta_m^L(\mathbf{x})\ , \tag{2.16}$$

where $b_x^L(M)$ denotes the linear bias of x. For any combination of structures xy we have:

$$\xi_{xy}(\mathbf{r}) = b_x(M_x)\, b_y(M_y)\, \xi^L(\mathbf{r})\ , \tag{2.17}$$

where we have dropped the L apex on the linear bias to ease the notation. Two conditions have to hold: the total matter density of the Universe has to be equal to the sum of the total matter density in halos and voids, and matter does not have to be biased with respect to itself. These two conditions lead to the two following constraints:

$$\overline{\rho}_h + \overline{\rho}_v = \overline{\rho}_m \tag{2.18}$$

$$1 - \overline{b}_h - \overline{b}_v = 0\ , \tag{2.19}$$

where

$$\overline{\rho}_h = \int \mathrm{d}M\, M \frac{\mathrm{d}n_h}{\mathrm{d}M} \tag{2.20}$$

$$\overline{\rho}_v = \int \mathrm{d}M\, M \frac{\mathrm{d}n_v}{\mathrm{d}M}\ , \tag{2.21}$$

and

$$\overline{b}_h = \frac{1}{\overline{\rho}_m} \int \mathrm{d}M\, M \frac{\mathrm{d}n_h}{\mathrm{d}M} b_h(M) \tag{2.22}$$

$$\overline{b}_v = \frac{1}{\overline{\rho}_m} \int \mathrm{d}M\, M \frac{\mathrm{d}n_v}{\mathrm{d}M} b_v(M)\ . \tag{2.23}$$

Assuming spherical symmetry ($\rho_x(\mathbf{r}\,|\,M) = \rho_x(r\,|\,M)$ for $x = h,\, v$) and Fourier transforming eqs. (2.11)-(2.15) we have:

$$P^{1H}(k) = \frac{1}{\overline{\rho}_m^2} \int \mathrm{d}M\ \frac{\mathrm{d}n_h}{\mathrm{d}M} |\rho_h(k\,|\,M)|^2 \tag{2.24}$$

$$P^{2H}(k) = \frac{1}{\overline{\rho}_m^2} \left[\int \mathrm{d}M\ \frac{\mathrm{d}n_h}{\mathrm{d}M} \rho_h(k\,|\,M) b_h(M) \right]^2 P^L(k) \tag{2.25}$$

$$P^{1V}(k) = \frac{1}{\overline{\rho}_m^2} \int \mathrm{d}M\ \frac{\mathrm{d}n_v}{\mathrm{d}M} |\rho_v(k\,|\,M)|^2 \tag{2.26}$$

$$P^{2V}(k) = \frac{1}{\overline{\rho}_m^2} \left[\int \mathrm{d}M\ \frac{\mathrm{d}n_v}{\mathrm{d}M} \rho_v(k\,|\,M) b_v(M) \right]^2 P^L(k) \tag{2.27}$$

$$P^{HV}(k) = \frac{1}{\bar{\rho}_m^2} \int \mathrm{d}M_1 \, \frac{\mathrm{d}n_h}{\mathrm{d}M_1} \rho_h(k \,|\, M_1) b_h(M_1) \int \mathrm{d}M_2 \, \frac{\mathrm{d}n_v}{\mathrm{d}M_2} \, \rho_v(k \,|\, M_2) b_v(M_2) \, P^L(k) \,, \tag{2.28}$$

where $P^L(k)$ is the linear matter power spectrum, given by the Fourier transform of the linear 2-point correlation function $\xi^L(r)$. Note how the HM is easily recovered when setting $\rho_v(k \,|\, M) = 0$. The total matter power spectrum is now given by:

$$P(k) = P^{1H}(k) + P^{2H}(k) + P^{1V}(k) + P^{2V}(k) + 2\, P^{HV}(k) \tag{2.29}$$

and, using eqs. (2.19) and (2.18), it can be shown that the total matter power spectrum reduces to the linear matter power spectrum on very large scales ($k \ll 1$ Mpc^{-1}). However, for the HM, these constraints return $\bar{b}_h = 1$ and $\overline{\rho}_h = 1$, which, for a standard halo mass function and bias, have a very slow convergence, requiring integration down to tiny and untested masses. The HVM solves this shortcoming by taking into account the matter within smaller halos in larger voids (see Sec. 2.2.3 and [28] for a brief discussion on this point).

In the following sections we discuss the ingredients required to compute the power spectrum: halo/void density profiles, mass functions and linear biases. For the last two, we adopt the recipes provided by ref. [28], derived from the excursion set theory with two static barriers [28, 271, 284]. Hence, the obtained mass functions and linear biases naturally incorporate the exclusion of voids inside halos and vice versa.

2.2.1 Density profile

We adopt for halos the standard Navarro-Frenk-White (NFW) profile [256], and for voids the Hamaus-Sutter-Wandelt (HSW) profile [286]. Both assume a spherical density distribution of matter in the structure.

Halos

The NFW density profile for a halo of virial mass M can be parameterized as follows [256]:

$$\rho_{\mathrm{NFW}}(r \,|\, M) = \frac{\rho_s}{c(M)\dfrac{r}{r_{\mathrm{vir}}} \left(1 + c(M)\dfrac{r}{r_{\mathrm{vir}}}\right)^2} \,, \tag{2.30}$$

where ρ_s is the characteristic density for which the volume-integrated profile returns the virial mass, r_{vir} is the virial radius[8] and $c(M)$ is the concentration parameter [287]. Its Fourier transform, truncated at r_{vir} is given by:

$$\rho_h(k \,|\, M) = 4\pi \int_0^{r_{\mathrm{vir}}} \mathrm{d}r \; r^2 \, \frac{\sin kr}{kr} \, \rho_{\mathrm{NFW}}(r \,|\, M) \,. \tag{2.31}$$

Voids

Given their low density, vastness and unsphericity at some scales, voids are troublesome to study both with observations and simulations. Most void finders show them as deeply underdense in

[8] The virial radius is defined through $M = \frac{4\pi}{3} \overline{\rho}_m \Delta_{\mathrm{vir}} r_{\mathrm{vir}}^3$, where $\overline{\rho}_m$ is the average matter density of the Universe and $\Delta_{\mathrm{vir}} \sim 330$ is the halo density contrast at the time of virialization for the fiducial cosmology.

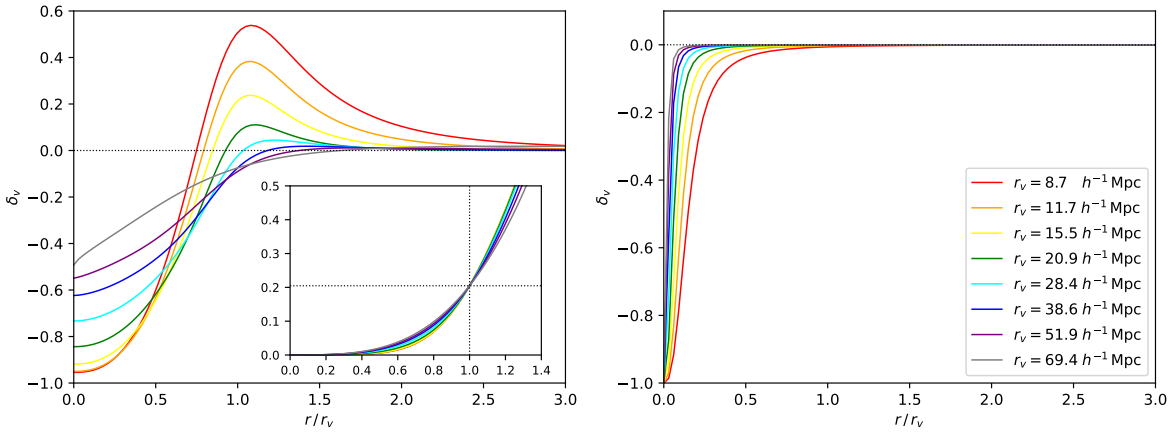

Figure 2.1: (*Left*): Hamaus-Sutter-Wandelt void density contrast [277], at $z = 0$, for different void radii. Smaller voids are more underdense in their central region but show higher compensation walls in their outskirt, i.e. they tend to be overcompensated. Larger voids are less underdense in their central region but show lower compensation walls in their outskirt, i.e. they tend to be undercompensated. In the small box we show the integrated overdensity, as a function of r/r_v, for a normalized HSW profile, so that the void overdensity $\Delta_v \simeq 0.2047$ is reached, for any void, at its radius. This allows us to consider spherical voids with fixed void overdensity. (*Right*): Void density contrast for the profile proposed in Ref. [28], based on empty centers and no compensation walls.

their interiors[9], and the profiles exhibit overdense compensation walls with a maximum located slightly outside their effective radii, shifting outwards for larger voids. The height of the compensation wall decreases with void size, causing the inner profile slope to become shallower and the wall to widen. This trend divides all voids into being either overcompensated or undercompensated, depending on whether the total mass within their compensation wall exceeds or falls behind their missing mass in the center, respectively. Ultimately, at sufficiently large distances to the void center, all profiles approach the mean background density. The HSW profile [277] is a simple empirical formula that can accurately capture the properties described above:

$$\frac{\rho_v(r\,|\,r_v)}{\overline{\rho}_m} - 1 = \delta_c \frac{1 - \left(\frac{r}{r_s}\right)^{\alpha}}{1 + \left(\frac{r}{r_v}\right)^{\beta}}\,, \tag{2.32}$$

where r_s is the characteristic radius for which $\rho_v = \overline{\rho}_m$, r_v is the effective radius of the considered void and $(\alpha,\ \beta,\ \delta_c)$ are free parameters. In particular, δ_c represents the central density contrast and α and β are the inner and outer slopes of the compensation wall. These parameters are usually determined through best-fits of N-body dark matter simulations but Hamaus et al. [277] also provide empirical functions, which we use in our analysis, relating them to r_s and r_v, therefore decreasing the degrees of freedom.

Nevertheless, the choice of the profile strongly depends on the void finder, which N-body simulations should be calibrated on. Other works have used void finders that neither rely on any central particle, but on Voroni vertices, nor show any compensation wall (see e.g. [28]). These

[9] Voids of smaller size show emptier central regions, while larger voids tend to be slightly denser in their centers [277].

properties can be summarized in the one-parameter empirical formula proposed in [28]:

$$\frac{\rho_v(r\,|\,r_v)}{\overline{\rho}_m} - 1 = \frac{1}{2}\left[1 + \tanh\left(\frac{y - y_0}{s(r_v)}\right)\right] - 1\,, \tag{2.33}$$

where $y = \ln(r/r_v)$ and $y_0 = \ln(r_0/r_v)$. The radius r_0 can be parameterized in terms of s, which remains the only free quantity. Ref. [28] shows, through N-body simulations, that its dependence on r_v is very weak and can be safely fixed to $s = 0.75$, for all void radii.

The left and right panel of fig. 2.1 show the void density contrast described by eq. (2.32) and eq. (2.33), respectively, for multiple bins in void radii, and follow efficiently all of the related properties outlined above.

The Fourier transform of the void profile is given by:

$$\rho_v(k\,|\,M(r_v)) = 4\pi \int_0^{r_v} \mathrm{d}r\; r^2\, \frac{\sin kr}{kr}\, \rho_v(r\,|\,M(r_v))\,, \tag{2.34}$$

where, in principle, $M(r_v) = 4\pi \int_0^{r_v} \mathrm{d}r\; r^2\, \rho_v(r\,|\,r_v)$. However, in the following discussion we will consider spherical voids with an overdensity $\Delta_v \simeq 0.2047$ (see e.g. [283]), whose mass can be computed through $M(r_v) = \frac{4\pi}{3}\,\overline{\rho}_m \Delta_v r_v^3$. Hence, the profile needs to be properly normalized in order for voids of any radius to reach the chosen overdensity Δ_v:

$$\rho_v(r\,|\,r_v) \longrightarrow \frac{\Delta_v}{\Delta(r_v)} \rho_v(r\,|\,r_v)\,, \tag{2.35}$$

where

$$\Delta(r_v) = \frac{3}{r_v^3} \int_0^{r_v} \mathrm{d}r\; r^2\, \frac{\rho_v(r\,|\,r_v)}{\overline{\rho}_m}\,. \tag{2.36}$$

Note how, by doing so, eq. (2.34) can be rewritten in terms of the normalized profile, but the integration should be performed up to a void radius extracted from a different $M(r_v)$ relation, in order to obtain the same value for the Fourier transform of the void profile. Calculating the latter through the normalized profile is only an expedient to ease the computation, nonetheless, the physical profile remains that shown in either panels of fig. 2.1, which follow the void properties previously discussed. The small box in the left panel of fig. 2.1 shows the evolution of eq. (2.36) as a function of the integration upper limit, for the HSW normalized profile. Independently of the void size, the required void overdensity Δ_v is reached when integrating up to the void radius.

Studies of voids' properties are yet at their early stages and the choice of the void profile usually depends on the used void finder. However, while for definiteness in the analyses shown below we adopt the HSW profile, nevertheless we have verified that the actual choice of the profile has only a sub-percent effect on the power spectra (see Sec. 2.3), and we leave further discussion on the use of different profiles, in the context of our work, to future studies.

2.2.2 Mass function

The halo/void mass functions used in the HVM are computed through the excursion set theory with two static linear barriers (2SB) [28, 271] to avoid double counting of matter. We show here a comparison of these mass functions with those computed following Sheth-Tormen [288], for halos, and standard Press-Schechter theory [289], for voids.

A central ingredient is the variance of the linear density field smoothed at some scale R (with

a top-hat window function $\widehat{W}$):

$$\sigma^2(R) = \int \frac{\mathrm{d}k}{2\pi^2}\, k^2 P^L(k) \widehat{W}^2(kR)\ , \tag{2.37}$$

where for any structure we have:

$$M = \frac{4\pi}{3}\,\overline{\rho}_m R^3\ . \tag{2.38}$$

Halos

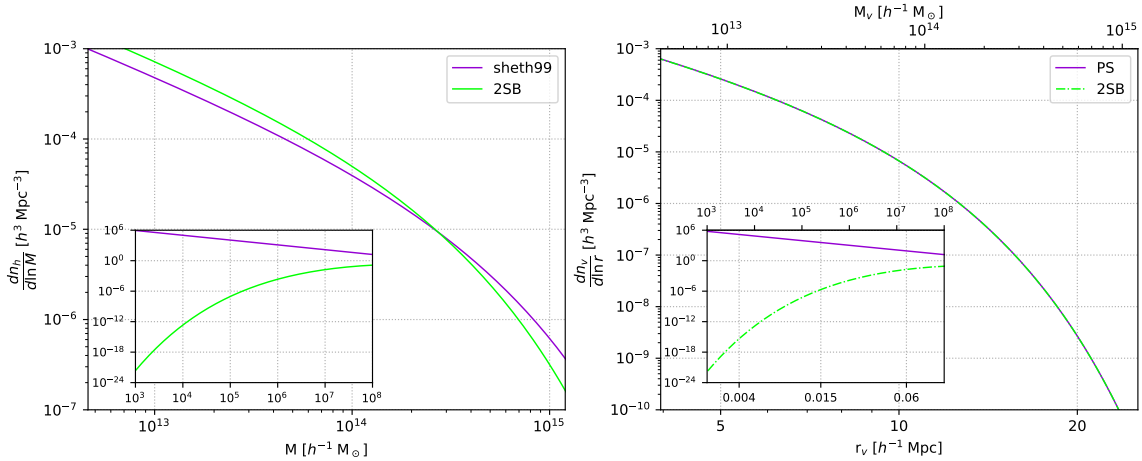

Figure 2.2: (*Left*): Halo mass function as a function of halo mass. (*Right*): Void mass function as a function of void radius/mass. Both results are computed at $z = 0$. We compare two different models: Sheth-Tormen for halos or Press-Schecther for voids (purple) and 2SB (green). The insets show how, at very small masses, the excursion set prediction decreases rapidly, differently from the standard Sheth-Tormen or Press-Schecther abundances.

The halo mass function can be written as:

$$\frac{\mathrm{d}n_h}{\mathrm{d}\ln M} = f_h(\sigma)\frac{\overline{\rho}_m}{M}\frac{\mathrm{d}\ln\sigma^{-1}}{\mathrm{d}\ln M}\ , \tag{2.39}$$

where $f_h(\sigma)$, the multiplicity function, determines the model. In this work, we consider the multiplicity functions:

$$f_h^{\mathrm{sheth99}}(\sigma) = 2A\nu\left(1+\frac{1}{(a\nu)^p}\right)\sqrt{\frac{a}{2\pi\nu}}\exp\left(-\frac{a\nu}{2}\right) \tag{2.40}$$

$$f_h^{\mathrm{2SB}}(\sigma) = 2\sum_n \frac{n\pi}{\delta_T^2}\sigma^2\,\sin\left(\frac{n\pi\delta_c}{\delta_T}\right)\exp\left[-\frac{n^2\pi^2}{2\delta_T^2}\sigma^2\right]\ , \tag{2.41}$$

where $\delta_T = \delta_c + |\delta_v|$ with $\delta_c \simeq 1.686$ and $\delta_v \simeq -2.717$ the linear critical (over and under) densities for halo and void formation, respectively. Here f_h^{sheth99} is the Sheth-Tormen multiplicity function [288], with $\nu = (\delta_c^2/\sigma^2)$ and (A, a, p) free parameters. f_h^{2SB} is the excursion set prediction for a model with two static barriers.

Note how f_h^{sheth99} is normalized to unity, whereas f_h^{2SB} is not, since it already accounts for the existence of voids. As a direct consequence, the excursion set predictions with two barriers

tend to decrease rapidly at small masses, as shown by the left panel of fig. 2.2. This directly reflects on no need to integrate eq. (2.20) down to very low and untested masses.

Voids

The void mass function is usually expressed in terms of its radius, rather than its mass:

$$\frac{\mathrm{d}n_v}{\mathrm{d}\ln r} = \Delta_v \left[\frac{f_v(\sigma)}{V(r_L)}\frac{\mathrm{d}\ln\sigma^{-1}}{\mathrm{d}\ln r_L}\right]_{r_L=r/1.7} , \tag{2.42}$$

where $\Delta_v = (r_L/r_v)^{1/3} \simeq 0.2$ is the void overdensity and $f_v(\sigma)$ determines the model. The last equation follows from eq.(2.39) and derives from the conservation requirement of the volume density, as discussed by Jennings et al. [285].

In this work, we consider the following multiplicity functions:

$$f_v^{\mathrm{PS}}(\sigma) = \sqrt{\frac{2}{\pi}}\frac{|\delta_v|}{\sigma}\exp^{-\frac{\delta_v^2}{2\sigma^2}} \tag{2.43}$$

$$f_v^{\mathrm{2SB}}(\sigma) = 2\sum_n \frac{n\pi}{\delta_T^2}\sigma^2 \sin\left(\frac{n\pi|\delta_v|}{\delta_T}\right)\exp\left[-\frac{n^2\pi^2}{2\delta_T^2}\sigma^2\right] , \tag{2.44}$$

where δ_c, δ_v and δ_T are the same parameters discussed for the halo mass function. Here f_v^{PS} is the Press-Schechter multiplicity function [289] and f_v^{2SB} is the excursion set prediction for a model with two static barriers.

In the right panel of fig. 2.2 we compare the Press-Schechter and 2SB void mass functions. Once again, we note how the excursion set prediction decreases rapidly at small masses (differently from Press-Schechter theory), avoiding the need to integrate eq. (2.21) down to tiny untested masses.

2.2.3 Linear bias

We present here the excursion set predictions [271, 283–285] of the linear bias proposed by ref. [28]. Using these biases makes the model fully self-consistent with the 2SB mass functions. Moreover, the combination of 2SB bias and mass function avoids double counting of matter, excluding the overlap of structures.

Halos

The relevant functions for halos that we use are:

$$b_h^{\mathrm{sheth99}}(\sigma) = 1 + \frac{a\nu - 1}{\delta_c} + \frac{2p}{\delta_c\,(1+(a\nu)^p)} \tag{2.45}$$

$$b_h^{\mathrm{2SB}}(\sigma) = 1 - \frac{\sum_n \frac{n\pi}{\delta_T^2}\sin\left(\frac{n\pi\delta_c}{\delta_T}\right)\exp\left[-\frac{n^2\pi^2}{2\delta_T^2}\sigma^2\right]\left[\mathrm{cotan}\left(\frac{n\pi\delta_c}{\delta_T}\right)\frac{n\pi}{\delta_T}\right]}{\sum_n \frac{n\pi}{\delta_T^2}\sin\left(\frac{n\pi\delta_c}{\delta_T}\right)\exp\left[-\frac{n^2\pi^2}{2\delta_T^2}\sigma^2\right]} . \tag{2.46}$$

Here b_h^{sheth99} is the Sheth-Tormen linear bias [290], with $\nu = \delta_c^2/\sigma^2$ and $(a,\, p)$ are the same free parameters of the Sheth-Tormen mass function (eq. (2.40)). The quantity b_h^{2SB} is the prediction for a model with two static barriers.

In the left panel of fig. 2.3, we compare the linear bias predictions for the functions above. Ref. [28] show how the 2SB linear bias is in very good agreement with simulations.

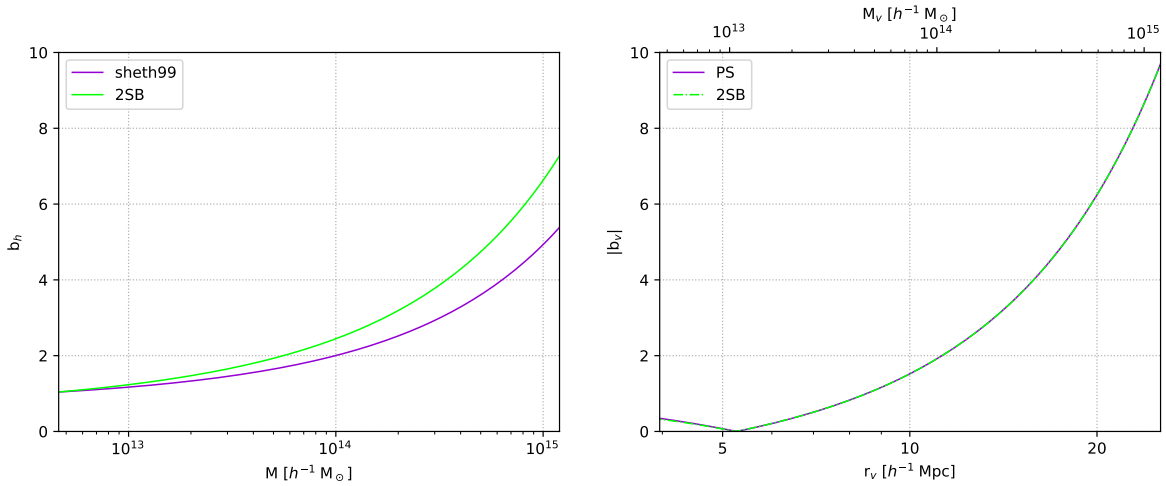

Figure 2.3: (*Left*): Halo linear bias as a function of halo mass. (*Right*): Void linear bias as a function of void radius/mass. Both results are computed at $z = 0$. We compare two different models: Sheth-Tormen for halos or Press-Schechter for voids (purple) and 2SB (green). For voids, we show the absolute value of the bias, as the latter is usually negative for larger voids. This is strictly connected to the absence of compensation walls for very large voids.

Voids

In this work we consider the following functions:

$$b_v^{\rm PS}(\sigma) = 1 + \frac{\nu - 1}{\delta_v} \tag{2.47}$$

$$b_v^{\rm 2SB}(\sigma) = 1 + \frac{\sum_n \frac{n\pi}{\delta_T^2} \sin\left(\frac{n\pi|\delta_v|}{\delta_T}\right) \exp\left[-\frac{n^2\pi^2}{2\delta_T^2}\sigma^2\right] \left[\frac{n\pi}{\delta_T}\text{cotan}\left(\frac{n\pi|\delta_v|}{\delta_T}\right)\right]}{\sum_n \frac{n\pi}{\delta_T^2} \sin\left(\frac{n\pi|\delta_v|}{\delta_T}\right) \exp\left[-\frac{n^2\pi^2}{2\delta_T^2}\sigma^2\right]}\,, \tag{2.48}$$

where δ_c, δ_v and δ_T are the same discussed for the halo mass function. Here, $b_v^{\rm PS}$ is the Press-Schechter linear bias [289], with $\nu = \delta_v^2/\sigma^2$. The quantity $b_v^{\rm 2SB}$ is the excursion set prediction for a model with two static barriers.

In the right panel of fig. 2.3, we compare the linear bias predictions for the functions above. Note that we show the absolute value of the bias since the latter is negative for larger voids in the 2SB model. This anti-correlation with the matter field is tightly connected with the compensation walls, as larger voids tend to have smaller compensation walls (see Sec. 2.2.1) and, therefore, to be under-compensated, resulting in a negative sign for the linear bias.

Convergence at small masses

As we know, the total power spectrum should follow linear theory on large scales. This is naturally achieved when the constraints of eqs. (2.20) and (2.19) are satisfied. The former ensures that the total matter contained in all structures matches the total matter in the Universe, while the latter ensures that matter is not biased with respect to itself.

These constraints can be rewritten as:

$$I^{\rho} = \frac{\overline{\rho}}{\overline{\rho}_m} = \frac{1}{\overline{\rho}_m} \int_0^{\infty} \mathrm{d}M \; M \, \frac{\mathrm{d}n}{\mathrm{d}M} = 1 \tag{2.49}$$

$$I^{b} = \overline{b} = \frac{1}{\overline{\rho}_m} \int_0^{\infty} \mathrm{d}M \; M \, \frac{\mathrm{d}n}{\mathrm{d}M} \, b(M) = 1 \; , \tag{2.50}$$

where both integrals are given by the sum of the contributions from all of the considered structures.

Ref. [28] studies the problem by varying the lower bound of the integrals in eqs. (2.49) and (2.50) for mass values $M_{\rm min} > 0$. They show that the standard HM (with Sheth-Tormen-like halo mass function and linear bias), does not converge to unity even down to very low masses ($M_{\rm min} < 10^4$ M$_\odot$), pointing out the difficulty of the HM to recover efficiently the linear matter power on large scales and implying the need to either integrate eqs. (2.49) and (2.50) down to very low masses or suitably normalize the 2Halo term. On the contrary, the sum of contributions from halos and voids, within the HVM, to eqs. (2.49) and (2.50) converges to unity already for $M_{\rm min} \simeq 10^9$ M$_\odot$. Hence, incorporating voids in a model of LSS eliminates the need for an exotic re-normalization and saves up computational-time.

In conclusion, allowing matter to lie within multiple structures, through the excursion set theory with two barriers [28, 271, 284], offers as a fully self-consistent model, that correctly recovers the matter power on large scales, and as an efficient tool to a variety of cosmological and astrophysical studies. The foundation of such a success lies in considering the mass of smaller halos within voids of larger size.

2.3 The 3D power spectra

Early decoupling of dark matter allowed for its perturbations to grow undisturbed and form deep potential wells that accreted baryonic matter after recombination. As a consequence, galaxies are tightly coupled with dark matter and offer as a powerful tracer of its distribution. At the same time, galaxies host astrophysical sources that emit in several energy bands and dark matter structures bend the light, from distant sources, in the weak lensing regime. We then expect a correlation between gravitational tracers, such as i) the galaxy distribution and ii) the cosmic shear, and gamma-ray emitters, such as a) annihilating/decaying dark matter and b) unresolved astrophysical sources. The latter, while being an interesting signal by itself in the study of the unresolved component of the gamma-ray sky, nevertheless represent an irreducible background for pure dark matter studies.

In this section we generalize the formalism introduced in the previous sections to adapt the 3D power spectrum to the cross-correlation signal between two different source fields. In particular, we are interested in correlating i-ii) with a-b) within the HVM. For any couple of observables i and j, the power spectra are:

$$P_{ij}^{1H}(k) = \int \mathrm{d}M \; \frac{\mathrm{d}n_h}{\mathrm{d}M} f_i^{h*}(k \,|\, M) f_j^{h}(k \,|\, M) \tag{2.51}$$

$$P_{ij}^{2H}(k) = \int \mathrm{d}M_1 \; \frac{\mathrm{d}n_h}{\mathrm{d}M_1} f_i^{h*}(k \,|\, M_1) b_h(M_1) \int \mathrm{d}M_2 \; \frac{\mathrm{d}n_h}{\mathrm{d}M_2} f_j^{h}(k \,|\, M_2) b_h(M_2) P^L(k) \tag{2.52}$$

$$P_{ij}^{1V}(k) = \int \mathrm{d}M \; \frac{\mathrm{d}n_v}{\mathrm{d}M} f_i^{v*}(k \,|\, M) f_j^{v}(k \,|\, M) \tag{2.53}$$

$$P_{ij}^{2V}(k) = \int \mathrm{d}M_1 \; \frac{\mathrm{d}n_v}{\mathrm{d}M_1} f_i^{v*}(k \,|\, M_1) b_v(M_1) \int \mathrm{d}M_2 \; \frac{\mathrm{d}n_v}{\mathrm{d}M_2} f_j^{v}(k \,|\, M_2) b_v(M_2) P^L(k) \tag{2.54}$$

$$P_{ij}^{HV}(k) = \int \mathrm{d}M_1 \, \frac{\mathrm{d}n_h}{\mathrm{d}M_1} f_{(i}^{h*}(k \,|\, M_1) b_h(M_1) \int \mathrm{d}M_2 \, \frac{\mathrm{d}n_v}{\mathrm{d}M_2} \, f_{j)}^{v}(k \,|\, M_2) b_v(M_2) \, P^L(k) \; , \tag{2.55}$$

where we have generalized eqs. (2.24)-(2.28) for any pair of source fields f_i, f_j. The Halo-Void term in eq. (2.55) is given by the sum of the symmetric permutations of the considered fields. In the notation, we have omitted the redshift dependence of the 3D power spectrum for simplicity, but it has been considered throughout the computation.

The main idea of this work relies on the observational ability to identify cosmic voids: this would then allow to perform the cross-correlations between the relevant gravitational tracers (related to halos or voids) and the corresponding gamma-ray emission (due to dark matter annihilation/decay or the astrophysical sources) from those structures. In this case, we can split the CAPS (2.2) into two terms, each one depending on the 3D power spectrum generated only from halos or voids:

$$P_{ij}^{h}(k, \, z) = P_{ij}^{1H}(k, \, z) + P_{ij}^{2H}(k, \, z) \tag{2.56}$$

$$P_{ij}^{v}(k, \, z) = P_{ij}^{1V}(k, \, z) + P_{ij}^{2V}(k, \, z) \; . \tag{2.57}$$

In order to calculate the power spectra of eqs. (2.56), (2.57) and the window functions of eq. (2.2), we need to specify the relation between gravitational tracers and the underlying large-scale structure as well as how the DM particles and astrophysical sources hosted in halos and voids produce the gamma-ray emission observed by our telescopes. In our work we consider cosmic shear and galaxy catalogs as our reference gravitational tracers. Clearly, in order to calculate the total signal, we need to add also the HV term.

Concerning the relation between the fields that define our signals with the underlying halo or void mass distribution, let us start with weak lensing, which directly depends on the distribution of dark matter across the line of sight; therefore the cosmic shear source field is intuitively proportional to the density profile of dark matter structures. Similarly, decaying dark matter is sourced by the distribution of dark matter itself, as it requires a single particle to occur in the decaying process, and therefore it directly traces the mass density. In both cases we have:

$$f_l^x(k, \, z \,|\, M) = f_d^x(k, \, z \,|\, M) = \frac{\mathcal{F}[\rho_x](k, \, z \,|\, M)}{\overline{\rho}_m(z)} \; , \tag{2.58}$$

where l stands for "lensing", d for "decaying dark matter", $x = (h, \, v)$ denotes the considered structure and $\mathcal{F}[\rho_x]$ denotes the Fourier transform of the density ρ_x.

Also the galaxy distribution is sourced by the density of dark matter structures, however the latter must be weighted through the halo occupation distribution (HOD) [216, 248, 291–294], namely $\langle \tilde{N}_g \rangle$, which is an indicator of the number of galaxies in each region of a dark matter halo:

$$f_g^x(k, \, z \,|\, M) = \frac{\langle \tilde{N}_g^x \rangle}{\overline{n}_g^x(z)} = \frac{\langle N_{\rm cen}(M) \rangle + \langle N_{\rm sat}(M) \rangle \mathcal{F}[\rho_x](k, \, z \,|\, M)/M}{\overline{n}_g^x(z)} \; , \tag{2.59}$$

where $\overline{n}_g^x = \int \mathrm{d}M \, \frac{\mathrm{d}n_x}{\mathrm{d}M} \left(\langle N_{\rm cen} \rangle + \langle N_{\rm sat} \rangle \right)$ the average number of galaxies. Following [216], and references therein, the average number of central galaxies $\langle N_{\rm cen} \rangle$ and satellite galaxies $\langle N_{\rm sat} \rangle$ in

halos can be modeled as:

$$\langle N_{\rm cen}\rangle = \frac{1}{2}\left[1+\mathrm{erf}\left(\frac{\log M-\log M_{\rm th}}{\sigma_{\log M}}\right)\right] \tag{2.60}$$

$$\langle N_{\rm sat}\rangle = \left(\frac{M}{M_*}\right)^{\alpha}\exp\left[-\frac{M_{\rm cut}}{M}\right] , \tag{2.61}$$

where $M_{\rm th}$ denotes the approximate halo mass required to populate the halo with the considered type of galaxies and $\sigma_{\log M}$ governs the width of the transition between 0 and 1 for the central galaxy. The satellite distribution is described by a power law (of order α) with an exponential cutoff $M_{\rm cut}$ at low masses. In this study, we consider the galaxy distribution from the 2MASS catalog [295], as it is one of the most extended almost-all-sky catalogs. Exploiting the HOD results of Ref. [296], we adopt a step function for central galaxies ($\langle N_{\rm cen}\rangle = 0$ for $M < 10^{12.1}$ $\mathrm{M}_\odot$ and $\langle N_{\rm cen}\rangle = 1$ for $M \geq 10^{12.1}$ $\mathrm{M}_\odot$) and take the following parameters for satellite galaxies: $\alpha = 1.2$, $M_* = 10^{13.5}$ $\mathrm{M}_\odot$ and $M_{\rm cut} = 0$.

In the case of voids, we need to adapt the HOD to a void occupation distribution (VOD). In this regard, we assume that the total number of galaxies is the same within halos and voids of the same mass. Intuitively, if the local density fractions of the Universe components remain unchanged in voids, we expect the fraction of matter contained in galaxies to be the same as in halos. Ref. [297] shows that voids usually contain bluer galaxies, however, the general properties (such as color distribution, bulge to total ratios, and concentrations) are remarkably similar to those in halos. The main difference resides in their distribution within the structure; in particular, the number of galaxies tends to increase with the radius of the void (see e.g. [277]), while void centers are expected to be extremely underdense, leaving arguably no space for central galaxies[10]. This can be accounted for by re-scaling the void density profile with a parametrization of the galaxy number density contrast (in voids) shown in [297]. We define the number density contrast of galaxies as $1+\delta_g(r) = n_g(r)/\overline{n}_v$ (where $n_g(r)$ is the radial number density of galaxies and $\overline{n}_v$ is the average density of the considered void). The density of galaxies within voids can be rewritten as

$$\rho_v^{\rm gal}(r) = \rho_v(r)\frac{n_g(r)}{\overline{n}_v} \equiv \rho_v(r)(1+\delta_g(r)) , \tag{2.62}$$

where the values for $\delta_g(r)$ have been extrapolated by the data of Ref. [297]. By plugging this expression in the HOD formula shown above and setting $\langle N_{\rm cen}(M)\rangle = 0$ for any void we obtain the needed VOD.

In the case of annihilating dark matter, the process requires both a particle and an antiparticle to occur. The source field is therefore proportional to the square of the density profile of dark matter structures:

$$f_a^x(k,\ z\,|\,M) = \frac{1}{\Delta_x^2(z)}\frac{\mathcal{F}[\rho_x^2](k,\ z\,|\,M)}{\overline{\rho}_m^2(z)} , \tag{2.63}$$

where a stands for "annihilating dark matter" and $\Delta_x^2(z)$ is the clumping factor, which acts as a transfer function between $\langle\rho^2\rangle$ and $\langle\rho\rangle^2$:

$$\Delta_x^2(z) = \frac{\langle\rho_x^2\rangle}{\overline{\rho}_m^2} = \int \mathrm{d}M\ \frac{\mathrm{d}n_x}{\mathrm{d}M}\int \mathrm{d}^3x\ \frac{\rho_x^2(\mathbf{x}\,|\,M)}{\overline{\rho}^2} . \tag{2.64}$$

[10]Indeed, void finders are usually based on tessellation methods around void centers, found as the minima in the density distribution, thus representing points sensibly far from the closest galaxies.

When considering astrophysical sources we have to replace the structure mass M with the luminosity L of the source, the mass function $\mathrm{d}n_x/\mathrm{d}M$ with the gamma-ray luminosity function (GLF) $\phi_x(L,\ z) = \mathrm{d}n_x/\mathrm{d}L$ and the linear bias with $b_s^x(M(L),\ z)$, following [208]. In this work we consider four different classes of unresolved gamma-ray astrophysical sources: BL Lacertae objects (BL Lacs), flat-spectrum radio quasars (FSRQs), misaligned AGN (mAGN) and star-forming galaxies (SFGs). The GLFs and mass-to-luminosity functions $M(L)$ of each astrophysical class are shown in section 2.4.1 and 2.4.2, respectively. The source field can be expressed as:

$$f_s^x(z \,|\, L) = \frac{L}{\langle g_s^x \rangle} \,, \tag{2.65}$$

where $\langle g_s^x(z) \rangle = \int \mathrm{d}L \; L \, \phi_x(L,\ z)$ is the average luminosity density of sources.

2.4 Astrophysical sources

Gamma-ray astrophysics has seen significant advancements over the past decade, with the detection of thousands of sources providing valuable insights into some of the most violent phenomena in the universe. However, the unresolved gamma-ray background (UGRB) remains only partially understood, with contributions from both known and potentially unknown astrophysical sources still under investigation.

Astrophysical sources are expected to play a key role in shaping the UGRB. Among the most important contributors are star-forming galaxies and active galactic nuclei. AGNs are the highly energetic central regions of galaxies, characterized by excess non-stellar emission across the entire electromagnetic spectrum. At the core of these active galaxies is typically a supermassive black hole, whose accretion of matter powers the production of two relativistic jets. The orientation of these jets relative to the observer's line of sight classifies AGNs into different categories. If the jets are directed towards Earth, the AGN is classified as a blazar [298], while if the jets are misaligned, the AGN is referred to as a misaligned active galactic nucleus (mAGN) [298, 299].

Blazars are further subdivided into two main classes: BL Lacertae objects (BL Lac) [114, 300] and flat-spectrum radio quasars (FSRQ). The primary distinction between these classes lies in their optical and radio emissions. FSRQs exhibit strong, broad optical emission lines and high radio luminosity, while BL Lacs are characterized by weaker optical lines and lower radio luminosity. Additionally, BL Lacs tend to have a harder energy spectrum in the MeV-GeV range [299] compared to FSRQs. The differences in the spectral properties of these sources contribute to the complexity of modeling their collective emission in the gamma-ray band.

The emission from these unresolved astrophysical sources is typically modeled using two key elements: the gamma-ray luminosity function and the spectral energy distribution (SED). The GLF describes the number of sources as a function of their gamma-ray luminosity, co-moving volume, and spectral index Γ ($\phi_\gamma = \mathrm{d}N_\gamma/(\mathrm{d}L\,\mathrm{d}V)$), while the SED characterizes the distribution of energy emitted across the gamma-ray spectrum. Together, these models provide a framework for estimating the contribution of star-forming galaxies, AGNs, and their sub-classes to the UGRB, which helps in disentangling the astrophysical background from other potential sources of gamma-ray emission, such as dark matter.

In this analysis, we assume the energy spectrum $G(E)$, which represents the number of γ-rays in the energy range $(E,\ E + \mathrm{d}E)$ per unit time, in absence of any absorption from the extragalactic background light, to follow a simple power-law

$$G(E) = \left(\frac{E}{\mathrm{GeV}} \right)^{-\Gamma} \tag{2.66}$$

	A [Mpc^{-3}]	$L_\star$ [erg s^{-1}]	γ_1	γ_2	p_1	p_2	$z_\star$	β
BL Lacs	9.20×10^{-11}	2.43×10^{48}	1.12	3.71	4.50	-12.88	1.67	4.46×10^{-2}
FSRQs	3.06×10^{-9}	0.84×10^{48}	0.21	1.58	7.35	-6.51	1.47	0.21

Table 2.1: Parameters of the gamma-ray luminosity function for BL Lacs and FSRQs.

β_l	$L_{l\star}$ [W/Hz]	$\rho_{l\star}$ [Mpc^{-3}]	$z_{l\star}$	k_l	β_h	$L_{h\star}$ [W/Hz]	ρ_h [Mpc^{-3}]	$z_{h\star}$
0.586	$10^{26.48}$	$10^{-7.523}$	0.71	3.48	2.42	$10^{27.39}$	$10^{-6.757}$	2.03

Table 2.2: Parameters of the radio luminosity function for mAGN.

where E is the observed photon energy and Γ the spectral index of the considered source, as outlined in the following sections. The spectra energy distribution yields

$$\frac{\mathrm{d}N}{\mathrm{d}E} = k\, G(E) \tag{2.67}$$

with k a normalization constant.

2.4.1 Luminosity function

We provide here the GLFs for each astrophysical class considered in our analysis.

Blazars

Following the LDDE model of Ref. [301], the GLF of BL Lacs and FSRQs can be parameterized as a broken power-law in luminosity and redshift:

$$\phi_\gamma\,(L,\,z) = \frac{A}{\ln(10)\,L}\left[\left(\frac{L}{L_\star}\right)^{\gamma_1} + \left(\frac{L}{L_\star}\right)^{\gamma_2}\right]^{-1} \times \left[\left(\frac{1+z}{1+z_c(L)}\right)^{-p_1} + \left(\frac{1+z}{1+z_c(L)}\right)^{-p_2}\right]^{-1}, \tag{2.68}$$

where $z_c = z_\star\,(L/10^{48}\mathrm{erg\ s^{-1}})^\beta$ and the other parameters are specified in table 2.1.

Misaligned active galactic nuclei

The GLF for mAGN can be derived from the radio luminosity function (RLF) through

$$\phi_\gamma(L,\,z) = \frac{k\,\eta}{(1+z)^{2-\Gamma}}\,\frac{1}{\ln(10)\,L_{\mathrm{tot}}^{151\ \mathrm{MHz}}}\,\frac{\mathrm{d}L_{\mathrm{tot}}^{151\ \mathrm{MHz}}}{\mathrm{d}L}\,\rho_r(L_{\mathrm{tot}}^{151\ \mathrm{MHz}}(L),\,z)\,, \tag{2.69}$$

where $k = 3.05$, $\Gamma = 2.37$ and

$$\eta = \frac{\mathrm{d}^2V_W/\mathrm{d}z\mathrm{d}\Omega}{\mathrm{d}^2V/\mathrm{d}z\mathrm{d}\Omega}\,. \tag{2.70}$$

The comoving volume $\frac{\mathrm{d}^2 V_W}{\mathrm{d}z\,\mathrm{d}\Omega}$ used by [302] and the one in the standard ΛCDM cosmology $\frac{\mathrm{d}^2 V}{\mathrm{d}z\,\mathrm{d}\Omega}$ are

$$\frac{\mathrm{d}^2 V_W}{\mathrm{d}z\,\mathrm{d}\Omega} = \frac{c^3\, z^2\, (2+z)^2}{4\, H_{0,W}^3\, (1+z)^3}\,, \tag{2.71}$$

$$\frac{\mathrm{d}^2 V}{\mathrm{d}z\,\mathrm{d}\Omega} = \frac{c\, d_L^2(z)}{H_0\,(1+z)^2\sqrt{(1-\Omega_\Lambda-\Omega_m)(1+z)^2+(1+z)^3\Omega_m+\Omega_\Lambda}}\,. \tag{2.72}$$

with $H_{0,W} = 50\ \mathrm{km\,s^{-1}\,Mpc^{-1}}$. The relation between core radio luminosity and gamma-ray luminosity is provided in [299], while [303] derived the correlation between core and total luminosities:

$$\log L = 2 + 1.008 \log L_{r,\mathrm{core}} \tag{2.73}$$

$$\log L_{r,\mathrm{core}}^{5\ \mathrm{GHz}} = 4.2 + 0.77 \log L_{r,\mathrm{tot}}^{1.4\ \mathrm{GHz}}\,. \tag{2.74}$$

The reference radio frequency in eq. (2.69) is 151 MHz thus, following [304], we consider the power-law scaling

$$\frac{L_r}{\nu} \propto v^{-\alpha_r} \tag{2.75}$$

with $\alpha_r = 0.80$. The radio luminosity function [302] can be expressed as the sum of two components,

$$\rho_r(L_r, z) = \rho_l(L_r, z) + \rho_h(L_r, z)\,, \tag{2.76}$$

where

$$\begin{cases} \rho_l = \rho_{l\star} \left(\dfrac{L_r}{L_{l\star}}\right)^{-\beta_l} \exp\left(-\dfrac{L_r}{L_{l\star}}\right) (1+z)^{k_l} & \text{for} \quad z < z_{l\star} \\ \rho_l = \rho_{l\star} \left(\dfrac{L_r}{L_{l\star}}\right)^{-\beta_l} \exp\left(-\dfrac{L_r}{L_{l\star}}\right) (1+z_{l\star})^{k_l} & \text{for} \quad z \geq z_{l\star} \end{cases} \tag{2.77}$$

and

$$\rho_h = \rho_{h\star} \left(\frac{L_r}{L_{h\star}}\right)^{-\beta_h} \exp\left(-\frac{L_{h\star}}{L}\right) \exp\left\{-\frac{1}{2}\left(\frac{z - z_{h\star}}{z_{h0}}\right)^2\right\}. \tag{2.78}$$

For $z < z_{h\star}$ we adopted $z_{h0} = 0.568$, while for $z \geq z_{h\star}$ we used $z_{h0} = 0.956$. All the parameters included in eqs.(2.77) and (2.78) are specified in table 2.2.

Star-forming galaxies

From the infrared luminosity function (ILF) $\phi_{\mathrm{IR}} = \frac{\mathrm{d}N_{\mathrm{IR}}}{\mathrm{d}\log_{10}(L_{\mathrm{IR}})\,\mathrm{d}V}$ we can obtain the GLF of SFGs:

	γ	σ	$\log_{10}(L_\star/L_\odot)$	$\log_{10}(\phi_\star/\mathrm{Mpc}^{-3})$	k_L	k_{R1}	k_{R2}	$z_\star$
spiral	1.0	0.50	9.78	−2.12	4.49	−0.54	−7.13	0.53
starburst	1.0	0.35	11.17	−4.46	1.96	3.79	−1.06	1.1
SF-AGN	1.2	0.40	10.80	−3.20	3.17	0.67	3.17	1.1

Table 2.3: Parameters of the infrared luminosity function for the three sub-classes of SFGs.

$$\phi_\gamma(L,\, z) = \phi_{\mathrm{IR}}\, \frac{\mathrm{d}\log_{10}(L_{8-1000\,\mu\mathrm{m}})}{\mathrm{d}L_{0.1-100\,\mathrm{GeV}}}\,. \tag{2.79}$$

The luminosity $L_{0.1-100\,\mathrm{GeV}}$ between 0.1 GeV and 100 GeV and the luminosity $L_{8-1000\,\mu\mathrm{m}}$ between 8 μm and 1000 μm are related via [305]

$$\log_{10}\left(\frac{L_{0.1-100\mathrm{GeV}}}{\mathrm{erg\ s^{-1}}}\right) = \alpha_{\mathrm{IR}}\ \log_{10}\left(\frac{L_{8-1000\,\mu\mathrm{m}}}{10^{10}\,L_\odot}\right) + \beta_{\mathrm{IR}} \tag{2.80}$$

with coefficients $\alpha_{\mathrm{IR}} = 1.09$ and $\beta_{\mathrm{IR}} = 39.19$. Following [306], the ILF can be written as the sum of quiescent spiral galaxies, starburst galaxies and SFG hosting a concealed or low-luminosity AGN:

$$\phi_{\mathrm{IR}} = \phi_{\mathrm{spiral}} + \phi_{\mathrm{starburst}} + \phi_{\mathrm{SF\text{-}AGN}}\,. \tag{2.81}$$

The ILF of each sub-class can be modeled as

$$\phi_i = \phi_{0,\,i}(z)\left(\frac{L_{8-1000\,\mu\mathrm{m}}}{L_{0,\,i}}\right)^{1-\gamma_i} \exp\left[-\frac{1}{2\sigma_i^2}\log_{10}^2\left(1+\frac{L_{8-1000\,\mu\mathrm{m}}}{L_{0,\,i}}\right)\right]\,, \tag{2.82}$$

where $i = \{\text{spiral, starburst, SF-AGN}\}$. The radio luminosity can be written as a function of the gamma-ray luminosity using eq. (2.80) and the normalization $\phi_{0,i}$ reads

$$\phi_{0,i} = \begin{cases} \phi_{\star,\,i}\left(\dfrac{1+z}{1.15}\right)^{k_{R1,\,i}} & \text{for } z \le z_{\star,i} \\ \phi_{\star,\,j}\left(\dfrac{1+z_{\star,i}}{1.15}\right)^{k_{R1,\,i}}\left(\dfrac{1+z}{1+z_{\star,i}}\right)^{k_{R2,\,\mathrm{i}}} & \text{for } z > z_{\star,i}\,. \end{cases} \tag{2.83}$$

All the parameters in eqs. (2.82) and (2.83) are specified in table 2.3.

2.4.2 Mass-to-luminosity relation

The astrophysical sources are better characterised by their luminosity, as opposed to the DM halos which are better characterized by the halo mass. Therefore, the power spectra involving the astrophysical components include an integral over the luminosity and the relation $M(L)$ between the luminosity of the astrophysical class and the host DM halo is required. Following

[214], the mass-to-luminosity relations for blazars (BL Lacs and FSRQs), mAGN and SFGs read

$$M_i(L) = 10^{13}\,M_\odot \left(\frac{M_{\star,i}}{10^{8.8}\,(1+z)^{1.4}}\right)^{0.645} \quad i = \text{blazar, mAGN} \tag{2.84}$$

$$M_{\rm SFG}(L) = \frac{10^{12}\,M_\odot}{(1+z)^{1.61}} \left(\frac{L}{6.8\cdot 10^{39}\ \text{erg/s}}\right)^{0.92} , \tag{2.85}$$

with

$$M_{\star,\rm blazar} = 10^9 \left(\frac{L}{10^{48}\ \text{erg/s}}\right)^{0.36} \tag{2.86}$$

$$M_{\star,\rm mAGN} = 4.6\cdot 10^9 \left(\frac{L}{10^{48}\ \text{erg/s}}\right)^{0.16} . \tag{2.87}$$

2.4.3 Distribution of sources in voids

Although gamma-ray astrophysics has deeply improved recently, previous works mostly focus on unresolved sources within dark matter halos, while their presence and properties within the most underdense regions of the Universe remain somewhat foggy and require further studies. Works on the properties of galaxies [297] and AGN [307, 308] in voids show that the environment makes very little impact on general properties. AGN are slightly more common in underdense regions, but only for the most luminous galaxies. At the same time, voids are generally younger than halos, due to the hierarchy in structure formation, showing bluer galaxies and increased rates of structure formation (the effect being evident only in the rare very massive galaxies). Nevertheless, the accretion rates do not show particular changes and we expect mostly negligible variations between the luminosity properties of sources hosted by galaxies in halos and those in voids of the same mass. Given these considerations, we assume the number of sources within voids and halos of the same mass to be constant, which is intuitively similar to what we have done for the void occupation distribution. Under this assumption, we can write the void GLF as the one of halos re-scaled by the volume fraction at fixed mass M_*[11]:

$$\phi_v(L,\ z) = \frac{V_h(M_*)}{V_v(M_*)}\,\phi_h(L,\ z) \sim 6.2\times 10^{-4}\,\phi_h(L,\ z) , \tag{2.88}$$

where $V_h(M_*)/V_v(M_*) = \Delta_v/\Delta_{h,\,\rm vir}$.

In the left panel of fig. 2.4, we show the total 3D power spectrum of the cross-correlation between cosmic shear and gamma-ray emitters (decaying/annihilating DM and the four classes of unresolved astrophysical sources discussed above) at $z = 0.5$, computed within the HVM through the sum of contributions from eqs. (2.51)-(2.55). We discuss, with more detail, the importance of each term in the Appendix. The same result is shown in the right panel of fig. 2.4 for the cross-correlation of the 2MASS galaxy catalog and the unresolved gamma-ray sky.

[11] Dimensionally speaking, the GLF is a number density per unit of luminosity; assuming no dependence of the luminosity properties on the environment and the number of sources to be constant among different structures of the same mass, the GLF goes as the inverse of a volume.

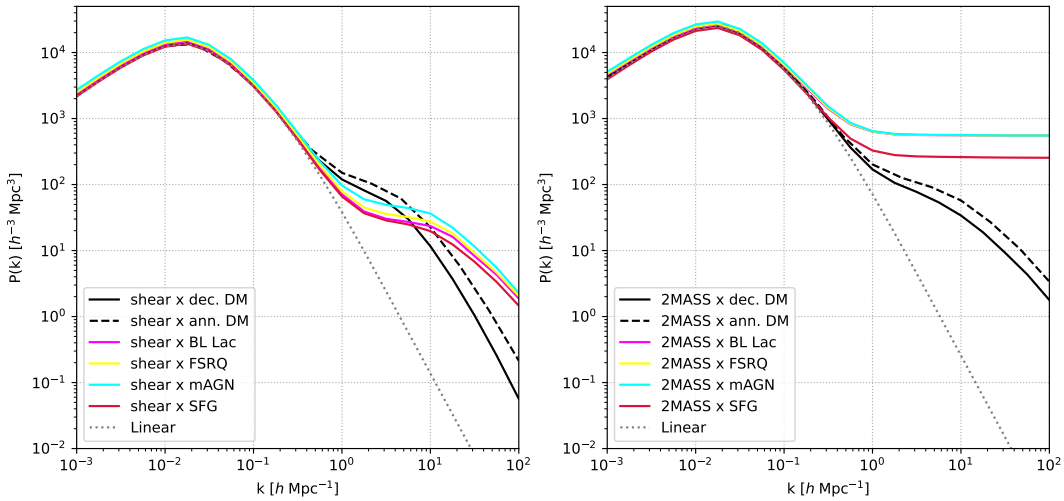

Figure 2.4: Comparison of the total cross-correlation 3D power spectrum between gamma-ray sources and gravitational tracers (at $z = 0.5$): cosmic shear (*Left*) and the 2MASS galaxy catalog (*Right*). The shown gamma-ray sources are DM decay (solid black), DM annihilation (dashed black), BL Lac (magenta), FSRQ (yellow), mAGN (cyan) and SFG (crimson red).

	Γ	$L_{\rm min}$ [erg s^{-1}]	$L_{\rm max}$ [erg s^{-1}]
BL Lacs [301]	2.11	7×10^{43}	10^{52}
FSRQ [309]	2.44	10^{44}	10^{52}
mAGN [299, 302]	2.37	10^{40}	10^{50}
SFG [306]	2.7	10^{37}	10^{42}

Table 2.4: Spectral index Γ, minimum and maximum luminosities and related references for the classes of unresolved gamma-ray astrophysical sources considered in this work.

2.5 Window functions

The final component required to compute the CAPS in eq. (2.2) is the window function $W(\chi)$ for the different observables considered. This function plays a crucial role, as it characterizes the redshift dependence of the underlying field. The interaction between the various window functions determines the shape and amplitude of the cross-correlation. Even a qualitative analysis of these functions can provide valuable insights into the potential outcomes.

2.5.1 Gravitational tracers

The two gravitational tracers considered in our analysis are weak lensing and the spatial distribution of galaxies. While the latter is a direct tracer of galaxy number counts across the sky, the former allows to track background sources through their gravitational wells.

The window function of weak lensing takes the form (see e.g. [310]):

$$W_l(\chi) = \frac{3}{2}\frac{H_0^2}{c^2}\Omega_m(1+z)\chi \int_\chi^\infty \mathrm{d}\chi' \, \frac{\chi'-\chi}{\chi'}\frac{\mathrm{d}N}{\mathrm{d}\chi'}(\chi') \,, \tag{2.89}$$

where $\mathrm{d}N/\mathrm{d}\chi$ denotes the redshift distribution of the background sources (see [17]), normalized to unit area.

For galaxies, the window function simply reduces to their redshift distribution (e.g. see [215]):

$$W_g(\chi) = \frac{\mathrm{d}N_g}{\mathrm{d}z}\frac{\mathrm{d}z}{\mathrm{d}\chi} = \frac{\mathrm{d}N_g}{\mathrm{d}z}\frac{H(z)}{c} \,. \tag{2.90}$$

As aforementioned, we consider the galaxy distribution from the 2MASS catalog [295].

2.5.2 Gamma-rays

The goal of this study is to separate the dark matter and astrophysical contributions to the unresolved gamma-ray background, which requires understanding how each radiation source is distributed across redshifts. This distribution is inherently tied to the spectral energy distribution of each source and how it evolves with redshift.

In the case of decaying dark matter we have:

$$W_d(E,\ z) = \frac{1}{4\pi}\frac{\Omega_{\rm DM}\rho_c}{m_{\rm DM}\tau_d}\frac{\mathrm{d}N_d}{\mathrm{d}E}\left[E(1+z)\right]\mathrm{e}^{-\tau[E(1+z),\,z]} \,, \tag{2.91}$$

where $\Omega_{\rm DM}$ is the cosmological abundance of DM and ρ_c the critical density of the Universe today. $m_{\rm DM}$ and τ_d denote the mass and decay lifetime of the DM particle (here we consider $m_{\rm DM} = 100$ GeV and $\tau_d = 3\times10^{27}$ s, from [209, 311], for definiteness, about at its conservative lower bound) and $\mathrm{d}N_d/\mathrm{d}E$ is the number of photons emitted by the decay in the energy band $[E,\ E+\mathrm{d}E]$, here for the decaying channel $b\bar{b}$ (see e.g. [312]). Finally, τ is the optical depth for absorption on the line of sight (taken here from [313]). The latter is relevant for gamma-rays mainly due to pair production on the extra-galactic background light emitted by galaxies in the ultraviolet, optical, and infrared bands.

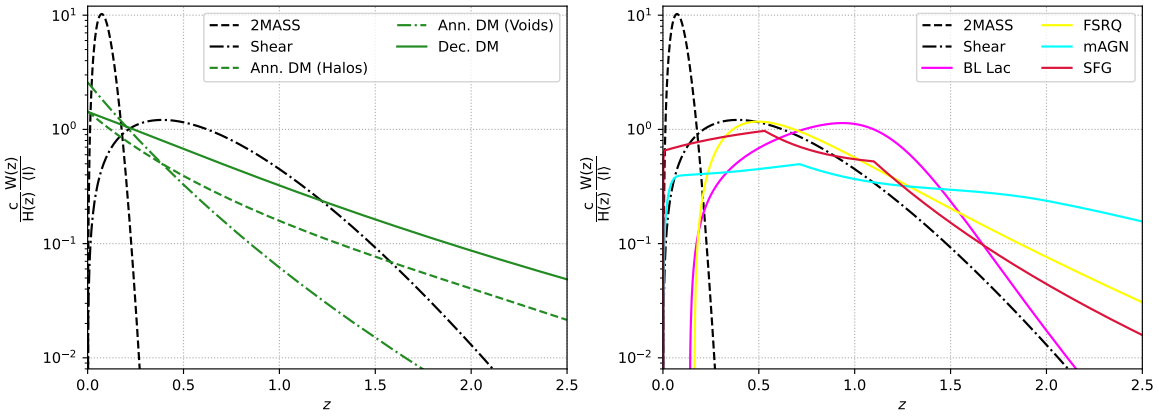

Figure 2.5: (*Left*): Comparison between the window functions of decaying/annihilating dark matter with those of the 2MASS galaxy distribution and weak lensing. (*Right*): Comparison between the window functions of each class of gamma-ray astrophysical sources and those of gravitational tracers. In both cases the functions are computed for gamma-rays with $E_\gamma = 5$ GeV, and normalized to the redshift integrated intensity.

For the case of annihilating dark matter, since the source field depends on ρ^2, the clumping factor of Eq. (2.64) enters the window function, leading to a dependence on the structure x,

differently from the decaying case:

$$W_a^x(E,\ z) = \frac{\left(\Omega_{\rm DM}\rho_c\right)^2}{4\pi}\frac{\langle\sigma_a v\rangle}{2m_{\rm DM}^2}(1+z^3)\Delta_x^2(z)\frac{{\rm d}N_a}{{\rm d}E}\left[E(1+z)\right]{\rm e}^{-\tau\left[E(1+z),\ z\right]}\ , \tag{2.92}$$

where $\langle\sigma_a v\rangle$ is the velocity averaged annihilating cross section (we consider the thermal value of 3×10^{-26} cm^{3}s^{-1} for a WIMP dark matter candidate with a mass around 100 GeV, see [209]) and ${\rm d}N_a/{\rm d}E$ is the number of photons emitted by annihilations in the energy band $[E,\ E+dE]$, we consider the channel $b\bar{b}$ [312].

The window function of astrophysical sources, within a structure x, yields (see e.g. [240]):

$$W_s^x(E,\ z) = \left(\frac{d_L(z)}{1+z}\right)^2\int_{L_{\rm min}}^{L_{\rm max}(z)}{\rm d}L\ \frac{{\rm d}N}{{\rm d}E}(E,\ L,\ z)\phi_x(L,\ z)\ , \tag{2.93}$$

where ϕ_x is the GLF, $d_L(z) = (1+z)\,\chi(z)$ the luminosity distance and ${\rm d}N/{\rm d}E$ the spectral energy distribution (SED) which, assuming a power law for the number of gamma-rays in the energy interval $(E,\ E+{\rm d}E)$, reads[12]:

$$\frac{{\rm d}N}{{\rm d}E}(E,\ L,\ z) = \frac{L}{4\pi d_L^2(z)}(1+z)^{2-\Gamma}(2-\Gamma)\left[100^{2-\Gamma}-0.1^{2-\Gamma}\right]^{-1}\left(\frac{E}{\rm GeV}\right)^{-\Gamma}\ {\rm GeV}^{-2}\ , \tag{2.94}$$

where Γ is the spectral index of the considered source class (see Table 2.4). The minimum and maximum luminosities in Eq. (2.93) depend on the intrinsic properties of the source class and are shown in Table 2.4. However, since we are dealing with the unresolved sky, $L_{\rm max}$ shall never be larger than the luminosity corresponding to the sensitivity of the detector. In this work we consider the *Fermi*-LAT telescope for gamma-ray surveys and assume a detector flux sensitivity $F_{\rm sens} = 10^{-10}$ cm^{-2}s^{-1}, for photons in the energy band $1-100$ GeV, which is well compatible with 8 years of data taking[13] and a slightly better sensitivity for a future improved detector, discussed below. Note that Eqs. (2.91), (2.92) and (2.93) must be integrated in the considered energy band, before being plugged into the CAPS of Eq. (2.2).

In fig. 2.5 we show the normalized (to the average intensity $\langle I\rangle = \int{\rm d}\chi\ W(\chi)$) window functions for gamma-rays with $E_\gamma = 5$ GeV. We compare the gravitational tracers (galaxy distribution from the 2MASS catalog and the cosmic shear) with the gamma-ray emitters: annihilating/decaying dark matter in the left panel and astrophysical sources in the right panel. We see how the latter peaks around redshifts $0.5-1$, while the former, being completely unresolved, peaks at very low redshifts and then rapidly decays.

2.6 Predicted sensitivity on the cross-correlation

As previously discussed, we underline the potential of cross-correlating gamma-ray emission from particle dark matter (either through annihilations or decays) with the most underdense regions of the Universe. Previous works have proposed [208, 213, 240] and used [215, 224, 231] the cross-correlation formalism between dark matter emission and gravitational tracers within dark matter

[12]The normalization factor in front of the energy power law comes from defining the luminosity in the energy range (0.1, 100) GeV.

[13]The constraint on $L_{\rm max}$ is more relevant at low redshift, where $L_{\rm sens} < L_{\rm max}$ and the window function tends to fall rapidly.

Bin	$E_{\rm min}$ [GeV]	$E_{\rm max}$ [GeV]	N^γ [cm^{-4}s^{-2}sr^{-1}]	$f_{\rm sky}$	$\sigma_0^{\rm Fermi}$ [deg]	E_b [GeV]
1	0.5	1.0	1.056×10^{-17}	0.134	0.87	0.71
2	1.0	1.7	3.548×10^{-18}	0.184	0.50	1.30
3	1.7	2.8	1.375×10^{-18}	0.398	0.33	2.18
4	2.8	4.8	8.324×10^{-19}	0.482	0.22	3.67
5	4.8	8.3	3.904×10^{-19}	0.549	0.15	6.31
6	8.3	14.5	1.768×10^{-19}	0.574	0.11	11.0
7	14.5	22.9	6.899×10^{-20}	0.574	0.09	18.2
8	22.9	39.8	3.895×10^{-20}	0.574	0.07	30.2
9	39.8	69.2	1.576×10^{-20}	0.574	0.07	52.5
10	69.2	120.2	6.205×10^{-21}	0.574	0.06	91.2
11	120.2	331.1	3.287×10^{-21}	0.597	0.06	199.5
12	331.1	1000	5.094×10^{-22}	0.597	0.06	575.4

Table 2.5: Gamma-ray energy bins used in this analysis, adherent with 8 years of data taking from *Fermi*-LAT Pass 8 (see [314]). N^γ is the auto-correlation noise, $f_{\rm sky}$ the observed fraction of the sky outside the combined Galactic and point-source masks and $\sigma_0^{\rm Fermi}$ the 68% containment angle of the PSF, referred to the geometric center of each energy bin $E_b = \sqrt{E_{\rm min}\, E_{\rm max}}$.

halos, and have shown how the gamma-ray signal generated by unresolved astrophysical sources typically surpasses that of dark matter, making the signal-to-noise ratio somehow unfavorable. As discussed in Sec. 2.3, the astrophysical signal depends on the GLF which can be more than three orders of magnitude lower in voids than in halos, assuming the number of sources to be constant for halos and voids with the same mass and no relevant changes in their general properties. For this reason, we show here that, while the dark matter signal from voids is reduced in size as compared to halos, nevertheless in comparison to its astrophysical background the cross-correlation signal can be favored with respect to astrophysical sources, ticking the potential usefulness of exploiting voids to research on the dark sector.

On the observational side, the most efficient gamma-ray detector today is the *Fermi*-LAT telescope, which has contributed strongly in the advancement of our knowledge on extremely powerful events in the Universe. With its excellent angular and energy resolutions and more than 10 years of service, it has been used to determine the composition of the UGRB [115, 217, 314, 315]. In this work we use, as a point of reference, the specifications adopted for the analysis of the UGRB performed in [314], based on 8 years of data taking and a selection of events with optimal angular resolution and background rejection. Ref. [314] is currently the most up-to-date analysis of the statistical fluctuations of the UGRB, and we therefore adopt the specifications (sensitivity, energy binning, angular resolution, noise) as a reference for this analysis. We will then forecast the reach of a future gamma-ray detector (called *Fermissimo* for definiteness and in continuity with previous analyses [214, 240]), as specified in [240] and which is modeled on improved specifications (like e.g. [316]).

We compute the cross-correlations on the 12 energy bins of [314] and reported in Table 2.5. For each energy bin we display the measured photon noise N^γ, the observed portion of the sky $f_{\rm sky}$ and the 68% containment angle of the *Fermi*-LAT point spread function (PSF) around the geometric center of the bin. These parameters are necessary to calculate the variance on the CAPS (see Eq. (2.3)). The beam function of the telescope depends on the photon event class and the energy spectrum and is available through the *Fermi* tools. An overall good analytical

approximation is given by (see [240]):

$$B_\ell^\gamma = \exp\left[-\frac{\sigma_b^2(\ell,\ E)\ell^2}{2}\right] , \tag{2.95}$$

where the dispersion angle of each energy bin evolves as (see [240]):

$$\sigma_b(\ell,\ E) = \sigma_0^{\rm Fermi}(E)\left[1 + 0.25\,\sigma_0^{\rm Fermi}(E)\ell\right]^{-1} , \tag{2.96}$$

for which $\sigma_0^{\rm Fermi}(E)$ is the 68% containment angle of the *Fermi*-LAT PSF and can be defined in terms of a referenced value $\sigma_0^{\rm Fermi}(E_{\rm ref} = 0.5\ {\rm GeV}) = 1.2$ deg (see [240]):

$$\sigma_0^{\rm Fermi}(E) = \sigma_0^{\rm Fermi}(E_{\rm ref})\left[\frac{E}{E_{\rm ref}}\right]^{-0.95} + 0.05\ {\rm deg}\ . \tag{2.97}$$

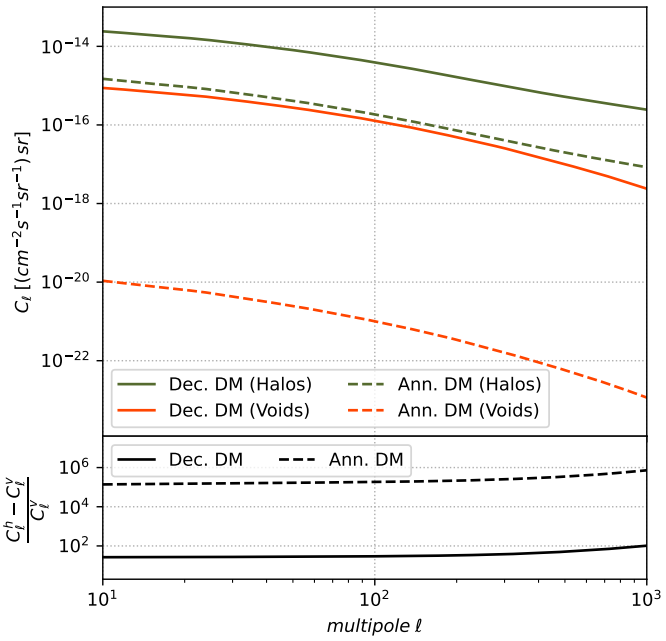

Figure 2.6: (*Top*): CAPS of decaying (solid)/annihilating (dashed) dark matter and cosmic shear both in halos (green) and voids (orange). (*Bottom*): Relative difference between the cross-correlation signal in halos and voids, for the two production cases. Note that in the case of voids, the annihilating signal is largely disfavored, being its relative difference much higher than for decaying dark matter. The dark matter particle is $m_{\rm DM} = 100$ GeV, the production channel is $b\bar{b}$, the annihilation rate is $\langle\sigma v\rangle = 3\times10^{-26}$ cm^{3}s^{-1}, the decay lifetime is $\tau_d = 3\times10^{27}$ s.

On the cosmic shear side the currently operating survey is DES [67], which provides weak lensing shape catalogs with more than 10^8 galaxies [317]. However, Euclid [14] will be the next generation galaxy survey and its forecasts [17] are extremely promising, especially for cosmic shear as the telescope is expected to be very sensitive to this effect. Galaxy surveys have achieved an incredibly high angular resolution and their beam function in harmonic space B_ℓ can be considered equal to unity in the multipole range of interest here, while the noise associated to the auto-correlation is, for Euclid: $N^{\rm Euclid} = \sigma_\epsilon^2/\overline{\rm N}_g$, where $\sigma_\epsilon = 0.3$ is the intrinsic ellipticity

and $\overline{\mathrm{N}}_g = 30$ arcmin^{-2} is the average number of galaxies per steradian (see e.g [214]). Similarly, for galaxies the beam function can be set to unity and the noise simply reduces to the average number of galaxies.

In the Gaussian error estimates on the signals of Eq. (2.3), the cross-correlation term is largely sub-dominant, while the gamma-ray auto-correlation term is dominated by the noise[14] (see e.g. [240]). The variance of the cross-correlation between gamma-rays and gravitational tracers (namely "t") can therefore be safely approximated by:

$$(\Delta C_\ell^{t\gamma})^2 \simeq \frac{1}{(2\ell+1) f_{\rm sky}} \left[\frac{N^\gamma}{(B_\ell^\gamma)^2} \left(C_\ell^{tt} + N^t \right) \right] . \tag{2.98}$$

For definiteness, as a representative case of WIMP, in the following we will consider a dark matter particle of 100 GeV mass and annihilating or decaying into the $b\bar{b}$ channel with a canonical-thermal-relic annihilation rate of $\langle \sigma_a v \rangle = 3 \times 10^{-26}$ cm^3 s^{-1} or a decay lifetime of $\tau_d = 3 \times 10^{27}$ s (close to its conservative lower bound [209, 311]), respectively.

Let us turn first to the discussion of the cross-correlation signal between dark matter gamma-ray emission and gravitational tracers. In particular, we first compare the decaying signal with the annihilating one (we chose to use only the cosmic shear as a reference for gravitational tracers, for simplicity). The CAPS of Eq. (2.2) depends on the spectra and window functions for dark matter and cosmic shear, whose prescriptions are shown in Secs. 2.3 and 2.5, respectively. In the top panel of fig. 2.6 we show the CAPS of dark matter decay (solid lines) and annihilation (dashed lines), separately for halos (green) and voids (orange). The signal produced by decaying dark matter is higher than that of annihilating dark matter across the whole range of multipoles and for both types of structures. While both annihilating and decaying signals can be modified by changing $\langle \sigma v \rangle$ or τ (which we have set here close to their bounds), nonetheless, as a general property, the relative difference between the signal in voids and halos is highly disfavored for annihilations. In fact, as shown by the bottom panel of fig. 2.6, in the case of decay the signal in voids is about a factor of 50 smaller than the corresponding signal in halos, while for annihilations the ratio is significantly depressed. This behavior is intuitively connected to the dependence of the source function on the square of the density, enhancing the already conspicuous ratio between the density of halos and voids. We conclude that underdense regions are not an efficient probe of annihilating dark matter and we will focus only on decaying dark matter for the following discussion.

Remaining in the realm of decaying dark matter, the relevant angular power spectra are shown in fig. 2.7 for the cross-correlation between cosmic shear and gamma-ray emitters, and in fig. 2.8 for that between the galaxy distribution and gamma-ray emitters. In each figure, we display the contribution from the four classes of unresolved astrophysical sources (BL Lac, FSRQ, mAGN and SFG) and from decaying dark matter, both for halos (in the left panel) and voids (in the right panel). The results refer to the sum of contributions from all the energy bins of Table 2.5. Among astrophysical sources, for the cosmic shear case, BL Lacs and SFGs provide for the dominant terms, while FSRQs are strongly sub-leading. In the case of galaxies, however, BL Lacs give way to mAGN, which climb up to the dominant contribution, together with SFGs, for high multipoles. This derives from a complex interplay between the redshift and energy dependence of the CAPS. Intuitively, mAGN have a greater impact when cross-correlating with galaxies as the 2MASS window function is peaked at lower redshift (where blazars tend to have extremely low power, due to the detector sensitivity cutoff) than the cosmic shear one, which,

[14] This is only true when considering the specifications of *Fermi*-LAT, while when considering an improved future detector, namely *Fermissimo*, the noise and beam function are largely reduced and their contribution to the error is comparable with that of the gamma-ray auto-correlation, and therefore we include them in the error estimate.

on the contrary, peaks right around the maximum of the window function for BL Lacs, that is strongly suppressed at low redshift (these behaviors are trivial by looking at the right panel of fig. 2.5).

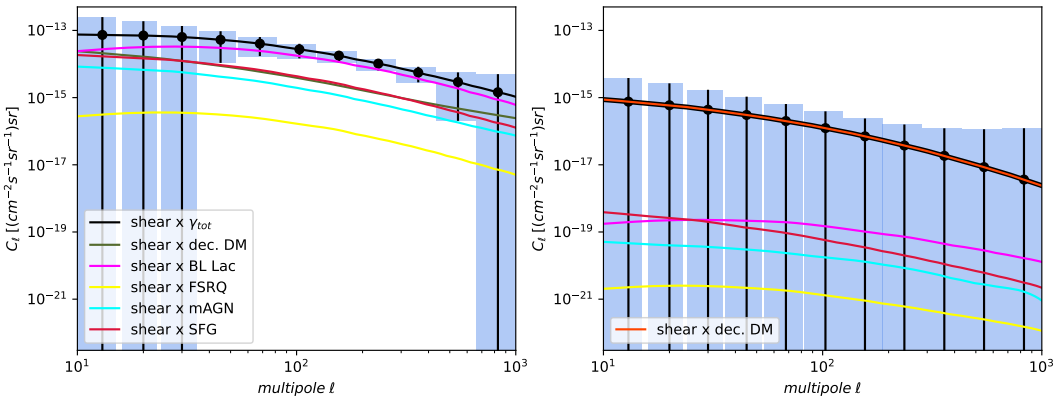

Figure 2.7: Cross-correlation angular power spectrum between cosmic shear and the unresolved gamma-ray sky. The total signal (solid black) is given by the sum of contributions from all gamma-ray sources: astrophysical sources and dark matter decays (we consider a DM mass $m_{\rm DM} = 100$ GeV and decay lifetime $\tau_d = 3 \times 10^{27}$ s). In the left panel we show the signals computed within halos and in the right panel those within voids. The result refers to the sum of contributions from all energy bins of Table 2.5 and the error bars are obtained from the Gaussian estimate of the variance of the signals. Error bars are calculated for the *Fermi*-LAT configuration discussed in the text.

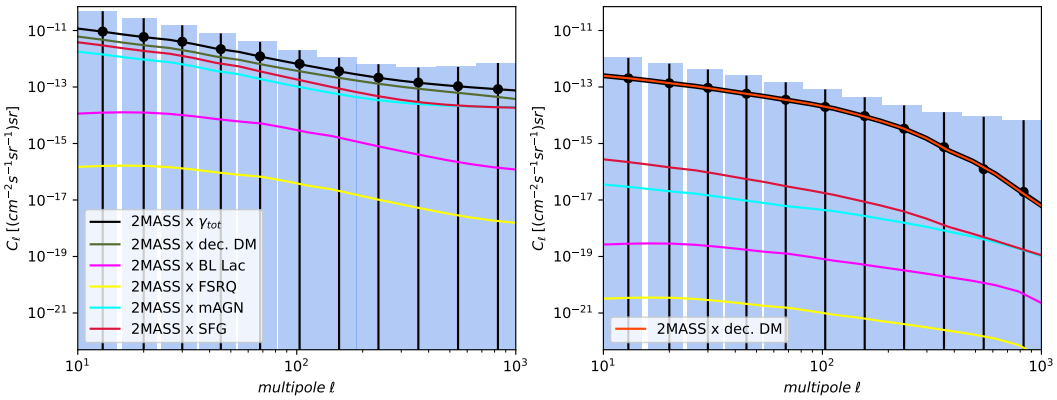

Figure 2.8: The same as fig. 2.7 for galaxies × gamma-rays.

The main observation relative to fig. 2.7 and 2.8 is that in the case of halos, the dark matter signal is either completely dominated by astrophysical sources or too close to their signal to be effectively distinguished by the present-day detectors. However, as shown by the right panel of figs. 2.7 and 2.8, in voids decaying DM provides the dominant contribution, even almost completely setting the total signal, dominating astrophysical sources by more than three orders of magnitude for the cosmic shear and from three to one order of magnitude (for increasing multipoles) for galaxies. This behavior is due to the expected much lower density of astrophysical sources in underdense environments, as discussed in Sec. 2.3 when examining the difference between the GLF in halos and voids.

In summary, though the UGRB signal is expected to be much lower in voids than in halos, the signal from decaying dark matter is expected to dominate over the astrophysical background by a sizeable amount, contrary to the case of halos, making this option (if accessible, given the sensitivity of gamma-ray detectors) a background-free signal for dark matter lifetimes 3-4 orders of magnitude smaller than current bounds. This can be seen by looking at fig. 2.9, where we

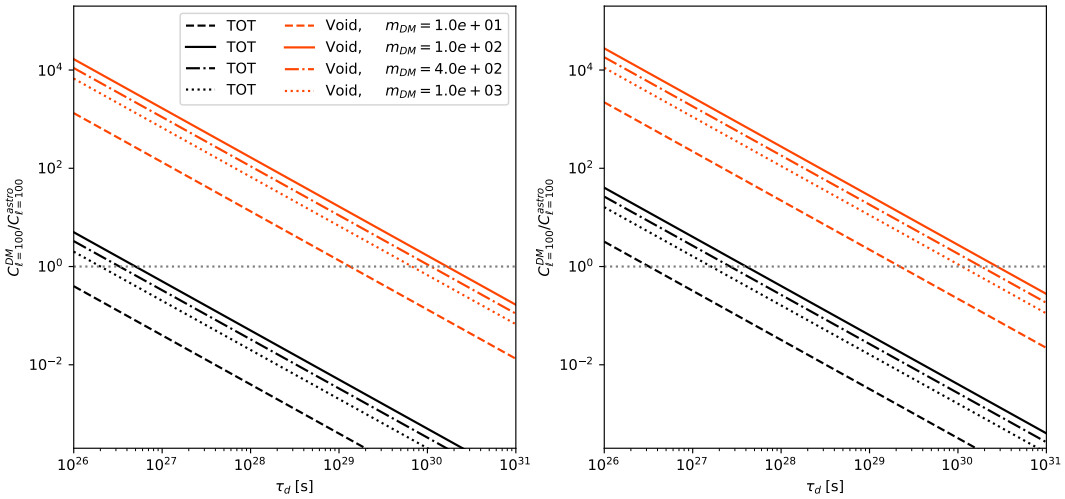

Figure 2.9: Signal-to-background ratio (at $\ell = 100$) as a function of the dark matter decay lifetime. In the left panel we show the result for the cross-correlation with cosmic shear, in the right panel that with galaxies. In both cases we report values for four different values of the WIMP mass. The signal-to-background ratio is shown in black for the all-sky cross-correlation (given by the sum of contributions from halos and voids) and in oranges for the correlation signal computed within cosmic voids only.

report the ratio between the dark matter signal and the astrophysical background as a function of the decay lifetime and for different WIMP masses. In the left panel we show the result for cosmic shear, in the right panel that of galaxies. The grey lines refer to the total contribution from both halos and voids and lead to a signal-to-background ratio (even significantly) lower than unity, if not for small values of the decay lifetime (basically already outside current bounds). On the contrary, the signal-to-background ratio within voids (orange lines) is way larger than unity also for very large values of the decay lifetime. This "background-free" situation for a relatively large fraction of the dark matter particle parameter space is analogous to the case of the galactic antideuteron signal, where a large signal-to-background ratio is present at low $\bar{D}$ energies [318]. These two channel ($\bar{D}$ and voids cross-correlation) share the feature of being potentially offering promising opportunities, though requiring high sensitivities [319].

The two gravitational tracers used here provide similar results. However, figs. 2.7 and 2.8 are helpful to determine which of them might be a better probe for decaying dark matter. In particular, the relative difference between the dark matter signal and that of astrophysical sources in voids, as discussed above, is on average higher for the cross-correlation with the cosmic shear, while being greater for galaxies for central multipoles as shown in fig. 2.9. At the same time, the difference between the total signal in halos and in voids is lower for galaxies, especially at low multipoles where is set around one order of magnitude, compared to the two orders of magnitude for the cosmic shear.

Concerning detectability of a signal, we need to consider that the errors on the signals computed through Eq. (2.3) with the *Fermi*-LAT configuration are large at single multipoles, as well for the individual energy bins of figs. 2.7 and 2.8. However, we can exploit the full range of multipoles accessible with the *Fermi*-LAT PSF, i.e. ranges between about $\ell \simeq 50$ (below which the large-scale galactic foreground is a limiting factor) and $\ell \simeq (200 \div 1000)$ depending on the energy bin [314]. This can be traced to the strong domination of the gamma-ray noise/beam term from *Fermi*-LAT, as mentioned above (see Eq. (2.98)).

In order to investigate the potentiality of the cross-correlation signals to probe dark matter, we consider a future gamma-ray detector with improved specifications, following [240]. First, we assume the exposure of the detector to be larger by a factor of 2 as compared with the current *Fermi*-LAT specification here considered. Second, we assume that the detector PSF can be

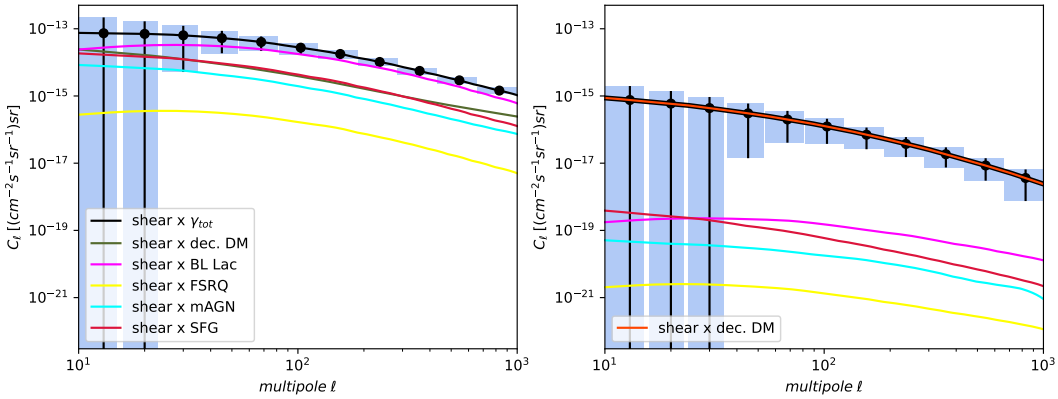

Figure 2.10: The same as fig. 2.7 using the *Fermissimo* configuration to compute error bars.

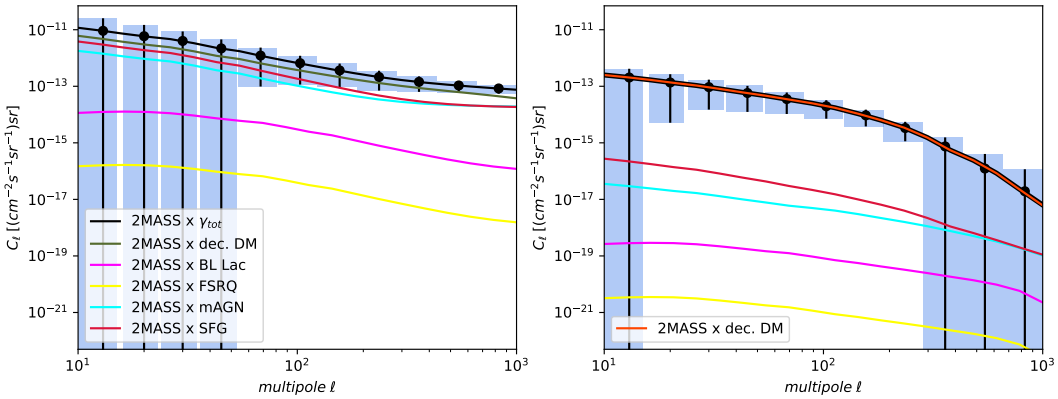

Figure 2.11: The same as fig. 2.8 using the *Fermissimo* configuration to compute error bars.

improved, adopting the same behavior of the beam function expressed in Eq. (2.95) but with a better angular resolution (see [240]):

$$\sigma_0(E) = \alpha_\sigma \times \sigma_0^{\rm Fermi}(E_{\rm ref}) \left[\frac{E}{E_{\rm ref}}\right]^{-0.95} + 0.001 \text{ deg} \,, \tag{2.99}$$

for which we assume $\alpha_\sigma = 0.2$, for definiteness. Finally, thanks to the better angular resolution, which means smaller mask, we adopt a (somewhat optimistic) larger sky-fraction coverage of $f_{\rm sky} = 0.8$, allowing to slightly reduce the impact of noise. Using the same energy bins of Table 2.5, we scale the noise as the inverse of the exposure, as in Ref. [240]. We refer to this configuration as *Fermissimo* and show its effect of reducing the variance on the cross-correlation signal in figs. 2.10 and 2.11 (for the cosmic shear and the 2MASS galaxy distribution, respectively), when compared to the *Fermi* results of figs. 2.7 and 2.8. Employing a Fisher analysis, as discussed in section 2.7, we find that our fiducial model ($m_{\rm DM} = 100$ GeV and $\tau_d = 3 \times 10^{27}$ s) would lead to a statistical significance of 5.7σ in the case of galaxies (being 1.6σ in the case of cosmic shear). The corresponding numbers for the *Fermi*-LAT configuration are 1.3σ and 0.6σ, respectively.

2.7 Bound on the WIMP lifetime

We now turn to quantifying the potential of the cross-correlation technique with voids to detect a signal or place constraints on dark matter properties. To achieve this, we employ the Fisher matrix formalism [320–322], a likelihood-based statistical method commonly used to predict the performance of future experiments. Let us therefore consider our observable, namely the C_ℓ's, modeled through a defined set of free parameters $\theta_{a=1,\dots,n}$ and with an associated covariance $\Gamma_{\ell\ell'}$; we can write the Fisher matrix (a representation of the covariance matrix for the model parameters, associated to a maximum-likelihood estimate) as:

$$F_{ab} = \sum_{\ell\ell'} \frac{\partial C_\ell}{\partial \theta_a} \Gamma^{-1}_{\ell\ell'} \frac{\partial C_{\ell'}}{\partial \theta_b} \ . \tag{2.100}$$

For any free parameter θ_a, its error can be estimated as $\sigma(\theta_a) = \sqrt{(F^{-1})_{aa}}$ and therefore we can set a bound at n-σ significance level through:

$$\theta_a^{\rm bound} = n \times \sigma(\theta_a) \ . \tag{2.101}$$

In our case, we model the total CAPS at fixed WIMP mass with seven free parameters:

$$\begin{aligned} C_\ell &= p\, \tilde{C}_\ell^{\rm DM} + A_{\rm 1V}\, \tilde{C}^{\rm astro}_{\ell,\,\rm 1V}(\Gamma_i) + A_{\rm 2V}\, \tilde{C}^{\rm astro}_{\ell,\,\rm 2V}(\Gamma_i) \ , \\ \tilde{C}^{\rm astro}_{\ell,\,\rm 1V/2V}(\Gamma_i) &= \sum_{\rm i=1}^{4} \tilde{C}^{i}_{\ell,\,\rm 1V/2V}(\Gamma_i) \ , \end{aligned} \tag{2.102}$$

where $p = (3 \times 10^{27}\ {\rm s}/\tau_d)$ is the decay lifetime-normalization with respect to the fiducial cross-correlation for DM computed with $\tau_d = 3 \times 10^{27}$ s and $A_{\rm 1V}$ and $A_{\rm 2V}$ are free normalizations for the 1V and 2V contributions to the total astrophysical signal, computed with our fiducial model (see section 2.4.1). The latter are given by the sum of the contributions from the four unresolved astrophysical sources (BL Lac, FSRQ, mAGN and SFG), each computed with the fiducial value for the related spectral index Γ_i from Table 2.4. The two normalizations account for variations in shape related to the multipoles, while the spectral indexes carry all of the information about the photon's energy dependence of the spectra (see Sec. 2.5). With our Gaussian theoretical assumptions, the covariance matrix can be assumed to be diagonal: $\Gamma_{\ell\ell'}(E) = \delta_{\ell\ell'}(\Delta C_\ell(E))^2 = \delta_{\ell\ell'}\sigma^2$. Therefore the Fisher matrix takes the form:

$$F = \begin{pmatrix} \sum_{\ell,E} \frac{(\tilde{C}_\ell^{\rm DM})^2}{\sigma^2} & \sum_{\ell,E} \frac{\tilde{C}_\ell^{\rm DM}\tilde{C}^{\rm astro}_{\ell,\,\rm 1V}}{\sigma^2} & \cdots \\ \sum_{\ell,E} \frac{\tilde{C}_\ell^{\rm DM}\tilde{C}^{\rm astro}_{\ell,\,\rm 1V}}{\sigma^2} & \sum_{\ell,E} \frac{(\tilde{C}^{\rm astro}_{\ell,\,\rm 1V})^2}{\sigma^2} & \cdots \\ \vdots & \vdots & \ddots \end{pmatrix} \ , \tag{2.103}$$

where the sums are over all considered multipoles and the energy bins of Table 2.5. It is a 7x7 symmetric square matrix since we are considering seven parameters: the DM normalization p, the two astrophysical normalizations $A_{\rm 1V}$ and $A_{\rm 2V}$ and the four spectral indexes $\Gamma_{\rm BL}$, $\Gamma_{\rm FSRQ}$,

$\Gamma_{\rm mAGN}$ and $\Gamma_{\rm SFG}$. From Eq. (2.101) we can then compute the bound on p and consequently on the decay lifetime τ_d, with respect to varying values of the WIMP mass. The Fisher formalism allows to efficiently consider all uncertainties on the chosen models and, in particular, to consider the impact of the astrophysical background noise on the detection of the dark matter signal.

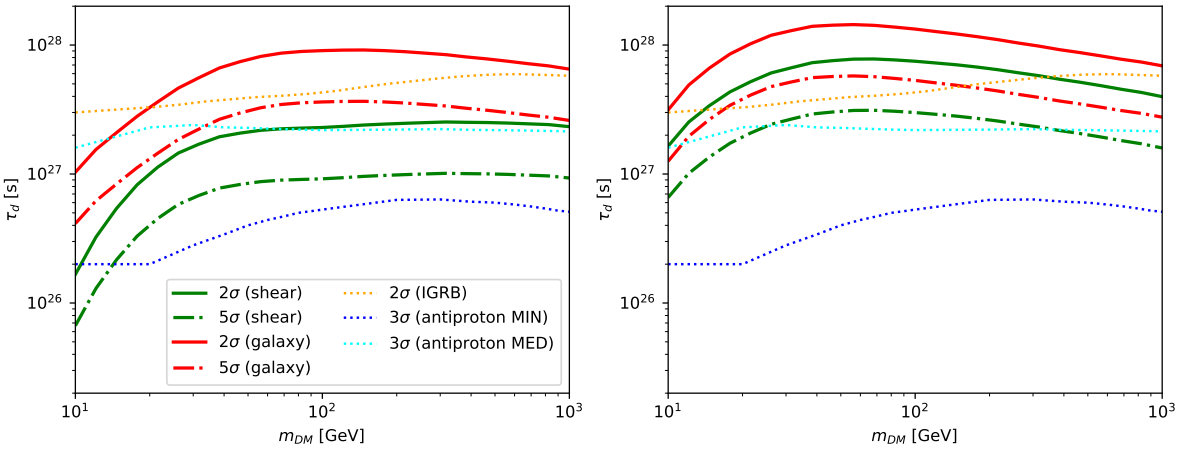

Figure 2.12: Forecast of the bounds on the DM properties (decay lifetime τ_d vs. WIMP mass m_{DM}) attainable through the study of the cross-correlation between the unresolved gamma-ray sky and either cosmic shear (green) or the galaxy distribution (red) within cosmic voids. We show both the 2σ bound and the 5σ detection reach, considering a highly efficient gamma-ray detector, namely *Fermissimo*. We also report previously derived bounds from cosmic-ray antiprotons [209] and from the isotropic gamma-ray background [311]. (*Left*): conservative bound. (*Right*): the bound accounts for priors on the non-DM parameters; $\pm$ 60% for astrophysical normalizations and $\pm$ 0.4 for spectral indexes.

In fig. 2.12 we show the 2σ (95% C.L. bound reach) and 5σ (detection limit) reach for the *Fermissimo* configuration, attainable with voids (cosmic shear in green and galaxies in red). We compare these forecasts with bounds obtained with cosmic antiprotons [209] and the isotropic gamma-ray background (IGRB) [311]. In the left panel we report the bound for the marginalized case (conservative). In the right panel we show the bounds obtained by accounting for priors on the non-DM parameters (determined from the measured uncertainties on the fiducial model parameters): for the astrophysical normalizations $A_{1\rm V}$ and $A_{2\rm V}$ we consider variations of $\pm$ 60%, while for spectral indexes we take a prior of ± 0.4 on the fiducial values of Γ_i. In general, the galaxies would allow to reach tighter bounds than cosmic shear. The forecasted bounds are competitive with previous works only for galaxies in the conservative scenario and for both galaxies and shear in the non-conservative scenario, when accounting for priors on the parameters. In particular, the current bounds could be improved (in the case of galaxies) for $m_{\rm DM} \sim 25 \div 900$ GeV in the conservative case (and in the whole range of considered masses for the non-conservative case), while being generally worse (conservative) or slightly worse (non-conservative) for cosmic shear. Let us notice that the drop in sensitivity toward lower masses is due to the fact that we are considering photon energies starting from 500 MeV (to conform to the specifications of Ref. [314], from which we adopt relevant information, like the photon noise, see Table 2.5): by decreasing the lower energy around 100 MeV would allow us to improve the forecasted bounds for lighter dark matter, making the lines flatter, since an energy threshold at 500 MeV cuts out a relevant fraction of the signal for dark matter masses close to 10 GeV, especially for the $b\bar{b}$ decay channel we are considering here. The detector PSF at those energies would be worse, though.

In conclusion, although voids lead to a much weaker cross-correlation signal than halos, their signal-to-background ratio is much larger than 1, for decay lifetimes up to 2×10^{30} s. This represents a situation in which a detection would point toward a dark matter interpretation, contrary to the case of a detection in halos, for which the signal-to-background ratio is unfavorable. The signal in voids is nevertheless difficult to achieve and requires improved sensitivities of gamma-

ray detectors: with improved specifications like those discussed in the text, the reach on bounds on the dark matter lifetime can exceed current bounds obtained through different techniques in a mass range between 25 GeV and 900 GeV.

2.8 Discussion and future prospects

In this chapter we have discussed the idea of using cosmic voids as probes for particle dark matter. We considered the cosmic shear and the galaxy distribution as gravitational tracers of the matter distribution in the Universe to investigate the nature of the unresolved gamma-ray background, which can hide a signal due to dark matter annihilation or decay. Large-scale structures are responsible for the bending of light in the weak lensing regime as well as for gamma-ray emission either from unresolved astrophysical sources or particle dark matter annihilations and decays. At the same time, the distribution of galaxies is tightly connected to the distribution of dark matter as well as to that of astrophysical sources hosted by them. We thus expect a positive correlation between these gravitational tracers and the unresolved gamma-ray emission.

We have therefore computed the cross-correlation angular power spectrum between the fluctuations due to the inhomogeneous distribution of matter in the Universe, traced by either the cosmic shear or the galaxy distribution, and those induced in the unresolved gamma-ray emission, by both astrophysical sources and dark matter annihilations/decays. We separated the signals into the contributions coming from voids and halos, respectively, to investigate the main differences among their properties within the two types of structures. We show that in voids, the cross-correlation signal generated by dark matter annihilation is strongly disfavored with respect to dark matter decay, as it depends on the square of the structure's density, leading to a much greater difference between the signal in halos and the signal in voids than the case of decaying dark matter.

On the other hand, in the case of voids and for decaying dark matter, we find that the dark matter cross-correlation signal can largely exceed the astrophysical counterpart, for an interestingly large section of the dark matter parameter space. For decay lifetimes up to 2×10^{30} s the signal-to-background ratio is (even significantly) larger than 1. This is at variance with the cross-correlation from halos, where the astrophysical signal dominates over the dark matter signal. This makes the signal from voids a potentially "background-free" option for dark matter searches for decay lifetimes about 3 orders of magnitude larger than current bounds.

The size of signal is nevertheless small, which makes observational opportunities to require next generation detectors. We found in fact that the combination of forthcoming galaxy surveys, such as Euclid, and the gamma-ray *Fermi*-LAT telescope is not able yet to detect the signal. However, potential detectability can be achieved by considering an improved gamma-ray detector, with better angular resolution and slightly larger exposure: we assumed a factor 2 larger exposure as compared to the *Fermi*-LAT, and an angular resolution a factor of 5 better than *Fermi*-LAT. In this case, the cross-correlation which uses galaxies as a dark matter tracer, would reach a 5.7σ stastistical significance for the fiducial dark matter models we adopted in the analysis ($m_{\rm DM} \sim 100$ GeV and $\tau_d = 3 \times 10^{27}$ s) and will be able to improve on current bounds on the dark matter decay lifetime for masses in the range $m_{\rm DM} \sim 25 \div 900$ GeV.

This analysis can be extended beyond the gamma-ray band to include unresolved radiation across other parts of the electromagnetic spectrum, where various dark matter candidates are thought to reside. For instance, axions can span a wide range of masses. These particles undergo a two-body decay into photons, producing a spectral energy distribution that closely resembles a delta function at half the axion's energy. Depending on their mass, axions can contribute to different regions of the spectrum: those with masses around the micro-electronvolt scale would produce photons in the radio band, while axions with masses near the electronvolt would generate infrared radiation.

In each case, the potential dark matter contribution to the unresolved radiation must be carefully compared with astrophysical sources emitting in the same range. For example, unresolved radio sources include Bremsstrahlung emission in star-forming regions, misaligned AGNs, and radio-loud quasars, while the cosmic infrared background is a combination of emissions from galaxies and significantly abundant accreting black holes. The task of separating dark matter signals from these astrophysical sources is critical, as each contributes to the unresolved sky in its respective band.

Expanding the cross-correlation analysis with cosmic voids to other photon energies provides a promising avenue to probe not only the properties but also the fundamental nature of dark matter. Cosmic voids, being relatively empty and less cluttered by astrophysical sources, offer an ideal environment to isolate potential dark matter signals. By extending our study to cover different dark matter candidates, particularly axions, this method can offer new insights into one of the most profound mysteries of modern physics. Such an approach would enable a comprehensive exploration of unresolved cosmic emission, helping to refine our understanding of dark matter across various energy scales and potentially uncover new aspects of its behavior and interactions.

This strategy highlights the significance of cross-correlation techniques in future observational efforts. By linking unresolved radiation across different energy bands with gravitational tracers like cosmic voids, we can enhance the sensitivity of dark matter searches, providing a clearer path toward detecting or constraining dark matter signals and disentangling them from astrophysical backgrounds. This multifaceted approach is crucial for pushing the boundaries of our knowledge of dark matter and its role in shaping the universe.

Chapter 3

Cosmic birefringence as a probe of axion-physics

As outlined in section 1.1, CMB stands as one of the most invaluable windows into the early universe, offering profound insights into the fundamental nature of cosmology. Over the years, successive data releases from the *Planck* satellite [18–21] have provided an unprecedented level of precision in mapping the temperature anisotropies of the CMB. These measurements have not only affirmed the predictions of the standard cosmological model but have also unveiled subtle discrepancies that challenge our current understanding. In this pursuit, the polarization data of the CMB has emerged as a pivotal tool, offering unique insights into the primordial universe. By probing the polarization patterns embedded within the CMB, researchers can delve deeper into the dynamics of cosmic inflation, test fundamental physics principles such as parity violation, and unravel the intricate tapestry of the early universe. In this context, a prominent consequence of violating parity is the in vacuo rotation of the linear polarization plane of CMB radiation, known as the cosmic birefringence (CB) effect[15]. Specifically, cosmic birefringence can be sourced by Chern-Simons terms in the electromagnetc Lagrangian [55, 56, 195, 196, 332], including quintessence couplings to the electromagnetic field [197, 333–337], by quantum-gravity motivated effective theories for electromagnetism [338–340], such as Lorentz-violating electrodynamics [46, 341], or by astrophysical sources [195, 337] (with a frequency-dependent effect). Quintessence, a hypothetical field permeating the Universe, may be accounted for by various mechanisms. These include minimally coupled scalar fields like axion-like particles (ALPs) [131, 138–140, 142, 151–153, 334, 342–349] and early dark energy (EDE) from the string axiverse [335, 350–355], or non-minimally coupled scalar fields found in scalar-tensor theories [356, 357] and early modified gravity [358]. Analysis techniques to measure the CB effect in CMB polarization data have been proposed and used in refs. [197, 328, 359–363] to obtain measurements of a non-vanishing isotropic CB angle, up to a 3-σ significance, both with the *Planck* PR3 [21] and PR4 [29] releases. Additionally, increasing interest is dedicated to investigating the variation of this effect across the sky, namely anisotropic cosmic birefringence, through data from *Planck* [364–366], BICEP/KECK [367] and SPT [165]. Cross-correlations between anisotropic cosmic birefringence and both CMB temperature and polarization have been studied in refs. [335, 336, 346, 368] as a tool for investigating the properties of EDE and axion models.

This chapter is based upon our work published in [3] and [4]. We expand upon previous studies by examining, for the first time, the cross-correlation between ALP-induced anisotropic birefringence and galaxy number counts. We compute this signal with a targeted modification of

[15]It's worth noting that birefringence represents just one potential outcome of parity-violating physics. Such physics can lead to a mixing of the CMB polarization modes, resulting in a non-zero EB correlation. Some models explore the possibility of explaining this correlation through, e.g., primordial chiral gravitational waves [323–331], without causing any rotation in the plane of linearly polarized waves.

the Boltzmann code `CLASS` [369, 370]. We show how this new probe can be particularly sensitive to ultralight ALPs, given that their late-time evolution aligns with the epoch of interest for the spatial distribution of galaxies. This correlation stems from a rotation of linearly polarized waves induced at the epoch of reionization, underscoring the novelty and worth of our approach in untangling the origin of birefringence. We focus on axions with masses $m_\phi = \left[10^{-33},\, 10^{-28}\right]$ eV, whose dynamic evolution initiates after the epoch of recombination. Within this domain, the lightest candidates experience significantly higher signal-to-noise ratios (S/N), often exceeding unity, when compared to heavier masses. This enhancement arises from the combination of upcoming CMB data and galaxy surveys. Building on this, we investigate the ALP parameter space and identify a region where the S/N of the cross-correlation not only surpasses one but also exceeds the sensitivity achieved by cosmic birefringence auto-correlation alone.[16] The effect is most pronounced around $m_\phi \sim 10^{-32}\,\mathrm{eV}$ and high initial misalignment angles θ_i, where the cross-correlation provides up to seven times more information than the auto-correlation.

Furthermore, we present a groundbreaking measurement of the underlying cross-correlation, as measured by the combination of CMB polarization data from *Planck* PR4 [29, 371] and the all-sky quasar catalog Quaia [30, 372–374]. We exploit a pseudo-C_ℓ approach (supported by QML estimates at low-ℓ's) over maps for anisotropic birefringence derived through the EB-estimator of ref. [366], based on [199, 375], and for galaxy number counts derived from Quaia [30]. The associated covariance is consistently calculated using 400 polarization plus noise simulations from *Planck* NPIPE [29], alongside an equal number of realizations from the quasar catalog. Our results reveal a cross-correlation well consistent with the null-hypothesis across the whole range of multipoles. Finally, we exploit this novel signal to constraint axion-parameters through a Gaussian likelihood approach over the aforementioned theoretical spectra. We introduce an unprecedented upper bound on the axion-photon coupling $g_{\phi\gamma}$ within the ultralight mass range $m_\phi = \left[10^{-33},\, 10^{-28}\right]$ eV. In conclusion, the innovative approach presented in this study not only offers a promising method for constraining axion-like particles and measuring birefringence but also has the potential to enhance our understanding of fundamental physics and cosmological phenomena.

Throughout the analysis we assume a spatially flat ΛCDM cosmology with cosmological parameters as derived by the *Planck* satellite in 2018 [21], otherwise specified.[17]

3.1 ALP-induced cosmic birefringence

Parity-violating terms in the electromagnetic Lagrangian give rise to different phase velocities of right- and left-handed states of photons, leading to a rotation of the plane of linear polarization on the sky (known as cosmic birefringence). Notably, Chern-Simons terms [195, 196] have been extensively investigated in this context. Here, an additional term in the electromagnetic Lagrangian is given by a pseudo-scalar field ϕ coupled to photons:

$$\mathcal{L} \supset -\frac{1}{2}\, g^{\mu\nu}\partial_\mu\phi\,\partial_\nu\phi - V(\phi) - \frac{1}{4}\, g_{\phi\gamma}\,\phi\, F_{\mu\nu}\tilde{F}^{\mu\nu}\ , \tag{3.1}$$

where $g^{\mu\nu}$ is the metric tensor, $V(\phi)$ the field potential, $g_{\phi\gamma}$ the field-to-photon coupling (later referred as axion-photon coupling, for the purpose of our work), and $\tilde{F}^{\mu\nu} = \epsilon^{\mu\nu\rho\sigma}F_{\rho\sigma}/2$ the Hodge dual of the Maxwell tensor $F_{\mu\nu}$, with $\epsilon^{\mu\nu\rho\sigma}$ being the Levi-Civita antisymmetric symbol. The field ϕ must retain a pseudo-scalar nature to preserve parity-invariance within the Lagrangian

[16] This constrained region is in agreement, to a large extent, with that able to reproduce the isotropic birefringence angle as measured by recent studies [349].

[17] Let us remind that ALPs are an extension of the underlying cosmological model.

density, as the term $F_{\mu\nu}\tilde{F}^{\mu\nu}$ violates parity.[18] Despite the field choice can be nearly arbitrary, axion-like fields emerge as compelling candidates [140, 142, 152, 342–344, 352, 354, 376, 377]. Indeed, interest in axion and axion-like physics has surged due to their manifold implications in string theories [134–138, 140–142, 378, 379], dark matter physics [131, 151, 334], quintessence models [336, 351], and possible solutions of the Hubble tension, through EDE models [335, 344, 350, 355, 380].

The main consequence of eq. (3.1) is a modification of Maxwell field equations, which admit plane wave solutions for the electric and magnetic field that correspond to left and right circularly polarized waves to lowest order, whose superposition is a linearly polarized wave [381]. However, due to the Chern-Simons' interaction they propagate at different speed, getting out of phase or, equivalently, inducing a rotation of the linear polarization in question (i.e. CMB). The angle of rotation along the pathway of CMB is given by

$$\alpha(\hat{\mathbf{n}}) = \frac{1}{2}\, g_{\phi\gamma} \int_{\tau_s}^{\tau_0} \mathrm{d}\tau \, \left(\frac{\partial}{\partial\tau} - \hat{\mathbf{n}}\cdot\nabla\right) \phi(\tau,\, \Delta\tau\,\hat{\mathbf{n}}) = \frac{1}{2}\, g_{\phi\gamma}\, [\phi(\tau_0,\, \mathbf{0}) - \phi(\tau_s,\, \Delta\tau_s\,\hat{\mathbf{n}})] \ , \tag{3.2}$$

with τ_0 and τ_s being the conformal time today and at recombination, respectively. The coming direction of the electromagnetic wave is $-\hat{\mathbf{n}}$, through which we can define the starting point of the photon's path $\mathbf{x} = \Delta\tau\,\hat{\mathbf{n}} = (\tau_0 - \tau)\,\hat{\mathbf{n}}$. Eq. (3.2) holds in the sudden recombination approximation, i.e., assuming that all photons are emitted instantaneously at the last scattering surface. However, photons of the CMB are not actually emitted all at the same time, but statistically distributed over the photon visibility function $g(\tau)$ [332, 335, 339, 349, 382–384]:

$$\alpha(\hat{\mathbf{n}}) = \frac{1}{2}\, g_{\phi\gamma}\, \phi(\tau_0,\, \mathbf{0}) - \frac{1}{2}\, g_{\phi\gamma} \int_0^{\tau_0} \mathrm{d}\tau \; g(\tau)\, \phi(\tau,\, \Delta\tau\,\hat{\mathbf{n}}) \ . \tag{3.3}$$

This equation reduces to Eq. (3.2) when the visibility function is approximated as a delta function centered in τ_s. Eqs. (3.2) and (3.3) show that birefringence is a propagation effect, hence, the longer the path, possibly the larger the effect. For this reason, CMB offers promising observational prospects. Cosmic birefringence violates parity symmetry[19] leading to a correlation between E and B modes in the CMB [57]. This arises from a rotation of the Stokes parameters Q and U

$$[Q \pm iU] \Rightarrow [Q \pm iU]\, \mathrm{e}^{\pm 2i\alpha} \, , \tag{3.4}$$

where α is the birefringence angle of eq. (3.3). The direct consequence is a modification of the observed CMB power spectra:

$$\begin{aligned}
C_\ell^{TE} &= \tilde{C}_\ell^{TE} \cos 2\bar{\alpha} \, , \\
C_\ell^{TB} &= \tilde{C}_\ell^{TE} \sin 2\bar{\alpha} \, , \\
C_\ell^{EE} &= \tilde{C}_\ell^{EE} \cos^2 2\bar{\alpha} + \tilde{C}_\ell^{BB} \sin^2 2\bar{\alpha} \, , \\
C_\ell^{BB} &= \tilde{C}_\ell^{EE} \sin^2 2\bar{\alpha} + \tilde{C}_\ell^{BB} \cos^2 2\bar{\alpha} \, , \\
C_\ell^{EB} &= \frac{1}{2}(\tilde{C}_\ell^{EE} - \tilde{C}_\ell^{BB}) \sin 4\bar{\alpha} \, .
\end{aligned} \tag{3.5}$$

[18] Let us note that the last term of eq. (3.1) violates parity when the field ϕ retains spacetime-dependence.

[19] While the Lagrangian of eq. (3.1), including the Chern-Simons term is parity-invariant, the time-dependence of the pseudoscalar field ϕ introduces an effective parity violation.

	$\bar{\alpha}$ [deg]
PR3 [361]	0.35 ± 0.14
PR4 [362]	0.30 ± 0.11
Planck + WMAP [386]	$0.342^{+0.094}_{-0.091}$

Table 3.1: Available isotropic birefringence measurements from polarization data.

Here, $\tilde{C}_\ell^{TE}$, $\tilde{C}_\ell^{EE}$ and $\tilde{C}_\ell^{BB}$ are the correlation spectra in absence of birefringence. The isotropic birefringence angle $\bar{\alpha}$ corresponds to the spatial independent counterpart of eq. (3.3), rising from the background field $\bar{\phi}$, and reads

$$\bar{\alpha} = \frac{g_{\phi\gamma}}{2}(\bar{\phi}_0 - \bar{\phi}_s)\,, \tag{3.6}$$

with $\bar{\phi}_0$ and $\bar{\phi}_s$ being the value of the background field today and at the last scattering, respectively. Given the robust scientific evidence supporting standard electromagnetic theory in accurately describing the propagation of light, it is reasonable to expect that the value of $\bar{\alpha}$ should be small. However, a π-phase ambiguity remains, as highlighted in [385]. Specifically, eq. (3.4) is mathematically identical for any $\alpha_n = \bar{\alpha} + n\pi$ (where $n \in \mathbb{Z}$). In recent years, there has been a growing body of observational constraints on isotropic birefringence. The first non-zero measurement emerged from the analysis of *Planck* PR3 data [361], and subsequent studies have improved these constraints by using the latest *Planck* PR4 release [362] and by combining *Planck* data with WMAP [386]. The results of these analyses are summarized in table 3.1. While it is possible that this effect is caused by interstellar dust emission [363, 387–389], future observations with higher statistical significance could have profound implications for fundamental physics if these detections are confirmed [390, 391]. The results presented in table 3.1 were made possible by a new technique that incorporates information from Galactic foreground emission. Relying solely on CMB power spectra would make it difficult to distinguish between $\bar{\alpha}$ and a miscalibration of the instrumental polarization angle; in such a case, these two angles would be degenerate [164, 392–395]. However, since $\bar{\alpha}$ is proportional to the photon path length and the polarized emission from our Galaxy is minimally affected by birefringence, this property can be used to break the degeneracy, allowing for the separation of these two rotation angles [198].

Cosmic birefringence can be deeply constrained at small angular scales by forthcoming ground-based experiment, such as Simons Observatory (SO) [23], South Pole Observatory [396] and CMB-S4 [24]. Meanwhile, larger scales can be precisely measured by LiteBIRD (LB) [22]. The target observational-scale of birefringence is strongly dependent on the properties of the underlying pseudo-scalar and will be extensively discussed in the following.

In addition to isotropic birefringence, fluctuations in the scalar field can induce anisotropies in the birefringence angle across the sky. To study these effects, it is useful to adopt a perturbative approach, distinguishing between the aforementioned isotropic component, caused by the background field $\bar{\phi}$, and its anisotropic counterpart, originating from field perturbations $\delta\phi$. Anisotropic birefringence has been the subject of active investigation, both observationally and theoretically. Observational efforts have used data from *Planck* [364, 365], BICEP/KECK [367], and the South Pole Telescope (SPT) [165]. These studies have been complemented by theoretical explorations, which examine cross-correlations with CMB data in axion-like particle (ALP) scenarios [346, 349, 368, 397] as well as in early dark energy (EDE) models [335, 336, 398]. These combined efforts are providing a clearer picture of both isotropic and anisotropic birefringence, offering key insights into the fundamental nature of the universe and potential new physics.

3.1.1 Background evolution

Including the Chern-Simons term of eq. (3.1), we derive the dynamics of the background field $\bar{\phi}$ via its equation of motion (EoM)

$$\bar{\phi}'' + 2\mathcal{H}\,\bar{\phi}' + a^2 \frac{\mathrm{d}V}{\mathrm{d}\bar{\phi}} = 0\,, \tag{3.7}$$

where a is the scale factor, $\mathcal{H}$ the conformal Hubble parameter and primes denote derivatives with respect to conformal time τ. The evolution is governed by the choice of the potential V and its interplay with the Hubble expansion rate. In this work, we focus on EDE models for ALPs, as discussed in section 3.1.3. However, for illustrative purposes, let us consider a quadratic potential $V = m_\phi^2\phi^2/2$ (resulting in $a^2\, m_\phi^2\phi$ as last term of eq. (3.7)). Assuming the field to be locked at early times ($\bar{\phi}' = 0$), it becomes evident from eq. (3.7) that it stays so as long as the Hubble expansion rate significantly exceeds the field's mass. Hence, lying within a slow-roll phase before transitioning to oscillations when $2\mathcal{H} \sim a\, m_\phi$. Notably, if $m_\phi > 10^{-28}\,\mathrm{eV}$, oscillations commence before the recombination epoch, whereas for smaller masses, the field evolves at a later stage.[20] Additionally, for $m_\phi < 10^{-33}\,\mathrm{eV}$, the field's evolution has not initiated, as $H_0 \sim 10^{-33}\,\mathrm{eV}$. This behavior is depicted in the right panel of fig. 3.1 for four values of the axion mass m_ϕ. The plot is also shown for the EDE potential under consideration in this analysis (see section 3.1.3) in the left panel of fig. 3.2.

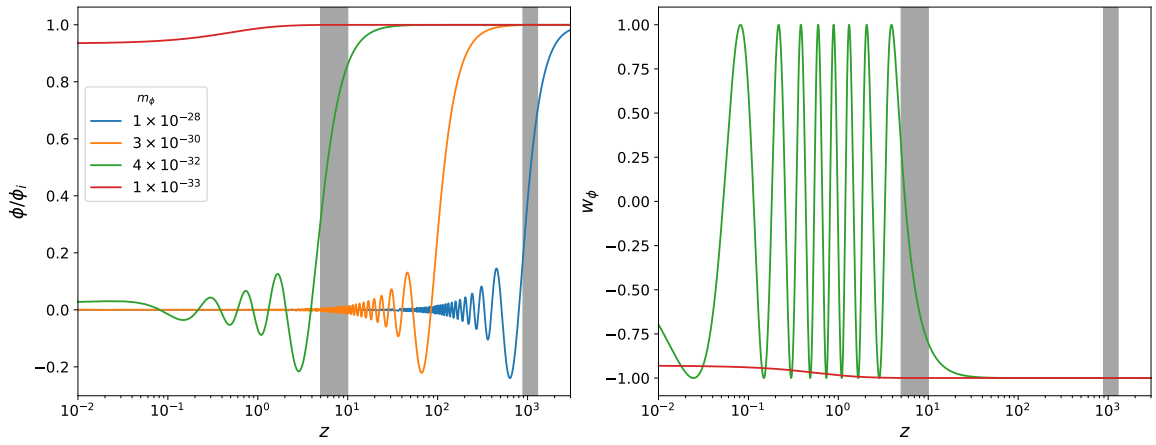

Figure 3.1: Both panels refer to a quadratic potential $V(\phi) = m_\phi^2\phi^2/2$ in eqs. (3.7) and (3.10). The two shaded region correspond to the epoch of reionization and recombination, respectively. (*Left*): background evolution of the axion field for different values of its mass m_ϕ, normalized to the initial value of the field $\bar{\phi}_i$. (*Right*): corresponding equation of state as a function of redshit. The orange and blue line are not shown due to the related high mass and consequent fast oscillations around zero, as compelling to a pressureless fluid.

Let us remind that the isotropic birefringence effect is solely determined by the difference in the field between recombination and the present time (as depicted in eq. (3.6)). Fields that start evolving sensibly before recombination (i.e. $m_\phi > 10^{-28}\,\mathrm{eV}$) would produce a fainter birefringence signal due to the relatively small difference between these two periods. Similarly, very light scalars ($m_\phi \sim 10^{-33}\,\mathrm{eV}$) would exhibit a comparable behavior since their evolution at very late times also results in a small difference. Hence, we expect intermediate mass ranges to give rise to the largest effect (see ref. [346, 368, 399] for a detailed discussion). The mass of the

[20] Let us notice that for $m_\phi \sim 10^{-32}\,\mathrm{eV}$, the evolution starts around the epoch of reionization, which aligns to the region interested by our findings (see section 3.3).

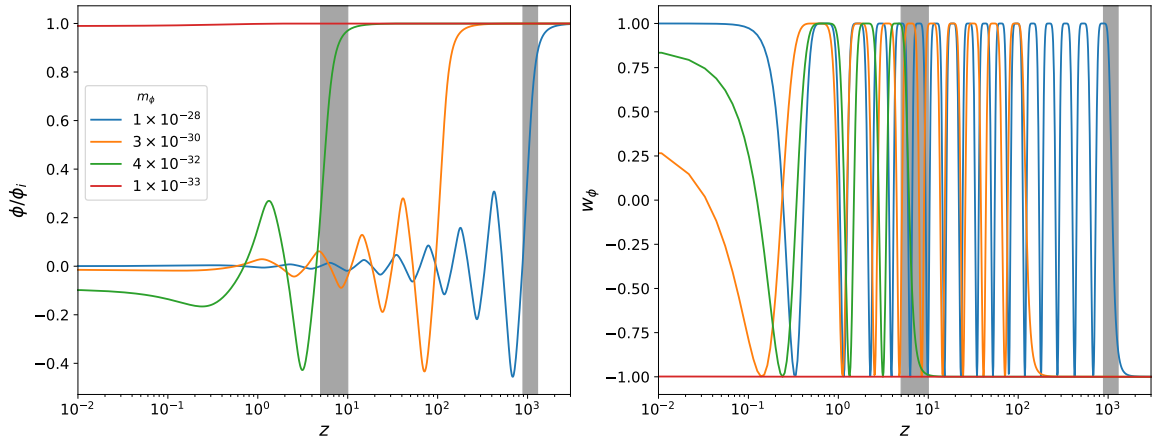

Figure 3.2: Same as fig. 3.1 for an EDE potential, as outlined in section 3.1.3.

scalar also governs its phenomenological behavior: if oscillations commence early enough they can contribute to sourcing matter perturbations, effectively behaving as dark matter; otherwise, a late evolution of the field can trigger an accelerated expansion of the Universe, mimicking the characteristics of dark energy. Achieving an accurate estimation of the critical mass, which separates these two regimes, necessitates a deep study of the field's equation of state. By varying the scalar sector of the Lagrangian, with respect to the metric tensor $g_{\mu\nu}$, we can derive the energy-momentum tensor of the field

$$T_{\mu\nu} = \partial_\mu\phi\,\partial_\nu\phi - g_{\mu\nu}\left(\frac{1}{2}g^{\sigma\rho}\,\partial_\sigma\phi\,\partial_\rho\phi + V(\phi)\right) , \tag{3.8}$$

and express its background density and pressure

$$\begin{aligned} \rho_{\bar{\phi}} &= -T^0{}_0 = \frac{1}{2a^2}\bar{\phi}'^2 + V(\phi) \\ P_{\bar{\phi}} &= \frac{1}{3}\delta^i{}_j T^j{}_i = \frac{1}{2a^2}\bar{\phi}'^2 - V(\phi) \, . \end{aligned} \tag{3.9}$$

Consequently, the equation of state reads

$$w_{\bar{\phi}} = \frac{P_{\bar{\phi}}}{\rho_{\bar{\phi}}} = \frac{\bar{\phi}'^2 - 2a^2\,V(\phi)}{\bar{\phi}'^2 + 2a^2\,V(\phi)} \, . \tag{3.10}$$

During its initial slow roll phase, characterized by $\bar{\phi}' \sim 0$, the field exhibits properties akin to dark energy and maintains this behavior as long as $w_{\bar{\phi}} < -1/3$. Subsequently, for large enough masses, it transitions to an oscillatory state, resembling a pressure-less fluid, reminiscent of dark matter. As noted in previous works [346, 399], fields with masses lower than the current Hubble rate ($m_\phi \lesssim 10^{-33}\,\mathrm{eV}$) continue to manifest characteristics akin to dark energy today, with a tendency towards larger equations of state for higher masses. Instead, for masses exceeding $m_\phi \gtrsim 10^{-31}\,\mathrm{eV}$, these fields behave akin to dark matter in the present epoch, even though they may have contributed to dark energy in earlier stages. A snapshot of this phenomenon is illustrated in the right panel of figs. 3.1 and 3.2, for a quadratic potential and the EDE potential from section 3.1.3, respectively. The two largest masses are not shown in the former

as they exhibit very fast oscillations around zero, behaving, as expected, akin to a pressureless fluid. This underscores the profound interest in exploring the parameter space of mass, offering insights into both potential ramifications on observations of birefringence and a comprehensive exploration of its phenomenological diversity.

Linear polarization is produced not only within a relatively narrow time-window at last scattering but also during reionization [400]. A detailed discussion on the birefringence effect generated by these two distinct epochs can be found in refs. [346, 399], nonetheless, in our work we will always consider the full visibility function, as our purpose is to constrain the pseudo-scalar parameter space rather than exploring the epoch-dependence of cosmic birefringence.

Finally, let us note that, for the whole discussion, we will set ourselves in the "spectator field approximation", assuming that the background field $\bar{\phi}$ does not contribute to Einstein equations (i.e. has no impact on the Hubble expansion rate and its energy budget is negligible with respect to the total energy of the Universe). In section 3.1.4, we provide a brief overview of the axion energy density behavior across the entire parameter space under consideration.

3.1.2 Perturbation evolution

As previously mentioned, anisotropies in the rotation angle of eq. (3.3) can be studied by separating the background field $\bar{\phi}$ (only time-dependent) and the perturbation field $\delta\phi$ (both time- and space-dependent),

$$\phi(\tau,\ \mathbf{x}) = \bar{\phi}(\tau) + \delta\phi(\tau,\ \mathbf{x})\ . \tag{3.11}$$

Again, by varying the kinematic action, the EoM of the field perturbation, expanded in Fourier space, reads

$$\delta\phi'' + 2\mathcal{H}\,\delta\phi' + \left(k^2 + a^2\frac{\mathrm{d}^2V}{\mathrm{d}\bar{\phi}^2}\right)\delta\phi = -\frac{1}{2}h'\bar{\phi}'\ , \tag{3.12}$$

where h is the metric perturbation in the synchronous gauge [401, 402]. Following the literature [346, 349, 369], we solve eq. (3.12) with initial perturbations and related derivative set to zero ($\delta\phi_{\rm ini} = 0$, $\delta\phi'_{\rm ini} = 0$), exploiting the attractor to adiabatic initial conditions incorporated in `CLASS`. The field starts to exhibit anisotropies when the background's oscillations and its potential inject power into the perturbations. The source term of eq. (3.12) remains null as long as the background field is locked (i.e. $\bar{\phi}' = 0$), hence, we anticipate perturbations to commence their evolution around the same time. Needless to say that the perturbation's evolution strongly depends on the nature of the field's potential, which governs the underlying phenomenology[21].

Introducing the perturbation of the pseudo-scalar in eq. (3.3) leads to anisotropic birefringence

$$\alpha(\hat{\mathbf{n}}) = \bar{\alpha} + \delta\alpha(\hat{\mathbf{n}})\ , \tag{3.13}$$

where $\bar{\alpha}$ is the isotropic counterpart (i.e., dependent on the background field, which does not vary with the direction on the sky) and $\delta\alpha(\hat{\mathbf{n}})$ can be expressed by expanding the perturbation-

[21] There exists a certain class of potentials for which the perturbative approach does not hold at every Fourier scale, and could potentially be interesting to be investigated. A more detailed discussion about it can be found in section 3.4.1.

dependent part of eq. (3.3) in spherical harmonics

$$\delta\alpha(\hat{\mathbf{n}}) = \sum_{\ell m} \alpha_{\ell m} Y_{\ell m}(\hat{\mathbf{n}}) \,. \tag{3.14}$$

A further expansion in Fourier space yields (see also refs. [55, 403])

$$\alpha_{\ell m} = \frac{i^\ell g_{\phi\gamma}}{(2\pi)^2} \int_0^{\tau_0} \mathrm{d}\tau \; g(\tau) \int \mathrm{d}^3\mathbf{k} \; Y^*_{\ell m}(\hat{\mathbf{k}}) \, \delta\phi(\tau, \; \mathbf{k}) j_\ell \left[k(\tau_0 - \tau)\right] \,, \tag{3.15}$$

$j_\ell \left[k(\tau_0 - \tau)\right]$ being the ℓ-th spherical Bessel function. Having this information at our disposal, deriving the related two-point statistics is straightforward, and we postpone this task to section 3.2.

3.1.3 The ALP potential

As discussed in section 1.3.2, axion-like particles are highly motivated from a theoretical perspective and can be generated through a variety of mechanisms. In this study, we focus on an early dark energy model inspired by the string axiverse [134, 138, 404], featuring a cosine-like potential that arises non-perturbatively,

$$V(\phi) = m_\phi^2 \, f_a^2 \left[1 - \cos\frac{\phi}{f_a}\right]^n \,, \tag{3.16}$$

where f_a is the scale of the spontaneous breakdown of a continuous symmetry, generating the pseudo Nambu-Goldstone boson, as a spin-0 degree of freedom. This potential is ideal both for dark energy and dark matter, given its residual shift-symmetry $\phi \to \phi + \text{const}$ and oscillatory behavior. At symmetry breaking the field is overdamped, being frozen by Hubble friction. Here, the axion field undergoes a coherent initial displacement, namely the initial misalignment $\theta_i = \phi_i / f_a$, that must be phase-confined between $-\pi$ and π for the QCD axion, owing to the construction of the potential. This does not hold for ALPs, that could potentially inhabit a distinct vacuum state, under shift symmetry. Nonetheless, additional interactions with the standard model could emerge in this case, yet we opt to adhere to the conventional parameter space ($-\pi < \theta_i < \pi$). Furthermore, we fix f_a to the *Planck* mass $M_{\rm Pl}$, and consider the field's mass m_ϕ, the initial misalignment angle θ_i and, of course, the axion-photon coupling $g_{\phi\gamma}$ as free parameters of our analysis. For the latter, we expect a somewhat proportionality to $1/f_a$, however, we can always fix the decay constant and remap the mass ($m_\phi \to m_\phi \, f_a$) and the initial misalignment ($\theta_i \to \theta_i / f_a$) to retain the coupling as a free, independent parameter.

When the Hubble rate drops below the effective mass of the field, the latter begins to oscillate around the minimum of the potential. Fast oscillations produce an effect similar to that of a fluid with averaged EoS $\langle w \rangle = (n-1)/(n+1)$ [405, 406]. For $n = 1$, we recover the classical axion potential [407], with a cold dark matter behavior around the potential's minimum ($\propto \phi^2$), since $\langle w \rangle = 0$. Whereas, $n = 2$ leads to a radiation-like component ($\langle w \rangle = 1/3$) [335, 346], and $n > 2$ to a fluid that dilutes faster than radiation. In particular, the case $n = 3$ has proved extremely interesting in the context of alleviating the Hubble tension [335] and reproducing the current constraint on isotropic birefringence [349][22]. Moreover, for $n \leq 2$, the axion-like field

[22] It's important to emphasize that this case study presents a component that dilutes more rapidly than any other standard components of the Universe, thereby having no impact on its late evolution.

ceases to be treatable perturbatively at some scales and different approaches should be taken into consideration. The case $n = 2$ is particularly cumbersome, as it reflects onto a divergent manifestation of Floquet theory [408], leading to an exponentially growing solution of the EoM [409, 410]. For these reasons, we will fix the exponent to 3 in the following and briefly discuss different cases in section 3.4.1.

3.1.4 The spectator field approximation

As mentioned in section 3.1.1, our analysis is conducted under the assumption that the spectator field approximation remains valid across the entire parameter space.[23] This ensures that the energy density, as expressed in eq. (3.9), remains negligible compared to the total energy budget of the universe at all times. Consequently, the axion field does not influence the expansion history or the current value of the Hubble parameter. However, it is insightful to examine how the energy density behaves throughout the m_ϕ-θ_i parameter space. In fig. 3.3, we present the axion energy density parameter $\Omega_\phi = \rho_\phi/\rho_c$ (where ρ_c is the universe's critical density) at the time of last scattering and today, shown in the left and right panel, respectively. These values are, at most, three orders of magnitude below unity and follow a predictable trend. Larger masses cause the evolution to begin closer to the recombination period, thus contributing more to the energy budget here. Conversely, smaller masses lead to later evolution, resulting in a greater contribution today. Additionally, higher initial misalignment angles yield larger contributions by amplifying the field's overall evolution.

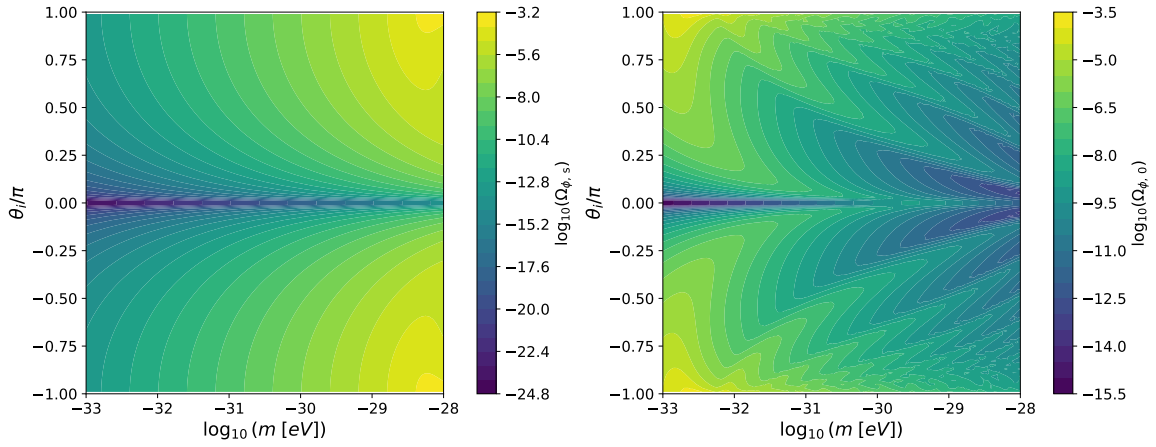

Figure 3.3: Axion energy density parameter for each mass-initial misalignment couple of our parameter space at last scattering $\Omega_{\phi,\,s}$ (*Left*) and today $\Omega_{\phi,\,0}$ (*Right*).

3.2 The cross-correlation signal of birefringence and galaxies

The ALPs' parameter space has been constrained in ref. [349, 351], exploiting the isotropic birefringence angle obtained by [361], with the *Planck* 2018 polarization data [21]. Moreover, its cross-correlation with CMB anisotropies has proven useful to constrain the underlying axion model [335, 349]. At the same time, galaxies are also powerful probes of axion-like physics [411, 412], especially in view of the forthcoming injection of new data from the recently launched *Euclid* survey [13], as well as DESI [69, 413] and SPHEREx [414]. In this work, we cross-correlate, for the first time, the information coming from cosmic birefringence with that of galaxy counts.

[23] As detailed in section 3.2.2, we consider $m_\phi \in \left[10^{-33},\, 10^{-28}\right]$ eV and $\theta_i \in (-\pi, \pi)$.

	σ_P [μK arcmin]	$\theta_{\rm fwhm}$ [arcmin]	$f_{\rm sky}$
LiteBIRD	3.11	30	0.7
Simons Observatory LAT	8.49	1.4	0.6
CMB-S4	4.24	1	0.6

Table 3.2: Forecast sensitivity on CMB polarization (σ_P), angular resolution ($\theta_{\rm fwhm}$) and observed fraction of the sky ($f_{\rm sky}$) for future CMB experiments.

We propose this angular cross-correlation as a novel way of constraining ALPs:

$$C_\ell^{\alpha G_i} = 4\pi \int \frac{{\rm d}k}{k}\, \mathcal{P}_\mathcal{R}(k) \Delta_\ell^\alpha(k) \Delta_\ell^{G_i}(k)\,, \tag{3.17}$$

where $\mathcal{P}_\mathcal{R}$ is the primordial power spectrum, and $\Delta_\ell^\alpha(k)$ is the birefringence kernel obtained from the angular coefficients $\alpha_{\ell m}$ of eq. (3.15) convolved with the photon visibility function $g(\tau)$ over the line of sight. This reads

$$\Delta_\ell^\alpha(k) = g_{\phi\gamma} \int_0^{\tau_0} {\rm d}\tau\; g(\tau) T_{\delta\phi}(\tau,\, k) j_\ell\left[k(\tau_0 - \tau)\right]\,. \tag{3.18}$$

Let us underline the physical richness of such a correlation, as both probes (birefringence anisotropies and galaxy overdensities) are sourced by scalar perturbations in the Einstein-Boltzmann equations [55, 346, 368]. In eq. (3.18), $T_{\delta\phi}(\tau,\, k)$ is a transfer function between the primordial power spectrum $\mathcal{P}_\mathcal{R}(k)$ and that of the field fluctuations $\delta\phi$, obtained from the latter dynamics[24], and enters the two-point cross-correlation function

$$\langle \delta\phi(\tau,\, \mathbf{k}) \delta\phi(\tau,\, \mathbf{k}')\rangle = \frac{2\pi^2}{k^3} \mathcal{P}_\mathcal{R}(k) T_{\delta\phi}(\tau, k) T_{\delta\phi}(\tau, k') (2\pi)^3 \delta^{(3)}(\mathbf{k} - \mathbf{k}')\,. \tag{3.19}$$

In eq. (3.17), $\Delta_\ell^{G_i}(k)$ is the galaxy kernel in the i-th redshift bin and reads

$$\Delta_\ell^{G_i} = \int {\rm d}z\, \frac{{\rm d}N}{{\rm d}z} W_i(z) \Delta_\ell(z,\, k)\,, \tag{3.20}$$

where ${\rm d}N(z)/{\rm d}z$ is the galaxy redshift distribution and $W_i(z)$ the selection function of the $i-$th redshift bin. While the analysis in the main text is performed considering a single redshift bin, a comparison with a tomographic approach, exploiting *Euclid* [17] standard prescription for the redshift bins and selection functions $W_i(z)$, can be found in section 3.4.2. Ultimately, $\Delta_\ell(z,\, k)$ is the galaxy kernel [369, 415, 416]

$$\begin{aligned} \Delta_\ell(z,\, k) = {} & \Delta_\ell^{\rm Den}(z,\, k,\, b_g,\, S_D) && \text{(Density term)} \\ & + \Delta_\ell^{\rm Len}(z,\, k,\, S_{\Phi+\Psi}) && \text{(Lensing term)} \end{aligned}$$

[24] By looking at the right hand side of eq. (3.12), it becomes evident how the evolution of axion's perturbations is directly sourced by gravitational potentials and thereby deeply connected to the primordial scalar perturbations.

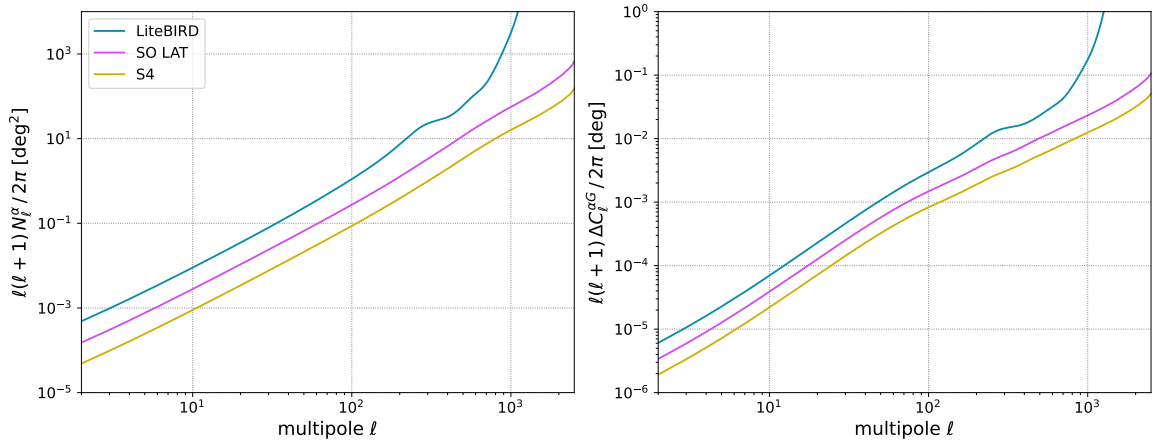

Figure 3.4: (*Left*): noise curves for the birefringence auto-correlation $C_\ell^{\alpha\alpha}$, computed through the harmonic estimator defined in [366, 417], with the instrument specifications of table 3.2, for the three related CMB experiments. (*Right*): noise dominated variance of the birefringence-galaxy cross-correlation ($C_\ell^{\alpha G}$). The result refers to eq. (3.24), assuming $\alpha = 0$. For galaxies we refer to the instrument specifications in the text below eq. (3.24).

$$
\begin{aligned}
&+ \left(\Delta_\ell^{\rm D1} + \Delta_\ell^{\rm D2}\right)(z,\, k,\, H,\, S_\Theta) && \text{(Doppler term)} \\
&+ \Delta_\ell^{\rm Red}(z,\, k,\, H,\, S_\Theta) && \text{(RSD term)} \\
&+ \left(\Delta_\ell^{\rm G1} + \ldots + \Delta_\ell^{\rm G5}\right)(z,\, k,\, H,\, H',\, S_\Phi,\, S_\Psi,\, S_{\Phi+\Psi},\, S_\Theta)\,. && \text{(Gravity term)}
\end{aligned}
\tag{3.21}
$$

Here, b_g is the galaxy bias, S_D a source function related to the growth of structure and S_Θ the velocity source function, while S_Φ, S_Ψ, $S_{\Phi+\Psi}$ are related to the Bardeen potentials Φ and Ψ. Finally, H is the Hubble parameter, and H' its derivative with respect to conformal time. Eq. (3.21) accounts for the usual density term, lensing and Doppler effects. All redshift space distortions (RSD) are embedded in the fourth line, whereas the last term includes gravity corrections, among which we have the integrated Sachs-Wolfe effect. It now becomes evident how both eq. (3.18) and eq. (3.20) are driven by the gravitational potentials, and thus the metric scalar perturbations, underscoring the indisputable relation between the two effects, if, how we show in the following, the temporal dependence allows the two kernels to peak each other out.

Similarly, from the kernels in eq. (3.18) and eq. (3.20) we obtain the birefringence and galaxy auto angular power spectra, respectively,

$$
C_\ell^{\alpha\alpha} = 4\pi \int \frac{{\rm d}k}{k}\, \mathcal{P}_\mathcal{R}(k)\, (\Delta_\ell^\alpha(k))^2 \tag{3.22}
$$

$$
C_\ell^{G_i G_j} = 4\pi \int \frac{{\rm d}k}{k}\, \mathcal{P}_\mathcal{R}(k) \Delta_\ell^{G_i}(k) \Delta_\ell^{G_j}(k)\,, \tag{3.23}
$$

where the latter accounts for correlations between the i-th and j-th redshift bin.

The cross-correlation of eq. (3.17), the two auto-correlations in eqs. (3.22)-(3.23) and the underlying axion model (described in previous sections) have been implemented in a properly modified version of the Boltzmann code `CLASS` [370, 418], following the prescription of `CLASSgal` [369], for galaxies, and those of ref. [346] for birefringence.

3.2.1 Noise estimation for future CMB experiments and galaxy surveys

In the following analysis we will be using a Gaussian-based variance of the correlations $(\Delta C_\ell^{XY})^2 \equiv \mathrm{Cov}(C_\ell^X,\, C_\ell^Y)$, in order to assess detectability of the predicted signals,

$$\left(\Delta C_\ell^{\alpha G_{ij}}\right)^2 = \frac{1}{(2\ell+1) f_{\rm sky}^{\alpha G}} \left[C_\ell^{\alpha G_i} C_\ell^{\alpha G_j} + (C_\ell^{\alpha\alpha} + N_\ell^\alpha)\left(C_\ell^{G_i G_j} + N_{ij}^G\right)\right] , \tag{3.24}$$

$$(\Delta C_\ell^{\alpha\alpha})^2 = \frac{2}{(2\ell+1) f_{\rm sky}^{\alpha}} (C_\ell^{\alpha\alpha} + N_\ell^\alpha)^2 \ . \tag{3.25}$$

Here, $f_{\rm sky}^{\alpha G}$ is the effective sky fraction observed by the combined analysis of the CMB telescope and the galaxy survey of interest (whose sky fraction read $f_{\rm sky}^{\alpha}$ and $f_{\rm sky}^{G}$, respectively), taken in the following as the lowest of the two. For the former refer to table 3.2, whilst for the latter we take the forecast DR3 fraction (36%). N_ℓ^α and N_{ij}^G are the related noise-level, respectively. The multipole dependence of N_ℓ^α stems from how the angular resolution of the underlying CMB experiment varies in harmonic space. In contrast, galaxy surveys have achieved an extremely high angular resolution, such that their beam function can be considered equal to unity over the entire range of scales under consideration. The galaxy shot noise is inversely proportional to the average number of measured galaxies per angular volume projected for the target survey ($N_{ij}^G = n_{\rm bin}/\bar{N}_g\, \delta_{ij}$, with $\bar{N}_g^{\rm Euclid} = 30$ arcmin^{-2} [17] and $n_{\rm bin}$ the number of selected redshift bins). Meanwhile, the term N_ℓ^α is computed following the approach of refs. [366, 417], relying on a harmonic estimator for birefringence constructed onto the CMB E and B mode cross-correlation. The left panel of fig. 3.4 shows the related noise curves for LiteBIRD, the Simons Observatory LAT and CMB-S4, whose sensitivity on polarization σ_P and angular resolution $\theta_{\rm fwhm}$ are reported in table 3.2. Alongside, in the right panel we illustrate the noise-dominated variance on the cross-correlation, without tomography, i.e. using a single redshift bin that goes from $z = 0.001$ up to $z = 2.5$. This is computed from eq. (3.24), assuming $C_\ell^{\alpha\alpha} = C_\ell^{\alpha G} = 0$.[25] The results outlined in the following section are also obtained through the non-tomographic approach, hence, we will be dropping the superscript referred to the i-th redshift bin from now on. Refer to section 3.4.2 for details on the impact of tomography and the dominant redshift-range of the underlying cross-correlation.

3.2.2 Signal dependence on ALP-parameters

The aim of this analysis is to present the cross-correlation between axion induced cosmic birefringence and galaxy counts as a novel tool to constraint axion-like physics. Previous works have extensively studied the cross-correlation of birefringence and CMB to test early dark energy models as a possible solution to the Hubble tension [335, 344] and explore the impact of the axion mass on the amplitude of the rotation effect [346, 349]. As discussed in section 3.1.1, masses higher than $\sim 10^{-28}$ eV induce oscillations in the field evolution prior to recombination, leading to a fainter birefringence signature due to the smaller difference between the field's present-day value and its value at the time of last scattering, see eq. (3.2), and to an even fainter signal for the birefringence from reionization. Moreover, lower masses have proven effective in reproducing the angle constrained by CMB data [361–363, 386], as shown in refs. [346, 349, 351, 384]. For these reasons and because of the numerical complications of dealing with higher masses[26],

[25] This is a suitable approximation as long as the axion-photon coupling remains fairly low, resulting in $C_\ell^{\alpha G} \ll C_\ell^{\alpha\alpha} \ll N_\ell^\alpha$.

[26] When $m_\phi > 10^{-28}$ eV, oscillations not only begin before the epoch of recombination but also accelerate as they progress towards the later stages of the Universe. Consequently, `CLASS` encounters numerical challenges when employing very small integration time-steps, leading to significantly longer execution times required to achieve

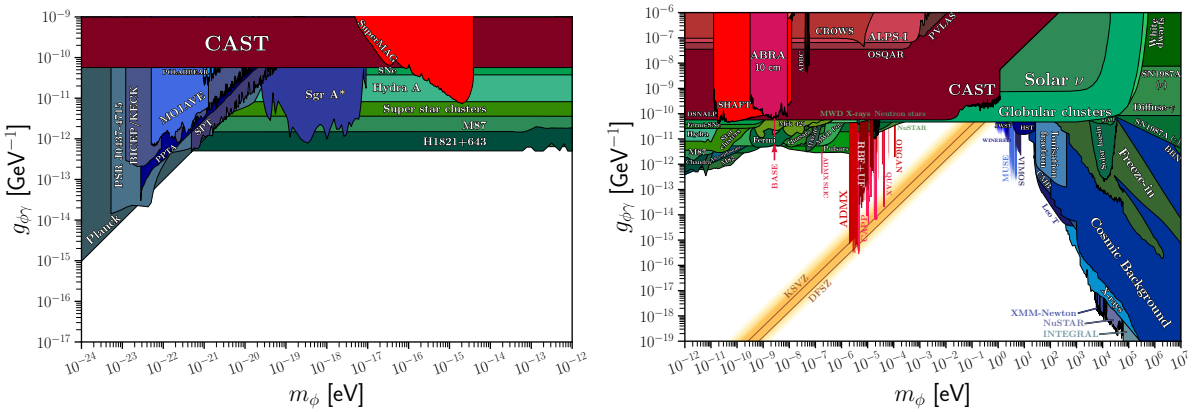

Figure 3.5: Current bounds on the axion-photon coupling, $g_{\phi\gamma}$, as a function of the axion mass, m_ϕ, as derived from various analysis (see [175]). (*Right*): standard constraints down to $m_\phi = 10^{-12}\,\text{eV}$. (*Left*): extension from cosmology down to $m_\phi = 10^{-24}\,\text{eV}$.

we concentrate our analysis on $10^{-33}\,\text{eV} \leq m_\phi \leq 10^{-28}\,\text{eV}$. Additionally, galaxies serve as low-redshift tracers, implying that we anticipate larger contributions to the cross-correlation for fields whose evolution commences at later epochs, associated with lower masses. Beyond mass considerations, we explore variations in the initial misalignment angle θ_i, establishing the "in vacuo" initial condition post-symmetry breakdown, and in the axion-photon coupling $g_{\phi\gamma}$, which determines the amplitude of the cross-correlation signal.

The level of coupling between axions and photons has been constrained by haloscopes, helioscopes, colliders and astrophysical searches (see `AxionLimits` [175] for all data and references) down to $m_\phi \sim 10^{-12}\,\text{eV}$ (see the right panel of fig. 3.5). Ref. [384] presents a novel constraint down to $m_\phi \sim 10^{-24}\,\text{eV}$ (shown in the left panel of fig. 3.5 alongside other cosmological bounds), derived from isotropic birefringence[27], while ref. [352] within a model of electroweak axion dark energy, accounting for the non-vanishing birefringence angle of ref. [361], at masses around $10^{-33}\,\text{eV}$. Similarly, ref. [349] constraints the axion-parameters for a mass range $m_\phi \in \left(10^{-33}, 10^{-26}\right)\,\text{eV}$, exploiting the isotropic birefringence angle of ref. [362]. Nonetheless, the targeted masses of our analysis remain poorly constrained due to their ultralight nature, far below the sensitivities of direct search experiments, and cosmology offers an excellent avenue for probing this region of the parameter space. On the account of these considerations, we adopt $g_{\phi\gamma} = 10^{-12}\,\text{GeV}^{-1}$ as an upper bound of our parameter space [175, 420, 421]. In summary, our focus lies within the following parameter range: $10^{-33}\,\text{eV} \leq m_\phi \leq 10^{-28}\,\text{eV}$, $-\pi < \theta_i \leq \pi$, $g_{\phi\gamma} \leq 10^{-12}\,\text{GeV}^{-1}$ (refer to section 3.1.3 for a discussion on the range of variation of the initial misalignment angle θ_i).

We have computed the cross-correlation signal with our modified version of `CLASS`, following the prescriptions of section 3.2 and accounting for an EDE model of the axion potential with $n = 3$, as discussed in section 3.1.3. For the following analysis, the angular power spectra are calculated in a non-tomographic framework, specifically for a single redshift bin up to $z = 2.5$. Nonetheless, we discuss the impact of tomography in section 3.4.2, exploiting the ten redshift bins of *Euclid* [17].[28] Fig. 3.6 illustrates the cross-correlation alongside with the corresponding variance from eq. (3.24) for the CMB experiments considered in our study (S4, SO and LB).

the necessary resolution for the cross-correlation under investigation.

[27] Ref. [419] derives a bound, in a similar mass range, based on cosmic birefringence around supermassive black holes.

[28] We expect the signal to grow as the redshift approaches the peak of the non-integrated galaxy kernel in eq. (3.20). However, this trend is influenced by a complex interplay between the ALP-parameters and the latter. For certain points in the parameter space, the cross-correlation peaks at redshifts exceeding 2.5, which may be explored by surveys other than the one currently under consideration, namely *Euclid*.

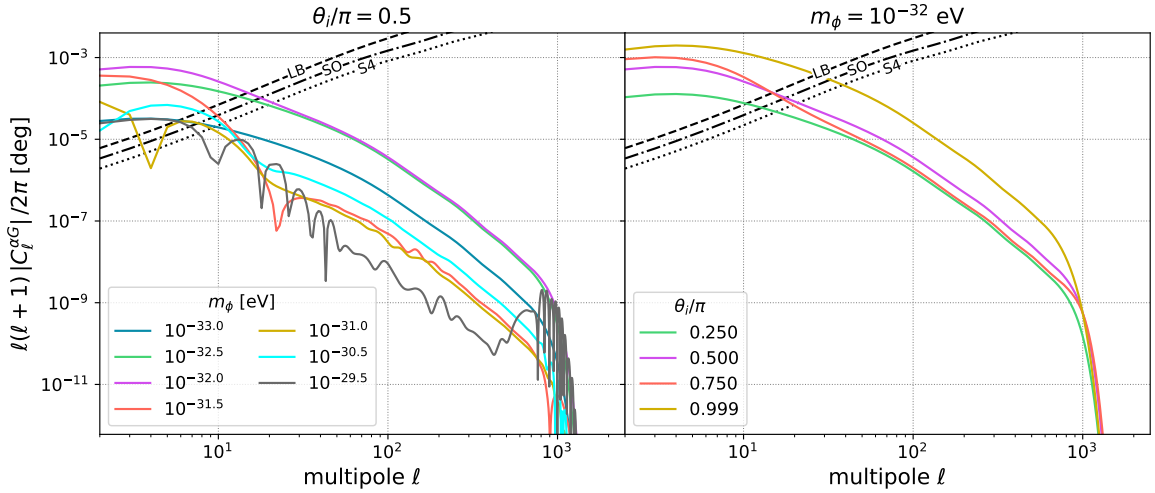

Figure 3.6: Cross-correlation angular power spectrum between anisotropic birefringence and galaxy number counts for multiple values of the ALP mass and fixed initial misalignment angle $\theta_i = \pi/2$ (*Left*), and multiple values of the initial misalignment angle and fixed mass $m_\phi = 10^{-32}\,\mathrm{eV}$ (*Right*). The black lines refer to the noise levels of eq. (3.24) for *Euclid* as a galaxy survey and the CMB experiments under consideration: CMB-S4 (dashed), Simons Observatory (dot-dashed) and LiteBIRD (dotted). All spectra are computed with an axion-photon coupling $g_{\phi\gamma} = 2 \times 10^{-14}\,\mathrm{GeV}^{-1}$, and scale linearly with increasing coupling values.

All the spectra in that figure have been computed with the axion-photon coupling fixed to $g_{\phi\gamma} = 2 \times 10^{-14}\,\mathrm{GeV}^{-1}$.[29] In the left panel, we illustrate the correlation's dependency on the field's mass, with the initial misalignment angle fixed at $\theta_i = \pi/2$. The signal tends to peak at large angular scales, with most of the signal-dominated information coming from $\ell < 100$. Subsequently, the signal starts to decrease, transitioning to an oscillatory pattern around zero for larger masses. This oscillation occurs at lower multipoles as the mass increases, stemming from a complicated interplay between the extended duration of oscillations and the galaxy tracer transfer function. The signal's amplitude peaks around $m_\phi \sim 10^{-32}\,\mathrm{eV}$, decreasing for masses smaller or larger than this value. The decrease is however less pronounced for smaller than for larger masses. We anticipate a stronger correlation for axion-like fields whose transfer function aligns with the peak of the galaxy transfer function. Given that galaxies serve as low-redshift tracers, fields initiating their evolution at later epochs are preferred (i.e., smaller masses). In the right panel of fig. 3.6, we show how the cross-correlation varies with respect to the initial misalignment angle, at fixed mass $m_\phi = 10^{-32}\,\mathrm{eV}$. A larger angle corresponds to a greater amplitude of the correlation. The initial misalignment angle not only determines the initial positioning of the field within its potential (see eq. (3.16)), thereby altering its oscillatory behavior, but also establishes the initial value of the field itself and subsequently influences the magnitude of its evolution. This effect is particularly pronounced for small masses, where oscillations have yet to commence today, and the field's value remains close to its initial condition.

Let us underline that the parameters discussed in eqs. (3.2) and (3.3) play a crucial role in predicting both the isotropic and anisotropic components of the birefringence angle. To this end, it is useful to explore the region of parameter space able to reproduce the isotropic angle, as constrained by available polarization data [361–363, 386]. An extensive analysis has been performed by some of us in ref. [349] for quadratic potentials, identifying a set of best fit parameters yielding the observed rotation angle ($\bar{\alpha} = 0.3^\circ \pm 0.11^\circ$ [362]). Additionally, figure

[29] By looking at eq. (3.18), it is evident that the cross-correlation increases linearly with the axion-photon coupling. Hence, as the latter grows, we anticipate the signal to stand out from the related variance, even at higher multipoles.

(5a) of ref. [349] shows the constrained 2-σ region in the parameter space m_ϕ-$g_{\phi\gamma}$ for the same EDE model under consideration in this work. However, the initial misalignment angle is fixed in that figure, as the isotropic component of birefringence is degenerate in the product $g_{\phi\gamma}\,\theta_i$. This does not hold for the cross-correlation presented here, offering as an excellent tool to break this degeneracy but, at the same time, making a direct comparison with the results of [349] not completely straightforward. For this reason, in the following we explore the axion-like parameter space mostly focusing on the detectability of the the cross-correlation alone. We will anyway provide a more detailed comparison with [349] below.

3.3 Exploring the ALP parameter space with the signal-to-noise ratio

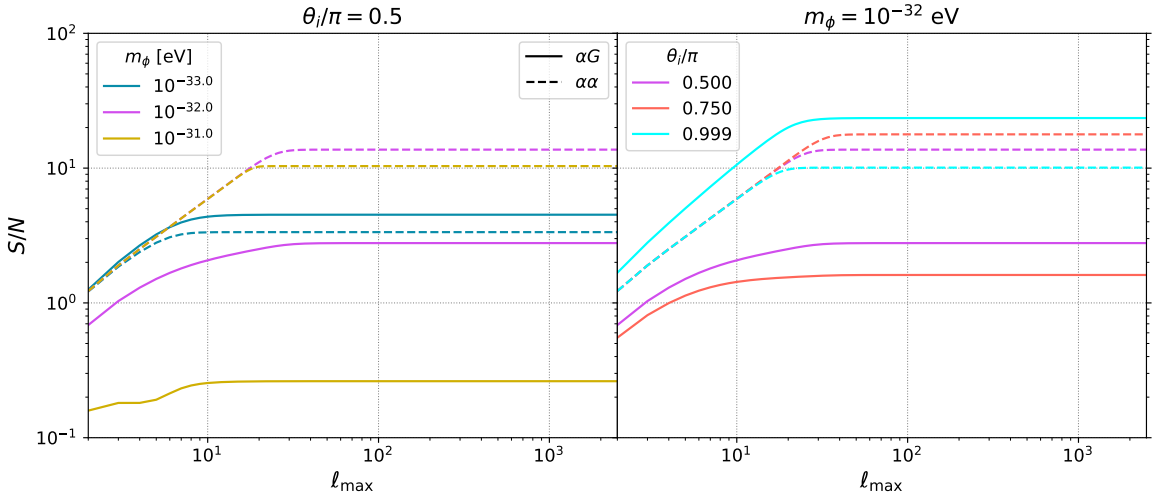

Figure 3.7: Signal-to-noise ratios of the birefringence-galaxy cross-correlation (solid) and birefringence auto-correlation (dashed) as a function of the maximum multipole $\ell_{\rm max}$. The result is shown separately for multiple points in the m_ϕ - θ_i parameter space at fixed misalignment angle and mass in the left and right panel, respectively (the axion-photon coupling is set to $2 \times 10^{-14}\,\mathrm{GeV}^{-1}$).

We aim to determine the potential detectability of the signal by combining upcoming data releases from the *Euclid* survey [17] with future and forthcoming polarization data from LiteBIRD [22], the Simons Observatory [23] and CMB-S4 [24]. To this purpose, we explore variations of the signal-to-noise ratio in the entire parameter space (m_ϕ, θ_i, $g_{\phi\gamma}$). We compute the (S/N) both for the cross-correlation $C_\ell^{\alpha G}$ and auto-correlation $C_\ell^{\alpha\alpha}$. Our goal is to identify regions where the cross-correlation surpasses a threshold of one, indicating potential detectability in experiments, and where it also exceeds the auto-correlation. This suggests that the cross-correlation offers potentially richer information compared to the auto-correlation alone. The corresponding signal-to-noise ratios read

$$(S/N)^{\alpha G} = \sqrt{\sum_{\ell=\ell_{\rm min}}^{\ell_{\rm max}} \left(\frac{C_\ell^{\alpha G}}{\Delta C_\ell^{\alpha G}}\right)^2}\,, \tag{3.26}$$

$$(S/N)^{\alpha\alpha} = \sqrt{\sum_{\ell=\ell_{\rm min}}^{\ell_{\rm max}} \left(\frac{C_\ell^{\alpha\alpha}}{\Delta C_\ell^{\alpha\alpha}}\right)^2}\,, \tag{3.27}$$

$(S/N)^{\alpha G}$ is computed in the non-tomographic scenario, focusing on a single redshift bin up to

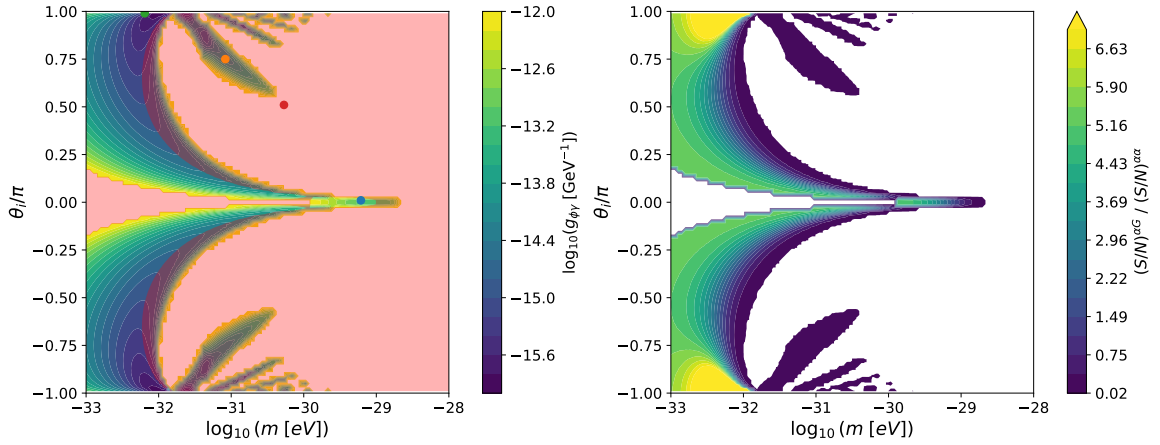

Figure 3.8: The signal-to-noise ratios presented here are computed with the instrument specifications of CMB-S4 (see table 3.2) and those of *Euclid* presented in section 3.2. We set the minimum observable multipole to $\ell_{\rm min} = 10$. (*Left*): axion-photon coupling $g_{\phi\gamma}$ needed to achieve unity in the (S/N) of the cross-correlation. The four dots correspond to particular points of the parameter space, for which we show the (S/N)-coupling relation in fig. 3.12. (*Right*): ratio between the (S/N) of the cross-correlation and the auto-correlation for the corresponding coupling values needed to achieve unity in $(S/N)^{\alpha G}$, for each point of the parameter space in the left panel. The red-shaded region identifies where this ratio is smaller than one, whilst missing points around the contour refer to where $(S/N)^{\alpha G} < 1$ even for the largest coupling considered in our analysis ($g_{\phi\gamma} = 10^{-12}\,\mathrm{GeV}^{-1}$). Let us stress how the constrained region is compatible, to a vast extent, with that able to reproduce the most recent measurements of the isotropic birefringence angle [349].

$z = 2.5$. It's worth mentioning briefly that we anticipate a slight improvement in the results when applying tomography and refer to section 3.4.2 for further discussion. In eqs. (3.26) and (3.27), $\ell_{\rm max}$ is the maximum multipole up to which the targeted experiments are sensitive to this novel cross-correlation. Although we fix it to the highest multipole computed by `CLASS`, let us notice that the (S/N) saturates at smaller multipoles. Examining fig. 3.6 we observe how the cross-correlation peaks at large angular scales (small ℓ's), with its variance notably exceeding the signal around $\ell = 30 - 40$.[30] Fig. 3.7 depicts the behavior of eqs. (3.26) and (3.27) with respect to $\ell_{\rm max}$ for multipole points in the m_ϕ - θ_i parameter space and $g_{\phi\gamma} = 2 \times 10^{-14}\,\mathrm{GeV}^{-1}$.[31] The multipole necessary for the (S/N) to saturate significantly depends on the ALP-parameters. However, it is reasonable to presume that all of the information is enclosed before $\ell = 100$.

Wide galaxy surveys such as *Euclid* are not anticipated to probe the largest scales due to their expected sky coverage. Following [17], we consider $\ell_{\rm min} = 10$ as our baseline, while also considering a more optimistic scenario where scales down to $\ell_{\rm min} = 5$ can be observed. Fig. 3.7 also demonstrates that the initial multipoles do not significantly impact the (S/N), as most of the contribution is added in for $\ell > 10$ especially for lower masses and high initial misalignment angle.

We ran our modified version of `CLASS` on a 100×100 grid in the θ_i-m_ϕ parameter space[32] and found the necessary value of the axion-photon coupling $g_{\phi\gamma}$ to get $(S/N)^{\alpha G} > 1$. The latter has a strong impact on the signal-to-noise ratio, as it appears as a multiplicative factor in the cross-correlation (see eq. (3.17)) and as its square in the auto-correlation (see eq. (3.22)), stemming from the angular coefficients of eq. (3.15). As long as the birefringence noise term dominates over

[30] The interplay between the signal and its variance is strongly dependent on the axion-photon coupling. As the latter increases, the variance surpasses the signal at higher multipoles

[31] Here, we set $\ell_{\rm min} = 2$ to show the impact of each multipole on the signal-to-noise ratio. However, in the subsequent analysis, we will adopt a higher minimum multipole in accordance with *Euclid*'s guidelines [17].

[32] In doing so, we ensured that the spectator field approximation always holds, by checking that the axion energy density is negligible with respect to standard ΛCDM components. Further insights can be found in section 3.1.4.

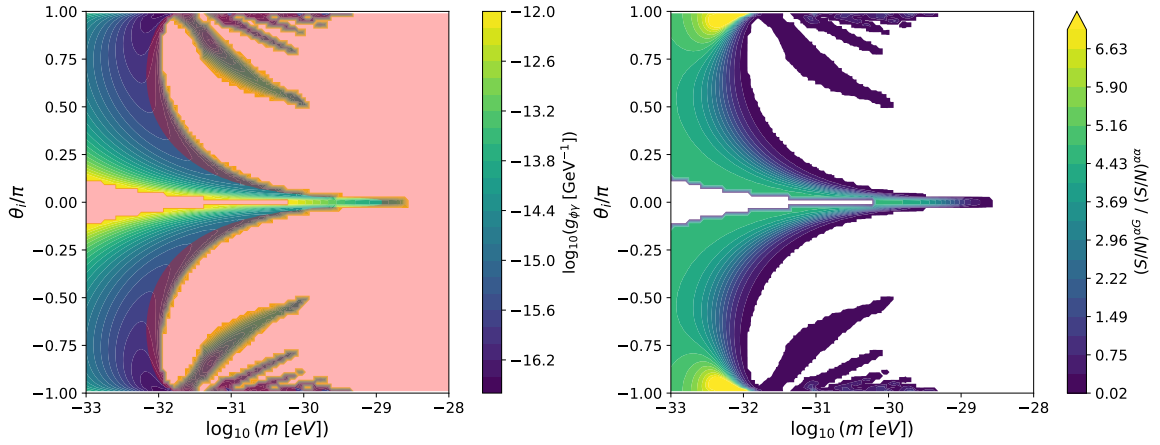

Figure 3.9: Same as fig. 3.8, with the minimum multipole of the signal-to-noise ratios in eqs. (3.26) and (3.27) brought down to 5.

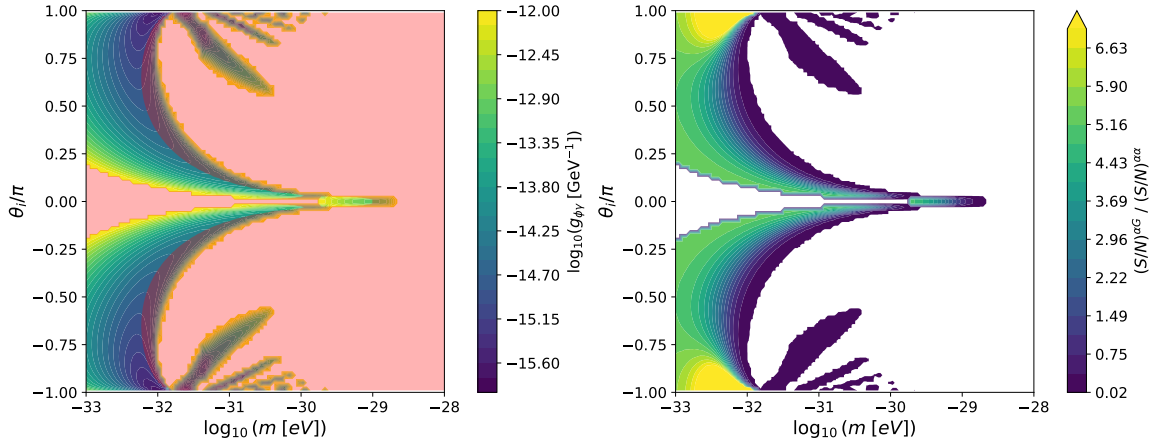

Figure 3.10: Same as fig. 3.8, with the instrument specifications of the Simons Observatory (see table 3.2).

the related auto-correlation in eqs. (3.26)-(3.27), $(S/N)^{\alpha G} \propto g_{\phi\gamma}$ and $(S/N)^{\alpha\alpha} \propto g_{\phi\gamma}^2$. However, this relationship no longer holds as the coupling increases. Eventually, when the auto-correlation significantly surpasses the noise, both signal-to-noise ratios will saturate to a $g_{\phi\gamma}$-independent value, since their numerator and denominator scale with the same power. This asymptotic behavior can be summarized as follows:

$$(S/N)^{\alpha G} \longrightarrow \sqrt{\sum_{\ell=\ell_{\min}}^{\ell_{\max}} \frac{\left(\tilde{C}_\ell^{\alpha G}\right)^2}{\tilde{C}_\ell^{\alpha\alpha}\left(C_\ell^{GG}+N^G\right)}(2\ell+1)f_{\rm sky}^{\alpha G}}\,, \tag{3.28}$$

$$(S/N)^{\alpha\alpha} \longrightarrow \sqrt{\sum_{\ell=\ell_{\min}}^{\ell_{\max}} \frac{2\ell+1}{2} f_{\rm sky}^{\alpha}}\,, \tag{3.29}$$

where $\tilde{C}_\ell^{\alpha G} = C_\ell^{\alpha G}/g_{\phi\gamma}$ and $\tilde{C}_\ell^{\alpha\alpha} = C_\ell^{\alpha\alpha}/g_{\phi\gamma}^2$ are the coupling-independent correlations. It's notable that this asymptotic value of the signal-to-noise ratio is solely dependent on the underlying ALP-parameters (m_ϕ and θ_i). Moreover, the cross-correlation is always disfavored with respect to the auto-correlation, when saturated. Predicting beforehand when this occurs in terms of

coupling is challenging. It may even happen after the coupling exceeds $g_{\phi\gamma} = 10^{-12}\,\mathrm{GeV}^{-1}$ (the upper limit set for our analysis, as discussed earlier in this section), potentially leaving a portion of the parameter space where a coupling value, within current constraints, yields a signal-to-noise ratio exceeding both unity and that of the auto-correlation.

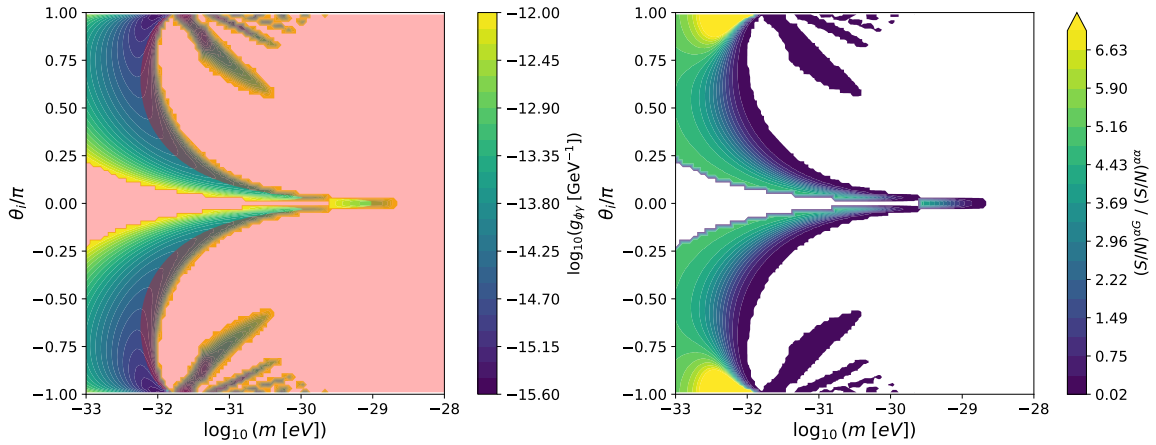

Figure 3.11: Same as fig. 3.8, with the instrument specifications of the LiteBIRD (see table 3.2).

The left panel of fig. 3.8 illustrates the required coupling value to achieve a (S/N) of order unity for the cross-correlation, allowing values smaller than $g_{\phi\gamma} = 10^{-12}\,\mathrm{GeV}^{-1}$ only. The signal-to-noise is computed with the instrument specifications of CMB-S4, as of table 3.2, and the *Euclid* prescriptions of section 3.2. Following [17], we set the minimum observable multipole to 10, as wide galaxy surveys are unlikely to observe the largest scales. The cross-correlation offers a measurable probe of birefringence, for masses $m_\phi \lesssim 10^{-32}\,\mathrm{eV}$ and[33] initial misalignment angles $|\theta_i| \gtrsim \pi/4$. In this range, a coupling value exists within current bounds, resulting in a signal-to-noise ratio exceeding unity. The region of interest extends to slightly lower values of $|\theta_i|$ as the mass increases up to $10^{-30.5}\,\mathrm{eV}$ and to a very small window around $m_\phi = 10^{-29}\,\mathrm{eV}$ when the initial misalignment angle is smaller than $\pi/100$. Let us stress that larger coupling values would yield larger signal-to-noise ratios, rendering regions where the required coupling value is minimal more promising in terms of detectability with forthcoming surveys. To this end, the most promising result is obtained for $m_\phi \sim 10^{-32}\,\mathrm{eV}$ and $|\theta_i| \sim \pi$, whereas, for smaller masses, the effect is less prominent as the amplitude of the underlying cross-correlation lowers (see fig. 3.6). Additionally, in the right panel of fig. 3.8, we present the ratio, in signal-to-noise, between the cross- and auto-correlation, corresponding to the axion-photon coupling that results in $(S/N)^{\alpha G} = 1$ for each point of the examined parameter space. Smaller masses and larger initial misalignment angles lead to higher ratios, indicating that the cross-correlation provides more information than the auto-correlation in this domain. In particular, we highlight this behavior in the left panel, by excluding the region of parameter space where this ratio is lower than unity (the red-shaded region). Also, in fig. 3.9 we assess the impact of decreasing the minimum multipole in the computation of the signal-to-noise-ratios in eqs. (3.26) and (3.27), adopting a more optimistic scenario where $\ell_{\mathrm{min}} = 5$. The constrained region is slightly enhanced, and the axion-photon coupling value needed to achieve unity in the (S/N) decreases. Nevertheless, as shown in fig. 3.7, most of the signal-dominated information comes from higher multipoles. Hence, we anticipate that a more thorough observational analysis able to probe scales below $\ell = 10$ would not significantly improve our results.

[33] These masses fall within the range where we anticipate a significant contribution to birefringence from photons emitted during the reionization period [346, 399]. Therefore, a future data analysis of this innovative cross-correlation could not only constrain the ALP-parameter space but also provide valuable insights into the origin of birefringence.

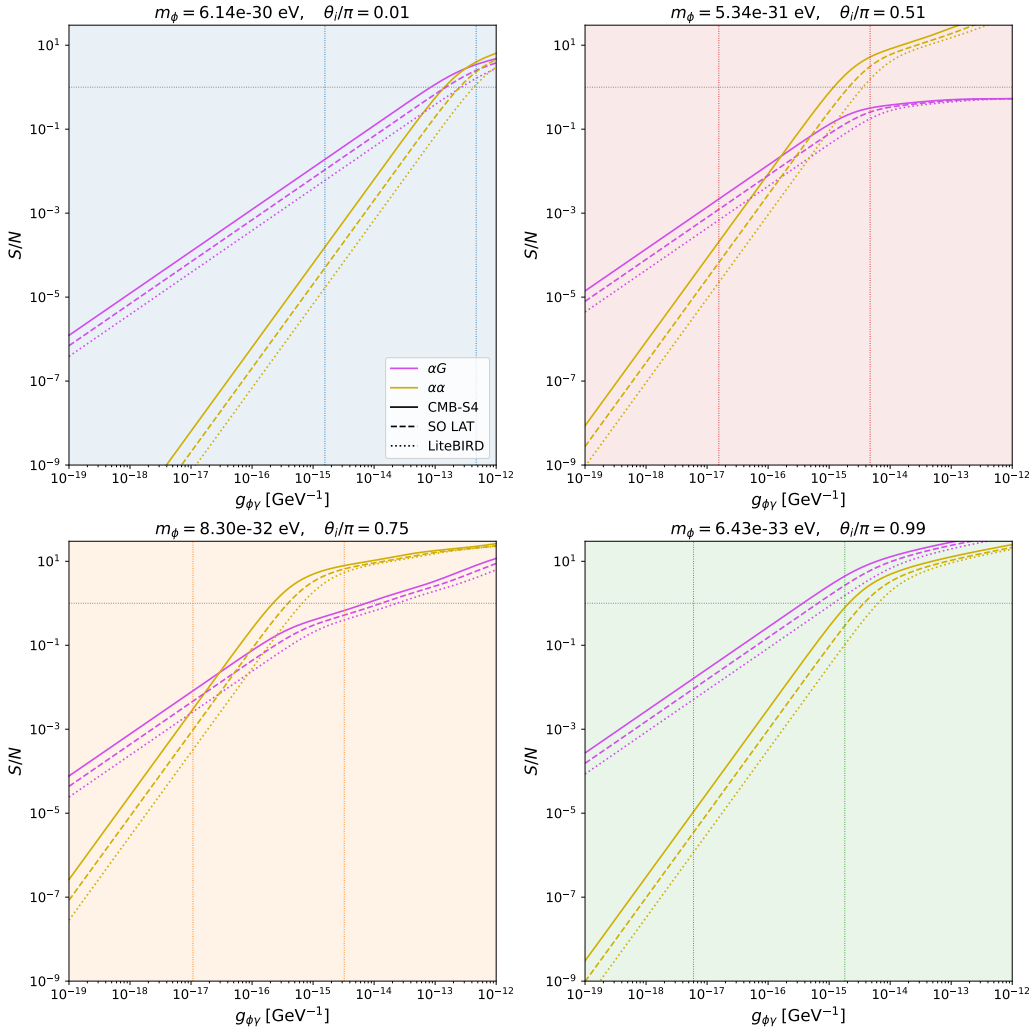

Figure 3.12: Signal-to-noise ratio for the cross- and auto-correlation as a function of the axion-photon coupling $g_{\phi\gamma}$, for four different points of the m_ϕ - θ_i parameter space (highlighted with corresponding colors in fig. 3.8). For each panel, we show the result for all three CMB experiments under considerations: S4 (solid lines), SO (dashed lines) and LB (dotted lines). The two vertical lines in each panel correspond to the coupling value yielding the isotropic birefringence measurement of ref. [362] and its first phase-shift (i.e., $\bar{\alpha} = 0.3°$ for the left line and $\alpha_1 = 180.3°$ for the right one).

Figs. 3.10 and 3.11 illustrate the same result when using the Simons Observatory and LiteBIRD as target experiments, respectively. The primary distinction lies in the higher coupling value required to achieve unity in the signal-to-noise ratio across the entire parameter space. The excluded region is also enlarged as the polarization-sensitivity and angular resolution of the target experiment decrease. Additionally, it's worth noting that while ground-based experiments such as SO and S4 are capable of observing the sky down to $\ell \sim 50$, information regarding large angular scales can still be derived from higher multipoles when constructing the birefringence maps [365, 366].

Fig. 3.12 shows the (S/N) as a function of the coupling, in the four highlighted points of the parameter space in the left panel of fig. 3.8. The green point (bottom right panel) represents a region where the necessary coupling for the (S/N) to reach unity is the smallest and there is further potential for enhancement with even higher coupling values. Additionally, it is never surpassed by the signal-to-noise ratio of the auto-correlation. In contrast, for the blue point (top left panel) the cross-correlation fails to always win over the auto-correlation and the (S/N)

achieves unity at much larger coupling values. The red point (top right panel) is within the excluded region of fig. 3.8, indeed its (S/N) never reaches unity. Finally, the orange point (bottom right) permits a coupling value that elevates its signal-to-noise ratio to one. However, the signal-to-noise ratio of the auto-correlation surpasses this value even before it is reached. In all cases, we show the trend for the three CMB experiments under considerations, observing a noticeable decrease in the signal-to-noise ratio for less sensitive surveys, as anticipated[34].

We now briefly come back to the comparison with the results of ref. [349], which delineates the contours for the ALP-parameters reproducing the isotropic birefringence angle of $(0.3° \pm 0.11°)$, constrained by [362]. We observe that, for the majority of points in their analysis, our parameter space offers a plethora of points with a signal-to-noise ratio exceeding unity. This is due to the rotation angle being degenerate with respect to the axion-photon coupling and initial misalignment angle (see eq. (3.2)). In contrast, the cross-correlation of birefringence and galaxies displays a non trivial dependence on these parameters (see eq. (3.17)) and can effectively break this degeneracy. For a more comprehensive comparison we refer to section 3.4.1. Additionally, it is important to remember the phase ambiguity of the isotropic measurement [385] (see section 3.1), as potential experiments cannot distinguish between $\bar{\alpha}$ and $\alpha_n = \bar{\alpha} + n \cdot 180°$. Consequently, we expect the findings presented in ref. [349] to extend to a broader parameter space. To clarify how our results compare with isotropic birefringence, we include a vertical line in each panel of fig. 3.12 corresponding to the coupling value that yields $\bar{\alpha} = 0.3°$ and its first phase-shift $\alpha_1 = 180.3°$. These values can be directly calculated from eq. (3.2) using $g^n_{\phi\gamma} = 2\,\alpha_n/(\phi_0 - \phi_s)$. They tend to decrease as the mass decreases or the initial misalignment increases. Axions with smaller masses begin evolving later, resulting in a larger difference between the field's present value and that at last scattering. Similarly, larger initial misalignment angles amplify the field's evolution. In all cases shown in fig. 3.12, $\bar{\alpha}$ lies before the region of interest, where the signal-to-noise ratio exceeds unity. However, α_1 aligns well with this region, and further phase-shifts would correspond to an even higher (S/N).

In conclusion, for $m_\phi \lesssim 10^{-32}\,\text{eV}$ (shifting towards $10^{-30.5}\,\text{eV}$ as $|\theta_i|$ approaches 0) and $|\theta_i| \gtrsim \pi/4$, we find an allowed value of the axion-photon coupling that results in a signal-to-noise ratio for the cross-correlation exceeding both unity and that of the auto-correlation. Moreover, this promising region of parameter space corresponds to axion-fields whose evolution commences around the epoch of reionization. This underlines this approach as an outstanding resource to constrain the origin of birefringence and axion-like physics. Furthermore, data analyses employing this approach have the potential to establish stringent bounds on the axion-photon coupling, as we predict viable values to leave within $g_{\phi\gamma} \in [10^{-16},\ 10^{-12}]\,\text{GeV}^{-1}$. A recent work of ours [4] depicts the first-ever bound on the axion-photon coupling for the ultralight axions under consideration, exploiting the combination of *Planck* NPIPE polarization data [29] and the Quaia quasar catalog [30]. Refer to section 3.5 for a detailed discussion.

3.4 Robustness of the theoretical prediction

The newly introduced cross-correlation between ALP-induced cosmic birefringence and galaxy number counts, as discussed in section 3.2, represents a powerful method for constraining axion properties. However, our theoretical analysis relies on several underlying assumptions, and it is essential to evaluate the robustness of our results when these assumptions are varied. Specifically, we demonstrate below that our conclusions remain consistent when adopting an alternative axion potential or performing a more comprehensive, fully-tomographic analysis.

[34] This decline ceases when the signal-to-noise ratio saturates, as explained by eqs. (3.28) and (3.29), where the noise term becomes negligible regardless of the target experiment.

3.4.1 Impact of the potential recipe

As discussed in section 3.1.3, we focused our work on early dark energy models from the string axiverse, characterized by the potential (same as eq. (3.16), although repeated here for convenience)

$$V(\phi) = m_\phi^2 f_a^2 \left[1 - \cos\frac{\phi}{f_a}\right]^n , \tag{3.30}$$

where the exponent n is fixed at 3, in order to align with previous works [344, 404]. This parameter governs the dynamics of the field, where for $n = 1$, we recover the classical axion potential resembling pressureless behavior, and for $n = 2$, the field evolves akin to a radiation-like fluid. However, when the exponent is equal to or less than 2, a resonance emerges in the evolution of perturbations (see eq. (3.12)) due to the frequency of the background oscillations matching that of perturbations, close to a specific Fourier scale k. This phenomenon can be thoroughly analyzed using Floquet theory [408], a branch of ordinary differential equations theory. When applied to EDE potentials, it leads to an exponentially growing solution of the EoM of perturbations [409, 410]. Hence, for these values of n a non-perturbative approach should be adopted and we leave it to future works.

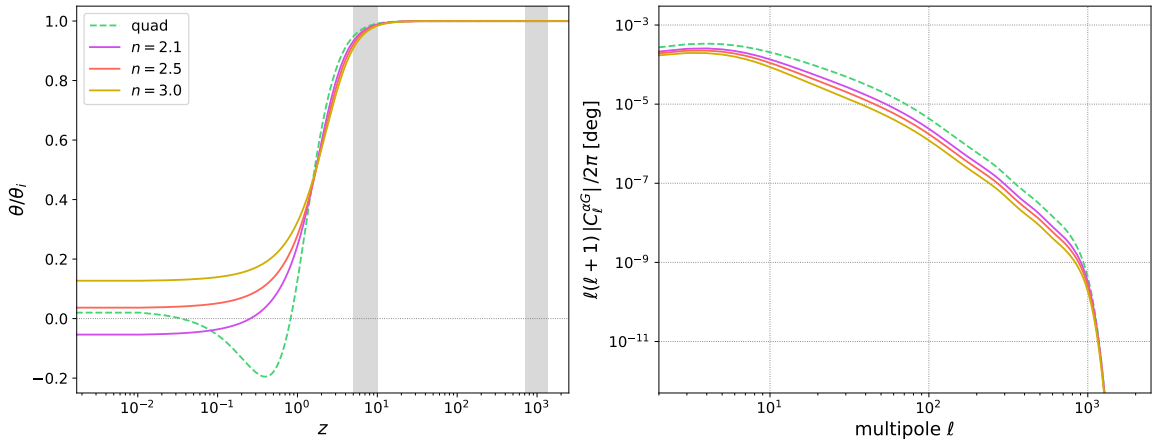

Figure 3.13: (*Left*): solution to the background equation of motion (eq. (3.7)), as a function of redshift, for three values of the exponent for an EDE potential, as shown in eq. (3.30), and for a quadratic potential (see eq. (3.31)). The two gray-shaded regions represent the windows of reionization and recombination, respectively. (*Right*): cross-correlation angular power spectrum between anisotropic birefringence and the spatial distribution of galaxies, corresponding to these four potential-settings. The results have been computed with the following ALP-parameters: $m_\phi = 10^{-32}\,\mathrm{eV}$, $\theta_i = \pi/2$, $g_{\phi\gamma} = 2 \times 10^{-14}\,\mathrm{GeV}^{-1}$.

Within the perturbative-allowed region ($n > 2$), we performed our analysis for different values of the exponent, as well as for a separate model, accounting for a simple quadratic potential

$$V(\phi) = \frac{1}{2} m_\phi^2 \phi^2 . \tag{3.31}$$

Let us notice, that the latter corresponds precisely to the expansion, near the minimum, of eq. (3.30), when $n = 1$. Consequently, we do expect a non-perturbative behavior at some scales. Specifically, we are unable to investigate regions of the parameter space where $m_\phi \gtrsim 2.2 \times 10^{-32}\,\mathrm{eV}$, due to the onset of oscillations early enough to trigger exponential growth in the perturbation evolution.

Fig. 3.13 illustrates, in the left panel, the solution to the background EoM for three dis-

tinct values of the exponent (within an EDE model described by eq. (3.30)), as well as for the aforementioned quadratic potential. For all cases, we considered the following ALP-parameters: $m_\phi = 10^{-32}\,\mathrm{eV}$, $\theta_i = \pi/2$, $g_{\phi\gamma} = 2 \times 10^{-14}\,\mathrm{GeV}^{-1}$. The field uniformly begins its evolution around the epoch of reionization, as the main parameter is the mass and its interplay with the Hubble expansion rate. Nevertheless, a larger value of the exponent reflects on the field diluting faster (see section 3.1.3). In the case of the quadratic potential, we anticipate a quicker onset of oscillations, which aligns with the $n = 1$ scenario. As a result, the cross-correlation signal, depicted in the right panel, is most pronounced for the latter case, gradually decreasing for larger exponent values.

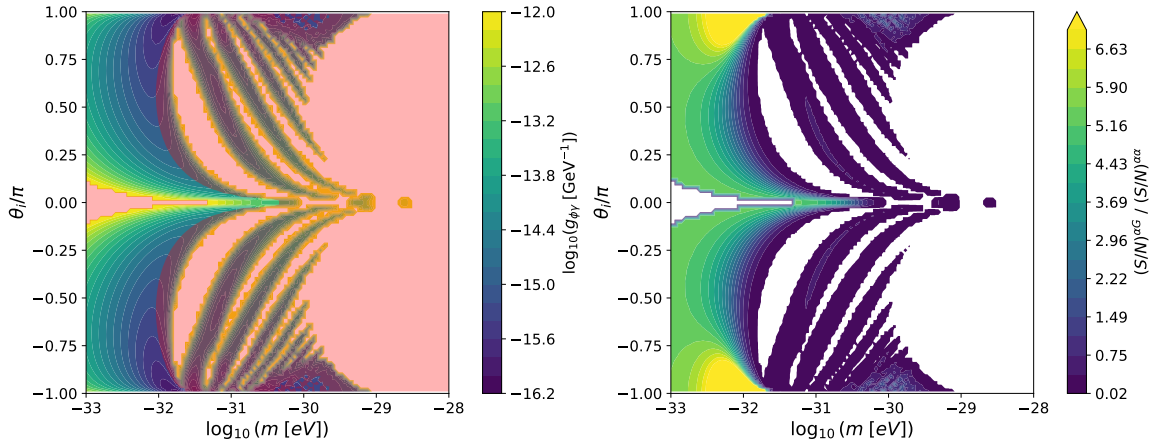

Figure 3.14: Same as fig. 3.8, with $n = 2.1$ as exponent of the EDE potential of eq. (3.30).

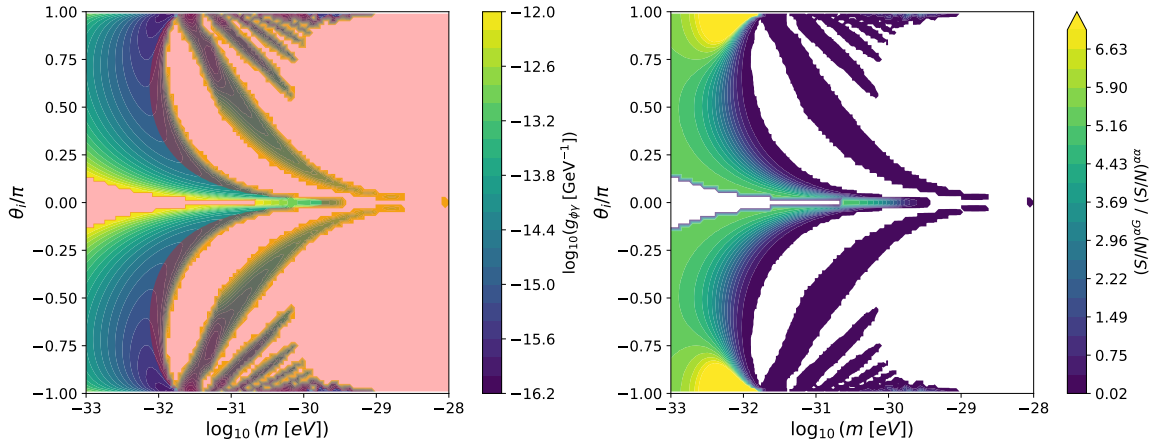

Figure 3.15: Same as fig. 3.8, with $n = 2.5$ as exponent of the EDE potential of eq. (3.30).

In terms of detectability, we show the contour plots for the axion-photon coupling needed to achieve unity in the signal-to-noise ratio, as detailed in section 3.3, in figs. 3.14, 3.15 and 3.16. The first two pertain to an EDE model with $n = 2.1$ and $n = 2.5$, respectively. The outcomes are akin to those obtained for $n = 3$, although the coupling values across the parameter space are diminished, and new features emerge at higher masses as the exponent decreases. Indeed, smaller values of n correspond to a fluid that dilutes more slowly, resulting in larger cross-correlation signals.

The constrained region for a quadratic potential is depicted in fig. 3.16 and displays a different behavior with respect to the previous cases. Nevertheless, the conclusions remain consistent, bringing about a preferred region of the parameter space for masses around $m_\phi = 10^{-32}\,\mathrm{eV}$ and large initial misalignment angles. It's important to note that we excluded all points with

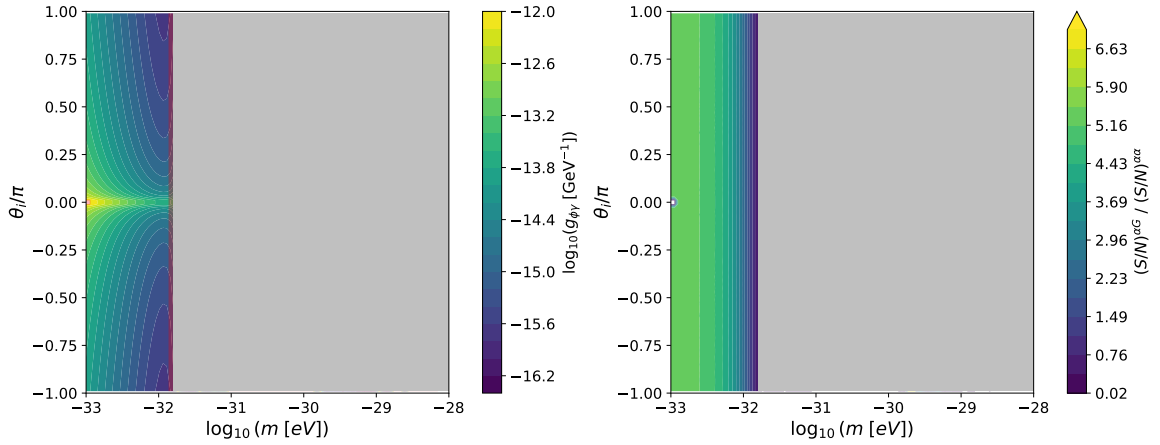

Figure 3.16: Same as fig. 3.8, with a quadratic potential as a reference model. Masses beyond $10^{-32}\,\mathrm{eV}$ are excluded, due to the perturbative approach not being applicable here.

$m_\phi > 2.2 \times 10^{-32}\,\mathrm{eV}$ as the perturbative approach is not reliable in this domain (see discussion above). In particular, the latter case can be compared to the region constrained by [349], where the isotropic measurement of the birefringence angle [362] is reproduced. Upon examining their fig. (1a) in the parameter space m_ϕ-$g_{\phi\gamma}\theta_i$, we observe how each point in their constrained region corresponds to numerous points in ours, as the cross-correlation is not degenerate in the couple $g_{\phi\gamma}$, θ_i. As a consequence, this study not only introduces a novel tool for constraining ALP-parameters and understanding the nature of cosmic birefringence but also aligns its results with current measurements of the isotropic birefringence angle.

3.4.2 Impact of tomography

Our work shows, for the first time, the usefulness of cross-correlating anisotropic cosmic birefringence with galaxies, as both are sourced by the metric perturbations. Through this innovative approach, we are able to constrain the region of m_ϕ - θ_i parameter space where axion-photon coupling values, within available bounds, allow for a measurable signal in future experiments. Our analysis adopts a non-tomographic approach, focusing on a single redshift bin within the Euclid prescriptions [13]. Nonetheless, it is crucial to estimate the impact of a full-tomographic strategy on our findings. Thus, we extend eq. (3.26) to incorporate the complete covariance across the 10 redshift bins of *Euclid* [17]:[35]

$$(S/N)^{\alpha G}_{\mathrm{tomo}} = \sqrt{\sum_{\ell=2}^{\ell_{\max}} \left(C_\ell^{\alpha G}\right)^\intercal \mathrm{Cov}^{-1}_{\alpha G} \left(C_\ell^{\alpha G}\right)}\,, \tag{3.32}$$

where $C_\ell^{\alpha G}$ is the vector containing the cross-correlation signal for each bin and $\mathrm{Cov}^{-1}_{\alpha G}$ the associated inverse covariance matrix, computed following eq. (3.24).

Fig. 3.17 illustrates the covariance matrix for $m_\phi = 10^{-32}\,\mathrm{eV}$, $\theta_i/\pi = 0.999$ and $g_{\phi\gamma} = 2\times10^{-14}\,\mathrm{GeV}^{-1}$, for two different multipoles ($\ell = 5$ in the left panel and $\ell = 30$ in the right). The i-th redshift bin corresponds to higher redshifts as i increases. Examining eq. (3.24), we anticipate the diagonal terms to be dominant as the galaxy shot noise only contributes here. Nevertheless, it's notable how the first off-diagonal terms are non-negligible and possibly important in the full-

[35] The edges of the 10 equi-populated bins are:
$z_{\mathrm{edge}} = \{0.001, 0.42, 0.56, 0.68, 0.79, 0.90, 1.02, 1.15, 1.32, 1.58, 2.50\}$.

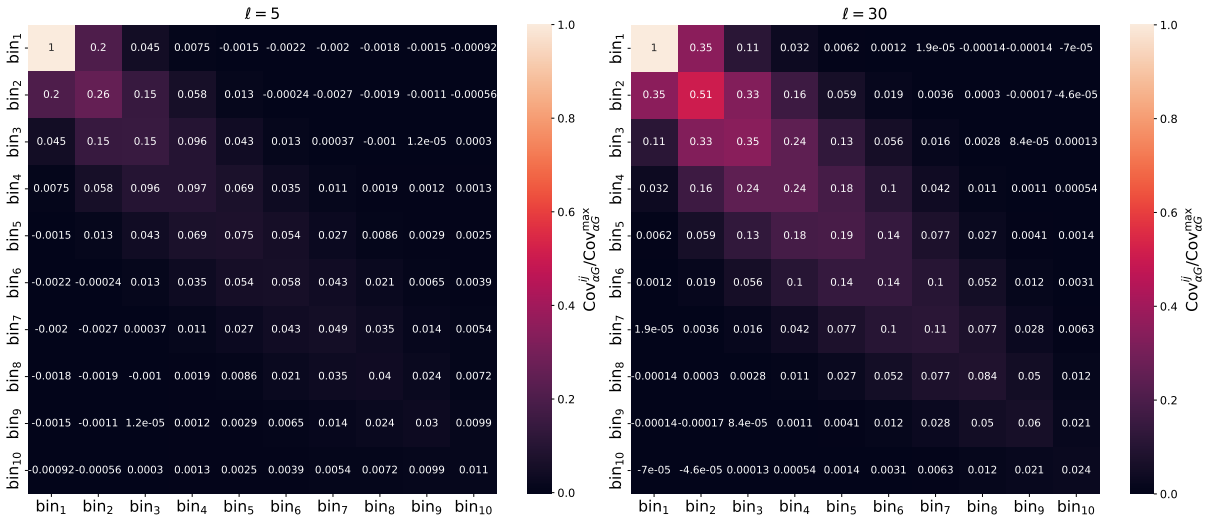

Figure 3.17: Covariance matrix for the birefringence-galaxy cross-correlation in the tomographic case, across the 10 redshift bins of *Euclid* [17] (higher i's correspond to higher redshifts) up to $z = 2.5$. The matrix is normalized to its maximum value and shown for $m_\phi = 10^{-32}\,\mathrm{eV}$, $\theta_i/\pi = 0.999$ and $g_{\phi\gamma} = 2 \times 10^{-14}\,\mathrm{GeV}^{-1}$. We show the result for $\ell = 5$ in the left panel and $\ell = 30$ in the right panel.

tomographic computation of the signal-to-noise ratios. Moreover, the covariance exhibits great variability with multipoles, with the latter behavior being more pronounced as the multipole increases. Similarly, in fig. 3.18 we calculate, following eq. (3.32), the contributions to the (S/N) from each bin$_i$ - bin$_j$ correlation[36], for the same point in the ALP-parameter space. This result not only reaffirms how the first off-diagonal terms are not negligible, but also shows how each bin$_i$ - bin$_j$ couple contributes to the total signal-to-noise ratio.

Finally, exploiting eq. (3.32) we compute the total (S/N) for each of the ten redshift bins[37], as well as the cumulative outcome from employing the full tomographic method, for two points within the ALP-parameter space. We compare them with the non-tomographic approach in fig. 3.19. It becomes apparent that the majority of information arises from the latter bins, corresponding to higher redshifts. This pattern is attributed to the anticipation of larger signals where the galaxy kernel peaks. Moreover, tomography allows for slightly better results, with the signal-to-noise ratio improving up to the 20% level. Given that our primary aim is to introduce the cross-correlation between birefringence and galaxy number counts as a valuable probe of ALPs, we defer the exploration of expanded analyses using a full tomographic approach to future studies.

3.5 Data analysis

The following sections are based on ref. [4], where we show the first measurement of the cross-correlation between anisotropic birefringence and the spatial distribution of galaxies, by combining CMB polarization data from *Planck* Release 4 (PR4) [29, 371], also known as NPIPE, and the all-sky quasar catalog Quaia [30, 372–374]. We exploit a pseudo-C_ℓ approach (supported by QML estimates at low-ℓ's) over maps for anisotropic birefringence derived through the EB-estimator of ref. [366], based on [199, 375], and for galaxy number counts derived from Quaia [30]. The associated covariance is consistently calculated using 400 polarization plus noise

[36] Despite the signal-to-noise ratio being positive definite overall, it can display negative contributions from any off-diagonal correlation (in case of an anti-correlation between bin$_i$ and bin$_j$).

[37] We consider solely the diagonal terms in the covariance matrix for the (S/N) computation in each of the ten redshift bins.

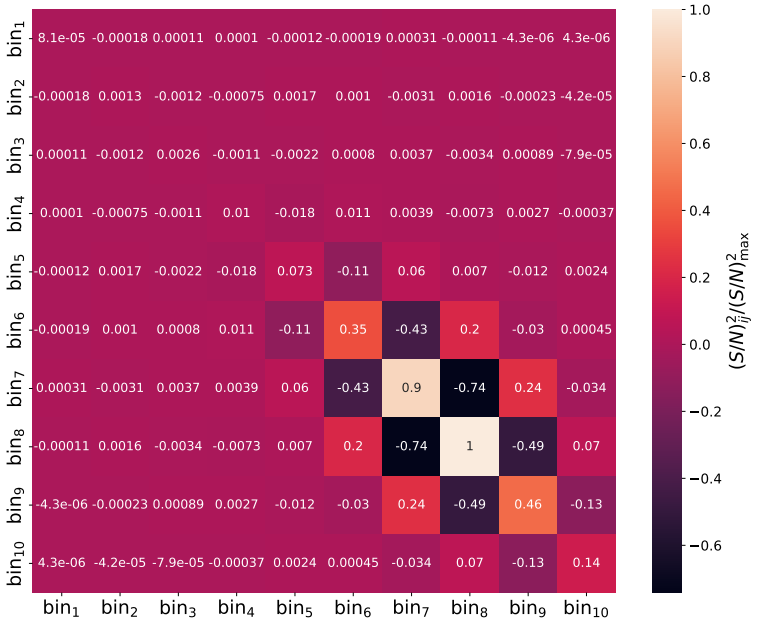

Figure 3.18: Contributions to the $(S/N)^{\alpha G}$ from each bin_i - bin_j correlation, across the 10 redshift bins of *Euclid* [17] (higher i's correspond to higher redshifts) up to $z = 2.5$. The result is normalized to its maximum value and shown for $m_\phi = 10^{-32}\,\mathrm{eV}$, $\theta_i/\pi = 0.999$ and $g_{\phi\gamma} = 2 \times 10^{-14}\,\mathrm{GeV}^{-1}$. Let us notice that negative terms arise from possible anti-correlations between different redshift bins, whilst the total sum exploited in eq. (3.32) is, of course, positive definite.

simulations from *Planck* NPIPE [29], alongside an equal number of realizations from the quasar catalog. Our results reveal a cross-correlation well consistent with the null-hypothesis across the whole range of multipoles.

We exploit this novel probe to constraint axion-parameters through a Gaussian likelihood over the theoretical spectra derived according to section 3.2 and below. We introduce an unprecedented upper bound on the axion-photon coupling $g_{\phi\gamma}$ within the same ultralight mass range of the aforementioned theoretical analysis ($m_\phi \in \left[10^{-33}, 10^{-28}\right]$ eV).

3.5.1 Planck NPIPE to estimate birefringence

Cosmic birefringence induces a rotation of linearly polarized light by an angle $\alpha(\hat{\mathbf{n}}) = \bar{\alpha} + \delta\alpha(\hat{\mathbf{n}})$, where the isotropic contribution $\bar{\alpha}$ arises from the background field, while field perturbations induce a dependence on the direction on the sky $\hat{\mathbf{n}}$ in the anisotropic counterpart $\delta\alpha(\hat{\mathbf{n}})$ (see section 3.1). As a consequence, the observed CMB E- and B-modes are rotated and mixed [57, 422] and inherit information on the rotation field. Harmonic estimators can be exploited to reconstruct birefringence from CMB polarization [199, 375]. In particular, focusing on the EB cross-correlation only allows to avoid the cosmic variance associated with the temperature field and rises as a promising tool, given the higher predicted signal-to-noise ratio with respect to e.g. TB. Following the EB-estimator implemented by [366], we are able to reconstruct the harmonic coefficients associated to anisotropic birefringence from *Planck* NPIPE data. The related `HEALPix` [423] map at $N_{\mathrm{side}} = 64$ is shown in the left panel of fig. 3.20. The latter is masked according to *Planck* NPIPE fiducial, with a corresponding sky fraction $f_{\mathrm{sky}} = 78\%$ (see right panel of fig. 3.20). In addition, this dataset provides 400 simulations of polarization + noise that we use to obtain realizations of the anisotropic birefringence sky for covariance estimation, as discussed in section 3.6.3.

The birefringence maps used are generated with a minimum CMB multipole $\ell_{\mathrm{min}}^{\mathrm{CMB}} = 2$,

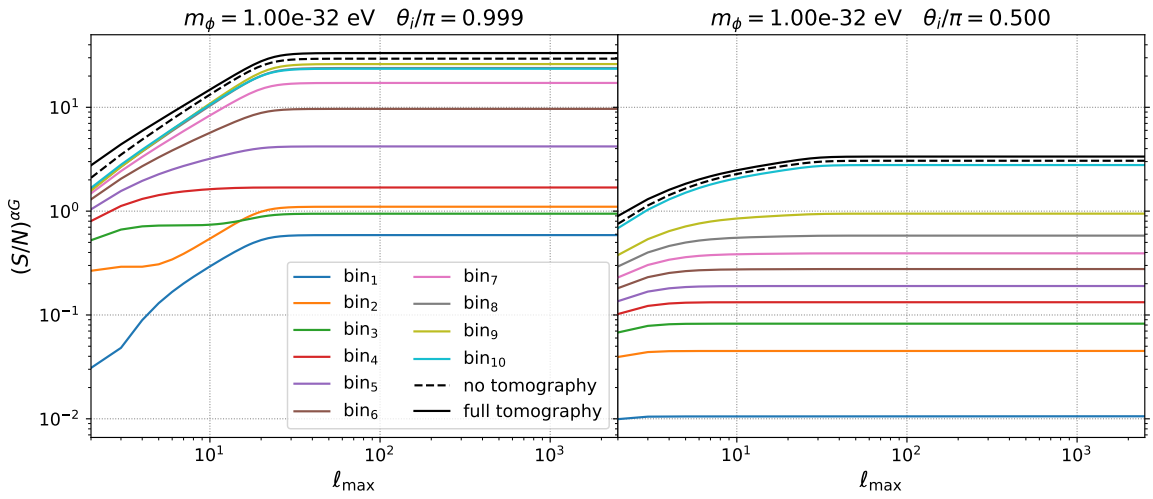

Figure 3.19: Signal-to-noise ratios of the birefringence-galaxy cross-correlation as a function of the maximum multipole $\ell_{\rm max}$ for two points in the m_ϕ - θ_i parameter space. The result is shown for the ten redshift bins of *Euclid* [17] (higher i's correspond to higher redshifts), as well as for the full tomographic approach of eq. (3.32) (solid). We compare with the non-tomographic approach (dashed) followed in the main text. Tomography leads up to a 20% improvement. The axion-photon coupling is set to $2 \times 10^{-14}\,\text{GeV}^{-1}$.

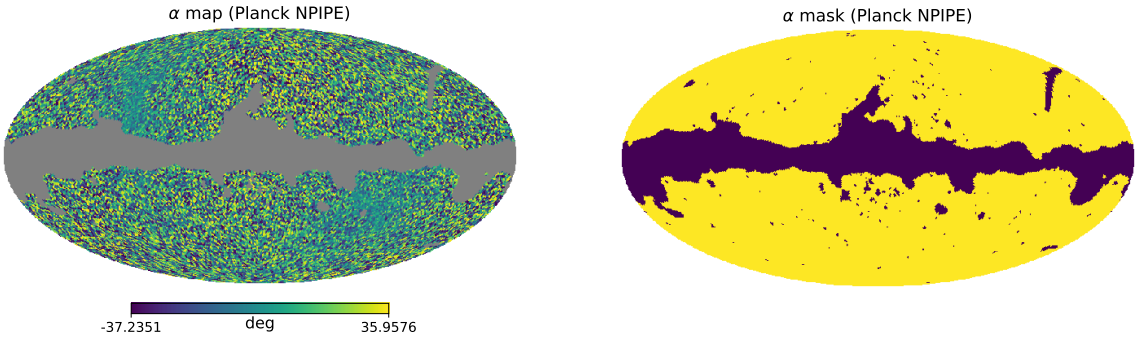

Figure 3.20: Anisotropic birefringence map derived from *Planck* NPIPE polarization data with the EB-estimator of ref. [366] (*Left*), and corresponding sky mask (*Right*).

in order to account for the polarization generated at all redshifts, particularly from both the recombination and reionization epochs. Ref. [366] demonstrates that the choice of $\ell_{\rm min}^{\rm CMB}$ has negligible impact on the birefringence auto-correlation, and we have tested that the same is true for the underlying cross-correlation. In this study, we aim to perform a 'blind' analysis to extract information on axion parameters from the complete birefringence signal, without isolating contributions from different cosmic epochs. Thus, the estimator from ref. [366] remains unaltered, though a different approach would be needed if our goal were to analyze birefringence at a specific redshift, as suggested by [424]. Given the extensive axion parameter space and the variability in dominant redshifts within it (see [3]), we avoid assumptions on the expected signal and proceed with an analysis on maps incorporating all birefringence contributions.

3.5.2 Quaia to estimate galaxy number counts

Quasars offer as a powerful tool to probe accretion physics [425, 426], galaxy formation [427], supermassive black holes [428] and black hole evolution [429], gravitational lensing [430], halo masses [431] and the intergalactic medium [432]. Furthermore, quasars are exceptional tracers of large-scale-structure cosmology due to their position within peaks of the dark matter distribution,

and can be exploited to constrain cosmological parameters [68, 372, 433–440]. We consider the *Gaia-unWISE* Quasar catalog (Quaia), which is an all-sky sample comprising almost 1.3 million objects with magnitude $G < 20.5$, up to redshift $z \sim 3$. The catalog stems from the combination of quasar candidates in the third data release of *Gaia* [374] and the *unWISE* [441, 442] infrared photometry, based on the Wide-field Infrared Survey Explorer (*WISE*) [443]. The corresponding `HEALPix` distribution of sources[38], at $N_{\rm side} = 64$, is illustrated in the top left panel of fig. 3.21. Following refs. [30, 372, 373] we obtain the projected galaxy-overdensity in each pixel $\hat{\mathbf{n}}$ as $\delta_g(\hat{\mathbf{n}}) = N(\hat{\mathbf{n}})/(\bar{N}\omega(\hat{\mathbf{n}}))-1$, where $N(\hat{\mathbf{n}})$ is the number of quasars in the pixel and $\omega(\hat{\mathbf{n}})$ the related selection function (shown in the top right panel of fig. 3.21). Finally, $\bar{N} = \sum_{\hat{\mathbf{n}}} N(\hat{\mathbf{n}}) / \sum_{\hat{\mathbf{n}}} \omega(\hat{\mathbf{n}})$ is the mean number of sources per pixel. The resulting galaxy-overdensity map is depicted in the bottom left panel of fig. 3.21. We mask all pixels in the sky where the selection function is lower than 0.5 (see bottom right panel of fig. 3.21). To match the 400 birefringence simulated maps for covariance estimation, we generate an equal number of realizations of δ_g by reshuffling a random catalog with ten times the sources of the data catalog outlined above.[39]

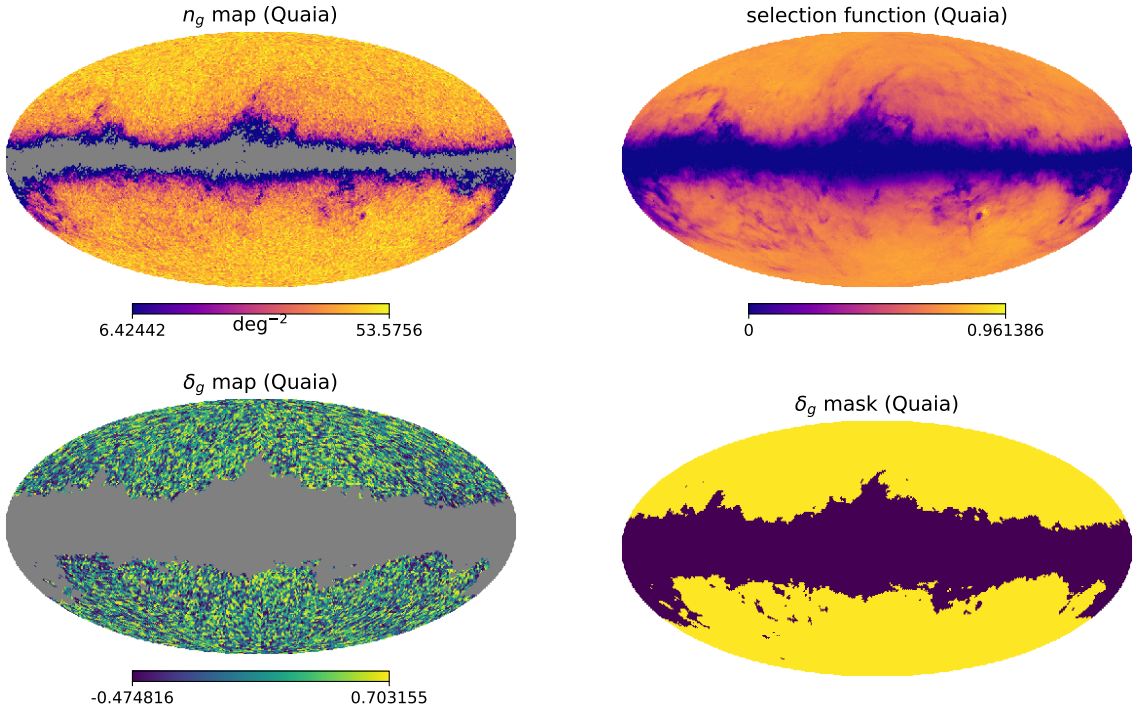

Figure 3.21: (*Top left*): pixel density of sources from the Quaia quasar catalog [30]; the map includes almost 1.3 million objects. (*Top right*): related selection function. (*Bottom left*): galaxy overdensity from Quaia derived as outlined in section 3.5.2. (*Bottom right*): Quaia sky mask.

3.6 Power spectrum estimation from data

We derive the observed cross-correlation angular power spectrum from the data of section 3.5 through a *pseudo-*C_ℓ estimator [444] at $\ell > 12$, whilst exploiting a quadratic maximum likelihood (QML) approach for the first multipoles.[40] Additionally, section 3.6.4 serves as a review of key ingredients chosen to adapt the theoretical framework of the underlying cross-correlation to the

[38] The Quaia related data products have been produced following ref. [30] and publicly available at `https://zenodo.org/records/8060755`.

[39] Each galaxy realization conserves the total number of sources of the data-map.

[40] Due to the *pseudo-*C_ℓ inability of effectively estimating large scales when dealing with masked skys.

aforementioned data.

3.6.1 Pseudo-C_ℓ

The *pseudo-C_ℓ* estimator works in harmonic space and, taking advantage of its extremely fast computation times, is particularly suited for large datasets. Nonetheless, dealing with spherical harmonic transforms of masked data introduces information loss and mode mixing, especially at the largest scales. Following the `NaMaster` [445] implementation the pseudo angular power spectrum is

$$\tilde{C}_\ell^{\alpha g} = \frac{1}{2\ell+1} \sum_{m=-\ell}^{+\ell} \tilde{a}_{\ell m}^{\alpha}\, \tilde{a}_{\ell m}^{g*}\,, \tag{3.33}$$

where the harmonic coefficients for a generic field $X(\hat{\mathbf{n}})$ come from its expansion on spherical harmonics over a masked region of the sky, defined by the weight function $w_{\hat{\mathbf{n}}}^X$,

$$\tilde{a}_{\ell m}^X = \int \mathrm{d}\Omega\; X(\hat{\mathbf{n}})\, w_{\hat{\mathbf{n}}}^X\, Y_{\ell m}^*(\hat{\mathbf{n}})\,. \tag{3.34}$$

The unbiased estimator of the true power spectrum for our cross-correlation[41] is then:

$$\hat{C}_\ell^{\alpha g} = \sum_{\ell'} M_{\ell\ell'}^{-1} \tilde{C}_{\ell'}^{\alpha g}\,, \tag{3.35}$$

with $M_{\ell\ell'}^{-1}$ accounting for the incomplete sky coverage

$$\begin{aligned} M_{\ell\ell'}^{\alpha g} &= \frac{(2\ell'+1)}{4\pi} \sum_{\ell''} (2\ell''+1)\, \tilde{W}_{\ell''}^{\alpha g} \begin{pmatrix} \ell & \ell' & \ell'' \\ 0 & 0 & 0 \end{pmatrix}^2, \\ \tilde{W}_\ell^{\alpha g} &= \frac{1}{2\ell+1} \sum_{m=-\ell}^{\ell} \tilde{w}_{\ell m}^{\alpha}\, \tilde{w}_{\ell m}^{g*}\,. \end{aligned} \tag{3.36}$$

Here, the last term in the first line is a Wigner 3-j symbol, whilst $w_{\ell m}^\alpha$ and $w_{\ell m}^g$ are the spherical harmonic coefficients of the two probes' masks, respectively. Due to large errors, brought in by eq. (3.36), for a single realization, the estimated value at large scales may differ significantly from the true one. Hence, we trust only estimates for $\ell > 12$, up to $\ell_{\max} = 3N_{\mathrm{side}} - 1$.

3.6.2 Quadratic maximum likelihood

The QML estimator [446, 447], on the contrary, works in pixel space, sensibly reducing masking effects at low multipoles. However, dealing with several pixel-pixel matrices is computationally demanding. The underlying algebra yields

$$\hat{C}_\ell^{\alpha g} = F_{\ell\ell'}^{-1}\, y_{\ell'}\,, \tag{3.37}$$

[41] Let us notice how eq. (3.35) does not include a noise power spectrum, as the latter only appears for auto-correlations.

where the Fisher matrix $F_{\ell\ell'}$ and the minimum-variance quadratic estimator y_ℓ are defined as follows:

$$\begin{aligned} F_{\ell\ell'} &= \mathrm{Tr}\left[\mathbf{C}_{\alpha\alpha}^{-1}\,\mathbf{P}_\ell\mathbf{C}_{gg}^{-1}\,\mathbf{P}_{\ell'}^{T}\right]\,, \\ y_\ell &= \boldsymbol{\alpha}^T\mathbf{C}_{\alpha\alpha}^{-1}\,\mathbf{P}_\ell\mathbf{C}_{gg}^{-1}\boldsymbol{\delta_g}\,. \end{aligned} \tag{3.38}$$

$\mathbf{C}_{\alpha\alpha}$ and $\mathbf{C}_{gg}$ are the signal covariance matrices, related to the two data vectors in pixel space $\boldsymbol{\alpha}$ and $\boldsymbol{\delta_g}$. The matrix $\mathbf{P}_\ell = (2\ell+1)/4\pi\; p_\ell(\hat{\mathbf{n}}_i\cdot\hat{\mathbf{n}}_j)$ is defined through the Legendre polynomials $p_\ell(\hat{\mathbf{n}}_i\cdot\hat{\mathbf{n}}_j)$. Eq. (3.37) is an unbiased estimator of the underlying cross-correlation ($\langle\hat{C}_\ell^{\alpha g}\rangle = C_\ell^{\alpha g}$), and we utilize it to derive the power spectrum at $\ell \leq 12$.

3.6.3 Covariance estimation

We estimate the covariance matrix of the cross-correlation $\mathsf{C}_{\ell\ell'}^{\alpha g}$ as

$$\hat{\mathsf{C}}_{\ell\ell'}^{\alpha g} = \frac{1}{n-1}\sum_{k=1}^{n}\hat{C}_\ell^{\alpha g(k)}\hat{C}_{\ell'}^{\alpha g(k)}\,, \tag{3.39}$$

with $n = 400$ realizations of anisotropic birefringence and galaxy overdensity outlined in section 3.5. It can be demonstrated that this provides an unbiased estimate of the true covariance matrix $\boldsymbol{\Sigma}$ as long as $p < n-1$, with p being the length of the data vector $\hat{C}_\ell^{\alpha g}$. However, for our analysis, we require the inverse covariance matrix for both goodness-of-fit assessments and parameter estimation (see section 3.7). As shown in ref. [448], $(\hat{\mathsf{C}}_{\ell\ell'}^{\alpha g})^{-1}$ is a biased estimator of the true inverse covariance $\boldsymbol{\Sigma}^{-1}$ due to noise injected in $\hat{\mathsf{C}}_{\ell\ell'}^{\alpha g}$ as p approaches n. To first order, this issue can be mitigated by either re-normalizing the estimated inverse covariance [448] or marginalizing over the true covariance matrix, conditioned on its estimate [449]. Furthermore, binning the data vector helps to reduce the noise in the off-diagonal elements of the estimated covariance by compensating for the limited number of realizations. Ideally, the data vector length should be reduced to $\tilde{p}$, the maximum size that still allows for reliable covariance estimation given the number of simulations n, satisfying $\tilde{p}(\tilde{p}+1)/2 < n$. For 400 realizations, this yields $\tilde{p} \sim 27$. In what follows, we will adopt the least aggressive binning scheme possible and further examine the impact of binning in appendix B.1.

Additionally, the random catalog utilized to extract the 400 realizations of galaxy overdensity lacks the large-scale systematics present in the associated data. To address this, we calibrate the effective degrees of freedom, ν_{eff}, from the aforementioned realizations and subsequently re-normalize the covariance of eq. (3.39) by the variance analytically derived from the data with the calibrated ν_{eff}. This process can be summarized as follows

$$\begin{aligned} \hat{\mathsf{C}}_{\mathrm{new}}^{\alpha g} &= \hat{\mathsf{C}}^{\alpha g}\,\frac{\sigma_{\mathrm{dat,\,eff}}\otimes\sigma_{\mathrm{dat,\,eff}}}{\sigma_{\mathrm{sim}}\otimes\sigma_{\mathrm{sim}}}\,, \\ \sigma_{\mathrm{sim}} &= \sqrt{\mathrm{diag}(\hat{\mathsf{C}}^{\alpha g})}\,, \\ \sigma_{\mathrm{dat,\,eff}} &= \sqrt{\frac{1}{\nu_{\mathrm{eff}}}\left((\hat{C}_{\ell,\,\mathrm{dat}}^{\alpha g})^2 + \hat{C}_{\ell,\,\mathrm{dat}}^{\alpha\alpha}\hat{C}_{\ell,\,\mathrm{dat}}^{gg}\right)}\,, \\ \nu_{\mathrm{eff}} &= \frac{(\hat{C}_{\ell,\,\mathrm{sim}}^{\alpha g})^2 + \hat{C}_{\ell,\,\mathrm{sim}}^{\alpha\alpha}\hat{C}_{\ell,\,\mathrm{sim}}^{gg}}{\sigma_{\mathrm{sim}}^2}\,, \end{aligned} \tag{3.40}$$

where $\sigma_{\rm sim}$ represents the standard deviation derived from eq. (3.39) exploiting the 400 realizations of the underlying spectra, with their means denoted as $\hat{C}^{\alpha g}_{\ell,\rm sim}$, $\hat{C}^{\alpha\alpha}_{\ell,\rm sim}$ and $\hat{C}^{gg}_{\ell,\rm sim}$. Meanwhile, $\sigma_{\rm dat,\,eff}$ refers to the analytical standard deviation calculated from data ($\hat{C}^{\alpha g}_{\ell,\rm dat}$, $\hat{C}^{\alpha\alpha}_{\ell,\rm dat}$ and $\hat{C}^{gg}_{\ell,\rm dat}$), adjusted using the effective degrees of freedom $\nu_{\rm eff}$. The $\otimes$ product refers to the outer product to compute the correlation matrix ρ related to both simulations and data ($\rho = \sigma \otimes \sigma$). The covariance structure is illustrated in Fig. 3.22, where we present $\hat{\mathsf{C}}^{\alpha g}_{\rm new}/\sqrt{\rm diag(\hat{\mathsf{C}}^{\alpha g}_{\rm new})} \otimes \sqrt{\rm diag(\hat{\mathsf{C}}^{\alpha g}_{\rm new})}$, excluding the diagonal elements. This representation is valuable for analyzing the off-diagonal contributions and shows how binning reduces correlations coming from the off-diagonal structure. For the least aggressive cases, the initial off-diagonal terms exhibit mild anti-correlation.

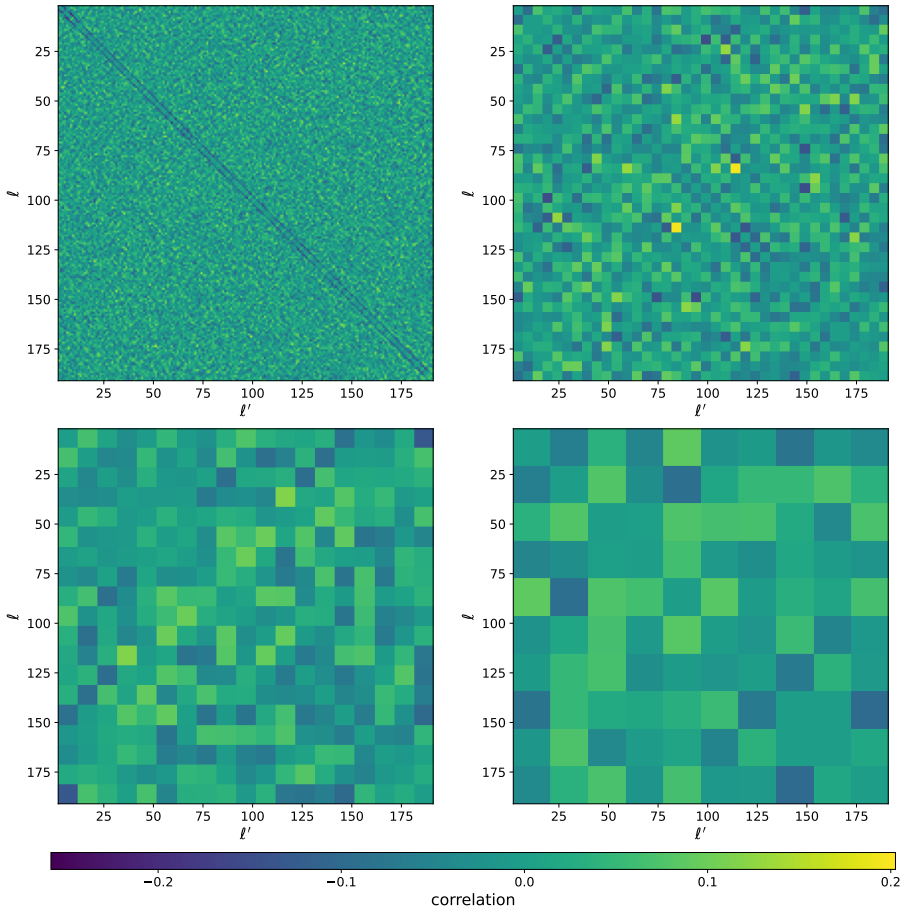

Figure 3.22: Correlation matrix obtained from the covariance of eq. (3.40) with the diagonal subtracted. (*Top left*): no binning, $\Delta\ell = 1$. (*Top right*): 5 multipoles per bandpower, $\Delta\ell = 3$ (45 bins). (*Bottom left*): 10 multipoles per bandpower, $\Delta\ell = 10$ (19 bins). (*Bottom right*): 19 multipoles per bandpower, $\Delta\ell = 19$ (10 bins).

3.6.4 Adapting the theoretical model to the data

In this study, we regard two different probes: the anisotropic birefringence $\alpha(\hat{\mathbf{n}})$ and the spatial distribution of galaxies as measured by the Quaia quasar overdensity $\delta_g(\hat{\mathbf{n}})$. As discussed in section 3.1, the former can be generated by parity violating couplings of ALPs to the electromagnetic sector, and we expect a non-zero correlation due to both probes being sourced by the metric perturbations and related gravitational potentials [55, 346, 368]. We thoroughly discussed the theoretical framework of such a correlation in section 3.2 and repeat here its definition (see

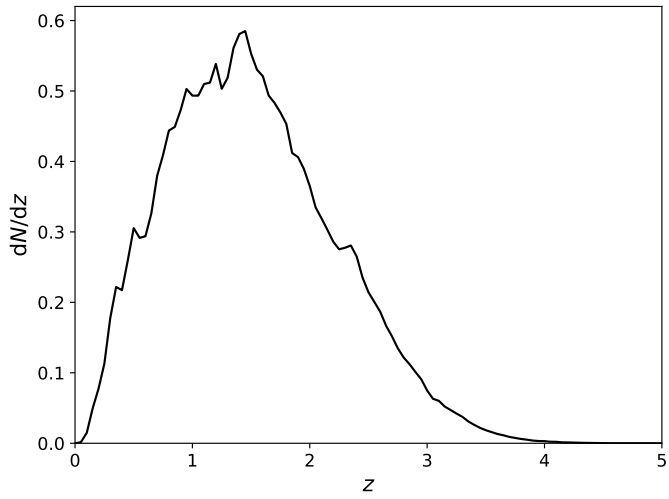

Figure 3.23: Redshift distribution of sources within the Quaia catalog [30], used as the selection function in eq. (3.20) for the computation of the theoretical cross-correlation.

eq (3.17)) for convenience:

$$C_\ell^{\alpha g} = 4\pi \int \frac{\mathrm{d}k}{k}\, \mathcal{P}_\mathcal{R}(k) \Delta_\ell^\alpha(k) \Delta_\ell^g(k)\,. \tag{3.41}$$

Following eqs. (3.18) and (3.20) the respective kernels for birefringence and galaxies read

$$\Delta_\ell^\alpha(k) = g_{\phi\gamma} \int_0^{\tau_0} \mathrm{d}\tau\; g(\tau) T_{\delta\phi}(\tau,\, k) j_\ell\left[k(\tau_0 - \tau)\right]\,, \tag{3.42}$$

$$\Delta_\ell^g = \int \mathrm{d}z\; \frac{\mathrm{d}N}{\mathrm{d}z} b(z) S_D(z,\, k) j_\ell\left[k\, r(z)\right]\,, \tag{3.43}$$

where we refer to the aforementioned equations for definitions. Here, in the galaxy kernel, we consider only the density term of eq. (3.21) to align with the Quaia dataset [30]. Additionally, we perform the following analysis with no tomography. Finally, let us remind that $T_{\delta\phi}(\tau,\, k)$ is a transfer function between the primordial power spectrum $\mathcal{P}_\mathcal{R}(k)$ and that of the field fluctuations $\delta\phi$. Hence, the birefringence kernel is governed by the Klein-Gordon equation of axion-perturbations (see eq. (3.12)). Similarly to the theoretical investigation presented in previous sections, we utilize an axion-potential stemming from EDE models of the string axiverse [134, 138, 404]

$$V(\phi) = m_\phi^2 f_a^2 \left[1 - \cos\frac{\phi}{f_a}\right]^3\,. \tag{3.44}$$

In eq. (3.43), $\mathrm{d}N(z)/\mathrm{d}z$ is the galaxy redshift distribution, $b(z)$ the linear bias between the galaxy and matter overdensity, S_D a source function related to the growth of structure and the Bardeen potentials and $r(z)$ the comoving radial distance. The former is taken directly from the data products of Quaia discussed in section 3.5.2 and shown in fig. 3.23. For the galaxy bias, we follow the prescription of [450]:

$$b(z) = 0.278\left[(1+z)^2 - 6.565\right] + 2.393\,. \tag{3.45}$$

To compute eq. (3.41) we exploit the same modified version of `CLASS` described in section 3.2, based on the birefringence implementation of ref. [346] and the galaxy guidelines of `CLASSgal` [369].

3.7 First measurement of birefringence-galaxy cross-correlation

The focus of this data analysis is to present, for the first time, a measurement of the cross-correlation between anisotropic birefringence and galaxies. Both probes stem from the metric perturbations and a detection of such a signal would not only rise valuable insights about cosmic birefringence, but also allow to constrain the underlying axion-parameters [3]. As discussed in

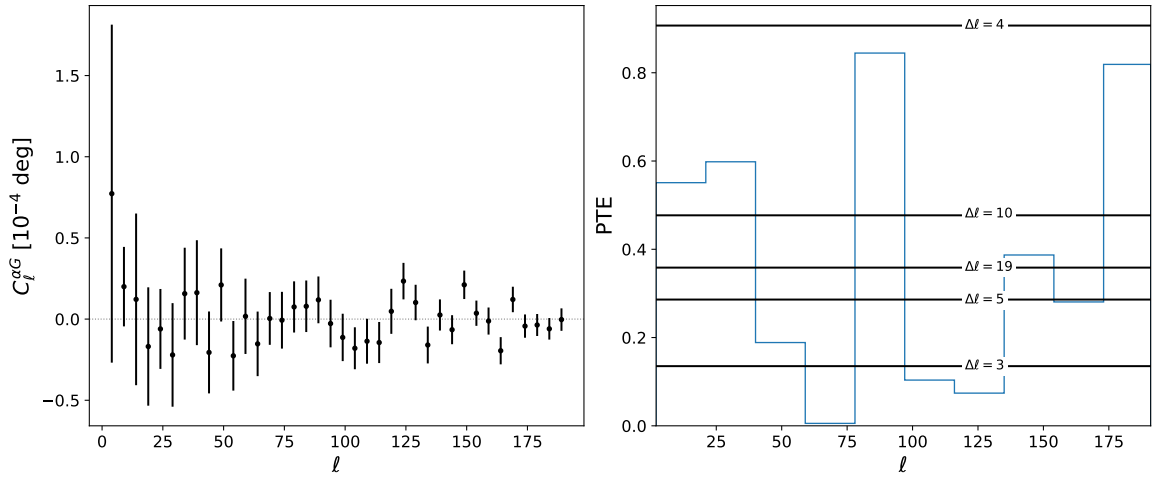

Figure 3.24: (*Left*): cross-correlation angular power spectrum between anisotropic birefringence and galaxy number counts, as measured by the combination of *Planck* NPIPE polarization data and the quasar catalog Quaia. The signal is binned with $\Delta\ell = 5$ and error bars are computed from a covariance estimated with 400 realizations of the two probes (see section 3.6.3). (*Right*): the black horizontal line corresponds to the PTE obtained across the entire range of multipoles without binning. The blue line represents the PTE achievable within a specific chunk of multipoles and $\Delta\ell = 1$.

section 3.6, we estimate the underlying cross-correlation angular power spectrum utilizing a QML estimator for $\ell = [2, 12]$ and a *pseudo-*C_ℓ estimator for $\ell = [13, 191]$.[42] The maximum multipole of our analysis stems from the resolution of the datasets under consideration ($\ell_{\rm max} = 3N_{\rm side} - 1$ with $N_{\rm side} = 64$). The estimators are applied to the maps, and related masks, presented in section 3.5. Anisotropic birefringence is associated to the *Planck* NPIPE polarization dataset, whilst the spatial distribution of galaxies is derived from the Quaia quasar catalog.

The result is shown in the left panel of fig. 3.24 with 5-multipoles per bandpowers. The associated error bars spring from the diagonal of the covariance in eq. (3.40). This signal is well compatible with the null-hypothesis with a probability to exceed (PTE) of 29%. The compatibility is retained across different binning strategies and shown in the right panel of fig. 3.24 for $\Delta\ell = 3$, 4, 5, 10 and 19. Only the unbinned and $\Delta\ell = 2$ spectrum yield poor compatibility with the null-hypothesis (PTE $\ll 5\%$) due to the high level of correlation in the off-diagonal structure of the covariance (see fig 3.22). Let us highlight that the following results show little to no change when varying the binning scheme (for further detail on the impact of binning refer to appendix B.1). The right panel of fig. 3.24 also illustrates how the measured cross-correlation

[42] This choice is due the inefficiency of *pseudo-*C_ℓ's to correctly estimate power spectra at large scales, where masking effects in harmonic space are dominant.

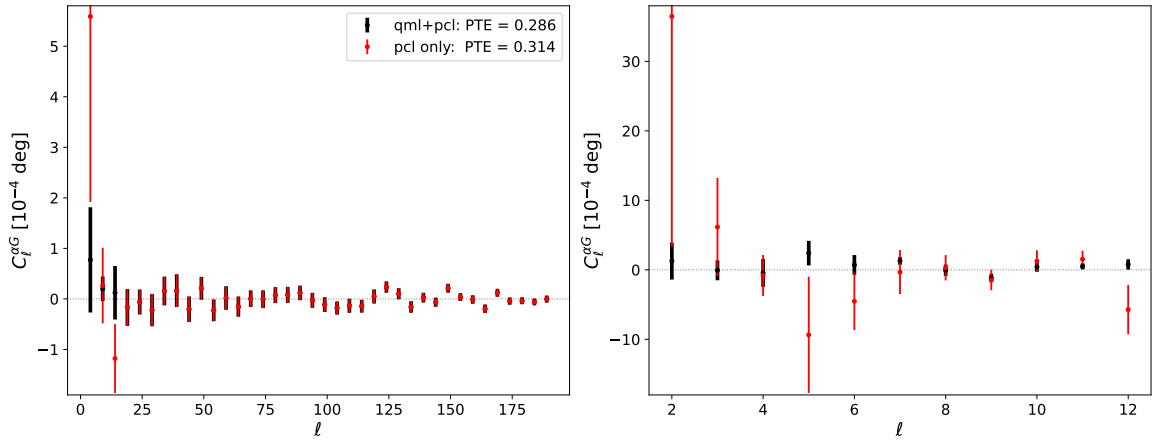

Figure 3.25: Comparison between *pseudo-*C_ℓ (red) and QML (black) estimates of the birefringence-galaxy cross-correlation. The QML estimator is used only up to $\ell = 12$, with *pseudo-*C_ℓ estimates applied at smaller scales. The *left* panel shows the full spectrum with 5 ℓ's per bandpower, while the *right* panel displays the unbinned spectrum for the first 11 multipoles.

stems compatibility with the null-hypothesis in selected chunks of multipoles.[43] Each of the ten chunks contains 19 multipoles, with a $\Delta\ell = 1$ bandwidth.

For parameter estimation, in section 3.7, we will utilize the following binning scheme: $\Delta\ell = 1$ for the first 10 multipoles, $\Delta\ell = 2$ for the following 20 multipoles, $\Delta\ell = 5$ for the consequent 50 multipoles and $\Delta\ell = 10$ for the rest. This approach minimizes information loss on large scales, where our theoretical analysis predicts the greatest power [3]. This binning strategy remains compatible with zero, with a PTE of 37%. Fig. 3.26 illustrates the corresponding Gaussian null-hypothesis χ^2 for data, overlapped with the distribution given by the 400 realizations used to estimate the covariance matrix.

We emphasize how this is the first measurement of such a correlation and future CMB polarization experiments [22–24], together with forthcoming galaxy surveys [13, 17, 69, 413], could enhance the signal-to-noise ratio and eventually reveal an excess of power (see e.g. [3]).

To facilitate a comprehensive understanding of the estimators under consideration, we compare the *pseudo-*C_ℓ and QML approaches in fig. 3.25. The full result is presented in the left panel, with a binning of $\Delta\ell = 5$, while the right panel highlights the first 11 multipoles. As discussed in Section 3.6, it is evident that the *pseudo-*C_ℓ estimates exhibit significantly larger errors at large scales.

3.7.1 Scale invariant amplitude

As an extra test of data compatibility with the null-hypothesis, we perform a Gaussian likelihood on a scale-invariant amplitude A:

$$-2\log\mathcal{L}(A) = (C_\ell - A)\,(\mathsf{C}^{-1})_{\ell\ell'}\,(C_{\ell'} - A)^T\,, \tag{3.46}$$

where the superscript αg is implied and $(\mathsf{C}^{-1})_{\ell\ell'}$ is the inverse covariance matrix derived from eq. (3.40). From eq. (3.46) we derive the best fit value of the amplitude and the related 68% and (95%) confidence interval(we use a 5-multipole per bandpower binning scheme): $A^{C_\ell} = [0.23 \pm 1.80(3.59)] \times 10^{-6}$ deg. We also fit a constant amplitude on $\mathcal{D}_\ell = \ell(\ell+1)/2\pi\, C_\ell$, by replacing it to C_ℓ both for the data vector and the covariance of eq. (3.46). We obtain $A^{\mathcal{D}_\ell} =$

[43] Only the chunk around $\ell = 60$ results in a low PTE due to the off-diagonal terms of the covariance being the strongest in this region (see fig, 3.22).

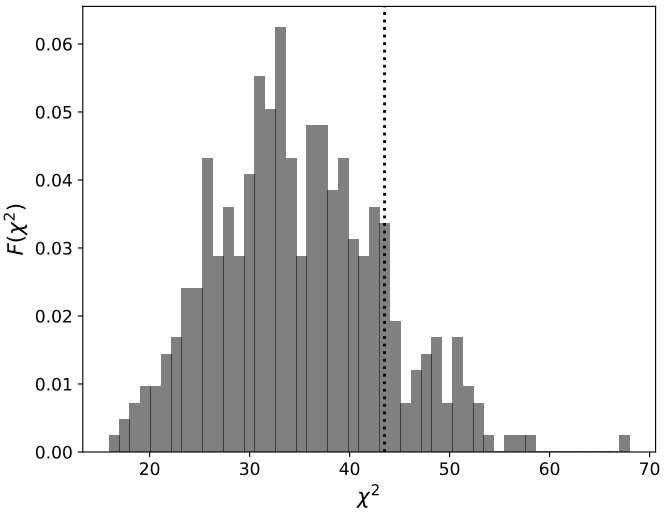

Figure 3.26: Gaussian chi-squared distribution from the 400 realizations for the following binning scheme: no binning for the first 10 multipoles, 10 bins with 2 multipoles, 10 bin with 5 multipoles and 10 multiples per bandpower afterwards. The dotted vertical line refers to the data χ^2.

$[2.22 \pm 2.09(4.18)] \times 10^{-4}$ deg. The two results are depicted in fig. 3.27. Additionally, we calculated both values using an unbiased inverse covariance following Hartlap et al. [448], and by adjusting the likelihood in eq. (3.46) according to the method in ref. [449], which marginalizes over the true covariance matrix. As discussed in section 3.6.3, these approaches account for the limited number of realizations and broaden the posterior distribution. Consequently, the resulting confidence levels are increased by approximately 3% (the effect would be larger for less aggressive binning schemes).

3.7.2 Impact of covariance estimation on data compatibility

As mentioned in Section 3.6.3, we estimate the covariance matrix using 400 realizations of birefringence and galaxies, and subsequently apply corrections for the following effects:

- Absence of systematics in galaxy simulations: the 400 realizations of Quaia are derived from a random catalog that does not include large-scale systematics. To address this, we recalibrate the effective degrees of freedom based on the data vector, which does include such systematics, following the procedure detailed in Eq. (3.40). This correction primarily results in an increased variance at low multipoles, especially for data points that deviate significantly from zero. Fig. 3.28 illustrates this behavior in the left panel for a binned spectrum, using 3 multipoles per bandpower, while the right panel provides a close-up of the unbinned spectrum at large scales.

- Limited number of available simulations: Accurate covariance estimation from simulated data requires the number of realizations to significantly exceed the length of the data vector. In our case, we have 400 simulations compared to a 190-element data vector, which can lead to inaccuracies in the covariance estimation. To mitigate this, we bin our data to effectively reduce anomalous off-diagonal correlations. As noted, alternative solutions include applying the Hartlap factor [448], which uniformly increases the error bars, or modifying the likelihood [449] (see appendix B.1 for further details).

It is also valuable to compare this covariance with the one obtained analytically using `NaMaster`. In fig. 3.29, we present this comparison, indicating that simulations tend to underestimate the variance on large scales due to a combination of the factors discussed above.

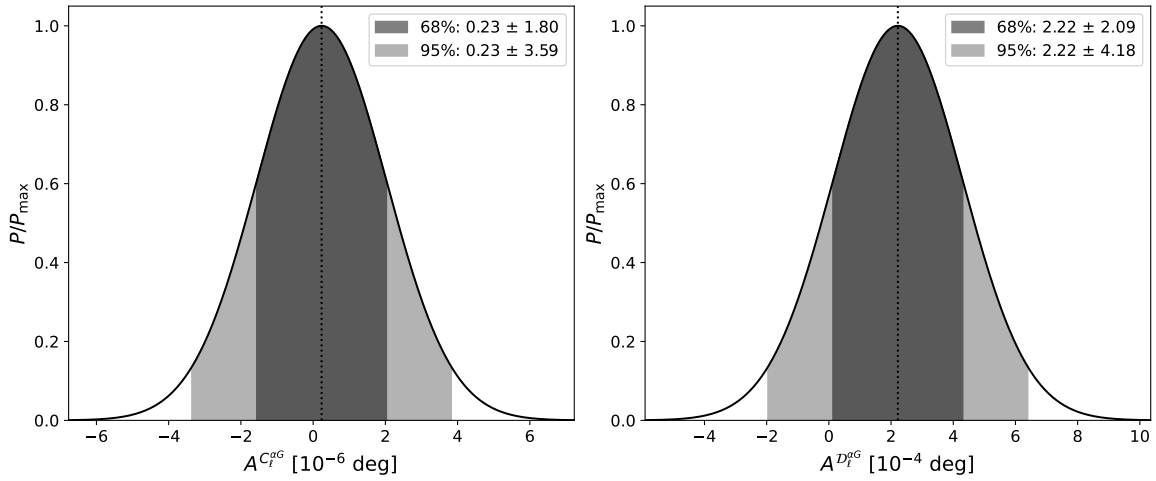

Figure 3.27: Posterior on a scale invariant amplitude A, fitted on the observed spectrum of fig. 3.24 with a Gaussian likelihood, both for C_ℓ's (*Left*) and $\mathcal{D}_\ell$'s (*Right*). The dark(light) shaded region corresponds to the 68(95)% confidence level.

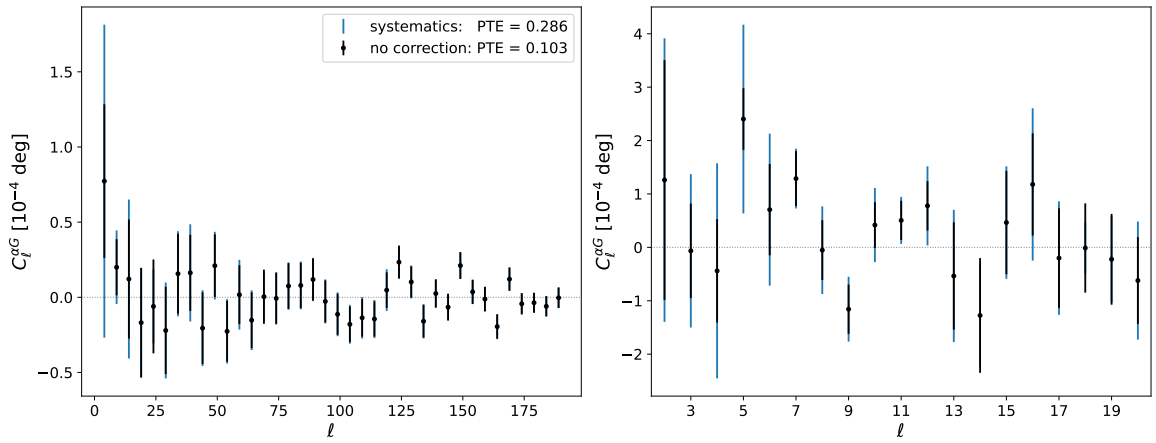

Figure 3.28: Variation of variance after applying the systematic correction of eq. (3.40), due to the lack of large scale systematics in Quaia random catalog. (*Left*): binned spectrum with $\Delta\ell = 5$. (*Right*): unbinned spectrum.

A detailed assessment of the impact of each correction is presented in fig. 3.30, showing the relative difference in the standard deviation compared to the uncorrected case based on the 400 realizations. The results are displayed for both the binned and unbinned cases in the left and right panels, respectively. As previously noted, the green line—representing the analytical computation—shows an underestimation of the variance at low multipoles, which we address using eq. (3.40), yielding the blue line.[44] The limited number of simulations is intrinsically accounted for by binning, while applying an additional correction as the Hartlap factor would further enhance the error bars (see appendix B.1 for more details). For each case, we calculate the corresponding χ^2 for a null-compatibility test and represent the related PTE in corresponding figures (see figs. 3.28 and 3.29). The systematic correction alone is able to increase the latter from 10% up to 29% for the binned scenario.

[44] At first glance, one might conclude that the systematic correction would outperform the analytical counterpart in terms of compatibility with the null hypothesis, owing to the larger standard deviation. However, as discussed in section 3.6.3 and illustrated in fig. 3.22, the former maintains a highly correlated off-diagonal structure, which diminishes the expected PTE (refer to figs.3.28 and 3.29).

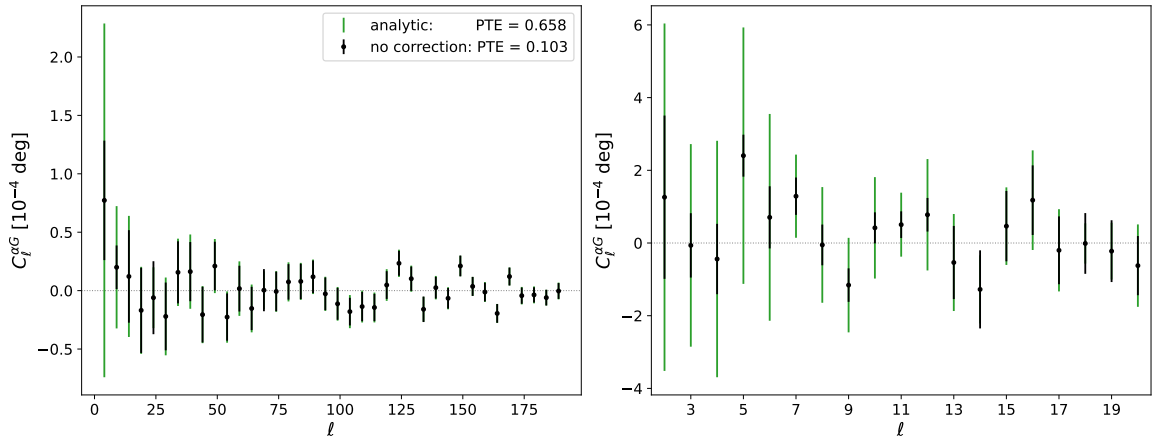

Figure 3.29: Comparison of variance between the non-corrected variance from simulation of eq. (3.39) and that attainable analytically from the data. (*Left*): binned spectrum with $\Delta\ell = 5$. (*Right*): unbinned spectrum.

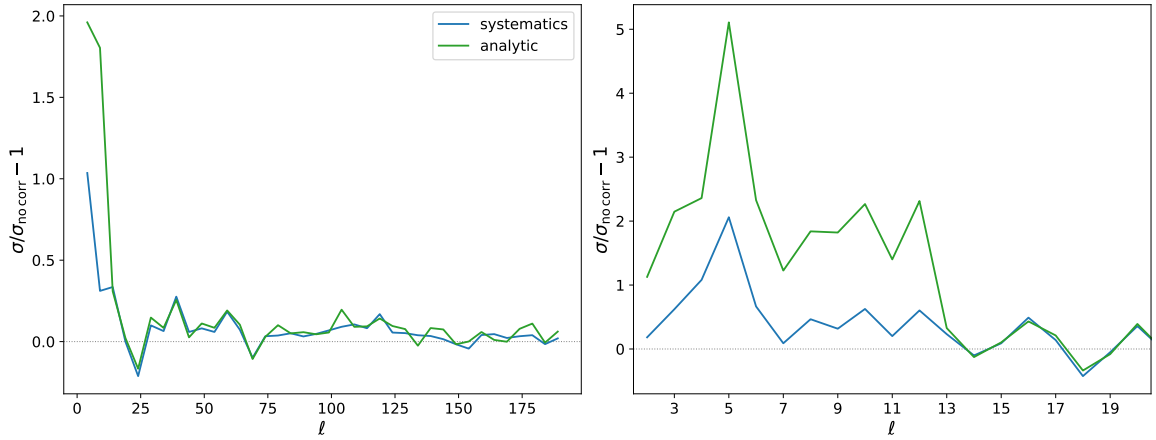

Figure 3.30: Comparison of the variance attainable when accounting for large scale systematics and when computing it analytically. For each case, we display the relative difference with respect to the variance estimated from simulations when no correction is applied. (*Left*): binned spectrum with $\Delta\ell = 5$. (*Right*): unbinned spectrum.

3.8 Fitting data on theoretical models

In section 3.6.4 we have reviewed the theoretical formulation of the birefringence-galaxy cross-correlation and its implementation in our modified version of `CLASS`. The latter depends on the axion mass m_ϕ, the initial misalignment angle θ_i and the axion-photon coupling $g_{\phi\gamma}$. As extensively outlined in refs. [3, 346, 349], ultralight axions with $m_\phi < 10^{-28}\,\text{eV}$ offer as a promising tool to constrain birefringence and can provide for the latest measurements of the isotropic CB angle [363, 390]. While the mass and the misalignment mainly govern the shape of the predicted cross-correlation signal, due to their non trivial behavior within eq. (3.41), the axion-photon coupling controls directly the amplitude, appearing as a multiplicative factor. Refer to section 3.2 and below for a detailed discussion on the impact of axion-parameters on theoretical predictions.

We anticipate a probability close to unity for all "small enough" couplings, given the measured power spectrum's compatibility with the null-hypothesis, whilst as the coupling increases the theoretical model will exceed observations and eventually an upper bound on $g_{\phi\gamma}$ can be imposed. As extensively outlined in section 3.3, previous works have constrained this coupling through haloscopes, helioscopes, colliders, and astrophysical searches (for comprehensive data

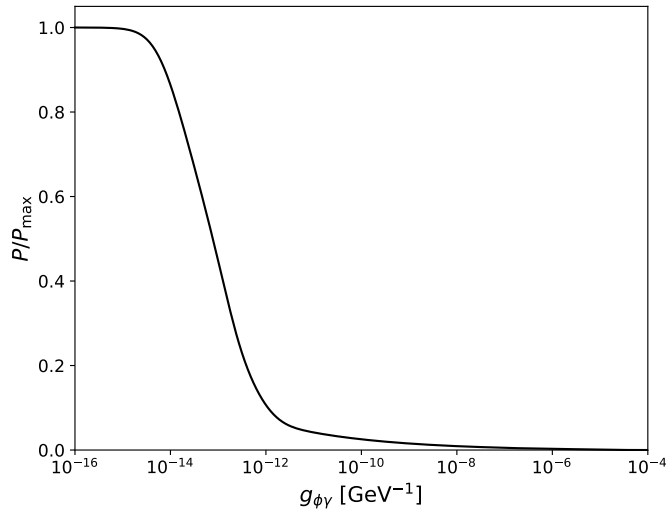

Figure 3.31: Posterior distribution on the axion-photon coupling $g_{\phi\gamma}$ marginalized on the other two free parameters (mass and initial misalignment). As the coupling increases, the predicted spectrum from eq. (3.17) becomes larger, eventually deviating from observations and thus resulting in a lower probability.

and references refer to `AxionLimits` [175]). These constraints extend down to $m_\phi \sim 10^{-12}\,\mathrm{eV}$, with spurious extensions to $10^{-24}\,\mathrm{eV}$ from cosmological analyses [349, 384, 451]. In this work, we focus on sensibly lower masses for which no bound exists in the literature.

We explore the axion-parameter space with a Gaussian likelihood

$$-2\log\mathcal{L}(\Theta) = (C_\ell^{\mathrm{th}}(\Theta) - C_\ell^{\mathrm{obs}})\,(\mathsf{C}^{-1})_{\ell\ell'}\,(C_\ell^{\mathrm{th}}(\Theta) - C_\ell^{\mathrm{obs}})^T\,, \tag{3.47}$$

where C_ℓ^{th} is the predicted power spectrum from the theoretical model of eq. (3.41) with parameters $\Theta = (m_\phi,\, \theta_i,\, g_{\phi\gamma})$, C_ℓ^{obs} the observed power spectrum as discussed in section 3.7, and $(\mathsf{C}^{-1})_{\ell\ell'}$ the inverse of the covariance matrix of eq. (3.40). We consider $m_\phi \in \left[10^{-33},\, 10^{-28}\right]$ eV,[45] and $\theta_i \in (-\pi,\, \pi)$, whereas we let the coupling vary, in principle, between 0 and ∞.

3.8.1 Bound on the axion-photon coupling

The marginalized posterior distribution on $g_{\phi\gamma}$ is shown in fig. 3.31. The region of highest probability contains couplings smaller than $\sim 10^{-12}\,\mathrm{GeV}^{-1}$, but a significant portion of the probability density extends to the tail of the distribution. At the 95% confidence level, the upper bound reaches over $10^{-5}\,\mathrm{GeV}^{-1}$. This is primarily due to a degeneracy with the initial misalignment, which also determines the starting value of the axion field. Consequently, when $|\theta_i| \sim 0$, the cross-correlation is null regardless of the coupling value. To address this, we derive an upper bound for each point in the m_ϕ-θ_i parameter space, presenting our results in fig. 3.32. The regions with the strongest upper bounds are those where $m_\phi \sim 10^{-32}\,\mathrm{eV}$ and the misalignment angle is high. This result aligns with our previous theoretical analysis [3] (see fig. 3.9). In fig. 3.33, we also show the corresponding curves in the coupling-mass plane at fixed values of θ_i. It is clear that the closer the initial misalignment is to zero, the less stringent the obtained bound becomes. To compare our result to current bounds we extend the astrophysical limits shown in fig. 3.5 to our mass range and plot our best result from fig. 3.33 in fig. 3.34. In conclusion, cross-correlating anisotropic birefringence with galaxies using the currently available

[45] The lowest mass roughly corresponds to the Hubble parameter today and even lower masses would lead to fields whose dynamical evolution has not commenced yet. We do not explore the region where $m_\phi > 10^{-28}\,\mathrm{eV}$ as it is computationally demanding and the perturbative approach breaks (see section 3.4.1).

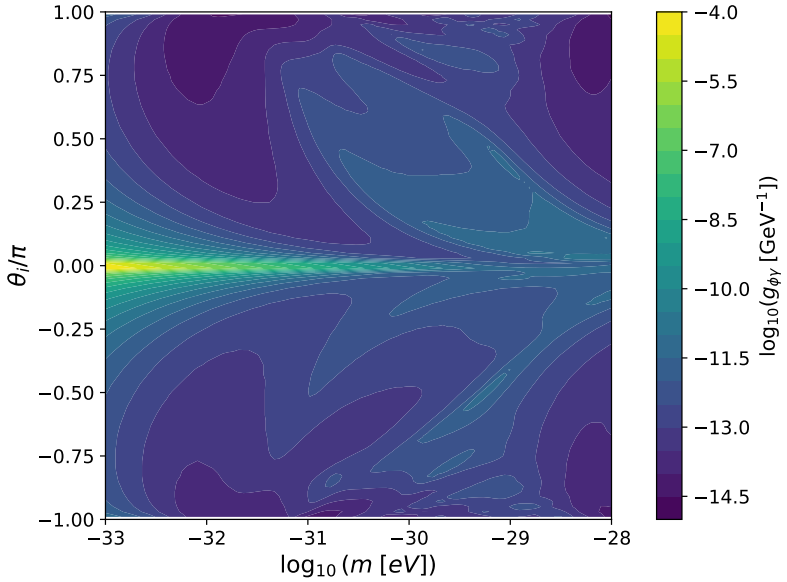

Figure 3.32: Achievable upper bound on the axion-photon coupling, at the 95% confidence level, for each point in the m_ϕ-θ_i parameter space. For very small misalignment angles, the theoretical power spectrum is significantly reduced, requiring a higher value of $g_{\phi\gamma}$ to enhance the signal sufficiently away of observations.

data allows us to set an upper bound on the axion-photon coupling down to $\sim 10^{-15}\,\mathrm{GeV}^{-1}$ in the most favorable region of our parameter space.

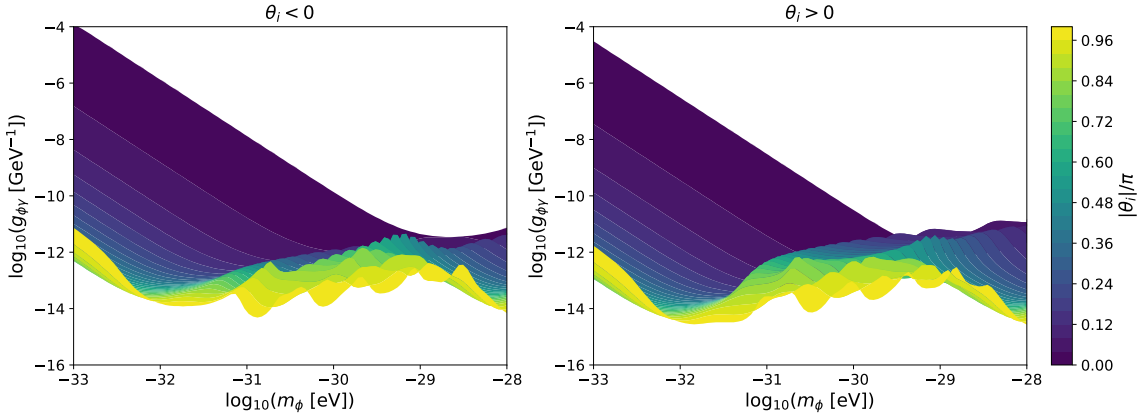

Figure 3.33: Upper bound on the axion-photon coupling as a function of the axion mass. Each line is drawn for a fixed value of the initial misalignment angle, depicted in the colorbar. It is evident how the tightest constraints are obtained for high values of the latter, where there is no degeneracy with the coupling.

3.9 Discussion and future prospects

In this chapter, we have discussed, for the first time, the cross-correlation between anisotropic cosmic birefringence and galaxy number counts as a probe of axion-like physics. Parity violating terms in the electromagnetic Lagrangian, such as ALPs coupling to photons, induce the "in vacuo" rotation of the plane of linearly polarized waves (i.e. cosmic birefringence). The magnitude of this effect is heavily influenced by the path traveled by photons. Therefore, the cosmic microwave background, being the oldest light remnant observable today and having traveled vast

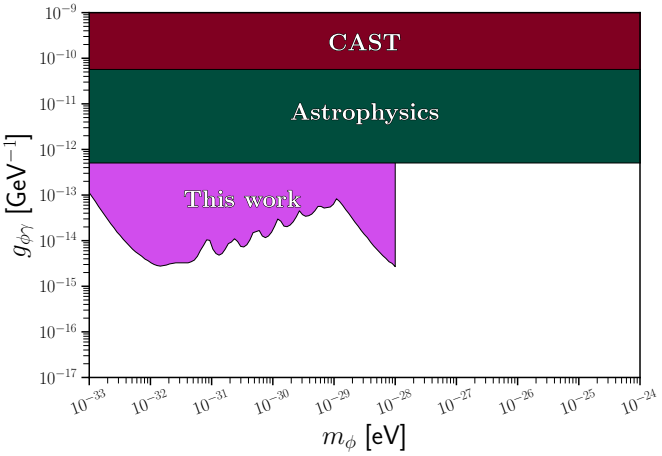

Figure 3.34: Best achievable upper bound on the axion-photon coupling, $g_{\phi\gamma}$ as a function of the axion mass, m_ϕ, as derived from the cross-correlation analysis of *Planck* PR4 birefringence and Quaia galaxy number counts. We compare the results with the extension of current bounds for higher masses (see section 3.2.2).

distances to reach us, serves as a crucial tool for cosmology. It provides valuable information about the early universe, offering insights into fundamental cosmological parameters and the processes that shaped cosmic evolution. Moreover, the characteristics of the underlying axion model significantly impact the predicted rotation angle. We focus on ultralight axion-like particles, whose field oscillations begin at relatively late cosmological times. This aligns with the period when the density term from galaxy number counts tends to peak, underscoring the valuable insights that can be gleaned from this approach. We leverage EDE models from the string axiverse and explore their implications on this phenomenon.

We have computed this novel cross-correlation by following the background and perturbation evolution of the axion-like field, within a properly modified version of the Boltzmann code `CLASS`. Our analysis revealed significant variations in the correlation's amplitude across the parameter space characterizing the axion-like particle ($10^{-33}\,\mathrm{eV} \leq m_\phi \leq 10^{-28}\,\mathrm{eV}$, $-\pi < \theta_i \leq \pi$). We found a non negligible signal especially for large and intermediate angular scales ($\ell < 100$). Additionally, we investigated how the axion-photon coupling dictates the amplitude of the birefringence angle and consequently influences the observed signal.

With the intent of finding when the cross-correlation is measurable by observations, we have explored the ALP-parameter space over a 100×100 grid on m_ϕ - θ_i and computed the signal-to-noise ratio, exploiting the *Euclid* survey's forecast specifications combined with those of future CMB experiments (LiteBIRD, Simons Observatory and CMB-S4). In particular, for CMB-S4 - the best performing of the three - we found the needed value of the coupling to reach unity in the (S/N), conservatively keeping it below current bounds ($g_{\phi\gamma} \leq 10^{-12}\,\mathrm{GeV}^{-1}$). We also calculated the signal-to-noise ratio for the auto-correlation of birefringence, demonstrating that for $m_\phi \lesssim 10^{-32}\,\mathrm{eV}$ and $|\theta_i| \gtrsim \pi/4$, there is not only a "relatively small" coupling value where the signal-to-noise ratio of the cross-correlation reaches unity, but the cross-correlation also provides more discernible information in terms of measurability compared to the auto-correlation alone. Additionally, these axion-parameters are linked to a late-time evolution of the field, occurring around reionization. This alignment with the epoch and the scales of interest of the galaxy counterpart serves to enhance the signal. This elucidation underscores the effectiveness of this approach in unraveling the quest to understand the origin of birefringence.

Given the upcoming release of DR1 from the *Euclid* survey and the substantial influx of polarization data anticipated over the next decade, this approach stands as an exceptional tool for testing axion-like physics and investigating anisotropic cosmic birefringence. To assess this

with available data we have derived the first measurement of the underlying cross-correlation. We computed the observed power spectrum by combining *Planck* NPIPE polarization data with the Quaia quasar catalog. By applying an EB-estimator on the former, we obtained a birefringence map across the sky at $N_{\rm side} = 64$. Similarly, we calculated the corresponding galaxy overdensity map using the 1.3 million sources from the latest Quaia release. We applied a QML estimator at $\ell \leq 12$, integrated with a *pseudo-*C_ℓ estimator at larger multipoles. We calculated the related covariance matrix from 400 realizations of the two probes and showed that our measurement is well compatible with zero, with a PTE between 20% and 80% depending on the binning scheme.

With the aim of setting an unprecedented upper bound on the axion-photon coupling for the underlying ultralight candidates, we performed a Gaussian likelihood analysis on the same free parameters of the aforementioned theoretical analysis: mass m_ϕ, initial misalignment angle θ_i, and axion-photon coupling $g_{\phi\gamma}$. Due to a degeneracy of the coupling with the very small end of the initial misalignment, we were unable to retrieve a competitive upper bound with a full marginalization over the other two parameters. Nonetheless, we explored the attainable bound at each point in the mass-misalignment parameter space and found values down to $10^{-15}\,\mathrm{GeV}^{-1}$.

In light of the incoming data from next-generation galaxy surveys and CMB polarization experiments, the novelty of this probe lies in its capability to effectively constrain the axion-parameter in a poorly bounded mass range. Additionally, a detection of such a signal could significantly contribute to the open question of the existence of cosmic birefringence and the underlying parity-violating physics.

Chapter 4

Unveiling the integrated Sachs-Wolf effect in *Euclid* data

As discussed in chapter 1, we are currently in an exciting era of precision cosmology, where highly specialized surveys are crucial for advancing our understanding. In the realm of large-scale structure cosmology, upcoming galaxy surveys are expected to map the sky with unprecedented accuracy, potentially revealing some of the most profound mysteries underlying cosmic evolution. Among them, the *Euclid* mission, part of the European Space Agency (ESA) Cosmic Vision 2015–2025 program, is poised to play a critical role in advancing our understanding of cosmology by providing high-resolution optical and near-infrared imaging and spectroscopy across 14,000 $\deg^2$ of the sky. The current standard cosmological model, ΛCDM, has successfully described a wide range of observations with only a few parameters. However, it is unsatisfactory in many respects, particularly due to its reliance on dark matter and dark energy—two components whose nature remains fundamentally unknown. Despite decades of precision measurements, especially from CMB experiments such as WMAP and *Planck*, the underlying assumptions about the universe's initial conditions and the theory of gravity remain areas of deep uncertainty [452, 453].

CMB measurements, while critical in establishing the ΛCDM model, probe conditions in the early universe, specifically at the time of recombination when dark energy was negligible. These observations are inherently limited in their ability to shed light on the universe's late-time evolution and the role dark energy plays in driving cosmic acceleration [436, 454–457]. The physical simplicity of interpreting CMB data, given the stable environment of space-based experiments, has been one of its greatest strengths, yet it also highlights the need for complementary probes. To fully understand the dynamic interplay between dark matter and dark energy over time, new data is needed—data that can chart the cosmic history from the time when dark energy became a significant factor in the universe's expansion.

This is where *Euclid*'s LSS surveys become essential. By capturing detailed information on the distribution and evolution of galaxies, *Euclid* will allow us to map the expansion history of the universe and the growth of structures over the past ten billion years, a period when dark energy has had a profound impact. The real strength of *Euclid* lies in its ability to cross-correlate galaxy clustering data with late-time CMB effects, such as the integrated Sachs-Wolf (iSW) effect [40, 457–459]. The iSW effect, which arises from the interaction between CMB photons and evolving gravitational potentials, provides a unique way to test the impact of dark energy on large-scale structure formation. By combining *Euclid*'s galaxy data with CMB data, we can test whether cosmic expansion and structure growth follow the predictions of general relativity or point to possible modifications of gravity on cosmological scales.

Beyond the iSW effect, cross-correlating *Euclid* data with other late-time CMB phenomena will refine constraints on the nature of dark energy and its evolution. It could help in testing alternative theories to the cosmological constant, such as quintessence or other dynamical models.

Moreover, these cross-correlations may provide more precise constraints on neutrino masses, another key area of modern cosmology. The ability to robustly interpret and complement the CMB results with *Euclid*'s exquisite data will advance our understanding of fundamental physics, potentially uncovering new physics beyond the standard cosmological model. In this context, the role of *Euclid* goes beyond just mapping the universe—it provides essential data for testing some of the most profound questions in cosmology today.

4.1 *Euclid* in a nutshell

As aforementioned, the *Euclid* mission is designed to address some of the most pressing questions in cosmology: the nature of dark energy and dark matter, and the evolution of large-scale structure in the Universe. By observing the distribution of galaxies and the weak gravitational lensing of their shapes, *Euclid* will map the expansion history of the universe over the past 10 billion years, probing a redshift range up to $z \approx 2.5$ [2, 17]. These measurements will help test the current standard cosmological model, ΛCDM, by providing crucial insights into the growth of cosmic structures and the nature of gravity on cosmological scales, offering a stringent test of deviations from General Relativity.

At the heart of the *Euclid* mission are its two scientific instruments: the visible imager (VIS) and the near-infrared spectrometer and photometer (NISP). The VIS instrument is a wide-field camera operating in the visible wavelength range (550–900 nm) and is optimized to measure the shapes of galaxies with unparalleled precision. Its large focal plane, consisting of 36 charge coupled devices with 0.1"/pixel resolution, allows VIS to capture detailed images over vast sky areas, offering the highest-resolution wide-field imaging capability from space. In a single day, VIS will cover more sky than the Hubble Space Telescope has observed in its entire mission, while maintaining a similar level of detail. This capability is essential for *Euclid*'s weak lensing studies, which rely on precise measurements of the shapes of millions of galaxies to probe the distribution of dark matter and the impact of dark energy on cosmic structures.

Complementing VIS is the NISP instrument, which operates in the near-infrared (920–2000 nm) and serves dual roles as both a photometer and a spectrometer. NISP's photometric mode utilizes three broadband filters, while its spectroscopic mode, using a set of grisms, provides accurate redshift measurements through slitless spectroscopy. This ability to measure redshifts is fundamental to *Euclid*'s mission to trace the evolution of galaxies and structures over cosmic time. With a mosaic of 16 Teledyne's Hawaii 2RG infrared detectors, NISP achieves a resolution of 0.3"/pixel, enabling it to capture crucial redshift information for over a billion galaxies, allowing the mission to reconstruct the universe's expansion history and study the dynamics of dark energy.

One of *Euclid*'s core scientific objectives is to generate the largest and most comprehensive catalog of galaxies ever assembled [2]. By combining VIS and NISP data with observations from external surveys such as the Rubin Observatory's LSST [70], Pan-STARRS [460], DECcam [461], OmegaCAM [462], MegaCAM [463], JPCAM [464], HSC [465], and others, *Euclid* will create detailed multi-wavelength photometric catalogs. These catalogs will serve as a critical resource for cosmological studies, enabling the detailed mapping of galaxy clustering and cosmic shear on unprecedented scales. The mission's ability to detect and study galaxy clustering will provide new insights into the distribution of dark matter, the impact of cosmic inflation, and the role of dark energy in shaping large-scale cosmic structures.

The study of galaxy clustering is particularly significant because it allows cosmologists to trace the distribution of matter over time. *Euclid* will probe galaxy clustering with exceptional precision, but to fully exploit this data, it requires tight control over systematics such as redshift uncertainties and galaxy bias. The subtle effects of gravitational lensing, which alter both the magnification and apparent positions of galaxies, must also be accurately modeled. *Euclid*'s

observations, which will span scales comparable to the current cosmic horizon, will be sensitive to effects that test General Relativity, as well as potential modifications to gravity on large scales. In addition, *Euclid*'s spectroscopic capabilities will be crucial for constraining non-linear structure formation, essential for understanding smaller-scale clustering and galaxy dynamics.

Weak gravitational lensing, another key probe of cosmology for *Euclid*, relies on the bending of light by intervening matter, causing distortions in the shapes of distant galaxies. This phenomenon, known as cosmic shear, provides direct insight into the distribution of dark matter and the geometry of the universe. However, measuring weak lensing requires extremely accurate shape measurements, as the effect is subtle and easily confounded by the intrinsic alignment of galaxies. By correlating the shapes of galaxies over large sky areas, *Euclid* will detect cosmic shear with high statistical significance, allowing for tight constraints on cosmological parameters such as the dark energy equation of state and the growth rate of structure.

Euclid's impact extends far beyond weak lensing and galaxy clustering. Its vast, high-quality dataset will serve as a foundation for a wide range of scientific investigations, from testing inflationary models by probing matter distribution on the largest cosmic scales to constraining neutrino masses and exploring modifications to gravity [17]. The mission will also play a critical role in complementing other cosmological surveys, such as DESI and LSST, by providing space-based data with superior control over systematics and minimal atmospheric interference.

Overall, *Euclid* is set to redefine precision cosmology, providing the most detailed map of the universe's large-scale structure to date and offering invaluable insights into the fundamental nature of dark matter, dark energy, and gravity. Its successful launch and mission execution will mark a major milestone in humanity's quest to unravel the mysteries of the cosmos.

4.2 The integrated Sachs-Wolf effect

The integrated Sachs-Wolfe (iSW) effect is a subtle but crucial phenomenon in cosmology that occurs when cosmic microwave background photons interact with time-varying gravitational potentials as they travel through the universe. As photons pass through large gravitational wells—regions of enhanced mass—they are blue-shifted when falling into the potential and red-shifted when climbing out. If the gravitational potential remains constant, these shifts cancel out, and the photon's energy remains unchanged. However, when the potential evolves while the photon is in transit, the energy change is not zero, resulting in temperature anisotropies in the CMB.

The iSW effect arises during two distinct phases of cosmic evolution. The first phase, known as the early iSW effect, occurs after recombination, around the transition from a radiation-dominated universe to a matter-dominated one. During this period, gravitational potentials were evolving due to the diminishing influence of radiation, and this evolution leaves an imprint on the CMB by slightly altering the energy of photons. This process enhances the height of the first acoustic peak in the CMB power spectrum, reflecting the influence of this early-time evolution on small angular scales.

The second phase, the late iSW effect, occurs much later, during the epoch when dark energy becomes the dominant force[46] driving the accelerated expansion of the universe. In this phase, as dark energy causes the universe's expansion to accelerate, large-scale gravitational potentials begin to decay. CMB photons passing through these decaying potentials experience a net energy gain, which enhances temperature fluctuations on the largest angular scales (low multipoles in the CMB power spectrum). Detecting this late iSW effect is challenging due to cosmic variance on large scales, but it plays a critical role in understanding dark energy and the dynamics of cosmic expansion.

[46] This occurs after a long period of matter domination with constant gravitational potentials.

The importance of studying the iSW effect lies in its ability to probe the evolution of the universe and the behavior of its large-scale structure. The late iSW effect, in particular, is one of the few observational signatures directly linked to dark energy and its influence on gravitational potentials. By measuring this effect—especially through cross-correlations between the CMB temperature map and large-scale structure surveys—cosmologists can gain insights into the nature of dark energy, the geometry of the universe, and the validity of general relativity on cosmological scales. Thus, the iSW effect is a powerful tool for understanding the evolution of the universe and testing fundamental theories of cosmology.

4.3 Cross-correlating galaxies with the late-iSW

The cross-correlation between the late-iSW effect and galaxy surveys is particularly advantageous due to the timing of these two probes [466]. Galaxies represent a relatively late-stage phenomenon in the cosmic timeline, reflecting conditions shaped by the universe's evolution under the influence of dark energy. In contrast, the late-iSW effect arises from the interaction of CMB photons with evolving gravitational potentials, specifically during epochs when dark energy dominates the universe's energy content. This alignment makes the correlation between CMB anisotropies and galaxy distributions highly relevant for understanding late-time cosmic dynamics.

By correlating late-iSW with galaxy surveys, we gain valuable insights into how gravitational potentials evolve as dark energy influences cosmic expansion. This relationship is crucial for probing the effects of dark energy on large-scale structure, as the late-iSW effect is sensitive to the gravitational wells associated with galaxy formation. Since galaxies are influenced by the same matter distribution that affects the CMB, their spatial distribution can enhance our ability to detect the weak late-iSW signal and constrain cosmological models more effectively [15, 467, 468].

Numerous studies have demonstrated the potential of this approach, such as the *Planck* 2015 analysis, which detected the iSW effect with a significance of 2.7σ [458] through cross-correlation with the Sloan Digital Sky Survey [469]. The significance of the detection increased when multiple large-scale structure surveys (SDSS, NVSS [470] and 2MASS [295]) were combined, and further improved by including CMB lensing data [15, 467, 468]. This highlights the effectiveness of cross-correlation methods in boosting signal detection and refining our understanding of cosmological parameters. For instance, *Planck*'s analysis also provided a 3σ detection of dark energy's contribution to the universe's energy density, Ω_Λ.

Looking forward, the *Euclid* mission will play a pivotal role in enhancing the detection of the late-iSW effect through its high-precision galaxy clustering (GC) surveys. The expected strong correlation between the matter distribution traced by *Euclid* and CMB temperature anisotropies will significantly improve sensitivity to the late-iSW signal. Forecasts show that combining *Euclid* data with CMB measurements will substantially tighten constraints on cosmological parameters, including the dark energy equation of state, while reducing the impact of nuisance parameters and systematic errors [15].

This cross-correlation approach also opens new avenues for exploring models that alter the late-time dynamics of the universe, such as modified gravity theories or evolving dark energy models. These aspects are particularly important since they are challenging to constrain with CMB data alone, which predominantly reflects early-universe conditions. The work of the CMB cross-correlation Science Working Group (CMBX-SWG) of *Euclid*, which I am part of, is crucial in this effort, focusing on the development and validation of the analysis pipeline for detecting and interpreting the iSW signal. This synergy between CMB and galaxy data promises to provide deeper insights into the nature of dark energy and the overall dynamics of the universe.

In the linear regime, the expression for the angular power spectrum of the cross-correlation between CMB temperature anisotropies (T) and galaxy number counts in the i-th redshift bin

(G_i) is:

$$C_\ell^{TG_i} = \frac{2}{\pi}\int \mathrm{d}k\, k^2 P(k) \int \mathrm{d}z\, W^{\mathrm{iSW}}(z,k)\, j_\ell(k\chi(z)) \int \mathrm{d}z'\, W^{G_i}(z')\, j_\ell(k\chi(z'))\,, \tag{4.1}$$

where $P(k)$ is the matter power spectrum today, j_ℓ is the spherical Bessel function of index ℓ, χ is the comoving distance at redshift z, and W^{iSW} and W^{G_i} are the window functions of the iSW anisotropy and the galaxy number counts in the $i-$th redshift bin, respectively:

$$W^{\mathrm{iSW}}(z,k) = 3\,\frac{\Omega_m H_0^2}{k^2}\,\mathrm{e}^{-\tau(z)}\,\frac{\mathrm{d}}{\mathrm{d}z}\left[D(z)(1+z)\mu(z)\frac{1+\gamma(z)}{2}\right], \tag{4.2a}$$

$$W^{G_i}(z) = n_i(z)\, b_g(z)\, D(z)\,. \tag{4.2b}$$

Here, Ω_m is the total matter density parameter, H_0 the Hubble expansion rate today and $D(z)$ the growth factor. The optical depth $\tau(z)$ as a function of redshift z can be considered constant since we are interested in the late-time evolution. In these equations, we assume a linear galaxy bias $b_g(z)$ that is scale-independent. However, this latter assumption will be relaxed for models that account for departures from the Gaussian nature of primordial perturbations. Finally, $n_i(z)$ is the galaxy selection function which, together with the bias, will be further discussed in the following sections.

Eq. (4.1) assumes that the evolution of density perturbations is separable in k and z at linear scales. This is not the case, for example, in models with massive neutrinos or, more generally, with non-cold dark matter components [160, 471, 472]. The expressions for the window functions further assume vanishing spatial curvature [473] and do not account for relativistic effects [415].

In this analysis, we compute the relevant theoretical angular power spectra with the `camb` Boltzmann code [474, 475] or its extension `MGcamb` [476–479]. Being interested in the iSW effect that is most relevant on large-angular scales, we calculate the $P(k)$ in the linear perturbation regime.

4.3.1 Model

The fiducial cosmology in our analysis is the spatially flat ΛCDM model with parameters given in *Euclid* [17]. The corresponding values are reported in table 4.1; they include: the dimensionless Hubble parameter $h = H_0/100$ km/s/Mpc; the baryon Ω_b and dark energy Ω_Λ density parameters; the amplitude A_s and spectral index n_s of the primordial power spectrum of scalar perturbations; the Universe optical depth to reionization τ; and a total neutrino mass of 0.06 eV, with a single massive neutrino and two massless neutrinos.

As already anticipated, in this section we study cosmological constraints that can be derived only from measurements of the cross-correlation of CMB temperature anisotropies and galaxy clustering (TG-spectrum). As a consequence, we only explore models that are more sensitive to the iSW effect (all cosmological parameters are fixed to those in table 4.1, otherwise specified). Specifically, we consider:

- ΛCDM, varying Ω_Λ, the dark energy density parameter.
- ΛCDM+A_{iSW}, where we introduce an overall amplitude parameter that multiplies the TG-spectrum and can capture possible deviations from the standard model.
- w_0CDM, where w_0 gives the value of the DE equation-of-state at present ($z = 0$), which reduces to the cosmological constant case for $w_0 = -1$. We vary both w_0-Ω_Λ together and w_0 alone.

- $w_0\,w_a$CDM, we allow for the DE component to be dynamical, with an equation-of-state that depends on redshift as $w(z) = w_0 + w_a\,z/(1+z)$ [480, 481]. In this well-known parametrization, w_0 gives the value at present ($z = 0$), while w_a accounts for the time variation.

- $\mu\,\gamma$ CDM, a MG scenario following the parameterization first introduced in [482]:

$$\begin{aligned} k^2\Psi &= -4\pi G\,\mu(a,\,k)a^2\,[\rho\Delta + 3(\rho+P)\sigma]\ , \\ k^2(\Phi - \gamma(a,\,k)\Psi) &= 12\pi G\,\mu(a,\,k)a^2(\rho+P)\sigma\,. \end{aligned} \tag{4.3}$$

  The phenomenological functions μ and $\Sigma \equiv \mu(1+\gamma)/2$ describe the gravitational coupling felt by matter and by light, respectively. The former probes the growth of structures, while the latter probes lensing. The function γ is called gravitational slip and in absence of anisotropic stresses gives the ratio of the gravitational potentials: $\gamma \equiv \Psi/\Phi$. We consider a scale independent parametrization of μ and γ such that gravity deviates from GR only in the late Universe.

$$\begin{aligned} \mu(a) &= 1 + E_{11}\Omega_\Lambda(a)\,, \\ \gamma(a) &= 1 + E_{22}\Omega_\Lambda(a)\,. \end{aligned} \tag{4.4}$$

  When E_{11} and E_{22} equal zero GR is recovered.

- ΛCDM+$f_{\rm NL}$, which is a model allowing for primordial non-Gaussianity of the local type. In this case, correlations in the primordial potential between short-scale modes (which form halos) and long-scale modes result in a galaxy bias that not only can evolve with redshift but also depends on the scale k [483–485]:

$$b(k,z) = b_g(z)\left[1 + f_{\rm NL}\frac{\delta_c}{\alpha(k,z)}\right]\,. \tag{4.5}$$

  In this expression, $\delta_c = 1.686$ is the critical density for gravitational collapse, $f_{\rm NL}$ parameterizes the departures from Gaussianity, and

$$\alpha(k,z) = \frac{k^2 T(k) D(z)}{3\Omega_m H_0^2}\,, \tag{4.6}$$

  where $T(k)$ is the matter transfer function, $D(z)$ is the linear growth factor normalized to equal the scale factor in the matter dominated era and Ω_m is the total matter density parameter. Overall, the resulting bias exhibits a characteristic k^{-2} scale dependence that leads to an enhancement in clustering on the largest scales.

4.3.2 Survey specifications

Here we describe in more detail the survey specifications used in our analysis for both the photometric and spectroscopic *Euclid* surveys. Unless otherwise stated, we will adopt the same choices of [17].

The galaxy selection function $n_i(z)$ gives the (normalized) number density of galaxies that are assigned to the $i-$th redshift bin. As such, it is a convolution, over the bin, of the number

h	$\Omega_b h^2$	Ω_Λ	$10^9\, A_s$	n_s	τ	$\sum m_\nu$ [eV]
0.67	0.0224	0.68	2.1115	0.96	0.058	0.06

Table 4.1: Cosmological parameters of the fiducial ΛCDM model adopted in this work and taken from *Euclid* [17].

Survey	σ_b	z_b	c_b	σ_0	z_0	c_0	$f_{\rm out}$
Photometric	0.05	0.0	1.0	0.05	0.1	1.0	0.1
Spectroscopic	0.001	0.0	1.0	–	–	–	0.0

Table 4.2: Analysis settings for the photometric and spectroscopic redshift errors. Parameters refer to those in Eq. (4.8).

density of galaxies with *true* redshift z, $n(z)$, with the probability that a galaxy at redshift z is assigned a measured redshift z_m. This probability function $p(z_m|z)$ models the error on redshift measurements.

The galaxy selection function is thus obtained as:

$$n_i(z) = \frac{\int_{z_i^-}^{z_i^+} dz_m n(z) p(z_m|z)}{\int_{z_{\rm min}}^{z_{\rm max}} dz \int_{z_i^-}^{z_i^+} dz_m n(z) p(z_m|z)}\,, \tag{4.7}$$

where $\left[z_i^-, z_i^+\right]$ are the edges of the i-th bin, and $[z_{\rm min}, z_{\rm max}]$ is the whole observable redshift range.

The probability of z_m given z is:

$$\begin{aligned} p(z_m|z) \;=\; & \frac{1-f_{out}}{\sqrt{2\pi}\sigma_b\,(1+z)} \exp\left\{-\frac{1}{2}\left[\frac{z-c_b z_m - z_b}{\sigma_b\,(1+z)}\right]^2\right\} \\ & + \frac{f_{out}}{\sqrt{2\pi}\sigma_0\,(1+z)} \exp\left\{-\frac{1}{2}\left[\frac{z-c_0 z_m - z_0}{\sigma_0\,(1+z)}\right]^2\right\}, \end{aligned} \tag{4.8}$$

where σ_b is the uncertainty, c_b a multiplicative bias and z_b an additive bias in the redshift determination for a fraction of sources with reasonably well-measured redshifts, while σ_0, c_0 and z_0 are the corresponding quantities for catastrophic outliers, and $f_{\rm out}$ is their fraction. The *Euclid* baseline for these analysis settings is shown in Table 4.2.

Photometric survey

In this analysis, we follow two approaches to model the photometric survey. For the first one, which will be our baseline, we model the selection function following Eq. (4.7) with the *true* galaxy distribution $n(z)$ given in the *Euclid* redbook [486]:

$$n(z) \propto \left(\frac{z}{z_0}\right)^2 \exp\left[-\left(\frac{z}{z_0}\right)^{3/2}\right], \tag{4.9}$$

where $z_0 = z_M/\sqrt{2}$, with the median redshift $z_M = 0.9$. The overall normalization is set by the requirement that the galaxy surface density is $\bar{n} = 30\,\mathrm{arcmin}^{-2}$. Following [17], we split the sample in 10 equi-populated redshift bins over a redshift range $[z_{\min}, z_{\max}] = [0.001, 2.50]$, with all the photo-$z$ parameters assumed to be constant across the bins. Fig. 4.1 shows the $n_i(z)$ for each redshift bin compared with the total galaxy distribution of the sample, $n(z)$. The galaxy bias $b_g(z)$ describes the relationship between the spatial distribution of galaxies and the underlying matter density field. We take a step-wise function as baseline for our analysis:

$$b_{g,\,i}(z) = \sqrt{1 + z_i}\,, \tag{4.10}$$

where z_i is the centroid of the $i-$th redshift bin (see fig. 4.2).

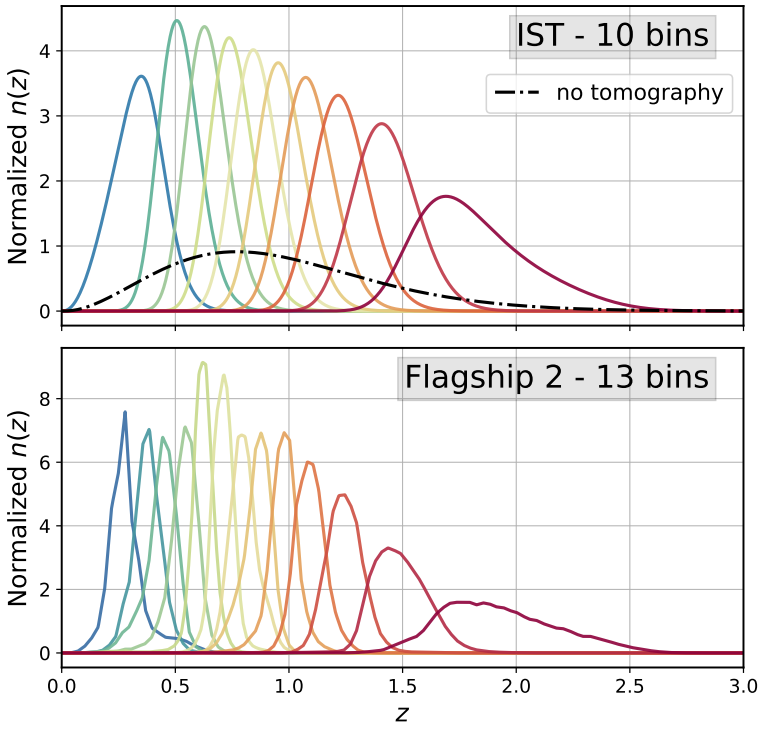

Figure 4.1: (*Top*): Normalized redshift distribution for each tomographic bin, $n_i(z)$ following the prescription of 10 equi-populated redshift bins from *Euclid* IST [17]. The black dash-dotted line is the $n(z)$ for the non-tomographic case. (*Bottom*): Normalized redshift distribution, as inferred from the Flagship 2 simulation [16]. The sample is split into 13 equally populated redshift bins. **CREDIT: *Euclid* CMBX-SWG**.

As a second approach, we model the galaxy sample from *Euclid* Flagship 2 simulation [16]. The selection function has 13 equi-populated redshift bins, shown in fig. 4.1, with an overall galaxy density $\bar{n} = 24.3\,\mathrm{arcmin}^{-2}$. The bias is fitted by a polynomial:

$$b_{g,\,\mathrm{FS2}}(z) = a_0 + a_1\,z + a_2\,z^2 + a_3\,z^3 \tag{4.11}$$

with $(a_0,\,a_1,\,a_2,\,a_3) = (0.8,\,1.2,\,-0.9,\,0.4)$, and it is shown in fig. 4.2.

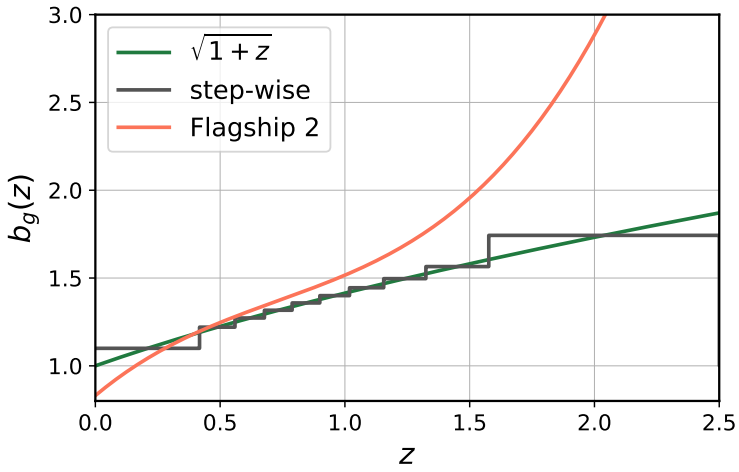

Figure 4.2: Different galaxy bias prescriptions. The baseline adopted in this work is the step-wise galaxy bias (dark gray line). **CREDIT: *Euclid* CMBX-SWG**.

Spectroscopic Survey

The *Euclid* spectroscopic sample will be made up of $H\alpha$-line emitters distributed over the redshift range $[z_{\rm min}, z_{\rm max}] = [0.9, 1.8]$. The expected number counts in four tomographic redshift bins have been modeled following [487] and are given in table 3 of [17]. They correspond to an overall surface galaxy density of $\bar{n} = 1.6$ arcmin^{-2}. For each redshift bin, a value is also assigned to the linear galaxy bias, which is modeled as a piece-wise constant function. Finally, we assume the uncertainties on redshift measurements to be described by eq. (4.8) with parameters given in table 4.2, where we have considered that the fraction of outliers is expected to be negligible for the spectroscopic survey [486].

4.3.3 Expected significance of the iSW-GC cross-correlation

We expect *Euclid* to provide an optimal dataset for iSW studies. Thanks to the wide coverage both in sky area and redshift, *Euclid* will map a large number of galaxies over the redshift range where the iSW signal is sourced. Moreover, *Euclid* will enable a tomographic analysis, which enhances the detection's significance and allows for testing the redshift evolution in non-standard cosmological models.

To evaluate the expected significance of measuring the iSW effect from the cross-angular power spectrum C_ℓ^{TG} between CMB temperature anisotropies and galaxy clustering, we calculate the squared signal-to-noise ratio for each multipole as:

$$\left(\frac{\rm S}{\rm N}\right)^2_\ell = \sum_{\ell'} \sum_{G_i G_j} C_\ell^{TG_i} \left[{\rm Cov}^{-1}\right]_{\ell\ell'} C_{\ell'}^{TG_j} \tag{4.12}$$

where G_i, G_j run over the different redshift bins. Starting from this, the corresponding cumulative value over some range of multipoles $[\ell_{\rm min}, \ell_{\rm max}]$ is obtained as:

$$\frac{\rm S}{\rm N} = \sqrt{\sum_{\ell=\ell_{\rm min}}^{\ell_{\rm max}} \left(\frac{\rm S}{\rm N}\right)^2_\ell}. \tag{4.13}$$

			Photometric		Spectroscopic	
	Year	$f_{\rm sky}$	1 bin	10 bins	1 bin	4 bins
DR1	Y1	6.3%	1.59	1.67	0.92	0.92
DR2	Y2	13.0%	2.28	2.40	1.32	1.33
	Y3	19.6%	2.80	2.95	1.62	1.63
DR3	Y4	25.9%	3.22	3.39	1.87	1.87
	Y5	31.6%	3.55	3.75	2.06	2.07
	Y6	36.0%	3.79	4.00	2.20	2.21

Table 4.3: Expected iSW × G signal-to-noise for the photometric and spectroscopic surveys, as a function of the observed sky fraction per year, and corresponding data release (DR). We consider the multipole range from $\ell_{\rm min} = 2$ to $\ell_{\rm max} = 500$.

In the above expression, the covariance matrices are defined as:

$$[\mathrm{Cov}]_{\ell\ell'} = \frac{\delta_{\ell\ell'}}{(2\ell+1)\,\mathrm{f}_{\rm sky}^{\rm eff}} \left[\left(C_\ell^{TT} + N_\ell^{TT}\right) \left(C_{\ell'}^{G_iG_j} + N_{\ell'}^{G_iG_j}\right) + \left(C_\ell^{TG_i} C_{\ell'}^{TG_j}\right) \right] , \tag{4.14}$$

where $\mathrm{f}_{\rm sky}^{\rm eff}$ is the *effective* fraction of the sky that is jointly mapped by the different probes. $N_\ell^{G_iG_j}$ is the shot-noise of the galaxy density contrast maps and is different from zero only when $G_i = G_j$. N_ℓ^{TT} is the power spectrum of the noise associated to the CMB temperature anisotropy map. During the *Euclid* lifespan, the CMB temperature anisotropy maps from *Planck* are going to be the main dataset available for iSW-GC cross-correlation studies. For this dataset, it is reasonable to assume that instrumental noise and foreground residuals on large angular scales are negligible [458, 488]. This will be our working hypothesis throughout the analysis.

In table 4.3 we report the expected evolution for the cumulative S/N levels of the cross-correlation, eq. (4.13), across the years. We consider both the photometric and spectroscopic surveys. Owing to the larger redshift coverage and higher number density of sources, the photometric survey is expected to deliver higher significance measurements, with the spectroscopic survey being able to provide a $\sim 2\,\sigma$ detection. For this reason, in the remainder of the analysis, we will focus exclusively on the photometric survey. For the photometric survey, the anticipated level of shot-noise does not have an impact on the S/N, which is mainly limited by the variance of CMB primary anisotropies (see also [489]). A way to increase the significance of the detection can be to use CMB polarization data to remove part of the primary anisotropies in the temperature maps, as proposed by [490]. This is expected to provide a $16-23\%$ improvement in the S/N. However, this approach is not feasible with *Planck* data, which have complex systematic effects to be modeled in polarization at large scales [458]. We will need to wait for future space missions aiming at CMB polarization, like LiteBIRD, as they will provide the needed sky coverage and instrumental systematic control.

Another way to improve the significance of the iSW detection is by using CMB lensing. Cross-correlation of the iSW with the CMB lensing allows to trace the high redshift contribution to the iSW signal. At present, this cross-correlation has been measured with *Planck* data at a $3\,\sigma$ level and has been demonstrated to be a valuable observable for cosmology [458, 491].

4.4 Impact of analysis settings on cosmological parameters

My main contribution to the *Euclid* CMBX-SWG resides in testing how different analysis settings might affect the recovery of cosmological parameters. We focus on the cosmological scenarios introduced in section 4.3.1, varying one or two parameters at a time from those listed in table 4.4 and keeping the other ΛCDM parameters fixed to the values given in table 4.1.

For all the analyses presented in this study, we assume a fiducial Gaussian likelihood [492], in which the probability of the observed TG angular power spectra, $C_\ell^{TG_i}$, as a function of the theoretical spectra $\hat{C}_\ell^{TG_i}$,[47] reads:

$$-2\ln\mathcal{L}(C_\ell^{TG_i}) = \sum_\ell \left(\hat{C}_\ell^{TG_i} - C_\ell^{TG_i}\right) \left[\mathrm{Cov}^{-1}\right]_{\ell\ell}^{ij} \left(\hat{C}_\ell^{TG_j} - C_\ell^{TG_j}\right) . \tag{4.15}$$

The expression is valid for an arbitrary number of redshift bins and summation over the bin indices i, j is understood. The covariance matrix is diagonal and given by the analytical expression in eq. (4.14), with TG, GG and TT spectra corresponding to the fiducial cosmology in table 4.1.

Using this likelihood, we derive forecasts for the posterior distributions of the cosmological parameters that are varied in each of the considered models. To quantify the impact of different analysis settings on iSW measurements, we compare the 68% confidence intervals (CIs) of the parameters derived when varying some of the analysis settings against the baseline. Results are discussed in the following and summarized in fig. 4.3, which shows the relative variations in the 68% CIs. As a reference, best-fit values and associated CIs for the baseline are given in table 4.5. It is important to emphasize that for the w_0w_aCDM model, where we varied two parameters simultaneously, we report results only for w_0. This is because of the well-known lack of constraining power on the dynamical dark energy parameter w_a [15, 17, 467]. Fig. 4.4 displays the two-dimensional posterior distribution for w_0 and w_a under the baseline analysis settings (see table 4.2).

Baseline configuration. Following refs. [17] and [15], we consider a galaxy sample with an average number density of 30 galaxies/arcmin^2 distributed over 36% of the sky, corresponding to the area covered by the final Y6 data release (see table 4.3). The sample is divided into 10 equi-populated redshift bins ranging from $z = 0.001$ to 2.5 (section 4.3.2). We adopt the galaxy distribution model in eq. (4.9) and set the parameters entering the photometric uncertainties in eq. (4.8) to their fiducial values listed in table 4.2. The galaxy bias is modeled with the step-wise function in eq. (4.10). For the baseline multipole range, we assume $\ell_{\min} = 2$ and $\ell_{\max} = 500$.

Alternative configurations. We explore the impact of different choices for:

1. Sky coverage.
2. Multipole range.
3. Photometric redshift uncertainties.
4. Number of redshift bins.
5. Photometric sample from Flagship 2.

[47] This theoretical spectrum refers to that obtained by using the fiducial parameter values for each model.

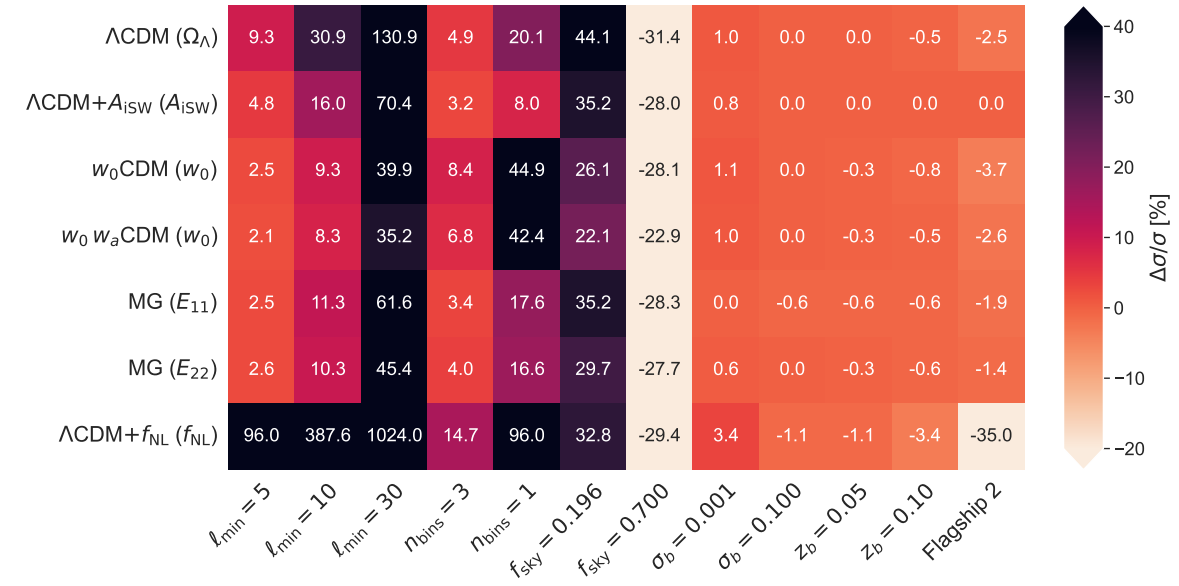

Figure 4.3: Percentage relative difference in the 68% confidence intervals (σ) on the posteriors of cosmological parameters with respect to different analysis settings of the *Euclid* photometric survey. Results are shown for the whole set of theoretical models presented in section 4.3.1. The ratios are between the displayed analysis setting and the related fiducial values in table 4.2.

Ω_Λ	$A_{\rm iSW}$	w_0	w_a	E_{11}	E_{22}	f_{NL}
0.68	1.0	-1.0	0.0	0.0	0.0	0.0

Table 4.4: Fiducial values for the cosmological parameters varied in section 4.4.

4.4.1 Varying the observed fraction of the sky

For iSW cross-correlation studies, having extensive sky coverage is essential. Reducing the survey's sky coverage, $f_{\rm sky}$, increases uncertainties in all cosmological parameters. Fig. 4.5 demonstrates this for the iSW amplitude $A_{\rm iSW}$ and the dark energy equation of state w_0. Our baseline assumes a coverage of 36%, but we also consider $f_{\rm sky} \sim 0.2$ (corresponding to 3 years of *Euclid* observations) and $f_{\rm sky} \sim 0.7$ (a hypothetical scenario using the full foreground-cleaned CMB map of *Planck*). In this analysis, we account for reduced sky coverage via the $f_{\rm sky}$ correction in the covariance matrix, eq. (4.14), neglecting mask-related complications. Fig. 4.3 shows the percentage differences in the 68% CIs relative to the baseline.

4.4.2 Varying the minimum multipole

As expected, raising the minimum multipole from $\ell_{\rm min} = 2$ to 5, 10, or 30 significantly increases the uncertainties in all cosmological parameters, since most of the iSW signal is concentrated at large angular scales. Fig. 4.6 demonstrates this for the iSW amplitude $A_{\rm iSW}$ and the dark energy equation of state w_0. The percentage differences in the 68% CIs relative to the baseline

ΛCDM (Ω_Λ)	ΛCDM+$A_{\rm iSW}$ ($A_{\rm iSW}$)	ω_0CDM (ω_0)	$\omega_0\,\omega_a$CDM (ω_0)	MG (E_{11})	MG (E_{22})	ΛCDM+$f_{\rm NL}$ ($f_{\rm NL}$)
$0.68^{+0.07}_{-0.11}$	1.00 ± 0.25	$-1.00^{+0.15}_{-0.20}$	$-1.00^{+0.16}_{-0.23}$	0.00 ± 0.07	0.00 ± 0.16	$0.0^{+17.6}_{-17.8}$

Table 4.5: Bestfit values and 68% confidence levels for cosmological parameters with the baseline analysis settings.

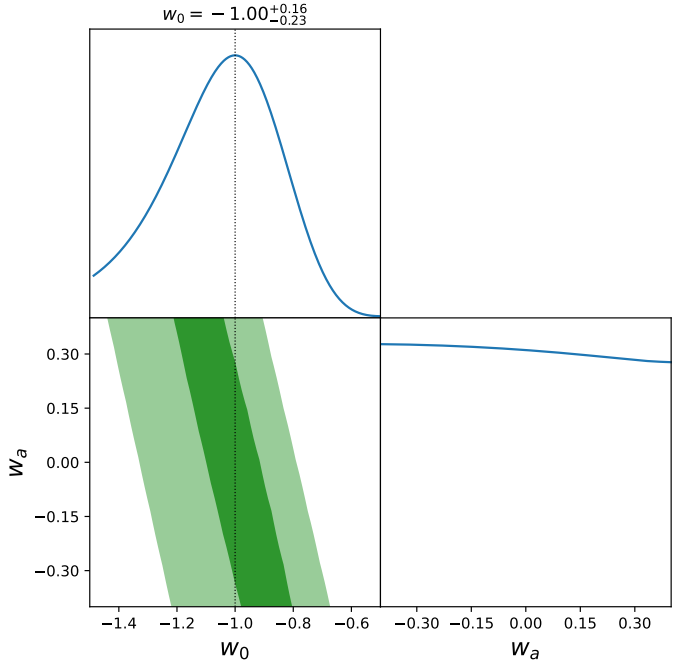

Figure 4.4: 2D posterior distribution for $w_0 w_a$CDM. The result refers to the baseline analysis settings of table 4.2.

$\ell_{\rm min} = 2$ are shown for all parameters in the first three columns of fig. 4.3. The maximum multipole is fixed at $\ell_{\rm max} = 500$. The increased uncertainties are particularly pronounced for the $f_{\rm NL}$ parameter, where most of the constraining power comes from $\ell \lesssim 10$.

4.4.3 Varying the photometric uncertainty parameters

While maintaining the baseline galaxy distribution model $n(z)$ with 10 equi-populated redshift bins, we examined the effect of varying parameters in the photometric uncertainty model of eq.(4.8). Varying the photometric error σ_b or adding an additive bias z_b has little effect on the 68% CIs of all cosmological parameters. The percentage differences in the 68% CIs for these cases are shown in Fig.4.3, relative to the baseline in table 4.2. Differences remain within 1% for most scenarios, peaking at $\sim 3\%$ for $f_{\rm NL}$. Additionally, we found that changing the fraction of catastrophic outliers, $f_{\rm out}$, does not significantly affect the uncertainties, and thus it is omitted from the figure.

4.4.4 Varying the number of redshift bins

We tested the impact of varying the number of equi-populated redshift bins in eq.(4.7), while keeping the models for the galaxy distribution $n(z)$ and photometric uncertainty $p(z_m|z)$ fixed. We specifically tested the cases of $n_{\rm bins} = 3$ and $n_{\rm bins} = 1$, where the latter corresponds to a non-tomographic analysis of the entire sample. The galaxy bias is described using a step-wise function for all cases, following eq.(4.10), adjusting the bin edges accordingly. For the single-bin case, the bias is assumed constant across the redshift range. Performing a tomographic analysis increases the constraining power for all cosmological parameters, as shown in fig.4.3. The largest improvements are observed for w_0 (see also fig.4.7) and f_{NL}, as these parameters are expected to have a stronger dependence on redshift. Fig. 4.7 illustrates the result for the iSW amplitude $A_{\rm iSW}$ and w_0.

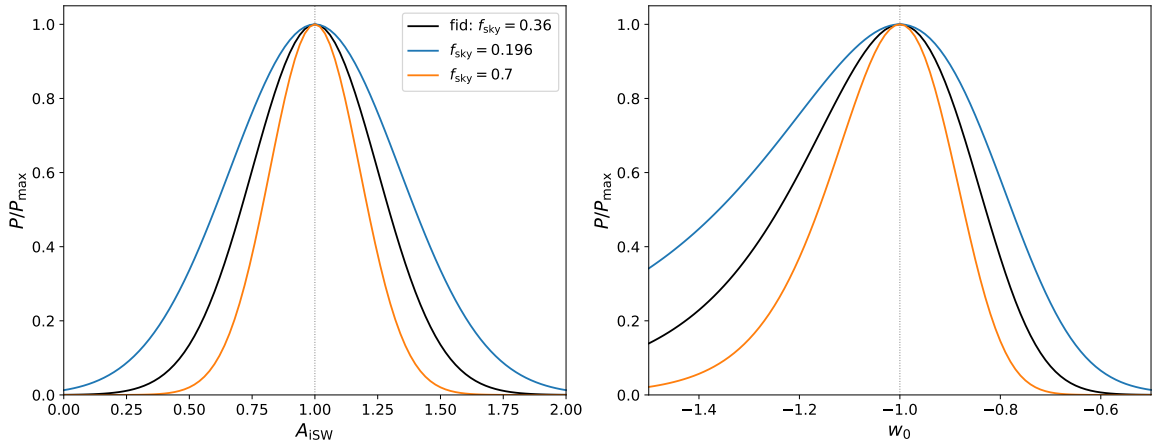

Figure 4.5: Posterior distribution of the iSW amplitude parameter $A_{\rm iSW}$ (*Left*) and the dark energy equation of state parameter w_0 (*Right*), varying the sky coverage $f_{\rm sky}$.

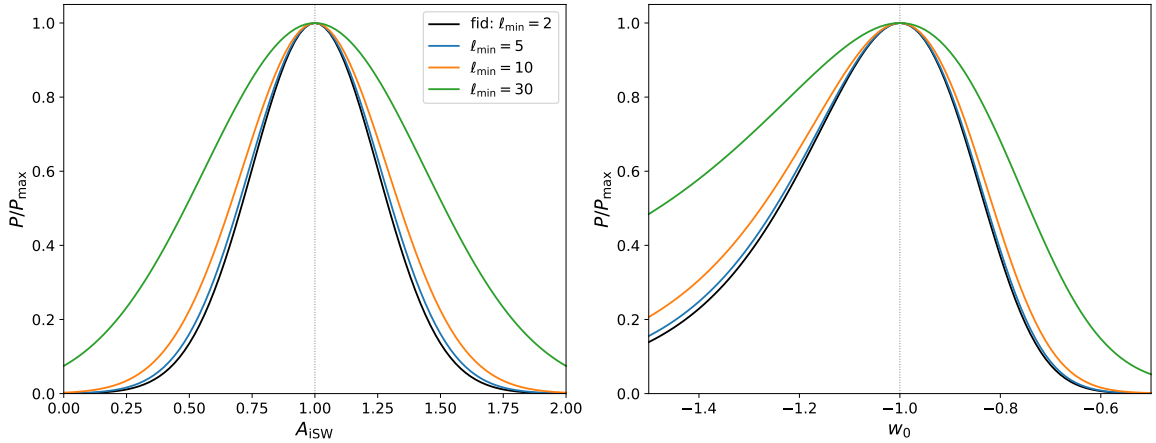

Figure 4.6: Posterior distribution of the iSW amplitude parameter $A_{\rm iSW}$ (*Left*) and the dark energy equation of state parameter w_0 (*Right*), varying the minimum multipole in the analysis $\ell_{\rm min}$.

4.4.5 Testing the photometric sample from Flagship 2

We repeated the cosmological parameter analysis using the photometric sample specifications derived from the Flagship 2 simulation (see sec. 4.3.2). As seen in fig. 4.3, the constraints on $A_{\rm iSW}$ remain unchanged compared to the baseline. For the other parameters, we observe a slight improvement in constraining power, generally by a few percent, except for f_{NL}, where the improvement reaches approximately 35%. This result is mainly driven by the significantly higher galaxy bias at high redshift compared to the baseline (see fig. 4.2). Fig. 4.7 displays our findings for the iSW amplitude $A_{\rm iSW}$ and the dark energy equation of state w_0.

Additionally, we evaluated the impact of analytical marginalization over the galaxy bias. Following the method used for CMB calibration in ref. [493], an extra term is added to the covariance matrix, eq. (3.39), equal to $\sigma_{b_i}^2\, C_\ell^{TG_i}(C_\ell^{TG_i})^T$, where σ_{b_i} are the widths of the Gaussian priors. For the baseline tomographic case, we used $\sigma_{b_i} = [0.01, 0.01, 0.01, 0.01, 0.01, 0.01, 0.02, 0.02, 0.02, 0.02]$. The percentage relative difference in the 68% CIs of $A_{\rm iSW}$, assuming a ΛCDM + $A_{\rm iSW}$ model, is about 0.01%. Increasing the σ_{b_i} values by an order of magnitude results in a difference of around 1%. In the non-tomographic case with $\sigma_b = 0.01$, we found a difference of less than 0.01%.

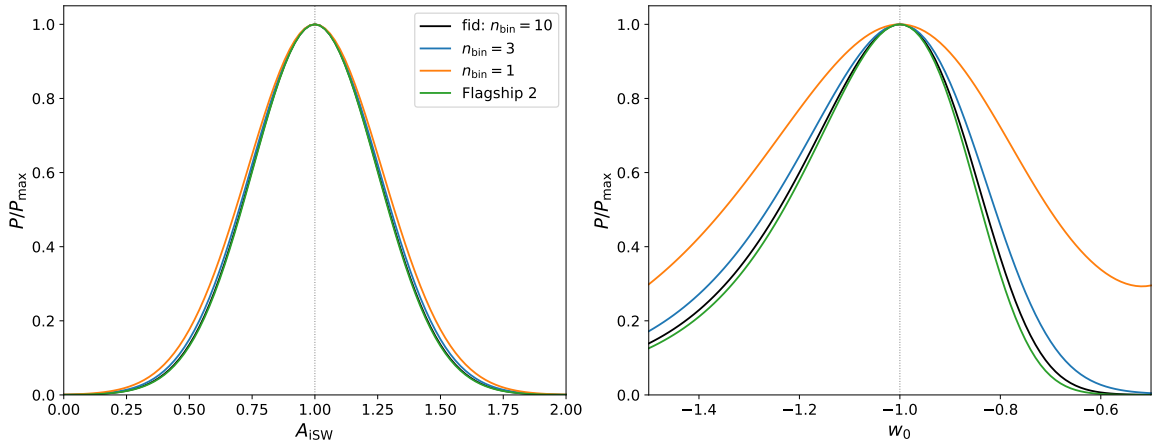

Figure 4.7: Posterior distribution of the iSW amplitude parameter $A_{\rm iSW}$ (*Left*) and the dark energy equation of state parameter w_0 (*Right*), varying the number of redshift bins in the analysis $n_{\rm bin}$. The *Euclid* Flagship 2 configuration with 13 equi-populated bins is also displayed.

4.4.6 Impact of wrong fiducials in the covariance matrix

In this section, we evaluate how inaccuracies in the covariance approximation affect parameter estimation. In all previous tests, we used the same fiducial model to compute both the covariance matrix and the theoretical spectra in eq. (4.15). To test the impact of using an incorrect fiducial cosmology, we calculated the covariance matrix using a "wrong" fiducial model, which significantly differs from the one used for $\hat{C}_\ell^{TG_i}$. The "wrong" model was deliberately chosen by shifting some cosmological parameters from table 4.1. We performed tests on two models: ΛCDM with a shifted Ω_Λ, and w_0CDM with a shifted w_0. The parameter shifts were set to three times the 1σ uncertainties from *Planck* 2018 [20]: $\Delta\Omega_\Lambda = -0.0066$ and $\Delta w_0 = 0.0105$.[48]

We derived the posterior distributions for the aforementioned cosmological parameters both with and without tomography. Our findings show no significant effect on the best-fit values of w_0 and Ω_Λ. The CI for w_0 remains unchanged when using the "wrong" covariance matrix. For Ω_Λ, we observe a small variation in the CI, with a 4% difference in the non-tomographic case and a 6% difference in the tomographic case.

4.5 Prospects for DR1

As we approach the Data Release 1 (DR1) from the *Euclid* mission, the synergy between galaxy surveys and the integrated Sachs-Wolfe effect is set to unlock new frontiers in cosmology. The meticulous efforts of the CMBX-SWG to establish a robust framework for analyzing the cross-correlation between *Euclid*'s galaxy data and CMB late-iSW signals promise to yield transformative insights. The arrival of real *Euclid* data represents a critical juncture for testing cosmological theories, particularly regarding the enigmatic nature of dark energy and its influence on cosmic structures.

The innovative approach of cross-correlating late-iSW with *Euclid*'s high-precision galaxy clustering data enhances our understanding of gravitational potentials shaped by dark energy. This method provides a more nuanced perspective on cosmic expansion and allows for more precise measurements of cosmological parameters. Given the historical context in which cross-correlation analyses with existing datasets led to significant discoveries—such as the *Planck* satellite's detection of dark energy in the form of a cosmological constant—*Euclid*'s data is expected to push these boundaries even further.

[48] As the distribution for w_0 is asymmetric, we take the mean value of the left and right uncertainties.

With its extensive coverage and precise photometric measurements, *Euclid* facilitates a deeper investigation into the cosmic web, which is crucial for disentangling dark energy effects from other cosmic influences. The anticipated high signal-to-noise ratio will greatly enhance the statistical power of our analyses, potentially leading to stronger constraints on models of dark energy, including those incorporating modifications to gravity.

Furthermore, the CMBX-SWG's development of a comprehensive analysis pipeline will ensure that integrating *Euclid* data into existing cosmological frameworks is both efficient and scientifically rigorous. By addressing potential systematic uncertainties and optimizing analysis settings, we can maximize the reliability of the constraints derived from cross-correlation studies.

In summary, the forthcoming DR1 from Euclid represents a significant opportunity to advance our understanding of fundamental cosmological questions. The groundwork laid by the CMBX-SWG paves the way for innovative analyses that leverage the unique strengths of both CMB and galaxy survey data, fostering a deeper comprehension of the universe's structure and the role of dark energy in its evolution. As we prepare for this pivotal release, the potential for groundbreaking discoveries looms large, setting the stage for a new era of cosmological exploration.

Chapter 5

Overview and conclusions

Over the past decades, our understanding of the Universe has been revolutionized. In the era of precision cosmology, a wealth of cosmological observations has allowed for the establishment of the concordance ΛCDM model, which describes the evolution of our Universe from its early stages until today in terms of just six parameters. At the same time, the Standard Model of particle physics, which describes our Universe at the subnuclear level, has been tested with impressive precision in a number of laboratory and collider experiments. Nevertheless, numerous open issues remain, such as the nature of dark matter and dark energy or the physics underlying inflation. Moreover, the stunning level of accuracy that cosmological observations have reached allows us to test with increasing precision possible departures from the standard models of cosmology and particle physics. This is the topic of this Thesis, where we have used the latest measurements of the cosmic microwave background and the large-scale structure of the Universe to constrain fundamental physics scenarios that go beyond the two aforementioned standard models.

Chapter 2 presented the Halo-Void model, an innovative framework for probing particle dark matter, which I developed. In this approach, we cross-correlated unresolved sky radiation with gravitational tracers located in the universe's most desolate areas—cosmic voids. We examined cosmic shear and galaxy distribution as gravitational tracers, investigating the unresolved gamma-ray background that could conceal signals from dark matter annihilation or decay. Our analysis revealed that in cosmic voids, the cross-correlation signal generated by dark matter decay could significantly surpass that of astrophysical sources, particularly for decay lifetimes up to 2×10^{30}s. This stark contrast to halos, where astrophysical signals dominate, positioning voids as a promising "background-free" option for dark matter searches. While our findings suggested that current observational capabilities with the *Fermi*-LAT telescope were insufficient, the potential for next-generation detectors—specifically those with improved angular resolution and exposure—could enable the detection of these signals. Specifically, we enhanced the existing constraints on the dark matter decay lifetime for masses ranging from $m_{\rm DM} \sim 25$ to 900 GeV. Furthermore, our approach highlighted the exciting prospect of extending the analysis to unresolved radiation across other parts of the electromagnetic spectrum, particularly for axions. This multifaceted strategy could unlock new insights into dark matter properties and interactions, reinforcing the potential of cosmic voids as a critical tool in future dark matter exploration.

Chapter 3 shifted focus to the intriguing realm of axion-like particles and cosmic birefringence. We (I am the main contributor and corresponding author to the work) introduced, for the first time, the cross-correlation between anisotropic cosmic birefringence and galaxy number counts as a means to probe axion-like physics. Our comprehensive analysis, utilizing a modified Boltzmann code, uncovered significant variations in the correlation's amplitude across the axion parameter space, especially at large and intermediate angular scales. We concentrated on ultralight axion-like particles with masses in the range from $m_\phi = 10^{-33}$ to 10^{-28} eV. We determined that the cross-correlation could be effectively measured with upcoming surveys, particularly in

conjunction with the anticipated *Euclid* data. Notably, our work set unprecedented upper bounds on the axion-photon coupling by combining birefringence data and galaxy maps from *Planck* PR4 and Quaia, reaching values as low as $10^{-15}\,\mathrm{GeV}^{-1}$. This remarkable achievement not only enhanced our understanding of the fundamental nature of dark matter but also positioned cosmic birefringence as a vital indicator of underlying parity-violating physics. With the release of new polarization data and continued advancements in observational techniques, this framework offers a powerful tool for unraveling the mysteries of the dark sector and its role in cosmic evolution.

Chapter 4 examined the preparations for the Data Release 1 from the *Euclid* mission, which promised to revolutionize our understanding of cosmology. Our efforts within the CMBX-SWG, which I am a full member of, established a robust framework for analyzing the cross-correlation between *Euclid*'s galaxy clustering data and the late integrated Sachs-Wolfe effect. After outlining the anticipated survey capabilities, we demonstrated how variations in analysis settings influence the ability to constrain various cosmological parameters. This innovative approach enhances our understanding of gravitational potentials shaped by dark energy, allowing for more precise measurements of cosmological parameters. The groundwork laid by our team ensures that the integration of *Euclid* data into existing cosmological frameworks would be both efficient and scientifically rigorous. As we anticipate the arrival of real *Euclid* data, we stand on the cusp of significant discoveries that would deepen our comprehension of dark energy's role in cosmic evolution and potentially illuminate the enigmatic nature of the universe itself.

As we stand on the threshold of a new era in cosmology, we are poised to embark on a thrilling journey fueled by an explosion of data that promises to reshape our understanding of the universe. This thesis has delved into the power of cross-correlating cosmological probes across various frameworks, revealing rich avenues for exploration and insight. With advanced observational techniques and the impending release of groundbreaking data, we are set to illuminate some of the universe's most perplexing mysteries.

Despite the myriad questions that continue to linger in the cosmic ether, the increasing precision of future cosmological surveys offers us an unprecedented opportunity to tackle these challenges head-on. As we refine our analytical methods and expand our observational capabilities, we inch closer to answering fundamental questions about the nature of dark matter, dark energy, and the intricate web of cosmic structures. The interconnectedness of different cosmological phenomena underscores the importance of a holistic approach, emphasizing that by studying the universe from multiple angles, we can uncover deeper truths that single probes might miss.

In this grand quest for knowledge, we may finally unlock the secrets of the cosmos—like what it's really made of and why it seems to revel in its mysteries! As we prepare for the next wave of data, it feels as though the universe is ready to share its tales, albeit with fewer plot twists than your average cosmic drama. With this impending influx of knowledge, we can only anticipate a cascade of revelations that will propel our understanding of the universe to unprecedented heights.

So, as we buckle up for this exciting ride, let's embrace the unknown with open arms and a sense of humor. After all, if the universe can explode into existence with a Big Bang, we can certainly look forward to a similarly explosive journey of discovery ahead! Who knows what intriguing discoveries await us? Perhaps we'll uncover not just the building blocks of reality, but also the universe's best-kept secrets, leaving us with more questions than answers—just the way it likes it! Whatever the outcome, one thing is certain: the adventure is just beginning, and the cosmos has a lot more in store for us.

Appendix A

Additional material for cross-correlations in cosmic voids

A.1 Terms of the 3D power spectrum and variations on the void profile

When computing the 3D power spectrum within the HVM, three additional terms, with respect to the HM, arise: the correlation between points within the same void (1Void term), within two different voids (2Void term) and between points belonging to a halo and a void, respectively (Halo-Void term). In Figs. A.1 and A.2 we show the 3D power spectrum of the cross-correlation between gamma-ray emitters (decaying/annihilating DM, BL Lacs, FSRQs, mAGN and SFGs) and either cosmic shear or the 2MASS galaxy catalog, respectively (calculated at $z = 0.5$). For each panel of the figures, we report the contributions from the terms of Eqs. (2.51)-(2.55). In general, the linear power on large scales is well recovered and the transition between linear and non-linear scales (around $k \sim 1\ h\,\mathrm{Mpc}^{-1}$) is clearly visible in all cases.

Note how the 1Halo and 1Void terms in the cross-correlation with galaxies (Fig. A.2) act as a shot noise, since the integrand of Eqs. (2.51) and (2.53) are fairly constant with the scale k, for the relevant source functions.

The 3D power spectrum depends on the considered structure's profile for all cross-correlations used in this work (see Sec. 2.3). However, while the halo density profile has been studied for a long time and the NFW profile is typically considered the standard choice, the void density profile is debated in the literature and strongly depends on the used void finder (as discussed in Sec. 2.2.1). Here, we considered both voids with a radius-dependent central density, showing compensation walls, and voids with empty centers and no compensation walls. The former are well reproduced by the Hamaus-Sutter-Wandelt profile [277] of Eq. (2.32) and the latter by the profile proposed in Voivodic et al. [28], shown in Eq. (2.33). Despite having different properties, Fig. A.3 shows how the choice of the void profile leads to sub-percent variations of the 3D power spectrum, for all cross-correlations.

A.2 Parameter correlation in the Fisher analysis

In Sec. 2.7 we showed the forecasted bound on the DM decay lifetime, computed through a Fisher matrix analysis with seven parameters: one normalization for the DM signal, two normalizations for the astrophysical signal and the four spectral indexes of unresolved astrophysical sources, accounting for energy-dependent variations of the C_ℓ's. The Fisher matrix in Eq. (2.103) can be seen as the inverse covariance of the model's free parameters. Thus, it can be used to perform a multivariate study on the degeneration of the parameter. In particular, we can consider the

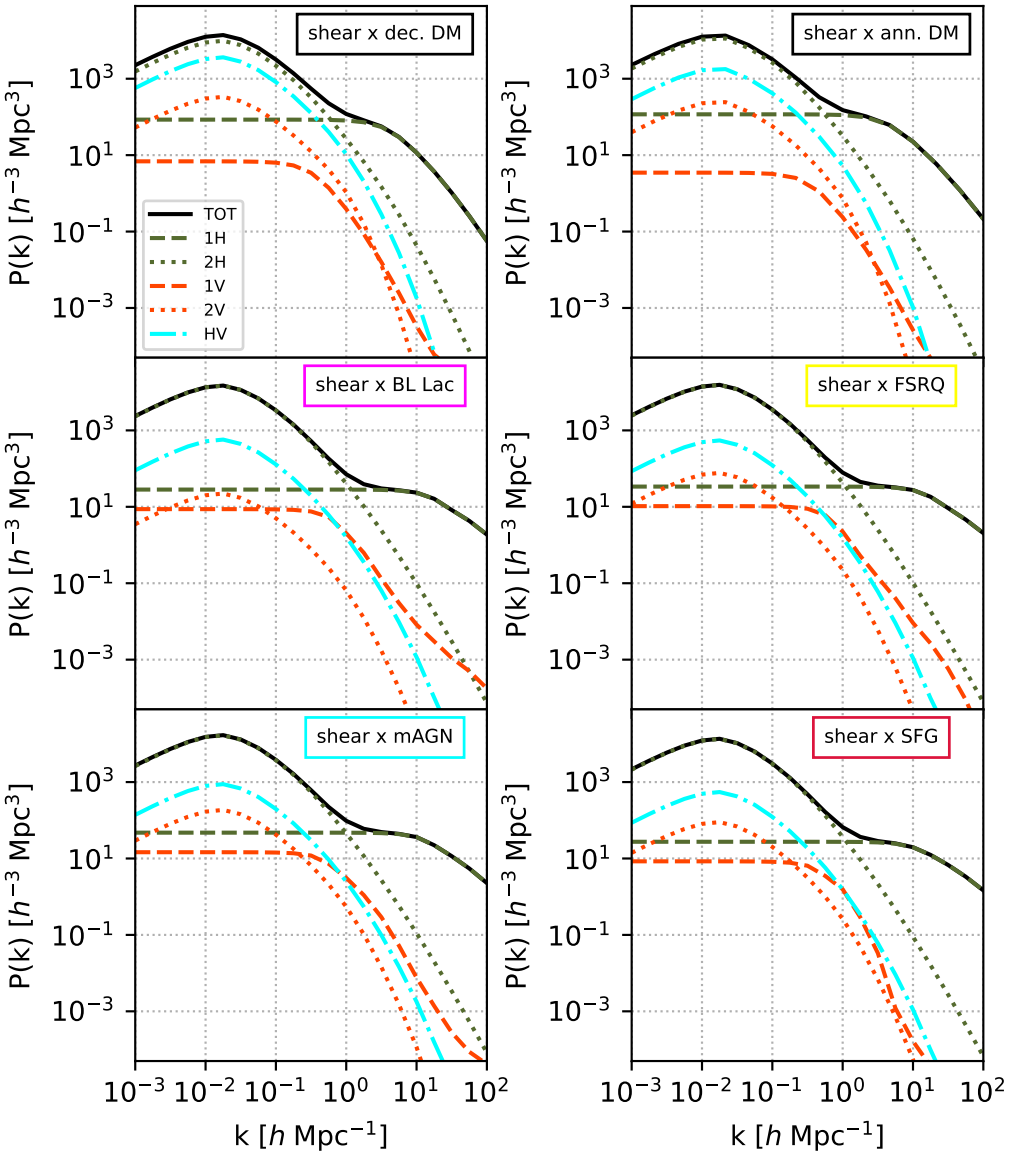

Figure A.1: 3D power spectrum of the cross-correlation between cosmic shear and gamma-ray emitters (decaying/annihilating DM and unresolved astrophysical sources), at $z = 0.5$, divided into the contributions from a single halo (1H), two halos (2H), a single void (1V), two voids (2V) and an halo and a void (HV).

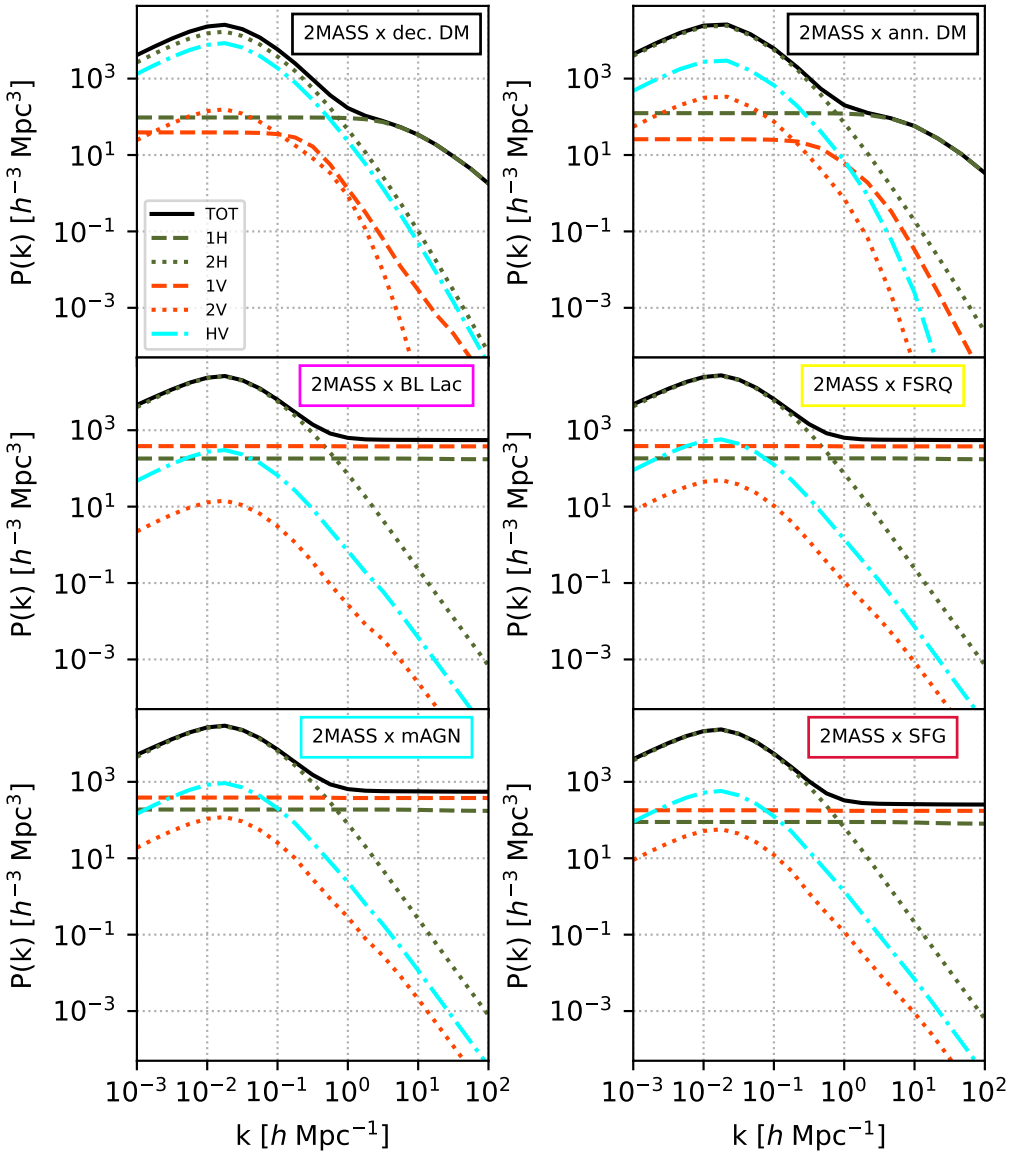

Figure A.2: The same as Fig. A.1 for the cross-correlation of gamma-ray emitters with the 2MASS galaxy catalog.

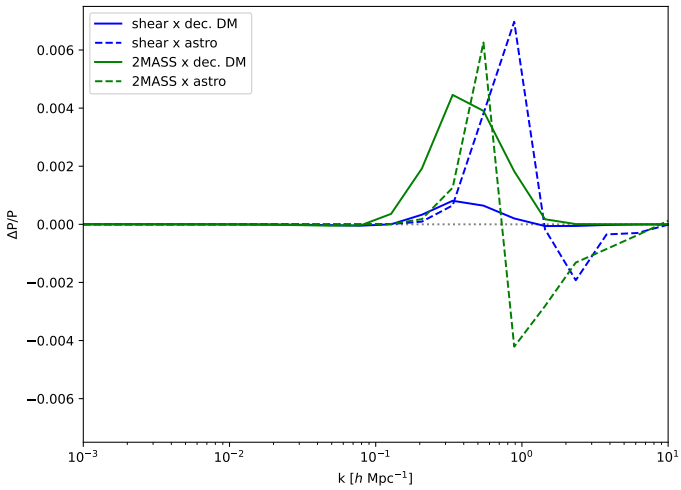

Figure A.3: Relative variations on the 3D power spectrum upon using the HSW profile [277] or the tanh-profile [28]. We show them for the cross-correlation of the 2MASS galaxy catalog (green) or the cosmic shear (blue) with the decaying dark matter signal (solid) and the total unresolved astrophysical signal (dashed). Differences are confined well below the few per mille level.

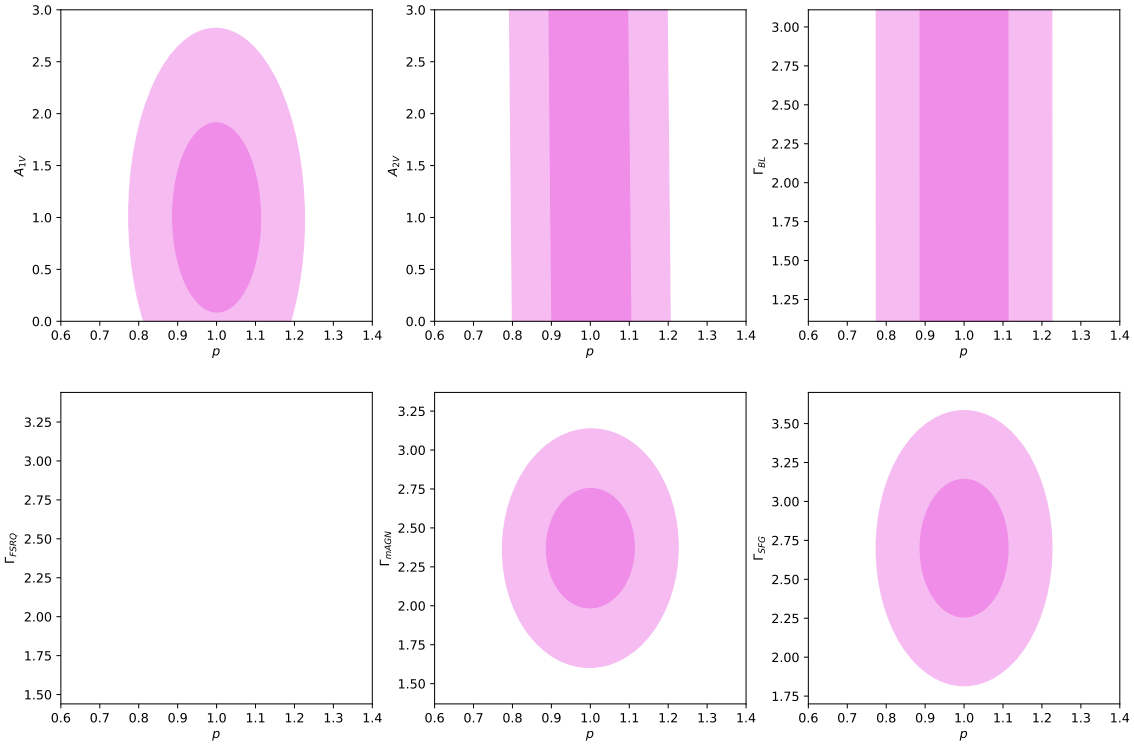

Figure A.4: Bivariate correlations between the DM free parameter of the Fisher matrix analysis p and the six non-DM parameters. All are referred to a WIMP with $m_{\rm DM} = 100$ GeV.

six submatrixes related to the correlations between the DM parameter p and each of the non-DM parameters $A_{1\mathrm{V}}$, $A_{2\mathrm{V}}$, Γ_{BL}, Γ_{FSRQ}, Γ_{mAGN} and Γ_{SFG}. In Fig. A.4 we show the bivariate correlations for a WIMP with a mass of 100 GeV. In general, no strong correlation is present and the non-DM parameters have little impact on the constraining power of p (and consequently on that of the DM decay lifetime).

Appendix B

Additional material for cross-correlating cosmic birefringence

B.1 Impact of binning on data analysis

As discussed in section 3.6.3, the covariance matrix in eq. (3.39) may exhibit excessive noise in its off-diagonal elements due to the limited number of realizations used for estimation, potentially leading to bias in the inverse covariance matrix. Increasing the level of binning helps mitigate this bias by reducing strong or anomalous correlations in off-diagonal terms, though at the cost of some information loss, which may warrant alternative strategies. Hartlap et al. [448] provide a first-order correction for this bias through a constant (Hartlap) factor, dependent on the length of the data vector p and the number of simulations n used to estimate the covariance:

$$(\hat{\mathsf{C}}^{-1})^{\alpha g}_{\ell\ell'} = \frac{n-p-2}{n-1}(\hat{\mathsf{C}}^{\alpha g}_{\ell\ell'})^{-1} \quad \text{for } p < n-2\,. \tag{B.1}$$

In this context, the inverse matrix of eq. (3.39) tends to be increasingly overestimated as the length of the data vector approaches the number of available simulations. Notably, when $p \ll n$, the correction factor in eq. (B.1) is close to unity. In cosmology, this often results in an artificially heightened constraining power for parameter estimation. Applying the Hartlap correction factor addresses this by broadening posterior distributions and thereby increasing confidence intervals on parameter estimates. Sellentin and Heavens [449] suggest that this adjustment introduces heavy tails in the posterior, and propose a more precise method that involves marginalizing over the true covariance matrix, conditioned on its estimate, thus relaxing the Gaussian assumption in the likelihood. This approach effectively results in a t-distribution, where both the mean and variance are treated as random variables. The modified likelihood thus becomes

$$-2\ln\mathcal{L} = n\ln\left(1+\frac{\chi^2}{n-1}\right), \tag{B.2}$$

where χ^2 is the standard Gaussian likelihood.

We evaluated the effects of using a binning scheme and applying each correction on our results. The cross-correlation signal shown in fig.3.24 remains consistent with zero regardless of the binning choice, and neither the Hartlap factor nor the modified likelihood affects goodness-of-fit tests.[49] The left panel of fig. B.1 shows the PTE of the null-hypothesis as a function of

[49]This occurs because the data's χ^2 shifts along with the underlying distribution, resulting in an unchanged

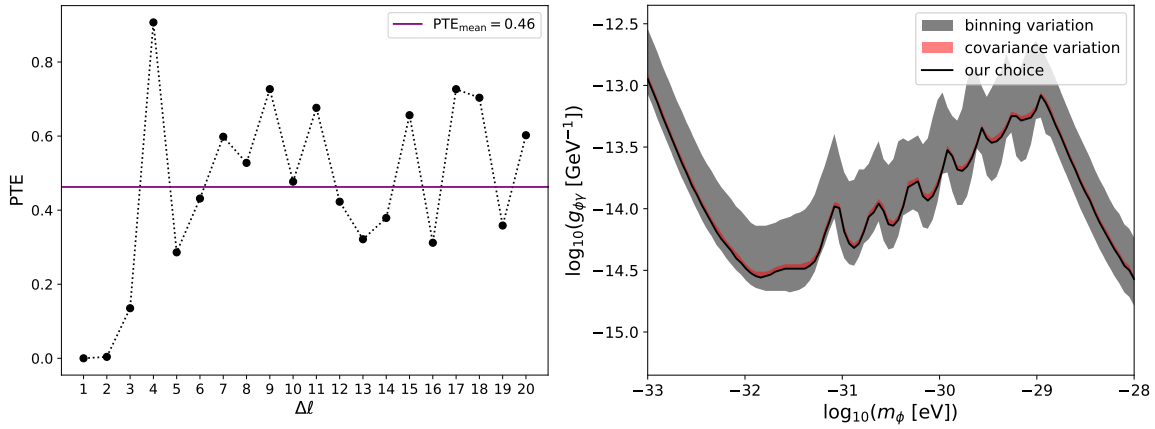

Figure B.1: (*Left*): value of the PTE as a function of binning bandwidth $\Delta\ell$. Each value corresponds to the compatibility of the measured cross-correlation with zero. (*Right*): maximal variation of the axion-photon coupling, as a function of mass, upon variations of the binning bandwidth (gray) or the covariance estimation and consequent likelihood choice (red). The black line refers to our baseline: no correction applied on the covariance and and a mixed binning (10 bins with $\Delta\ell = 1$, 10 with $\Delta\ell = 2$, 10 with $\Delta\ell = 5$ and $\Delta\ell = 10$ afterwards).

binning bandwidth, $\Delta\ell$. Only the unbinned and 2 multipoles per bin cases produce a value below 5%, due to significant off-diagonal correlations in the covariance matrix, which are mitigated with increased binning bandwidth. In fig. B.2, we also present the χ^2 distribution from 400 realizations, with the data value (marked as a vertical line) well within the distribution for all but the first two cases.

For parameter estimation, the achievable upper bound on the axion-photon coupling is modestly influenced by the choice of binning scheme. More aggressive binning results in less stringent bounds due to information loss on large scales, where the theoretical signal is expected to be strongest [3]. The maximum observed variation in the best $g_{\phi\gamma}$-m_ϕ bound of fig. 3.33 reaches about half an order of magnitude. This variation diminishes to a few percent as the binning bandwidth exceeds $\Delta\ell \sim 5$, likely indicating that no further large-scale information is being lost. This outcome is shown in the right panel of fig. B.1 as a gray-shaded band, overlaying the black line that represents our selected binning scheme as discussed in section 3.7. The red-shaded region shows the maximal variation when applying either the Hartlap correction or the Sellentin and Heavens modified likelihood, with the former reducing constraining power by approximately 10%, and the latter by about 1%.

PTE.

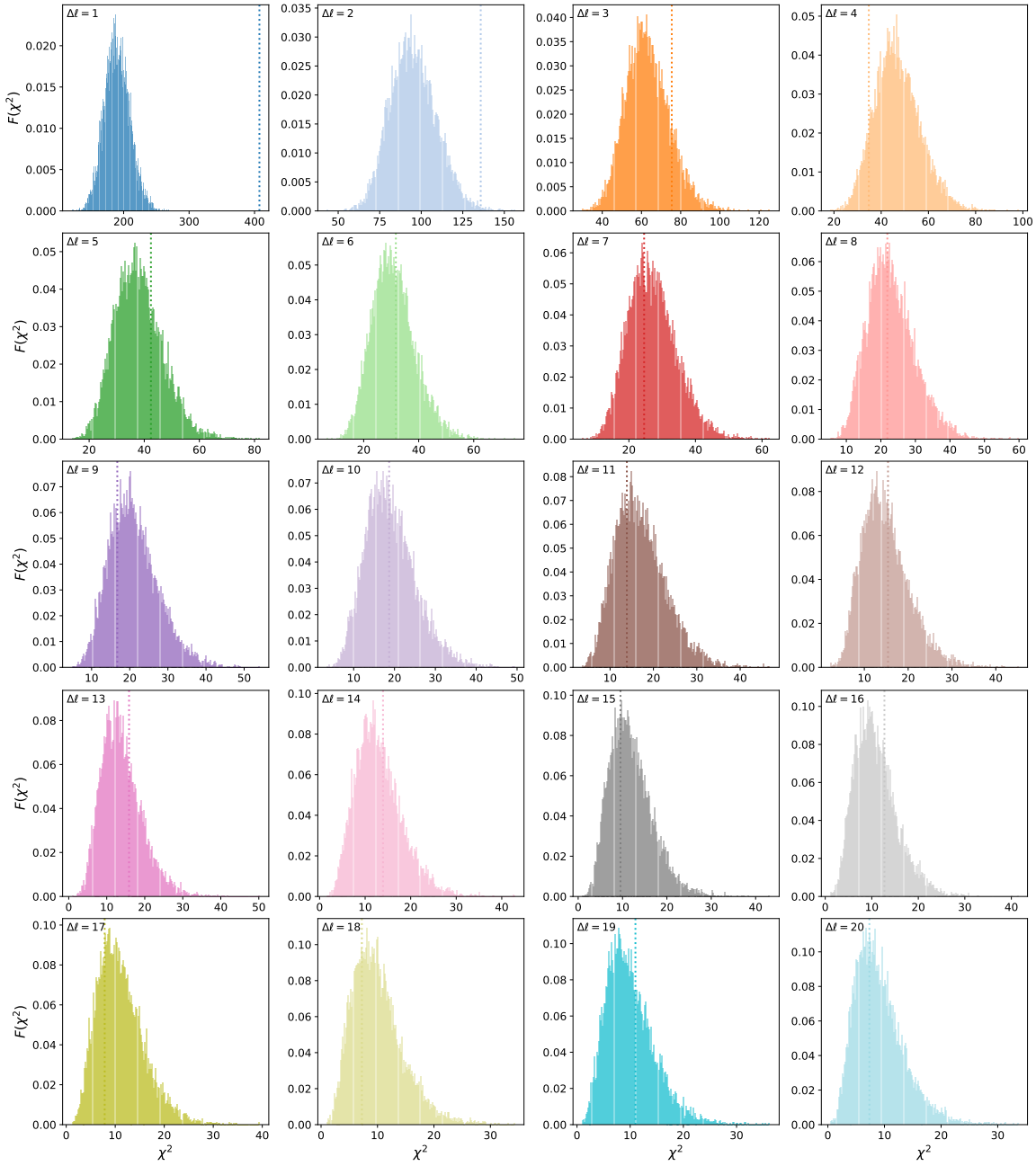

Figure B.2: Chi-squared distributions for different binning bandwidths $\Delta\ell$, obtained from the 400 realizations. The vertical dotted lines indicates the χ^2 of data.

Bibliography

[1] S. Arcari, E. Pinetti and N. Fornengo, *Got plenty of nothing: cosmic voids as a probe of particle dark matter*, *JCAP* **11** (2022) 011 [2205.03360].

[2] Euclid collaboration, *Euclid. I. Overview of the Euclid mission*, 2405.13491.

[3] S. Arcari, N. Bartolo, A. Greco, A. Gruppuso, M. Lattanzi and P. Natoli, *Conversations in the dark: cross-correlating birefringence and LSS to constrain axions*, *JCAP* **10** (2024) 101 [2407.02144].

[4] S. Arcari, N. Bartolo, G. Fabbian, A. Greco, A. Gruppuso, M. Lattanzi et al., *Stairway to Axions: the cross-correlation of birefringence and galaxies from NPIPE and Quaia*, **in prep** (2025) .

[5] Euclid collaboration, *Euclid Preparation: Estimators of the ISW-GC cross-correlation*, **in prep** (2025) .

[6] Euclid collaboration, *Euclid Preparation: Cosmology Likelihood for Observables in Euclid (CLOE): Code implementation*, **in prep** (2025) .

[7] D. Sidious et al., *Echoes from a long time ago: Chewbacca inflation*, 2403.20143.

[8] S. Weinberg, *Cosmology*, Oxford University Press (2008).

[9] P.J.E. Peebles, *Principles of Physical Cosmology*, Princeton University Press (9, 2020).

[10] P. Coles and F. Lucchin, *Cosmology: The Origin and evolution of cosmic structure*, John Wiley & Sons (1995).

[11] S. Dodelson, *Modern Cosmology*, Academic Press, Amsterdam (2003).

[12] A.R. Liddle and D.H. Lyth, *Cosmological inflation and large scale structure*, Cambridge University Press (2000), 10.1017/CBO9781139175180.

[13] Euclid collaboration, *Euclid preparation - I. The Euclid Wide Survey*, *Astron. Astrophys.* **662** (2022) A112 [2108.01201].

[14] Euclid Theory Working Group collaboration, *Cosmology and fundamental physics with the Euclid satellite*, *Living Rev. Rel.* **16** (2013) 6 [1206.1225].

[15] Euclid collaboration, *Euclid preparation. XV. Forecasting cosmological constraints for the Euclid and CMB joint analysis*, *Astron. Astrophys.* **657** (2022) A91 [2106.08346].

[16] Euclid collaboration, *Euclid. V. The Flagship galaxy mock catalogue: a comprehensive simulation for the Euclid mission*, 2405.13495.

[17] Euclid collaboration, *Euclid preparation: VII. Forecast validation for Euclid cosmological probes*, *Astron. Astrophys.* **642** (2020) A191 [1910.09273].

[18] Planck collaboration, *Planck 2013 results. XVI. Cosmological parameters*, *Astron. Astrophys.* **571** (2014) A16 [1303.5076].

[19] Planck collaboration, *Planck 2015 results. XIII. Cosmological parameters*, *Astron. Astrophys.* **594** (2016) A13 [1502.01589].

[20] Planck collaboration, *Planck 2018 results. I. Overview and the cosmological legacy of Planck*, *Astron. Astrophys.* **641** (2020) A1 [1807.06205].

[21] Planck collaboration, *Planck 2018 results. VI. Cosmological parameters*, *Astron. Astrophys.* **641** (2020) A6 [1807.06209].

[22] LiteBIRD collaboration, *Probing Cosmic Inflation with the LiteBIRD Cosmic Microwave Background Polarization Survey*, *PTEP* **2023** (2023) 042F01 [2202.02773].

[23] Simons Observatory collaboration, *The Simons Observatory: Science goals and forecasts*, *JCAP* **02** (2019) 056 [1808.07445].

[24] CMB-S4 collaboration, *CMB-S4: Forecasting Constraints on Primordial Gravitational Waves*, *Astrophys. J.* **926** (2022) 54 [2008.12619].

[25] BOSS collaboration, *The clustering of galaxies in the completed SDSS-III Baryon Oscillation Spectroscopic Survey: cosmological analysis of the DR12 galaxy sample*, *Mon. Not. Roy. Astron. Soc.* **470** (2017) 2617 [1607.03155].

[26] F. Beutler, C. Blake, M. Colless, D.H. Jones, L. Staveley-Smith, L. Campbell et al., *The 6dF Galaxy Survey: Baryon Acoustic Oscillations and the Local Hubble Constant*, *Mon. Not. Roy. Astron. Soc.* **416** (2011) 3017 [1106.3366].

[27] A.J. Ross, L. Samushia, C. Howlett, W.J. Percival, A. Burden and M. Manera, *The clustering of the SDSS DR7 main Galaxy sample – I. A 4 per cent distance measure at* $z = 0.15$, *Mon. Not. Roy. Astron. Soc.* **449** (2015) 835 [1409.3242].

[28] R. Voivodic, H. Rubira and M. Lima, *The Halo Void (Dust) Model of Large Scale Structure*, *JCAP* **10** (2020) 033 [2003.06411].

[29] Planck collaboration, *Planck intermediate results. LVII. Joint Planck LFI and HFI data processing*, *Astron. Astrophys.* **643** (2020) A42 [2007.04997].

[30] K. Storey-Fisher, D.W. Hogg, H.-W. Rix, A.-C. Eilers, G. Fabbian, M.R. Blanton et al., *Quaia, the Gaia-unWISE Quasar Catalog: An All-sky Spectroscopic Quasar Sample*, *Astrophys. J.* **964** (2024) 69 [2306.17749].

[31] M. Planck, *The Theory of Heat Radiation*, P. Blakiston's Son & Co (1914).

[32] J.C. Mather et al., *Measurement of the Cosmic Microwave Background spectrum by the COBE FIRAS instrument*, *Astrophys. J.* **420** (1994) 439.

[33] D.J. Fixsen, *The Temperature of the Cosmic Microwave Background*, *Astrophys. J.* **707** (2009) 916 [0911.1955].

[34] M. Zaldarriaga and U. Seljak, *An all sky analysis of polarization in the microwave background*, *Phys. Rev. D* **55** (1997) 1830 [astro-ph/9609170].

[35] R.K. Sachs and A.M. Wolfe, *Perturbations of a cosmological model and angular variations of the microwave background*, *Astrophys. J.* **147** (1967) 73.

[36] M. Zaldarriaga and D.D. Harari, *Analytic approach to the polarization of the cosmic microwave background in flat and open universes*, *Phys. Rev. D* **52** (1995) 3276 [astro-ph/9504085].

[37] Z. Hou, R. Keisler, L. Knox, M. Millea and C. Reichardt, *How Massless Neutrinos Affect the Cosmic Microwave Background Damping Tail*, *Phys. Rev. D* **87** (2013) 083008 [1104.2333].

[38] M. Kamionkowski, A. Kosowsky and A. Stebbins, *Statistics of cosmic microwave background polarization*, *Phys. Rev. D* **55** (1997) 7368 [astro-ph/9611125].

[39] A. Kosowsky, *Cosmic microwave background polarization*, *Annals Phys.* **246** (1996) 49 [astro-ph/9501045].

[40] A. Cooray, A. Melchiorri and J. Silk, *Is the cosmic microwave background circularly polarized?*, *Phys. Lett. B* **554** (2003) 1 [astro-ph/0205214].

[41] M. Giovannini, *The V-mode polarization of the Cosmic Microwave Background*, *Phys. Rev. D* **80** (2009) 123013 [0909.3629].

[42] S. De and H. Tashiro, *Circular Polarization of the CMB: A probe of the First stars*, *Phys. Rev. D* **92** (2015) 123506 [1401.1371].

[43] P. Montero-Camacho and C.M. Hirata, *Exploring circular polarization in the CMB due to conventional sources of cosmic birefringence*, *JCAP* **08** (2018) 040 [1803.04505].

[44] N. Lemarchand, J. Grain, G. Hurier, F. Lacasa and A. Ferté, *Secondary CMB anisotropies from magnetized haloes - I. Power spectra of the Faraday rotation angle and conversion rate*, *Astron. Astrophys.* **630** (2019) A149 [1810.09221].

[45] D. Ejlli, *On the CMB circular polarization: I. The Cotton–Mouton effect*, *Eur. Phys. J. C* **79** (2019) 231 [1810.04947].

[46] V.A. Kostelecky and M. Mewes, *Lorentz-violating electrodynamics and the cosmic microwave background*, *Phys. Rev. Lett.* **99** (2007) 011601 [astro-ph/0702379].

[47] S. Alexander, J. Ochoa and A. Kosowsky, *Generation of Circular Polarization of the Cosmic Microwave Background*, *Phys. Rev. D* **79** (2009) 063524 [0810.2355].

[48] D. Ejlli, *Magneto-optic effects of the cosmic microwave background*, *Nucl. Phys. B* **935** (2018) 83 [1607.02094].

[49] D. Ejlli, *Millicharged fermion vacuum polarization in a cosmic magnetic field and generation of CMB elliptic polarization*, *Phys. Rev. D* **96** (2017) 023540 [1704.01894].

[50] N. Bartolo, A. Hoseinpour, S. Matarrese, G. Orlando and M. Zarei, *CMB Circular and B-mode Polarization from New Interactions*, *Phys. Rev. D* **100** (2019) 043516 [1903.04578].

[51] K. Inomata and M. Kamionkowski, *Circular polarization of the cosmic microwave background from vector and tensor perturbations*, *Phys. Rev. D* **99** (2019) 043501 [1811.04957].

[52] A. Hoseinpour, M. Zarei, G. Orlando, N. Bartolo and S. Matarrese, *CMB V modes from photon-photon forward scattering revisited*, *Phys. Rev. D* **102** (2020) 063501 [2006.14418].

[53] M. Kamionkowski, A. Kosowsky and A. Stebbins, *A Probe of primordial gravity waves and vorticity*, *Phys. Rev. Lett.* **78** (1997) 2058 [astro-ph/9609132].

[54] U. Seljak and M. Zaldarriaga, *Signature of gravity waves in polarization of the microwave background*, *Phys. Rev. Lett.* **78** (1997) 2054 [astro-ph/9609169].

[55] M. Li and X. Zhang, *Cosmological CPT violating effect on CMB polarization*, *Phys. Rev. D* **78** (2008) 103516 [0810.0403].

[56] M. Pospelov, A. Ritz, C. Skordis, A. Ritz and C. Skordis, *Pseudoscalar perturbations and polarization of the cosmic microwave background*, *Phys. Rev. Lett.* **103** (2009) 051302 [0808.0673].

[57] A. Lue, L.-M. Wang and M. Kamionkowski, *Cosmological signature of new parity violating interactions*, *Phys. Rev. Lett.* **83** (1999) 1506 [astro-ph/9812088].

[58] M. Zaldarriaga and U. Seljak, *Gravitational lensing effect on cosmic microwave background polarization*, *Phys. Rev. D* **58** (1998) 023003 [astro-ph/9803150].

[59] M. Kamionkowski and E.D. Kovetz, *The Quest for B Modes from Inflationary Gravitational Waves*, *Ann. Rev. Astron. Astrophys.* **54** (2016) 227 [1510.06042].

[60] P.J. Peebles, *The Large-Scale Structure of the Universe*, Princeton University Press (11, 1980).

[61] F. Bernardeau, S. Colombi, E. Gaztanaga and R. Scoccimarro, *Large scale structure of the universe and cosmological perturbation theory*, *Phys. Rept.* **367** (2002) 1 [astro-ph/0112551].

[62] D.J. Eisenstein and W. Hu, *Baryonic features in the matter transfer function*, *Astrophys. J.* **496** (1998) 605 [astro-ph/9709112].

[63] H.J. Mo and S.D.M. White, *An Analytic model for the spatial clustering of dark matter halos*, *Mon. Not. Roy. Astron. Soc.* **282** (1996) 347 [astro-ph/9512127].

[64] N. Kaiser, *Clustering in real space and in redshift space*, *Mon. Not. Roy. Astron. Soc.* **227** (1987) 1.

[65] SDSS collaboration, *The 2.5 m Telescope of the Sloan Digital Sky Survey*, *Astron. J.* **131** (2006) 2332 [astro-ph/0602326].

[66] eBOSS collaboration, *Sloan Digital Sky Survey IV: Mapping the Milky Way, Nearby Galaxies and the Distant Universe*, *Astron. J.* **154** (2017) 28 [1703.00052].

[67] DES collaboration, *The Dark Energy Survey*, astro-ph/0510346.

[68] eBOSS collaboration, *The Completed SDSS-IV extended Baryon Oscillation Spectroscopic Survey: BAO and RSD measurements from anisotropic clustering analysis of the Quasar Sample in configuration space between redshift 0.8 and 2.2*, *Mon. Not. Roy. Astron. Soc.* **500** (2020) 1201 [2007.08998].

[69] DESI collaboration, *The DESI Experiment, a whitepaper for Snowmass 2013*, 1308.0847.

[70] LSST collaboration, *LSST: from Science Drivers to Reference Design and Anticipated Data Products*, *Astrophys. J.* **873** (2019) 111 [0805.2366].

[71] A. Arbey and F. Mahmoudi, *Dark matter and the early Universe: a review*, *Prog. Part. Nucl. Phys.* **119** (2021) 103865 [2104.11488].

[72] P.J.E. Peebles, *Large scale background temperature and mass fluctuations due to scale invariant primeval perturbations*, *Astrophys. J. Lett.* **263** (1982) L1.

[73] M. Davis, G. Efstathiou, C.S. Frenk and S.D.M. White, *The Evolution of Large Scale Structure in a Universe Dominated by Cold Dark Matter*, *Astrophys. J.* **292** (1985) 371.

[74] G.R. Blumenthal, S.M. Faber, J.R. Primack and M.J. Rees, *Formation of Galaxies and Large Scale Structure with Cold Dark Matter*, *Nature* **311** (1984) 517.

[75] K. Garrett and G. Duda, *Dark Matter: A Primer*, *Adv. Astron.* **2011** (2011) 968283 [1006.2483].

[76] G. Bertone, D. Hooper and J. Silk, *Particle dark matter: Evidence, candidates and constraints*, *Phys. Rept.* **405** (2005) 279 [hep-ph/0404175].

[77] S.M. Faber and R.E. Jackson, *Velocity dispersions and mass to light ratios for elliptical galaxies*, *Astrophys. J.* **204** (1976) 668.

[78] F. Zwicky, *On the Masses of Nebulae and of Clusters of Nebulae*, *Astrophys. J.* **86** (1937) 217.

[79] D. Clowe, A. Gonzalez and M. Markevitch, *Weak lensing mass reconstruction of the interacting cluster 1E0657-558: Direct evidence for the existence of dark matter*, *Astrophys. J.* **604** (2004) 596 [astro-ph/0312273].

[80] D. Clowe, M. Bradac, A.H. Gonzalez, M. Markevitch, S.W. Randall, C. Jones et al., *A direct empirical proof of the existence of dark matter*, *Astrophys. J. Lett.* **648** (2006) L109 [astro-ph/0608407].

[81] M. Markevitch, A.H. Gonzalez, D. Clowe, A. Vikhlinin, L. David, W. Forman et al., *Direct constraints on the dark matter self-interaction cross-section from the merging galaxy cluster 1E0657-56*, *Astrophys. J.* **606** (2004) 819 [astro-ph/0309303].

[82] ACT collaboration, *Atacama Cosmology Telescope measurements of a large sample of candidates from the Massive and Distant Clusters of WISE Survey - Sunyaev-Zeldovich effect confirmation of MaDCoWS candidates using ACT*, *Astron. Astrophys.* **653** (2021) A135 [2105.00068].

[83] J.L. Feng, *Dark Matter Candidates from Particle Physics and Methods of Detection*, *Ann. Rev. Astron. Astrophys.* **48** (2010) 495 [1003.0904].

[84] R.D. Peccei and H.R. Quinn, *CP Conservation in the Presence of Instantons*, *Phys. Rev. Lett.* **38** (1977) 1440.

[85] R.D. Peccei and H.R. Quinn, *Constraints Imposed by CP Conservation in the Presence of Instantons*, *Phys. Rev. D* **16** (1977) 1791.

[86] M. Gell-Mann, P. Ramond and R. Slansky, *Complex Spinors and Unified Theories*, *Conf. Proc. C* **790927** (1979) 315 [1306.4669].

[87] P. Minkowski, $\mu \to e\gamma$ *at a Rate of One Out of* 10^9 *Muon Decays?*, *Phys. Lett. B* **67** (1977) 421.

[88] D.M. Jacobs, G.D. Starkman and B.W. Lynn, *Macro Dark Matter*, *Mon. Not. Roy. Astron. Soc.* **450** (2015) 3418 [1410.2236].

[89] B.J. Carr, *Primordial black holes*, in *Workshop on Conference on the Future of Theoretical Physics and Cosmology in Honor of Steven Hawking's 60th Birthday*, pp. 236–263, 1, 2002.

[90] B.J. Carr and A.M. Green, *The History of Primordial Black Holes*, 2406.05736.

[91] B.J. Carr, K. Kohri, Y. Sendouda and J. Yokoyama, *New cosmological constraints on primordial black holes*, *Phys. Rev. D* **81** (2010) 104019 [0912.5297].

[92] B. Carr, K. Kohri, Y. Sendouda and J. Yokoyama, *Constraints on primordial black holes*, *Rept. Prog. Phys.* **84** (2021) 116902 [2002.12778].

[93] D.N. Spergel and P.J. Steinhardt, *Observational evidence for selfinteracting cold dark matter*, *Phys. Rev. Lett.* **84** (2000) 3760 [astro-ph/9909386].

[94] S. Tulin and H.-B. Yu, *Dark Matter Self-interactions and Small Scale Structure*, *Phys. Rept.* **730** (2018) 1 [1705.02358].

[95] M. Milgrom, *A Modification of the Newtonian dynamics as a possible alternative to the hidden mass hypothesis*, *Astrophys. J.* **270** (1983) 365.

[96] B. Famaey and S. McGaugh, *Modified Newtonian Dynamics (MOND): Observational Phenomenology and Relativistic Extensions*, *Living Rev. Rel.* **15** (2012) 10 [1112.3960].

[97] G. Jungman, M. Kamionkowski and K. Griest, *Supersymmetric dark matter*, *Phys. Rept.* **267** (1996) 195 [hep-ph/9506380].

[98] P. Gondolo, J. Edsjo, P. Ullio, L. Bergstrom, M. Schelke and E.A. Baltz, *DarkSUSY: Computing supersymmetric dark matter properties numerically*, *JCAP* **07** (2004) 008 [astro-ph/0406204].

[99] J.R. Ellis, K.A. Olive, Y. Santoso and V.C. Spanos, *Supersymmetric dark matter in light of WMAP*, *Phys. Lett. B* **565** (2003) 176 [hep-ph/0303043].

[100] J.R. Ellis, A. Ferstl and K.A. Olive, *Reevaluation of the elastic scattering of supersymmetric dark matter*, *Phys. Lett. B* **481** (2000) 304 [hep-ph/0001005].

[101] C. Boehm, A. Djouadi and M. Drees, *Light scalar top quarks and supersymmetric dark matter*, *Phys. Rev. D* **62** (2000) 035012 [hep-ph/9911496].

[102] F. Donato, N. Fornengo and P. Salati, *Anti-deuterons as a signature of supersymmetric dark matter*, *Phys. Rev. D* **62** (2000) 043003 [hep-ph/9904481].

[103] L. Bergstrom, J. Edsjo and P. Ullio, *Cosmic anti-protons as a probe for supersymmetric dark matter?*, *Astrophys. J.* **526** (1999) 215 [astro-ph/9902012].

[104] K. Griest, M. Kamionkowski and M.S. Turner, *Supersymmetric Dark Matter Above the W Mass*, *Phys. Rev. D* **41** (1990) 3565.

[105] L. Randall and R. Sundrum, *A Large mass hierarchy from a small extra dimension*, *Phys. Rev. Lett.* **83** (1999) 3370 [hep-ph/9905221].

[106] J.L. Feng, M. Kaplinghat, H. Tu and H.-B. Yu, *Hidden Charged Dark Matter*, *JCAP* **07** (2009) 004 [0905.3039].

[107] N. Arkani-Hamed, S. Dimopoulos and G.R. Dvali, *The Hierarchy problem and new dimensions at a millimeter*, *Phys. Lett. B* **429** (1998) 263 [hep-ph/9803315].

[108] M. Cirelli, N. Fornengo and A. Strumia, *Minimal dark matter*, *Nucl. Phys. B* **753** (2006) 178 [hep-ph/0512090].

[109] LZ collaboration, *The LUX-ZEPLIN (LZ) Experiment*, *Nucl. Instrum. Meth. A* **953** (2020) 163047 [1910.09124].

[110] LZ collaboration, *First Dark Matter Search Results from the LUX-ZEPLIN (LZ) Experiment*, *Phys. Rev. Lett.* **131** (2023) 041002 [2207.03764].

[111] XENON collaboration, *The XENON1T Dark Matter Experiment*, *Eur. Phys. J. C* **77** (2017) 881 [1708.07051].

[112] R.J. Gaitskell, *Direct detection of dark matter*, *Ann. Rev. Nucl. Part. Sci.* **54** (2004) 315.

[113] T.R. Slatyer, *Indirect detection of dark matter.*, in *Theoretical Advanced Study Institute in Elementary Particle Physics: Anticipating the Next Discoveries in Particle Physics*, pp. 297–353, 2018, DOI [1710.05137].

[114] Fermi-LAT collaboration, *Fermi Large Area Telescope Third Source Catalog*, *Astrophys. J. Suppl.* **218** (2015) 23 [1501.02003].

[115] Fermi-LAT collaboration, *Anisotropies in the diffuse gamma-ray background measured by the Fermi LAT*, *Phys. Rev. D* **85** (2012) 083007 [1202.2856].

[116] IceCube collaboration, *Evidence for High-Energy Extraterrestrial Neutrinos at the IceCube Detector*, *Science* **342** (2013) 1242856 [1311.5238].

[117] IceCube collaboration, *Observation of High-Energy Astrophysical Neutrinos in Three Years of IceCube Data*, *Phys. Rev. Lett.* **113** (2014) 101101 [1405.5303].

[118] R.D. Peccei, *The Strong CP problem and axions*, *Lect. Notes Phys.* **741** (2008) 3 [hep-ph/0607268].

[119] C. Abel et al., *Measurement of the Permanent Electric Dipole Moment of the Neutron*, *Phys. Rev. Lett.* **124** (2020) 081803 [2001.11966].

[120] S. Weinberg, *A New Light Boson?*, *Phys. Rev. Lett.* **40** (1978) 223.

[121] F. Wilczek, *Problem of Strong P and T Invariance in the Presence of Instantons*, *Phys. Rev. Lett.* **40** (1978) 279.

[122] T.W. Donnelly, S.J. Freedman, R.S. Lytel, R.D. Peccei and M. Schwartz, *Do Axions Exist?*, *Phys. Rev. D* **18** (1978) 1607.

[123] L.J. Hall and M.B. Wise, *FLAVOR CHANGING HIGGS - BOSON COUPLINGS*, *Nucl. Phys. B* **187** (1981) 397.

[124] F. Wilczek, *Decays of Heavy Vector Mesons Into Higgs Particles*, *Phys. Rev. Lett.* **39** (1977) 1304.

[125] A. Zehnder, *Axion Search in a Monochromatic γ Transition: A New Lower Limit for the Axion Mass*, *Phys. Lett. B* **104** (1981) 494.

[126] J.E. Kim, *Weak Interaction Singlet and Strong CP Invariance*, *Phys. Rev. Lett.* **43** (1979) 103.

[127] M.A. Shifman, A.I. Vainshtein and V.I. Zakharov, *Can Confinement Ensure Natural CP Invariance of Strong Interactions?*, *Nucl. Phys. B* **166** (1980) 493.

[128] M. Dine, W. Fischler and M. Srednicki, *A Simple Solution to the Strong CP Problem with a Harmless Axion*, *Phys. Lett. B* **104** (1981) 199.

[129] A.R. Zhitnitsky, *On Possible Suppression of the Axion Hadron Interactions. (In Russian)*, *Sov. J. Nucl. Phys.* **31** (1980) 260.

[130] J. McDonald, *Gauge singlet scalars as cold dark matter*, *Phys. Rev. D* **50** (1994) 3637 [hep-ph/0702143].

[131] W. Lin and T.T. Yanagida, *Consistency of the string inspired electroweak axion with cosmic birefringence*, *Phys. Rev. D* **107** (2023) L021302 [2208.06843].

[132] G. Cacciapaglia, G. Ferretti, T. Flacke and H. Serôdio, *Light scalars in composite Higgs models*, *Front. in Phys.* **7** (2019) 22 [1902.06890].

[133] C.P. Burgess, M. Pospelov and T. ter Veldhuis, *The Minimal model of nonbaryonic dark matter: A Singlet scalar*, *Nucl. Phys. B* **619** (2001) 709 [hep-ph/0011335].

[134] P. Svrcek and E. Witten, *Axions In String Theory*, *JHEP* **06** (2006) 051 [hep-th/0605206].

[135] A. Vilenkin and A.E. Everett, *Cosmic Strings and Domain Walls in Models with Goldstone and PseudoGoldstone Bosons*, *Phys. Rev. Lett.* **48** (1982) 1867.

[136] M.C. Huang and P. Sikivie, *The Structure of Axionic Domain Walls*, *Phys. Rev. D* **32** (1985) 1560.

[137] R.L. Davis, *Cosmic Axions from Cosmic Strings*, *Phys. Lett. B* **180** (1986) 225.

[138] A. Arvanitaki, S. Dimopoulos, S. Dubovsky, N. Kaloper and J. March-Russell, *String Axiverse*, *Phys. Rev. D* **81** (2010) 123530 [0905.4720].

[139] R. Hlozek, D. Grin, D.J.E. Marsh and P.G. Ferreira, *A search for ultralight axions using precision cosmological data*, *Phys. Rev. D* **91** (2015) 103512 [1410.2896].

[140] D.J.E. Marsh, *Axion Cosmology*, *Phys. Rept.* **643** (2016) 1 [1510.07633].

[141] N. Kitajima, F. Kozai, F. Takahashi and W. Yin, *Power spectrum of domain-wall network, and its implications for isotropic and anisotropic cosmic birefringence*, *JCAP* **10** (2022) 043 [2205.05083].

[142] M. Jain, A.J. Long and M.A. Amin, *CMB birefringence from ultralight-axion string networks*, *JCAP* **05** (2021) 055 [2103.10962].

[143] K. Harigaya, M. Ibe, K. Schmitz and T.T. Yanagida, *Peccei-Quinn symmetry from a gauged discrete R symmetry*, *Phys. Rev. D* **88** (2013) 075022 [1308.1227].

[144] L. Di Luzio, E. Nardi and L. Ubaldi, *Accidental Peccei-Quinn symmetry protected to arbitrary order*, *Phys. Rev. Lett.* **119** (2017) 011801 [1704.01122].

[145] P. Arias, D. Cadamuro, M. Goodsell, J. Jaeckel, J. Redondo and A. Ringwald, *WISPy Cold Dark Matter*, *JCAP* **06** (2012) 013 [1201.5902].

[146] L. Visinelli, *Light axion-like dark matter must be present during inflation*, *Phys. Rev. D* **96** (2017) 023013 [1703.08798].

[147] P. Adshead, J.T. Giblin, M. Pieroni and Z.J. Weiner, *Constraining axion inflation with gravitational waves from preheating*, *Phys. Rev. D* **101** (2020) 083534 [1909.12842].

[148] G. Servant, *Baryogenesis from Strong CP Violation and the QCD Axion*, *Phys. Rev. Lett.* **113** (2014) 171803 [1407.0030].

[149] H. Georgi, D.B. Kaplan and L. Randall, *Manifesting the Invisible Axion at Low-energies*, *Phys. Lett. B* **169** (1986) 73.

[150] D. Aloni, Y. Soreq and M. Williams, *Coupling QCD-Scale Axionlike Particles to Gluons*, *Phys. Rev. Lett.* **123** (2019) 031803 [1811.03474].

[151] L.F. Abbott and P. Sikivie, *A Cosmological Bound on the Invisible Axion*, *Phys. Lett. B* **120** (1983) 133.

[152] J. Preskill, M.B. Wise and F. Wilczek, *Cosmology of the Invisible Axion*, *Phys. Lett. B* **120** (1983) 127.

[153] M. Dine and W. Fischler, *The Not So Harmless Axion*, *Phys. Lett. B* **120** (1983) 137.

[154] I.G. Irastorza and J. Redondo, *New experimental approaches in the search for axion-like particles*, *Prog. Part. Nucl. Phys.* **102** (2018) 89 [1801.08127].

[155] T.W.B. Kibble, *Some Implications of a Cosmological Phase Transition*, *Phys. Rept.* **67** (1980) 183.

[156] M. Kawasaki, K. Saikawa and T. Sekiguchi, *Axion dark matter from topological defects*, *Phys. Rev. D* **91** (2015) 065014 [1412.0789].

[157] M. Buschmann, J.W. Foster, A. Hook, A. Peterson, D.E. Willcox, W. Zhang et al., *Dark matter from axion strings with adaptive mesh refinement*, *Nature Commun.* **13** (2022) 1049 [2108.05368].

[158] M. Gorghetto and G. Villadoro, *Topological Susceptibility and QCD Axion Mass: QED and NNLO corrections*, *JHEP* **03** (2019) 033 [1812.01008].

[159] M. Gorghetto, E. Hardy and G. Villadoro, *More axions from strings*, *SciPost Phys.* **10** (2021) 050 [2007.04990].

[160] W. Hu and I. Sawicki, *A Parameterized Post-Friedmann Framework for Modified Gravity*, *Phys. Rev. D* **76** (2007) 104043 [0708.1190].

[161] W.H. Press, B.S. Ryden and D.N. Spergel, *Single Mechanism for Generating Large Scale Structure and Providing Dark Missing Matter*, *Phys. Rev. Lett.* **64** (1990) 1084.

[162] W. Hu, R. Barkana and A. Gruzinov, *Cold and fuzzy dark matter*, *Phys. Rev. Lett.* **85** (2000) 1158 [astro-ph/0003365].

[163] WMAP collaboration, *Seven-Year Wilkinson Microwave Anisotropy Probe (WMAP) Observations: Sky Maps, Systematic Errors, and Basic Results*, *Astrophys. J. Suppl.* **192** (2011) 14 [1001.4744].

[164] WMAP collaboration, *Nine-Year Wilkinson Microwave Anisotropy Probe (WMAP) Observations: Cosmological Parameter Results*, *Astrophys. J. Suppl.* **208** (2013) 19 [1212.5226].

[165] SPT collaboration, *Searching for Anisotropic Cosmic Birefringence with Polarization Data from SPTpol*, *Phys. Rev. D* **102** (2020) 083504 [2006.08061].

[166] M. Dentler, D.J.E. Marsh, R. Hložek, A. Laguë, K.K. Rogers and D. Grin, *Fuzzy dark matter and the Dark Energy Survey Year 1 data*, *Mon. Not. Roy. Astron. Soc.* **515** (2022) 5646 [2111.01199].

[167] V. Iršič, M. Viel, M.G. Haehnelt, J.S. Bolton and G.D. Becker, *First constraints on fuzzy dark matter from Lyman-α forest data and hydrodynamical simulations*, *Phys. Rev. Lett.* **119** (2017) 031302 [1703.04683].

[168] M.S. Turner, *Thermal Production of Not SO Invisible Axions in the Early Universe*, *Phys. Rev. Lett.* **59** (1987) 2489.

[169] A. Salvio, A. Strumia and W. Xue, *Thermal axion production*, *JCAP* **01** (2014) 011 [1310.6982].

[170] J.P. Conlon and M.C.D. Marsh, *The Cosmophenomenology of Axionic Dark Radiation*, *JHEP* **10** (2013) 214 [1304.1804].

[171] T. Higaki, K. Nakayama and F. Takahashi, *Moduli-Induced Axion Problem*, *JHEP* **07** (2013) 005 [1304.7987].

[172] M. Cicoli, J.P. Conlon and F. Quevedo, *Dark radiation in LARGE volume models*, *Phys. Rev. D* **87** (2013) 043520 [1208.3562].

[173] P. Di Vecchia, M. Giannotti, M. Lattanzi and A. Lindner, *Round Table on Axions and Axion-like Particles*, *PoS* **Confinement2018** (2019) 034 [1902.06567].

[174] P.W. Graham, I.G. Irastorza, S.K. Lamoreaux, A. Lindner and K.A. van Bibber, *Experimental Searches for the Axion and Axion-Like Particles*, *Ann. Rev. Nucl. Part. Sci.* **65** (2015) 485 [1602.00039].

[175] C. O'Hare, *Zenodo*, *https://cajohare.github.io/AxionLimits/* (2020) .

[176] ADMX collaboration, *Search for Invisible Axion Dark Matter in the 3.3–4.2 μeV Mass Range*, *Phys. Rev. Lett.* **127** (2021) 261803 [2110.06096].

[177] MADMAX collaboration, *A new experimental approach to probe QCD axion dark matter in the mass range above 40 μeV*, *Eur. Phys. J. C* **79** (2019) 186 [1901.07401].

[178] CAST collaboration, *New CAST Limit on the Axion-Photon Interaction*, *Nature Phys.* **13** (2017) 584 [1705.02290].

[179] K. Barth et al., *CAST constraints on the axion-electron coupling*, *JCAP* **05** (2013) 010 [1302.6283].

[180] E. Armengaud et al., *Conceptual Design of the International Axion Observatory (IAXO)*, *JINST* **9** (2014) T05002 [1401.3233].

[181] N. Vinyoles, A. Serenelli, F.L. Villante, S. Basu, J. Redondo and J. Isern, *New axion and hidden photon constraints from a solar data global fit*, *JCAP* **10** (2015) 015 [1501.01639].

[182] A. Ayala, I. Domínguez, M. Giannotti, A. Mirizzi and O. Straniero, *Revisiting the bound on axion-photon coupling from Globular Clusters*, *Phys. Rev. Lett.* **113** (2014) 191302 [1406.6053].

[183] P. Gondolo and G.G. Raffelt, *Solar neutrino limit on axions and keV-mass bosons*, *Phys. Rev. D* **79** (2009) 107301 [0807.2926].

[184] P. Carenza, T. Fischer, M. Giannotti, G. Guo, G. Martínez-Pinedo and A. Mirizzi, *Improved axion emissivity from a supernova via nucleon-nucleon bremsstrahlung*, *JCAP* **10** (2019) 016 [1906.11844].

[185] G.G. Raffelt, *Astrophysical axion bounds*, *Lect. Notes Phys.* **741** (2008) 51 [hep-ph/0611350].

[186] A. Caputo and G. Raffelt, *Astrophysical Axion Bounds: The 2024 Edition*, *PoS* **COSMICWISPers** (2024) 041 [2401.13728].

[187] F. Calore, P. Carenza, M. Giannotti, J. Jaeckel and A. Mirizzi, *Bounds on axionlike particles from the diffuse supernova flux*, *Phys. Rev. D* **102** (2020) 123005 [2008.11741].

[188] F. D'Eramo, E. Di Valentino, W. Giarè, F. Hajkarim, A. Melchiorri, O. Mena et al., *Cosmological bound on the QCD axion mass, redux*, *JCAP* **09** (2022) 022 [2205.07849].

[189] M. Millea, *New cosmological bounds on axions in the XENON1T window*, 2007.05659.

[190] P. Carenza, M. Lattanzi, A. Mirizzi and F. Forastieri, *Thermal axions with multi-eV masses are possible in low-reheating scenarios*, *JCAP* **07** (2021) 031 [2104.03982].

[191] S. Hannestad, A. Mirizzi, G.G. Raffelt and Y.Y.Y. Wong, *Cosmological constraints on neutrino plus axion hot dark matter: Update after WMAP-5*, *JCAP* **04** (2008) 019 [0803.1585].

[192] M. Archidiacono, S. Hannestad, A. Mirizzi, G. Raffelt and Y.Y.Y. Wong, *Axion hot dark matter bounds after Planck*, *JCAP* **10** (2013) 020 [1307.0615].

[193] E. Di Valentino, E. Giusarma, M. Lattanzi, A. Melchiorri and O. Mena, *Axion cold dark matter: status after Planck and BICEP2*, *Phys. Rev. D* **90** (2014) 043534 [1405.1860].

[194] E. Di Valentino, E. Giusarma, M. Lattanzi, O. Mena, A. Melchiorri and J. Silk, *Cosmological Axion and neutrino mass constraints from Planck 2015 temperature and polarization data*, *Phys. Lett. B* **752** (2016) 182 [1507.08665].

[195] S.M. Carroll, G.B. Field and R. Jackiw, *Limits on a Lorentz and Parity Violating Modification of Electrodynamics*, *Phys. Rev. D* **41** (1990) 1231.

[196] S.M. Carroll, *Quintessence and the rest of the world*, *Phys. Rev. Lett.* **81** (1998) 3067 [astro-ph/9806099].

[197] E. Komatsu, *New physics from the polarized light of the cosmic microwave background*, *Nature Rev. Phys.* **4** (2022) 452 [2202.13919].

[198] Y. Minami, H. Ochi, K. Ichiki, N. Katayama, E. Komatsu and T. Matsumura, *Simultaneous determination of the cosmic birefringence and miscalibrated polarization angles from CMB experiments*, *PTEP* **2019** (2019) 083E02 [1904.12440].

[199] T. Namikawa et al., *Atacama Cosmology Telescope: Constraints on cosmic birefringence*, *Phys. Rev. D* **101** (2020) 083527 [2001.10465].

[200] V. Gluscevic and M. Kamionkowski, *Testing Parity-Violating Mechanisms with Cosmic Microwave Background Experiments*, *Phys. Rev. D* **81** (2010) 123529 [1002.1308].

[201] WMAP collaboration, *Five-Year Wilkinson Microwave Anisotropy Probe (WMAP) Observations: Angular Power Spectra*, *Astrophys. J. Suppl.* **180** (2009) 296 [0803.0593].

[202] BOSS collaboration, *Baryon acoustic oscillations in the Lyα forest of BOSS DR11 quasars*, *Astron. Astrophys.* **574** (2015) A59 [1404.1801].

[203] G. Marcy, R.P. Butler, D. Fischer, S. Vogt, J.T. Wright, C.G. Tinney et al., *Observed properties of exoplanets: Masses, orbits, and metallicities*, *Prog. Theor. Phys. Suppl.* **158** (2005) 24 [astro-ph/0505003].

[204] A. Leger et al., *Transiting exoplanets from the CoRoT space mission VIII. CoRoT-7b: the first Super-Earth with measured radius*, *Astron. Astrophys.* **506** (2009) 287 [0908.0241].

[205] LIGO, VIRGO collaboration, *Observation of Gravitational Waves from a Binary Black Hole Merger*, in *Centennial of General Relativity: A Celebration*, C.A.Z. Vasconcellos, ed., pp. 291–311 (2017), DOI.

[206] LIGO Scientific, VIRGO collaboration, *GW150914: Observation of gravitational waves from a binary black hole merger*, *Nuovo Cim. C* **39** (2017) 310.

[207] G. Bertone and D. Hooper, *History of dark matter*, *Rev. Mod. Phys.* **90** (2018) 045002 [1605.04909].

[208] N. Fornengo and M. Regis, *Particle dark matter searches in the anisotropic sky*, *Front. Physics* **2** (2014) 6 [1312.4835].

[209] N. Fornengo, L. Maccione and A. Vittino, *Constraints on particle dark matter from cosmic-ray antiprotons*, *JCAP* **04** (2014) 003 [1312.3579].

[210] A. Cuoco, J. Heisig, L. Klamt, M. Korsmeier and M. Krämer, *Scrutinizing the evidence for dark matter in cosmic-ray antiprotons*, *Phys. Rev. D* **99** (2019) 103014 [1903.01472].

[211] F.W. Stecker and M.H. Salamon, *The Gamma-ray background from blazars: A New look*, *Astrophys. J.* **464** (1996) 600 [astro-ph/9601120].

[212] Fermi-LAT collaboration, *Resolving the Extragalactic γ-Ray Background above 50 GeV with the Fermi Large Area Telescope*, *Phys. Rev. Lett.* **116** (2016) 151105 [1511.00693].

[213] S. Camera, M. Fornasa, N. Fornengo and M. Regis, *A Novel Approach in the Weakly Interacting Massive Particle Quest: Cross-correlation of Gamma-Ray Anisotropies and Cosmic Shear*, *Astrophys. J. Lett.* **771** (2013) L5 [1212.5018].

[214] S. Camera, M. Fornasa, N. Fornengo and M. Regis, *Tomographic-spectral approach for dark matter detection in the cross-correlation between cosmic shear and diffuse γ-ray emission*, *JCAP* **06** (2015) 029 [1411.4651].

[215] J.-Q. Xia, A. Cuoco, E. Branchini and M. Viel, *Tomography of the Fermi-lat γ-ray Diffuse Extragalactic Signal via Cross Correlations With Galaxy Catalogs*, *Astrophys. J. Suppl.* **217** (2015) 15 [1503.05918].

[216] A. Cuoco, J.-Q. Xia, M. Regis, E. Branchini, N. Fornengo and M. Viel, *Dark Matter Searches in the Gamma-ray Extragalactic Background via Cross-correlations With Galaxy Catalogs*, *Astrophys. J. Suppl.* **221** (2015) 29 [1506.01030].

[217] M. Fornasa et al., *Angular power spectrum of the diffuse gamma-ray emission as measured by the Fermi Large Area Telescope and constraints on its dark matter interpretation*, *Phys. Rev. D* **94** (2016) 123005 [1608.07289].

[218] M. Regis, J.-Q. Xia, A. Cuoco, E. Branchini, N. Fornengo and M. Viel, *Particle dark matter searches outside the Local Group*, *Phys. Rev. Lett.* **114** (2015) 241301 [1503.05922].

[219] J.-Q. Xia, A. Cuoco, E. Branchini, M. Fornasa and M. Viel, *A cross-correlation study of the Fermi-LAT γ-ray diffuse extragalactic signal*, *Mon. Not. Roy. Astron. Soc.* **416** (2011) 2247 [1103.4861].

[220] M. Shirasaki, S. Horiuchi and N. Yoshida, *Cross-Correlation of the Extragalactic Gamma-ray Background with Luminous Red Galaxies*, *Phys. Rev. D* **92** (2015) 123540 [1511.07092].

[221] A. Cuoco, M. Bilicki, J.-Q. Xia and E. Branchini, *Tomographic imaging of the Fermi-LAT gamma-ray sky through cross-correlations: A wider and deeper look*, *Astrophys. J. Suppl.* **232** (2017) 10 [1709.01940].

[222] S. Ammazzalorso, N. Fornengo, S. Horiuchi and M. Regis, *Characterizing the local gamma-ray Universe via angular cross-correlations*, *Phys. Rev. D* **98** (2018) 103007 [1808.09225].

[223] D. Hashimoto, O. Macias, A.J. Nishizawa, K. Hayashi, M. Takada, M. Shirasaki et al., *Constraining dark matter annihilation with HSC Low Surface Brightness Galaxies*, *JCAP* **01** (2020) 059 [1906.06701].

[224] E. Branchini, S. Camera, A. Cuoco, N. Fornengo, M. Regis, M. Viel et al., *Cross-correlating the γ-ray sky with Catalogs of Galaxy Clusters*, *Astrophys. J. Suppl.* **228** (2017) 8 [1612.05788].

[225] D. Hashimoto, A.J. Nishizawa, M. Shirasaki, O. Macias, S. Horiuchi, H. Tashiro et al., *Measurement of redshift dependent cross correlation of HSC clusters and Fermi γ rays*, 1805.08139.

[226] M. Colavincenzo, X. Tan, S. Ammazzalorso, S. Camera, M. Regis, J.-Q. Xia et al., *Searching for gamma-ray emission from galaxy clusters at low redshift*, *Mon. Not. Roy. Astron. Soc.* **491** (2020) 3225 [1907.05264].

[227] X. Tan, M. Colavincenzo and S. Ammazzalorso, *Bounds on WIMP dark matter from galaxy clusters at low redshift*, *Mon. Not. Roy. Astron. Soc.* **495** (2020) 114 [1907.06905].

[228] N. Fornengo, L. Perotto, M. Regis and S. Camera, *Evidence of Cross-correlation between the CMB Lensing and the Γ-ray sky*, *Astrophys. J. Lett.* **802** (2015) L1 [1410.4997].

[229] C. Feng, A. Cooray and B. Keating, *Planck Lensing and Cosmic Infrared Background Cross-Correlation with Fermi-LAT: Tracing Dark Matter Signals in the Gamma-Ray Background*, *Astrophys. J.* **836** (2017) 127 [1608.04351].

[230] M. Shirasaki, S. Horiuchi and N. Yoshida, *Cross-Correlation of Cosmic Shear and Extragalactic Gamma-ray Background: Constraints on the Dark Matter Annihilation Cross-Section*, *Phys. Rev. D* **90** (2014) 063502 [1404.5503].

[231] T. Tröster et al., *Cross-correlation of weak lensing and gamma rays: implications for the nature of dark matter*, *Mon. Not. Roy. Astron. Soc.* **467** (2017) 2706 [1611.03554].

[232] M. Shirasaki, O. Macias, S. Horiuchi, S. Shirai and N. Yoshida, *Cosmological constraints on dark matter annihilation and decay: Cross-correlation analysis of the extragalactic γ-ray background and cosmic shear*, *Phys. Rev. D* **94** (2016) 063522 [1607.02187].

[233] M. Shirasaki, O. Macias, S. Horiuchi, N. Yoshida, C.-H. Lee and A.J. Nishizawa, *Correlation of extragalactic γ rays with cosmic matter density distributions from weak gravitational lensing*, *Phys. Rev. D* **97** (2018) 123015 [1802.10257].

[234] DES collaboration, *Detection of Cross-Correlation between Gravitational Lensing and γ Rays*, *Phys. Rev. Lett.* **124** (2020) 101102 [1907.13484].

[235] F. Zandanel, C. Weniger and S. Ando, *The role of the eROSITA all-sky survey in searches for sterile neutrino dark matter*, *JCAP* **09** (2015) 060 [1505.07829].

[236] A. Caputo, M. Regis and M. Taoso, *Searching for Sterile Neutrino with X-ray Intensity Mapping*, *JCAP* **03** (2020) 001 [1911.09120].

[237] P. Serra, G. Lagache, O. Doré, A. Pullen and M. White, *Cross-correlation of cosmic far-infrared background anisotropies with large scale structures*, *Astron. Astrophys.* **570** (2014) A98 [1404.1933].

[238] Y. Gong, A. Cooray, K. Mitchell-Wynne, X. Chen, M. Zemcov and J. Smidt, *Axion decay and anisotropy of near-IR extragalactic background light*, *Astrophys. J.* **825** (2016) 104 [1511.01577].

[239] A. Caputo, A. Vittino, N. Fornengo, M. Regis and M. Taoso, *Searching for axion-like particle decay in the near-infrared background: an updated analysis*, *JCAP* **05** (2021) 046 [2012.09179].

[240] E. Pinetti, S. Camera, N. Fornengo and M. Regis, *Synergies across the spectrum for particle dark matter indirect detection: how HI intensity mapping meets gamma rays*, *JCAP* **07** (2020) 044 [1911.04989].

[241] D.C. Pan, M.S. Vogeley, F. Hoyle, Y.-Y. Choi and C. Park, *Cosmic Voids in Sloan Digital Sky Survey Data Release 7*, *Mon. Not. Roy. Astron. Soc.* **421** (2012) 926 [1103.4156].

[242] K.A. Douglass, D. Veyrat and S. BenZvi, *Updated void catalogs of the SDSS DR7 main sample*, 2202.01226.

[243] Q. Mao et al., *A Cosmic Void Catalog of SDSS DR12 BOSS Galaxies*, *Astrophys. J.* **835** (2017) 161 [1602.02771].

[244] D. Limber, *The analysis of counts of the extragalactic nebulae in terms of a fluctuating density field*, *Astrophys. J.* **134** (1953) A6.

[245] D.N. Limber, *The Analysis of Counts of the Extragalactic Nebulae in Terms of a Fluctuating Density Field. II*, *Astrophys. J.* **119** (1954) 655.

[246] N. Kaiser, *Weak gravitational lensing of distant galaxies*, *Astrophys. J.* **388** (1992) 272.

[247] N. Kaiser, *Weak lensing and cosmology*, *Astrophys. J.* **498** (1998) 26 [astro-ph/9610120].

[248] A. Cooray and R.K. Sheth, *Halo Models of Large Scale Structure*, *Phys. Rept.* **372** (2002) 1 [astro-ph/0206508].

[249] D. Baumann, A. Nicolis, L. Senatore and M. Zaldarriaga, *Cosmological Non-Linearities as an Effective Fluid*, *JCAP* **07** (2012) 051 [1004.2488].

[250] J.J.M. Carrasco, M.P. Hertzberg and L. Senatore, *The Effective Field Theory of Cosmological Large Scale Structures*, *JHEP* **09** (2012) 082 [1206.2926].

[251] J.J.M. Carrasco, S. Foreman, D. Green and L. Senatore, *The Effective Field Theory of Large Scale Structures at Two Loops*, *JCAP* **07** (2014) 057 [1310.0464].

[252] T. Konstandin, R.A. Porto and H. Rubira, *The effective field theory of large scale structure at three loops*, *JCAP* **11** (2019) 027 [1906.00997].

[253] R. Teyssier, *Cosmological hydrodynamics with adaptive mesh refinement: a new high resolution code called RAMSES*, *Astron. Astrophys.* **385** (2002) 337 [astro-ph/0111367].

[254] V. Springel, *The Cosmological simulation code GADGET-2*, *Mon. Not. Roy. Astron. Soc.* **364** (2005) 1105 [astro-ph/0505010].

[255] B. Moore, T.R. Quinn, F. Governato, J. Stadel and G. Lake, *Cold collapse and the core catastrophe*, *Mon. Not. Roy. Astron. Soc.* **310** (1999) 1147 [astro-ph/9903164].

[256] J.F. Navarro, C.S. Frenk and S.D.M. White, *The Structure of cold dark matter halos*, *Astrophys. J.* **462** (1996) 563 [astro-ph/9508025].

[257] VIRGO collaboration, *Galaxy clusters in Hubble volume simulations: Cosmological constraints from sky survey populations*, *Astrophys. J.* **573** (2002) 7 [astro-ph/0110246].

[258] R.E. Angulo, C.M. Baugh, C.S. Frenk and C.G. Lacey, *Extending the halo mass resolution of N-body simulations*, *Mon. Not. Roy. Astron. Soc.* **442** (2014) 3256 [1310.3880].

[259] R.A. Sunyaev and Y.B. Zeldovich, *The Velocity of clusters of galaxies relative to the microwave background. The Possibility of its measurement*, *Mon. Not. Roy. Astron. Soc.* **190** (1980) 413.

[260] A. Mead, J. Peacock, C. Heymans, S. Joudaki and A. Heavens, *An accurate halo model for fitting non-linear cosmological power spectra and baryonic feedback models*, *Mon. Not. Roy. Astron. Soc.* **454** (2015) 1958 [1505.07833].

[261] F. Schmidt, *Towards a self-consistent halo model for the nonlinear large-scale structure*, *Phys. Rev. D* **93** (2016) 063512 [1511.02231].

[262] A.Y. Chen and N. Afshordi, *Amending the halo model to satisfy cosmological conservation laws*, *Phys. Rev. D* **101** (2020) 103522 [1912.04872].

[263] P. Valageas and T. Nishimichi, *Combining perturbation theories with halo models for the matter bispectrum*, *Astron. Astrophys.* **532** (2011) A4 [1102.0641].

[264] R. Biswas, E. Alizadeh and B.D. Wandelt, *Voids as a Precision Probe of Dark Energy*, *Phys. Rev. D* **82** (2010) 023002 [1002.0014].

[265] G. Pollina, M. Baldi, F. Marulli and L. Moscardini, *Cosmic voids in coupled dark energy cosmologies: the impact of halo bias*, *Mon. Not. Roy. Astron. Soc.* **455** (2016) 3075 [1506.08831].

[266] M. Sahlén, I.n. Zubeldía and J. Silk, *Cluster–void Degeneracy Breaking: Dark Energy, Planck, and the Largest Cluster and Void*, *Astrophys. J. Lett.* **820** (2016) L7 [1511.04075].

[267] A. Pisani, P.M. Sutter, N. Hamaus, E. Alizadeh, R. Biswas, B.D. Wandelt et al., *Counting voids to probe dark energy*, *Phys. Rev. D* **92** (2015) 083531 [1503.07690].

[268] A. Barreira, M. Cautun, B. Li, C. Baugh and S. Pascoli, *Weak lensing by voids in modified lensing potentials*, *JCAP* **08** (2015) 028 [1505.05809].

[269] Y.-C. Cai, N. Padilla and B. Li, *Testing Gravity using Cosmic Voids*, *Mon. Not. Roy. Astron. Soc.* **451** (2015) 1036 [1410.1510].

[270] E.L.D. Perico, R. Voivodic, M. Lima and D.F. Mota, *Cosmic voids in modified gravity scenarios*, *Astron. Astrophys.* **632** (2019) A52 [1905.12450].

[271] R. Voivodic, M. Lima, C. Llinares and D.F. Mota, *Modelling Void Abundance in Modified Gravity*, *Phys. Rev. D* **95** (2017) 024018 [1609.02544].

[272] G. D'Amico, M. Musso, J. Norena and A. Paranjape, *Excursion Sets and Non-Gaussian Void Statistics*, *Phys. Rev. D* **83** (2011) 023521 [1011.1229].

[273] K.C. Chan, N. Hamaus and M. Biagetti, *Constraint of Void Bias on Primordial non-Gaussianity*, *Phys. Rev. D* **99** (2019) 121304 [1812.04024].

[274] H. Song and J. Lee, *The Mass Distribution of SDSS Galaxy Groups in Void Regions and Its Implication on the Primordial non-Gaussianity*, *Astrophys. J. Lett.* **701** (2009) L25 [0811.1339].

[275] Y.-C. Cai, A. Taylor, J.A. Peacock and N. Padilla, *Redshift-space distortions around voids*, *Mon. Not. Roy. Astron. Soc.* **462** (2016) 2465 [1603.05184].

[276] T. Chantavat, U. Sawangwit, P.M. Sutter and B.D. Wandelt, *Cosmological parameter constraints from CMB lensing with cosmic voids*, *Phys. Rev. D* **93** (2016) 043523 [1409.3364].

[277] N. Hamaus, B.D. Wandelt, P.M. Sutter, G. Lavaux and M.S. Warren, *Cosmology with Void-Galaxy Correlations*, *Phys. Rev. Lett.* **112** (2014) 041304 [1307.2571].

[278] N. Hamaus, P.M. Sutter, G. Lavaux and B.D. Wandelt, *Probing cosmology and gravity with redshift-space distortions around voids*, *JCAP* **11** (2015) 036 [1507.04363].

[279] N. Hamaus, A. Pisani, P.M. Sutter, G. Lavaux, S. Escoffier, B.D. Wandelt et al., *Constraints on Cosmology and Gravity from the Dynamics of Voids*, *Phys. Rev. Lett.* **117** (2016) 091302 [1602.01784].

[280] C.-H. Chuang, F.-S. Kitaura, Y. Liang, A. Font-Ribera, C. Zhao, P. McDonald et al., *Linear redshift space distortions for cosmic voids based on galaxies in redshift space*, *Phys. Rev. D* **95** (2017) 063528 [1605.05352].

[281] G. Lavaux and B.D. Wandelt, *Precision cosmography with stacked voids*, *Astrophys. J.* **754** (2012) 109 [1110.0345].

[282] J.R. Bond, S. Cole, G. Efstathiou and N. Kaiser, *Excursion set mass functions for hierarchical Gaussian fluctuations*, *Astrophys. J.* **379** (1991) 440.

[283] R.K. Sheth and R. van de Weygaert, *A Hierarchy of voids: Much ado about nothing*, *Mon. Not. Roy. Astron. Soc.* **350** (2004) 517 [astro-ph/0311260].

[284] A. De Simone, M. Maggiore and A. Riotto, *Excursion Set Theory for generic moving barriers and non-Gaussian initial conditions*, *Mon. Not. Roy. Astron. Soc.* **412** (2011) 2587 [1007.1903].

[285] E. Jennings, Y. Li and W. Hu, *The abundance of voids and the excursion set formalism*, *Mon. Not. Roy. Astron. Soc.* **434** (2013) 2167 [1304.6087].

[286] N. Hamaus, P.M. Sutter and B.D. Wandelt, *Universal Density Profile for Cosmic Voids*, *Phys. Rev. Lett.* **112** (2014) 251302 [1403.5499].

[287] A.R. Duffy, J. Schaye, S.T. Kay and C. Dalla Vecchia, *Dark matter halo concentrations in the Wilkinson Microwave Anisotropy Probe year 5 cosmology*, *Mon. Not. Roy. Astron. Soc.* **390** (2008) L64 [0804.2486].

[288] R.K. Sheth and G. Tormen, *Large scale bias and the peak background split*, *Mon. Not. Roy. Astron. Soc.* **308** (1999) 119 [astro-ph/9901122].

[289] W.H. Press and P. Schechter, *Formation of galaxies and clusters of galaxies by selfsimilar gravitational condensation*, *Astrophys. J.* **187** (1974) 425.

[290] R.K. Sheth, H.J. Mo and G. Tormen, *Ellipsoidal collapse and an improved model for the number and spatial distribution of dark matter haloes*, *Mon. Not. Roy. Astron. Soc.* **323** (2001) 1 [astro-ph/9907024].

[291] A.A. Berlind and D.H. Weinberg, *The Halo occupation distribution: Towards an empirical determination of the relation between galaxies and mass*, *Astrophys. J.* **575** (2002) 587 [astro-ph/0109001].

[292] A.A. Berlind, D.H. Weinberg, A.J. Benson, C.M. Baugh, S. Cole, R. Dave et al., *The Halo occupation distribution and the physics of galaxy formation*, *Astrophys. J.* **593** (2003) 1 [astro-ph/0212357].

[293] Z. Zheng, A.L. Coil and I. Zehavi, *Galaxy Evolution from Halo Occupation Distribution Modeling of DEEP2 and SDSS Galaxy Clustering*, *Astrophys. J.* **667** (2007) 760 [astro-ph/0703457].

[294] Z. Zheng, A.A. Berlind, D.H. Weinberg, A.J. Benson, C.M. Baugh, S. Cole et al., *Theoretical models of the halo occupation distribution: Separating central and satellite galaxies*, *Astrophys. J.* **633** (2005) 791 [astro-ph/0408564].

[295] 2MASS collaboration, *The Two Micron All Sky Survey (2MASS)*, *Astron. J.* **131** (2006) 1163.

[296] SDSS collaboration, *The Luminosity and color dependence of the galaxy correlation function*, *Astrophys. J.* **630** (2005) 1 [astro-ph/0408569].

[297] S.G. Patiri, F. Prada, J. Holtzman, A. Klypin and J. Betancort-Rijo, *The Properties of Galaxies in Voids*, *Mon. Not. Roy. Astron. Soc.* **372** (2006) 1710 [astro-ph/0605703].

[298] C.M. Urry and P. Padovani, *Unified schemes for radio-loud active galactic nuclei*, *Publ. Astron. Soc. Pac.* **107** (1995) 803 [astro-ph/9506063].

[299] M. Di Mauro, F. Calore, F. Donato, M. Ajello and L. Latronico, *Diffuse γ-ray emission from misaligned active galactic nuclei*, *Astrophys. J.* **780** (2014) 161 [1304.0908].

[300] P. Padovani et al., *Active galactic nuclei: what's in a name?*, *Astron. Astrophys. Rev.* **25** (2017) 2 [1707.07134].

[301] M. Ajello et al., *The Cosmic Evolution of Fermi BL Lacertae Objects*, *Astrophys. J.* **780** (2014) 73 [1310.0006].

[302] C.J. Willott, S. Rawlings, K.M. Blundell, M. Lacy and S.A. Eales, *The radio luminosity function from the low-frequency 3crr, 6ce & 7crs complete samples*, *Mon. Not. Roy. Astron. Soc.* **322** (2001) 536 [astro-ph/0010419].

[303] L. Lara, G. Giovannini, W.D. Cotton, L. Feretti, J.M. Marcaide, I. Marquez et al., *A New sample of large angular size radio galaxies. 3. Statistics and evolution of the grown population*, *Astron. Astrophys.* **421** (2004) 899 [astro-ph/0404373].

[304] Y. Inoue, *Contribution of the Gamma-ray Loud Radio Galaxies Core Emissions to the Cosmic MeV and GeV Gamma-Ray Background Radiation*, *Astrophys. J.* **733** (2011) 66 [1103.3946].

[305] Fermi-LAT collaboration, *GeV Observations of Star-forming Galaxies with Fermi LAT*, *Astrophys. J.* **755** (2012) 164 [1206.1346].

[306] C. Gruppioni et al., *The Herschel PEP/HerMES Luminosity Function. I: Probing the Evolution of PACS selected Galaxies to z˜4*, *Mon. Not. Roy. Astron. Soc.* **432** (2013) 23 [1302.5209].

[307] A. Constantin, F. Hoyle and M.S. Vogeley, *Active Galactic Nuclei in Void Regions*, *Astrophys. J.* **673** (2008) 715 [0710.1631].

[308] A. Furniss, P.M. Sutter, J.R. Primack and A. Domínguez, *A Correlation Between Hard Gamma-ray Sources and Cosmic Voids Along the Line of Sight*, *Mon. Not. Roy. Astron. Soc.* **446** (2015) 2267 [1407.6370].

[309] M. Ajello et al., *The Luminosity Function of Fermi-detected Flat-Spectrum Radio Quasars*, *Astrophys. J.* **751** (2012) 108 [1110.3787].

[310] M. Bartelmann, *Gravitational Lensing*, *Class. Quant. Grav.* **27** (2010) 233001 [1010.3829].

[311] C. Blanco and D. Hooper, *Constraints on Decaying Dark Matter from the Isotropic Gamma-Ray Background*, *JCAP* **03** (2019) 019 [1811.05988].

[312] J.A.R. Cembranos, A. de la Cruz-Dombriz, A. Dobado, R.A. Lineros and A.L. Maroto, *Photon spectra from WIMP annihilation*, *Phys. Rev. D* **83** (2011) 083507 [1009.4936].

[313] S. Razzaque, C.D. Dermer and J.D. Finke, *The stellar contribution to the extra-galactic background light and absorption of TeV gamma-rays*, *Astrophys. J.* **697** (2009) 483 [0807.4294].

[314] Fermi-LAT collaboration, *Unresolved Gamma-Ray Sky through its Angular Power Spectrum*, *Phys. Rev. Lett.* **121** (2018) 241101 [1812.02079].

[315] Fermi-LAT collaboration, *The spectrum of isotropic diffuse gamma-ray emission between 100 MeV and 820 GeV*, *Astrophys. J.* **799** (2015) 86 [1410.3696].

[316] N. Topchiev et al., *High-energy gamma-ray studying with GAMMA-400*, *PoS* **ICRC2017** (2018) 802 [1707.04882].

[317] DES collaboration, *Dark Energy Survey Year 3 results: Cosmological constraints from galaxy clustering and weak lensing*, *Phys. Rev. D* **105** (2022) 023520 [2105.13549].

[318] F. Donato, N. Fornengo and D. Maurin, *Antideuteron fluxes from dark matter annihilation in diffusion models*, *Phys. Rev. D* **78** (2008) 043506 [0803.2640].

[319] T. Aramaki et al., *Review of the theoretical and experimental status of dark matter identification with cosmic-ray antideuterons*, *Phys. Rept.* **618** (2016) 1 [1505.07785].

[320] H. Jeffreys, *Theory of Probability*, Oxford Classic Texts in the Physical Sciences, Oxford University Press,, Oxford, U.K. (1939).

[321] M.S. Vogeley and A.S. Szalay, *Eigenmode analysis of galaxy redshift surveys I. theory and methods*, *Astrophys. J.* **465** (1996) 34 [astro-ph/9601185].

[322] M. Tegmark, A. Taylor and A. Heavens, *Karhunen-Loeve eigenvalue problems in cosmology: How should we tackle large data sets?*, *Astrophys. J.* **480** (1997) 22 [astro-ph/9603021].

[323] S. Alexander and J. Martin, *Birefringent gravitational waves and the consistency check of inflation*, *Phys. Rev. D* **71** (2005) 063526 [hep-th/0410230].

[324] D.H. Lyth, C. Quimbay and Y. Rodriguez, *Leptogenesis and tensor polarisation from a gravitational Chern-Simons term*, *JHEP* **03** (2005) 016 [hep-th/0501153].

[325] S. Alexander and N. Yunes, *Chern-Simons Modified General Relativity*, *Phys. Rept.* **480** (2009) 1 [0907.2562].

[326] S. Dyda, E.E. Flanagan and M. Kamionkowski, *Vacuum Instability in Chern-Simons Gravity*, *Phys. Rev. D* **86** (2012) 124031 [1208.4871].

[327] M. Gerbino, A. Gruppuso, P. Natoli, M. Shiraishi and A. Melchiorri, *Testing chirality of primordial gravitational waves with Planck and future CMB data: no hope from angular power spectra*, *JCAP* **07** (2016) 044 [1605.09357].

[328] T. Fujita, Y. Minami, M. Shiraishi and S. Yokoyama, *Can primordial parity violation explain the observed cosmic birefringence?*, *Phys. Rev. D* **106** (2022) 103529 [2208.08101].

[329] N. Bartolo and G. Orlando, *Parity breaking signatures from a Chern-Simons coupling during inflation: the case of non-Gaussian gravitational waves*, *JCAP* **07** (2017) 034 [1706.04627].

[330] N. Bartolo, G. Orlando and M. Shiraishi, *Measuring chiral gravitational waves in Chern-Simons gravity with CMB bispectra*, *JCAP* **01** (2019) 050 [1809.11170].

[331] N. Bartolo, L. Caloni, G. Orlando and A. Ricciardone, *Tensor non-Gaussianity in chiral scalar-tensor theories of gravity*, *JCAP* **03** (2021) 073 [2008.01715].

[332] F. Finelli and M. Galaverni, *Rotation of Linear Polarization Plane and Circular Polarization from Cosmological Pseudo-Scalar Fields*, *Phys. Rev. D* **79** (2009) 063002 [0802.4210].

[333] K.R.S. Balaji, R.H. Brandenberger and D.A. Easson, *Spectral dependence of CMB polarization and parity*, *JCAP* **12** (2003) 008 [hep-ph/0310368].

[334] G.-C. Liu and K.-W. Ng, *Axion Dark Matter Induced Cosmic Microwave Background B-modes*, *Phys. Dark Univ.* **16** (2017) 22 [1612.02104].

[335] L.M. Capparelli, R.R. Caldwell and A. Melchiorri, *Cosmic birefringence test of the Hubble tension*, *Phys. Rev. D* **101** (2020) 123529 [1909.04621].

[336] R.R. Caldwell, V. Gluscevic and M. Kamionkowski, *Cross-Correlation of Cosmological Birefringence with CMB Temperature*, *Phys. Rev. D* **84** (2011) 043504 [1104.1634].

[337] M. Galaverni, G. Gubitosi, F. Paci and F. Finelli, *Cosmological birefringence constraints from CMB and astrophysical polarization data*, *JCAP* **08** (2015) 031 [1411.6287].

[338] R.C. Myers and M. Pospelov, *Ultraviolet modifications of dispersion relations in effective field theory*, *Phys. Rev. Lett.* **90** (2003) 211601 [hep-ph/0301124].

[339] G. Gubitosi, L. Pagano, G. Amelino-Camelia, A. Melchiorri and A. Cooray, *A Constraint on Planck-scale Modifications to Electrodynamics with CMB polarization data*, *JCAP* **08** (2009) 021 [0904.3201].

[340] G. Gubitosi, G. Genovese, G. Amelino-Camelia and A. Melchiorri, *Planck-scale modifications to Electrodynamics characterized by a space-like symmetry-breaking vector*, *Phys. Rev. D* **82** (2010) 024013 [1003.0878].

[341] L. Caloni, S. Giardiello, M. Lembo, M. Gerbino, G. Gubitosi, M. Lattanzi et al., *Probing Lorentz-violating electrodynamics with CMB polarization*, *JCAP* **03** (2023) 018 [2212.04867].

[342] S. Nakagawa, F. Takahashi and M. Yamada, *Cosmic Birefringence Triggered by Dark Matter Domination*, *Phys. Rev. Lett.* **127** (2021) 181103 [2103.08153].

[343] I. Obata, *Implications of the cosmic birefringence measurement for the axion dark matter search*, *JCAP* **09** (2022) 062 [2108.02150].

[344] V. Poulin, T.L. Smith, D. Grin, T. Karwal and M. Kamionkowski, *Cosmological implications of ultralight axionlike fields*, *Phys. Rev. D* **98** (2018) 083525 [1806.10608].

[345] D. Kim, Y. Kim, Y.K. Semertzidis, Y.C. Shin and W. Yin, *Cosmic axion force*, *Phys. Rev. D* **104** (2021) 095010 [2105.03422].

[346] A. Greco, N. Bartolo and A. Gruppuso, *Probing Axions through Tomography of Anisotropic Cosmic Birefringence*, *JCAP* **05** (2023) 026 [2211.06380].

[347] D. Gonzalez, N. Kitajima, F. Takahashi and W. Yin, *Stability of domain wall network with initial inflationary fluctuations and its implications for cosmic birefringence*, *Phys. Lett. B* **843** (2023) 137990 [2211.06849].

[348] S. Gasparotto and E.I. Sfakianakis, *Cosmic birefringence from the Axiverse*, *JCAP* **11** (2023) 017 [2306.16355].

[349] A. Greco, N. Bartolo and A. Gruppuso, *A New Solution for the Observed Isotropic Cosmic Birefringence Angle and its Implications for the Anisotropic Counterpart through a Boltzmann Approach*, 2401.07079.

[350] V. Poulin, T.L. Smith, T. Karwal and M. Kamionkowski, *Early Dark Energy Can Resolve The Hubble Tension*, *Phys. Rev. Lett.* **122** (2019) 221301 [1811.04083].

[351] T. Fujita, K. Murai, H. Nakatsuka and S. Tsujikawa, *Detection of isotropic cosmic birefringence and its implications for axionlike particles including dark energy*, *Phys. Rev. D* **103** (2021) 043509 [2011.11894].

[352] G. Choi, W. Lin, L. Visinelli and T.T. Yanagida, *Cosmic birefringence and electroweak axion dark energy*, *Phys. Rev. D* **104** (2021) L101302 [2106.12602].

[353] K. Murai, F. Naokawa, T. Namikawa and E. Komatsu, *Isotropic cosmic birefringence from early dark energy*, *Phys. Rev. D* **107** (2023) L041302 [2209.07804].

[354] S. Gasparotto and I. Obata, *Cosmic birefringence from monodromic axion dark energy*, *JCAP* **08** (2022) 025 [2203.09409].

[355] M. Kamionkowski and A.G. Riess, *The Hubble Tension and Early Dark Energy*, *Ann. Rev. Nucl. Part. Sci.* **73** (2023) 153 [2211.04492].

[356] M. Ballardini, M. Braglia, F. Finelli, D. Paoletti, A.A. Starobinsky and C. Umiltà, *Scalar-tensor theories of gravity, neutrino physics, and the H_0 tension*, *JCAP* **10** (2020) 044 [2004.14349].

[357] M. Ballardini, A.G. Ferrari and F. Finelli, *Phantom scalar-tensor models and cosmological tensions*, *JCAP* **04** (2023) 029 [2302.05291].

[358] M. Braglia, M. Ballardini, F. Finelli and K. Koyama, *Early modified gravity in light of the H_0 tension and LSS data*, *Phys. Rev. D* **103** (2021) 043528 [2011.12934].

[359] Planck collaboration, *Planck intermediate results. XLIX. Parity-violation constraints from polarization data*, *Astron. Astrophys.* **596** (2016) A110 [1605.08633].

[360] T. Namikawa, *CMB mode coupling with isotropic polarization rotation*, *Mon. Not. Roy. Astron. Soc.* **506** (2021) 1250 [2105.03367].

[361] Y. Minami and E. Komatsu, *New Extraction of the Cosmic Birefringence from the Planck 2018 Polarization Data*, *Phys. Rev. Lett.* **125** (2020) 221301 [2011.11254].

[362] P. Diego-Palazuelos et al., *Cosmic Birefringence from the Planck Data Release 4*, *Phys. Rev. Lett.* **128** (2022) 091302 [2201.07682].

[363] J.R. Eskilt, *Frequency-dependent constraints on cosmic birefringence from the LFI and HFI Planck Data Release 4*, *Astron. Astrophys.* **662** (2022) A10 [2201.13347].

[364] A. Gruppuso, D. Molinari, P. Natoli and L. Pagano, *Planck 2018 constraints on anisotropic birefringence and its cross-correlation with CMB anisotropy*, *JCAP* **11** (2020) 066 [2008.10334].

[365] M. Bortolami, M. Billi, A. Gruppuso, P. Natoli and L. Pagano, *Planck constraints on cross-correlations between anisotropic cosmic birefringence and CMB polarization*, *JCAP* **09** (2022) 075 [2206.01635].

[366] G. Zagatti, M. Bortolami, A. Gruppuso, P. Natoli, L. Pagano and G. Fabbian, *Planck constraints on Cosmic Birefringence and its cross-correlation with the CMB*, 2401.11973.

[367] BICEP/Keck collaboration, *BICEP/Keck. XVII. Line-of-sight Distortion Analysis: Estimates of Gravitational Lensing, Anisotropic Cosmic Birefringence, Patchy Reionization, and Systematic Errors*, *Astrophys. J.* **949** (2023) 43 [2210.08038].

[368] A. Greco, N. Bartolo and A. Gruppuso, *Cosmic birefrigence: cross-spectra and cross-bispectra with CMB anisotropies*, *JCAP* **03** (2022) 050 [2202.04584].

[369] E. Di Dio, F. Montanari, J. Lesgourgues and R. Durrer, *The CLASSgal code for Relativistic Cosmological Large Scale Structure*, *JCAP* **11** (2013) 044 [1307.1459].

[370] J. Lesgourgues, *The Cosmic Linear Anisotropy Solving System (CLASS) I: Overview*, 1104.2932.

[371] M. Tristram et al., *Cosmological parameters derived from the final Planck data release (PR4)*, *Astron. Astrophys.* **682** (2024) A37 [2309.10034].

[372] D. Alonso, G. Fabbian, K. Storey-Fisher, A.-C. Eilers, C. García-García, D.W. Hogg et al., *Constraining cosmology with the Gaia-unWISE Quasar Catalog and CMB lensing: structure growth*, *JCAP* **11** (2023) 043 [2306.17748].

[373] G. Piccirilli, G. Fabbian, D. Alonso, K. Storey-Fisher, J. Carron, A. Lewis et al., *Growth history and quasar bias evolution at $z < 3$ from Quaia*, *JCAP* **06** (2024) 012 [2402.05761].

[374] Gaia collaboration, *GaiaData Release 3: Summary of the content and survey properties*, *Astron. Astrophys.* **674** (2023) A1 [2208.00211].

[375] V. Gluscevic, D. Hanson, M. Kamionkowski and C.M. Hirata, *First CMB Constraints on Direction-Dependent Cosmological Birefringence from WMAP-7*, *Phys. Rev. D* **86** (2012) 103529 [1206.5546].

[376] F. Takahashi and W. Yin, *Kilobyte Cosmic Birefringence from ALP Domain Walls*, *JCAP* **04** (2021) 007 [2012.11576].

[377] P. Agrawal, M. Nee and M. Reig, *Axion couplings in grand unified theories*, *JHEP* **10** (2022) 141 [2206.07053].

[378] E. Witten, *Some Properties of O(32) Superstrings*, *Phys. Lett. B* **149** (1984) 351.

[379] J.P. Conlon, *The QCD axion and moduli stabilisation*, *JHEP* **05** (2006) 078 [hep-th/0602233].

[380] G. Efstathiou, E. Rosenberg and V. Poulin, *Improved Planck constraints on axion-like early dark energy as a resolution of the Hubble tension*, 2311.00524.

[381] D. Harari and P. Sikivie, *Effects of a Nambu-Goldstone boson on the polarization of radio galaxies and the cosmic microwave background*, *Phys. Lett. B* **289** (1992) 67.

[382] G.-C. Liu, S. Lee and K.-W. Ng, *Effect on cosmic microwave background polarization of coupling of quintessence to pseudoscalar formed from the electromagnetic field and its dual*, *Phys. Rev. Lett.* **97** (2006) 161303 [astro-ph/0606248].

[383] A. Kosowsky and A. Loeb, *Faraday rotation of microwave background polarization by a primordial magnetic field*, *Astrophys. J.* **469** (1996) 1 [astro-ph/9601055].

[384] M. Galaverni, F. Finelli and D. Paoletti, *Redshift evolution of cosmic birefringence in CMB anisotropies*, *Phys. Rev. D* **107** (2023) 083529 [2301.07971].

[385] F. Naokawa, T. Namikawa, K. Murai, I. Obata and K. Kamada, *$n\pi$ phase ambiguity of cosmic birefringence*, 2405.15538.

[386] J.R. Eskilt and E. Komatsu, *Improved constraints on cosmic birefringence from the WMAP and Planck cosmic microwave background polarization data*, *Phys. Rev. D* **106** (2022) 063503 [2205.13962].

[387] S.E. Clark, C.-G. Kim, J.C. Hill and B.S. Hensley, *The Origin of Parity Violation in Polarized Dust Emission and Implications for Cosmic Birefringence*, *Astrophys. J.* **919** (2021) 53 [2105.00120].

[388] A.J. Cukierman, S.E. Clark and G. Halal, *Magnetic Misalignment of Interstellar Dust Filaments*, *Astrophys. J.* **946** (2023) 106 [2208.07382].

[389] L. Vacher, J. Aumont, F. Boulanger, L. Montier, V. Guillet, A. Ritacco et al., *Frequency dependence of the thermal dust E/B ratio and EB correlation: Insights from the spin-moment expansion*, *Astron. Astrophys.* **672** (2023) A146 [2210.14768].

[390] P. Diego-Palazuelos et al., *Robustness of cosmic birefringence measurement against Galactic foreground emission and instrumental systematics*, *JCAP* **01** (2023) 044 [2210.07655].

[391] M. Monelli, E. Komatsu, A.E. Adler, M. Billi, P. Campeti, N. Dachlythra et al., *Impact of half-wave plate systematics on the measurement of cosmic birefringence from CMB polarization*, *JCAP* **03** (2023) 034 [2211.05685].

[392] B.G. Keating, M. Shimon and A.P.S. Yadav, *Self-Calibration of CMB Polarization Experiments*, *Astrophys. J. Lett.* **762** (2012) L23 [1211.5734].

[393] E. de la Hoz, P. Diego-Palazuelos, E. Martínez-González, P. Vielva, R.B. Barreiro and J.D. Bilbao-Ahedo, *Determination of polarization angles in CMB experiments and application to CMB component separation analyses*, *JCAP* **03** (2022) 032 [2110.14328].

[394] N.J. Miller, M. Shimon and B.G. Keating, *CMB Polarization Systematics Due to Beam Asymmetry: Impact on Cosmological Birefringence*, *Phys. Rev. D* **79** (2009) 103002 [0903.1116].

[395] B. Jost, J. Errard and R. Stompor, *Characterizing cosmic birefringence in the presence of Galactic foregrounds and instrumental systematic effects*, *Phys. Rev. D* **108** (2023) 082005 [2212.08007].

[396] L. Moncelsi et al., *Receiver development for BICEP Array, a next-generation CMB polarimeter at the South Pole*, *Proc. SPIE Int. Soc. Opt. Eng.* **11453** (2020) 1145314 [2012.04047].

[397] H. Zhai, S.-Y. Li, M. Li, H. Li and X. Zhang, *The effects on CMB power spectra and bispectra from the polarization rotation and its correlations with temperature and E-polarization*, *JCAP* **12** (2020) 051 [2006.01811].

[398] J.R. Eskilt, L. Herold, E. Komatsu, K. Murai, T. Namikawa and F. Naokawa, *Constraints on Early Dark Energy from Isotropic Cosmic Birefringence*, *Phys. Rev. Lett.* **131** (2023) 121001 [2303.15369].

[399] H. Nakatsuka, T. Namikawa and E. Komatsu, *Is cosmic birefringence due to dark energy or dark matter? A tomographic approach*, *Phys. Rev. D* **105** (2022) 123509 [2203.08560].

[400] M. Zaldarriaga, *Polarization of the microwave background in reionized models*, *Phys. Rev. D* **55** (1997) 1822 [astro-ph/9608050].

[401] E. Lifshitz, *Republication of: On the gravitational stability of the expanding universe*, *J. Phys. (USSR)* **10** (1946) 116.

[402] C.-P. Ma and E. Bertschinger, *Cosmological perturbation theory in the synchronous and conformal Newtonian gauges*, *Astrophys. J.* **455** (1995) 7 [astro-ph/9506072].

[403] W. Zhao and M. Li, *Fluctuations of cosmological birefringence and the effect on CMB B-mode polarization*, *Phys. Rev. D* **89** (2014) 103518 [1403.3997].

[404] M. Kamionkowski, J. Pradler and D.G.E. Walker, *Dark energy from the string axiverse*, *Phys. Rev. Lett.* **113** (2014) 251302 [1409.0549].

[405] M.S. Turner, *Coherent Scalar Field Oscillations in an Expanding Universe*, *Phys. Rev. D* **28** (1983) 1243.

[406] E. Masso, F. Rota and G. Zsembinszki, *Scalar field oscillations contributing to dark energy*, *Phys. Rev. D* **72** (2005) 084007 [astro-ph/0501381].

[407] D.J.E. Marsh and P.G. Ferreira, *Ultra-Light Scalar Fields and the Growth of Structure in the Universe*, *Phys. Rev. D* **82** (2010) 103528 [1009.3501].

[408] G. Floquet, *Sur les équations différentielles linéaires à coefficients périodiques*, *Annales scientifiques de l'École Normale Supérieure* **2e série, 12** (1883) 47.

[409] M.A. Amin, P. Zukin and E. Bertschinger, *Scale-Dependent Growth from a Transition in Dark Energy Dynamics*, *Phys. Rev. D* **85** (2012) 103510 [1108.1793].

[410] T.L. Smith, J.T. Giblin, M.A. Amin, M. Gerhardinger, E. Florio, M. Cerep et al., *A novel integrated Sachs-Wolfe effect from Early Dark Energy*, 2304.02028.

[411] A. Laguë, J.R. Bond, R. Hložek, K.K. Rogers, D.J.E. Marsh and D. Grin, *Constraining ultralight axions with galaxy surveys*, *JCAP* **01** (2022) 049 [2104.07802].

[412] J. Diehl and J. Weller, *Constraining ultra-light axions with galaxy cluster number counts*, *JCAP* **08** (2021) 004 [2103.08674].

[413] DESI collaboration, *The DESI Experiment Part I: Science,Targeting, and Survey Design*, 1611.00036.

[414] SPHEREx collaboration, *Cosmology with the SPHEREX All-Sky Spectral Survey*, 1412.4872.

[415] A. Challinor and A. Lewis, *The linear power spectrum of observed source number counts*, *Phys. Rev. D* **84** (2011) 043516 [1105.5292].

[416] C. Bonvin and R. Durrer, *What galaxy surveys really measure*, *Phys. Rev. D* **84** (2011) 063505 [1105.5280].

[417] V. Gluscevic, M. Kamionkowski and A. Cooray, *De-Rotation of the Cosmic Microwave Background Polarization: Full-Sky Formalism*, *Phys. Rev. D* **80** (2009) 023510 [0905.1687].

[418] D. Blas, J. Lesgourgues and T. Tram, *The Cosmic Linear Anisotropy Solving System (CLASS) II: Approximation schemes*, *JCAP* **07** (2011) 034 [1104.2933].

[419] X. Gan, L.-T. Wang and H. Xiao, *Detecting Axion Dark Matter with Black Hole Polarimetry*, 2311.02149.

[420] J.S. Reynés, J.H. Matthews, C.S. Reynolds, H.R. Russell, R.N. Smith and M.C.D. Marsh, *New constraints on light axion-like particles using Chandra transmission grating spectroscopy of the powerful cluster-hosted quasar H1821+643*, *Mon. Not. Roy. Astron. Soc.* **510** (2021) 1264 [2109.03261].

[421] C.S. Reynolds, M.C.D. Marsh, H.R. Russell, A.C. Fabian, R. Smith, F. Tombesi et al., *Astrophysical limits on very light axion-like particles from Chandra grating spectroscopy of NGC 1275*, *Astrophys. J.* **890** (2020) 59 [1907.05475].

[422] M. Kamionkowski, *How to De-Rotate the Cosmic Microwave Background Polarization*, *Phys. Rev. Lett.* **102** (2009) 111302 [0810.1286].

[423] K.M. Górski, E. Hivon, A.J. Banday, B.D. Wandelt, F.K. Hansen, M. Reinecke et al., *HEALPix - A Framework for high resolution discretization, and fast analysis of data distributed on the sphere*, *Astrophys. J.* **622** (2005) 759 [astro-ph/0409513].

[424] T. Namikawa, *Tomographic constraint on anisotropic cosmic birefringence*, 2410.05149.

[425] R.A. Sunyaev and Y.B. Zeldovich, *Small-scale fluctuations of relic radiation*, *Astrophys. Space Sci.* **7** (1970) 3.

[426] Z. Yu et al., *Quasar Accretion Disk Sizes from Continuum Reverberation Mapping in the DES Standard-star Fields*, *The Astrophysical Journal Supplement Series* **246** (2020) 16 [1811.03638].

[427] J. Kormendy and L.C. Ho, *Coevolution (Or Not) of Supermassive Black Holes and Host Galaxies*, *Ann. Rev. Astron. Astrophys.* **51** (2013) 511 [1304.7762].

[428] P.F. Hopkins, L. Hernquist, T.J. Cox, T. Di Matteo, B. Robertson and V. Springel, *A Unified, merger-driven model for the origin of starbursts, quasars, the cosmic x-ray background, supermassive black holes and galaxy spheroids*, *Astrophys. J. Suppl.* **163** (2006) 1 [astro-ph/0506398].

[429] M.C. Powell, C.M. Urry, N. Cappelluti, J.T. Johnson, S.M. LaMassa, T.T. Ananna et al., *The Clustering of X-Ray Luminous Quasars*, *The Astrophysical Journal* **891** (2020) 41 [2001.07730].

[430] J. Claeskens and J. Surdej, *Gravitational lensing in quasar samples*, *The Astron Astrophys Rev* **10** (2002) 263–311.

[431] M.A. DiPompeo, R.C. Hickox, S. Eftekharzadeh and A.D. Myers, *The characteristic halo masses of half-a-million WISE-selected quasars*, *Monthly Notices of the Royal Astronomical Society* **469** (2017) 4630–4643 [1705.05306].

[432] M. Rauch, *The lyman alpha forest in the spectra of quasistellar objects*, *Ann. Rev. Astron. Astrophys.* **36** (1998) 267 [astro-ph/9806286].

[433] C. García-García, J.R. Zapatero, D. Alonso, E. Bellini, P.G. Ferreira, E.-M. Mueller et al., *The growth of density perturbations in the last ∼10 billion years from tomographic large-scale structure data*, *JCAP* **10** (2021) 030 [2105.12108].

[434] B. Leistedt, H.V. Peiris and N. Roth, *Constraints on Primordial Non-Gaussianity from 800 000 Photometric Quasars*, *Phys. Rev. Lett.* **113** (2014) 221301 [1405.4315].

[435] eBOSS collaboration, *Redshift-weighted constraints on primordial non-Gaussianity from the clustering of the eBOSS DR14 quasars in Fourier space*, *JCAP* **09** (2019) 010 [1904.08859].

[436] SDSS collaboration, *Large scale clustering of Sloan Digital Sky Survey quasars: Impact of the baryon density and the cosmological constant*, *Publ. Astron. Soc. Jap.* **57** (2005) 529 [astro-ph/0412631].

[437] eBOSS collaboration, *The clustering of the SDSS-IV extended Baryon Oscillation Spectroscopic Survey DR14 quasar sample: first measurement of baryon acoustic oscillations between redshift 0.8 and 2.2*, *Mon. Not. Roy. Astron. Soc.* **473** (2018) 4773 [1705.06373].

[438] B.D. Sherwin et al., *The Atacama Cosmology Telescope: Cross-Correlation of CMB Lensing and Quasars*, *Phys. Rev. D* **86** (2012) 083006 [1207.4543].

[439] B. Menard and M. Bartelmann, *Cosmological information from quasar-galaxy correlations induced by weak lensing*, *Astron. Astrophys.* **386** (2002) 784 [astro-ph/0203163].

[440] G. Risaliti and E. Lusso, *A Hubble Diagram for Quasars*, *Astrophys. J.* **815** (2015) 33 [1505.07118].

[441] D. Lang, *unWISE: UNBLURRED COADDS OF THEWISEIMAGING*, *The Astronomical Journal* **147** (2014) 108 [1405.0308].

[442] A.M. Meisner, D. Lang, E.F. Schlafly and D.J. Schlegel, *unWISE Coadds: The Five-year Data Set*, *Publ. Astron. Soc. Pac.* **131** (2019) 124504 [1909.05444].

[443] E.L. Wright et al., *The Wide-field Infrared Survey Explorer (WISE): Mission Description and Initial On-orbit Performance*, *Astron. J.* **140** (2010) 1868 [1008.0031].

[444] E. Hivon, K.M. Gorski, C.B. Netterfield, B.P. Crill, S. Prunet and F. Hansen, *Master of the cosmic microwave background anisotropy power spectrum: a fast method for statistical analysis of large and complex cosmic microwave background data sets*, *Astrophys. J.* **567** (2002) 2 [astro-ph/0105302].

[445] LSST Dark Energy Science collaboration, *A unified pseudo-C_ℓ framework*, *Mon. Not. Roy. Astron. Soc.* **484** (2019) 4127 [1809.09603].

[446] M. Tegmark, *How to measure CMB power spectra without losing information*, *Phys. Rev. D* **55** (1997) 5895 [astro-ph/9611174].

[447] M. Tegmark and A. de Oliveira-Costa, *How to measure CMB polarization power spectra without losing information*, *Phys. Rev. D* **64** (2001) 063001 [astro-ph/0012120].

[448] J. Hartlap, P. Simon and P. Schneider, *Why your model parameter confidences might be too optimistic: Unbiased estimation of the inverse covariance matrix*, *Astron. Astrophys.* **464** (2007) 399 [astro-ph/0608064].

[449] E. Sellentin and A.F. Heavens, *Parameter inference with estimated covariance matrices*, *Mon. Not. Roy. Astron. Soc.* **456** (2016) L132 [1511.05969].

[450] eBOSS collaboration, *Clustering of quasars in SDSS-IV eBOSS : study of potential systematics and bias determination*, *JCAP* **07** (2017) 017 [1705.04718].

[451] M. Galaverni and F. Finelli, *Rotation of linear polarization plane from cosmological pseudoscalar fields*, *Nucl. Phys. B Proc. Suppl.* **194** (2009) 51.

[452] A. Albrecht et al., *Report of the Dark Energy Task Force*, astro-ph/0609591.

[453] L. Amendola et al., *Cosmology and fundamental physics with the Euclid satellite*, *Living Rev. Rel.* **21** (2018) 2 [1606.00180].

[454] Supernova Search Team collaboration, *Observational evidence from supernovae for an accelerating universe and a cosmological constant*, *Astron. J.* **116** (1998) 1009 [astro-ph/9805201].

[455] Supernova Cosmology Project collaboration, *Measurements of Ω and Λ from 42 High Redshift Supernovae*, *Astrophys. J.* **517** (1999) 565 [astro-ph/9812133].

[456] SDSS collaboration, *Detection of the Baryon Acoustic Peak in the Large-Scale Correlation Function of SDSS Luminous Red Galaxies*, *Astrophys. J.* **633** (2005) 560 [astro-ph/0501171].

[457] R.G. Crittenden and N. Turok, *Looking for Lambda with the Rees-Sciama effect*, *Phys. Rev. Lett.* **76** (1996) 575 [astro-ph/9510072].

[458] Planck collaboration, *Planck 2015 results. XXI. The integrated Sachs-Wolfe effect*, *Astron. Astrophys.* **594** (2016) A21 [1502.01595].

[459] H.V. Peiris and D.N. Spergel, *Cross-correlating the Sloan Digital Sky Survey with the microwave sky*, *Astrophys. J.* **540** (2000) 605 [astro-ph/0001393].

[460] N. Kaiser et al., *Pan-STARRS: A Large Synoptic Survey Telescope Array*, *Proc. SPIE Int. Soc. Opt. Eng.* **4836** (2002) 154.

[461] DES collaboration, *Dark Energy Survey Year 3 results: Cosmology from cosmic shear and robustness to data calibration*, *Phys. Rev. D* **105** (2022) 023514 [2105.13543].

[462] G.V. Kleijn, R. Vermeij, E. Valentijn and K. Kuijken, *The Secondary Standards programme for OmegaCAM at the VST*, *ASP Conf. Ser.* **364** (2007) 103 [astro-ph/0612469].

[463] S. Aune et al., *The CFHT MegaCam 40 CCDs camera: Cryogenic design and CCD integration*, in *Conference on Astronomical Telescopes and Instrumenation*, 8, 2002.

[464] K. Taylor et al., *JPCam: A 1.2Gpixel camera for the J-PAS survey*, 1301.4175.

[465] N. Dalal, C. Dvorkin, J. Heyl, B. Jain, M. Kamionkowski, P. Marshall et al., *Fundamental Physics with the Hubble Space Telescope*, 1712.04928.

[466] A. Cooray, *Integrated sachs-Wolfe effect: Large scale structure correlation*, *Phys. Rev. D* **65** (2002) 103510 [astro-ph/0112408].

[467] M. Ballardini, D. Paoletti, F. Finelli, L. Moscardini, B. Sartoris and L. Valenziano, *On the ISW-cluster cross-correlation in future surveys*, *Mon. Not. Roy. Astron. Soc.* **482** (2019) 2670 [1712.02380].

[468] J.R. Bermejo-Climent, M. Ballardini, F. Finelli, D. Paoletti, R. Maartens, J.A. Rubiño Martín et al., *Cosmological parameter forecasts by a joint 2D tomographic approach to CMB and galaxy clustering*, *Phys. Rev. D* **103** (2021) 103502 [2106.05267].

[469] SDSS collaboration, *The Eighteenth Data Release of the Sloan Digital Sky Surveys: Targeting and First Spectra from SDSS-V*, *Astrophys. J. Suppl.* **267** (2023) 44 [2301.07688].

[470] J.J. Condon, W.D. Cotton, E.W. Greisen, Q.F. Yin, R.A. Perley, G.B. Taylor et al., *The NRAO VLA Sky survey*, *Astron. J.* **115** (1998) 1693.

[471] J. Lesgourgues and S. Pastor, *Massive neutrinos and cosmology*, *Phys. Rept.* **429** (2006) 307 [astro-ph/0603494].

[472] P. Bode, J.P. Ostriker and N. Turok, *Halo formation in warm dark matter models*, *Astrophys. J.* **556** (2001) 93 [astro-ph/0010389].

[473] M. Kamionkowski, *Matter microwave correlations in an open universe*, *Phys. Rev. D* **54** (1996) 4169 [astro-ph/9602150].

[474] A. Lewis, A. Challinor and A. Lasenby, *Efficient computation of CMB anisotropies in closed FRW models*, *Astrophys. J.* **538** (2000) 473 [astro-ph/9911177].

[475] C. Howlett, A. Lewis, A. Hall and A. Challinor, *CMB power spectrum parameter degeneracies in the era of precision cosmology*, *JCAP* **04** (2012) 027 [1201.3654].

[476] G.-B. Zhao, L. Pogosian, A. Silvestri and J. Zylberberg, *Searching for modified growth patterns with tomographic surveys*, *Phys. Rev. D* **79** (2009) 083513 [0809.3791].

[477] A. Hojjati, L. Pogosian and G.-B. Zhao, *Testing gravity with CAMB and CosmoMC*, *JCAP* **08** (2011) 005 [1106.4543].

[478] A. Zucca, L. Pogosian, A. Silvestri and G.-B. Zhao, *MGCAMB with massive neutrinos and dynamical dark energy*, *JCAP* **05** (2019) 001 [1901.05956].

[479] Z. Wang, S.H. Mirpoorian, L. Pogosian, A. Silvestri and G.-B. Zhao, *New MGCAMB tests of gravity with CosmoMC and Cobaya*, *JCAP* **08** (2023) 038 [2305.05667].

[480] M. Chevallier and D. Polarski, *Accelerating universes with scaling dark matter*, *Int. J. Mod. Phys. D* **10** (2001) 213 [gr-qc/0009008].

[481] E.V. Linder, *Exploring the expansion history of the universe*, *Phys. Rev. Lett.* **90** (2003) 091301 [astro-ph/0208512].

[482] E. Bertschinger and P. Zukin, *Distinguishing Modified Gravity from Dark Energy*, *Phys. Rev. D* **78** (2008) 024015 [0801.2431].

[483] S. Matarrese and L. Verde, *The effect of primordial non-Gaussianity on halo bias*, *Astrophys. J. Lett.* **677** (2008) L77 [0801.4826].

[484] N. Dalal, O. Dore, D. Huterer and A. Shirokov, *The imprints of primordial non-gaussianities on large-scale structure: scale dependent bias and abundance of virialized objects*, *Phys. Rev. D* **77** (2008) 123514 [0710.4560].

[485] A. Slosar, C. Hirata, U. Seljak, S. Ho and N. Padmanabhan, *Constraints on local primordial non-Gaussianity from large scale structure*, *JCAP* **08** (2008) 031 [0805.3580].

[486] EUCLID collaboration, *Euclid Definition Study Report*, 1110.3193.

[487] L. Pozzetti, C.M. Hirata, J.E. Geach, A. Cimatti, C. Baugh, O. Cucciati et al., *Modelling the number density of Hα emitters for future spectroscopic near-IR space missions*, *Astron. Astrophys.* **590** (2016) A3 [1603.01453].

[488] Planck collaboration, *Planck 2013 results. XIX. The integrated Sachs-Wolfe effect*, *Astron. Astrophys.* **571** (2014) A19 [1303.5079].

[489] M. Douspis, P.G. Castro, C. Caprini and N. Aghanim, *Optimising large galaxy surveys for ISW detection*, *Astron. Astrophys.* **485** (2008) 395 [0802.0983].

[490] M. Frommert and T.A. Ensslin, *Ironing out primordial temperature fluctuations with polarisation: optimal detection of cosmic structure imprints*, 0811.4433.

[491] J. Carron, A. Lewis and G. Fabbian, *Planck integrated Sachs-Wolfe-lensing likelihood and the CMB temperature*, *Phys. Rev. D* **106** (2022) 103507 [2209.07395].

[492] M. Gerbino, M. Lattanzi, M. Migliaccio, L. Pagano, L. Salvati, L. Colombo et al., *Likelihood methods for CMB experiments*, *Front. in Phys.* **8** (2020) 15 [1909.09375].

[493] S.L. Bridle, R. Crittenden, A. Melchiorri, M.P. Hobson, R. Kneissl and A.N. Lasenby, *Analytic marginalization over CMB calibration and beam uncertainty*, *Mon. Not. Roy. Astron. Soc.* **335** (2002) 1193 [astro-ph/0112114].